Utilization of Rubber Seeds for Biofuels Production

Thesis submitted in partial fulfillment of the

requirements for the degree of

DOCTOR OF PHILOSOPHY

by

ALI SHEMSEDIN RESHAD

Department of Chemical Engineering

Indian Institute of Technology Guwahati

Guwahati–781039

Assam, India

Utilization of Rubber Seeds for Biofuels Production

Thesis submitted in partial fulfillment of the

requirements for the degree of

DOCTOR OF PHILOSOPHY

by

Ali Shemsedin Reshad

Department of Chemical Engineering

Indian Institute of Technology Guwahati

Guwahati–781039

Assam, India

April 2017

Utilization of Rubber Seeds for Biofuels Production

Ali Shemsedin Reshad

Dedicated

To

My Father

&

My beloved wife Keyrya (Hiwete)

who mean everything to me

DEPARTMENT OF CHEMICAL ENGINEERING

INDIAN INSTITUTE OF TECHNOLOGY GUWAHATI

STATEMENT

I do hereby declare that the content embodied in this thesis entitled "**UTILIZATION OF RUBBER SEEDS FOR BIOFUELS PRODUCTION**" is the result of investigations carried out by me at Department of Chemical Engineering, Indian Institute of Technology Guwahati, Guwahati, India, under the guidance of Dr. Vaibhav V. Goud and Dr. Pankaj Tiwari. In keeping with the general practice of reporting scientific observations, due acknowledgements have been made wherever the work described is based on the findings of other investigators.

Date: April 2017 Ali Shemsedin Reshad

DEPARTMENT OF CHEMICAL ENGINEERING

INDIAN INSTITUTE OF TECHNOLOGY GUWAHATI

CERTIFICATE

This is to certify that the thesis entitled **"UTILIZATION OF RUBBER SEEDS FOR BIOFUELS PRODUCTION"** submitted by **Mr. Ali Shemsedin Reshad (Roll No: 136107034)**, a research scholar in the Department of Chemical Engineering, Indian Institute of Technology Guwahati, for the award of the degree of Doctor of Philosophy, is a record of an original research work carried out by him under our supervision and guidance. The thesis has fulfilled all requirements as per the regulations of the institute and in our opinion has reached the standard needed for submission. The works documented in this thesis have not been submitted to any other University or Institute for the award of any degree.

(Dr. Vaibhav V Goud)
Associate Professor
Department of Chemical Engineering
Indian Institute of Technology Guwahati
Guwahati - 781039, Assam, India.

(Dr. Pankaj Tiwari)
Assistant Professor
Department of Chemical Engineering
Indian Institute of Technology Guwahati
Guwahati - 781039, Assam, India.

Acknowledgements

Firstly and foremost, I would like to express my deepest gratitude to my advisors **Dr. Vaibhav V. Goud and Dr. Pankaj Tiwari** for the continuous support during my Ph.D study and research, for their patience, motivation, and immense knowledge. Their guidance helped me in all the time of research and writing of this thesis. Their suggestions, encouragement and support were concrete in the completion of my Ph.D thesis. Without their precious support it would not be possible to complete this research.

Beside my advisors, sincere thanks also extended to my doctoral committee: Prof. Pallab Ghosh, Dr. Chandan Das from the Department of Chemical Engineering and Dr. Ajay Kalamdhad from the Department of Civil Engineering for their insightful comments towards the improvement of my research work and encouragement during all presentations.

My sincere gratitude goes to my course instructor Dr. Mahuya De, Prof. Uppaluri Ramgopal and Dr. Dipankar Bandyopadhyay from Department of Chemical Engineering and Prof. Kannan Pakshirajan from Department of Biosciences and Bioengineering, and all faculty members at Department of Chemical Engineering.

I am also thankful to all the staff members and scientific officers of the Chemical Engineering Department for their kind cooperation in analytical laboratory and others.

I am thankful to the Central Instruments Facility of IIT Guwahati for allowing me to carry out NMR, TGA-DSC, BET and FESEM analysis, which has been very important in this research work. In this regard, I should acknowledge the help of all members of CIF. Similarly, I am very happy to acknowledge Center for Energy for giving facility to do calorific value test which was very important for this research. It's my privilege to express my most sincere

gratitude to Dr. Vimal Katiyar for allowing me TGA-FTIR facility at Center of Excellence on Sustainable Polymers at Indian Institute of Technology Guwahati (CoESusPol IITG).

My sincere gratitude also goes to Ethiopian Ministry of Education and Adama Science and Technology University for fellowship and study leave for my PhD at IIT Guwahati.

I thank my fellow labmates such as Dr. Venu Babu Borugadda, Pallab Das, Atanu Kumar Paul, Raul Saha, Swaroopa Rani Dasari, Garima Srivastava, Abhishek Shukla, Robinson Timung, Chitta Ranjan Barik, Deoashish P. Mood Mohan, Sukumar Purohit, Sutapa Das, Prasenjit B., Jitendra Singh Rawat, Ankit Patidar, Nongmaithem Debeni Devi, Akash, Fekadu Mosisa Wako, Pushpita Das and Vikas Kumar for their fruitful discussions, feedback, cooperation and friend ship. In particular, I am grateful to Pallab Das for his help and cooperation in every aspect during all pyrolysis experiments and analysis. Also I thank my friends in the other laboratories and departments. Especial thanks also extended to "YeWendoch Guday" for memorable moments and several fruitful discussions in the past three years at IITG. I would like to express my gratitude to all those who helped me in different ways directly or indirectly in completing this research work within the time span.

My sincere gratitude goes to my parents and to my brothers and sisters for supporting me spiritually throughout journey of my life in general.

Finally, I would like to thank my beloved wife, Keyrya Adem Hussien. She is my life advisor and cheering me up all good time as well as bad time. Her single word makes me very energetic for all time.

Allahamdulilah "All are Allah's plan"

Abstract

Worldwide biodiesel is being produced mainly from edible and non-edible oils. The choice of oil depends primarily on availability, price, and the policy adopted by the governing agencies. The economic aspects of biodiesel production are the barriers for its commercial success. The production of biodiesel from non-edible oils may offer solutions for various issues involved in the assessment of biomass-based industry for energy generation. Currently, non-edible rubber seed oil extracted from the seeds of rubber trees is getting more attention for production of biofuel, because in the latex manufacturing process, rubber seeds are not historically collected and commercialized. The useful properties of the rubber seed oil make it similar to well-known linseed and soybean oil. Hence considering this as a motivation the entire work carried out in this research work is divided into three major parts; extraction of oil, transesterification and solid by product utilization to cover major aspects of biofuels production.

Rubber seed comprises of 40–48 wt% shell and 52–60 wt% kernel was subjected to oil extraction using conventional Soxhlet method. The effects of process parameters such as extraction time (3–12 h), kernel particle size range (0.5–3 mm), ratio of kernel to solvent (0.03–0.09 g/ml), and variety of solvents (polar and non-polar) on Soxhlet extraction process were studied. Response surface methodology (RSM) was applied to optimize the process parameters to achieve maximum oil yield (49.36 wt%) with hexane as solvent. ^{1}H NMR spectra of the rubber seed oil (RSO) revealed 13.17% (linolenic), 39.86% (linoleic), 27.06% (oleic) and 19.91% (saturated) fatty acids in its composition. The extracted RSO was found to contain high free fatty acid (FFA) (12%) as compared to edible vegetable oils (~1%). Since RSO is a high FFA oil, a two-step procedure, esterification using homogeneous catalyst

followed by transesterification with heterogeneous catalyst was used for rubber oil methyl ester (ROME) synthesis. The acid value of extracted RSO was reduced from 24 mg KOH/g to 2 mg KOH/g during esterification reaction using 1.5 wt% catalyst loading (H_2SO_4) and 15:1 methanol to oil molar ratio for 2 h reaction time at 30 °C. The 96% conversion of triglycerides of RSO to ROME using ultrasonic technique with ($Ba(OH)_2{\cdot}8H_2O$) as catalyst was achieved within 15 min, whereas when the same reaction was carried out with Na_3PO_4 (92.59%), CaO (97%), and calcinated egg shell (97.98%) the time taken to achieve the respective conversion was about 3 h. The highest transesterification yield was obtained with non-calcinated $Ba(OH)_2{\cdot}8H_2O$ catalyst compared to calcinated catalyst. Central composite design (CCD) using RSM was adopted to design the experimental matrix and to optimize the combined effect of process parameters; reaction time (5–15 min), catalyst loading (CL) (4–6 wt%) and methanol to oil molar ratio (MR) (6:1–9:1) on ROME conversion. The maximum conversion (~97%) was achieved at catalyst loading of 5.38 wt% with MR of 8.09:1 in 13.20 min.

Thermal degradation of RSO and ROME were investigated with the help of thermeogravimetry (TG) technique. The samples were pyrolyzed from 30 °C to 800 °C at a heating rate of 10 °C/min to 50 °C/min with 10 °C/min increment under nitrogen atmosphere. The lower thermal stability of product (ROME) compared to RSO observed in the present work attributed to decrease in the molecular weight of triglycerides during transesterification process. On the other hand, Fourier transform infrared (FT-IR) analysis of evolved gas products revealed the formation of water, carbon dioxide, carbon monoxide, saturated (alkanes), and unsaturated (alkenes) aliphatic hydrocarbons during thermal decomposition of the samples. Further, Friedman (FRD), Flynn-Wall-Ozawa (FWO) and modified Coat-

Redfern (MCR), Kissinger (KM) methods were applied to calculate the activation energy (*E*) of decomposition of RSO and ROME.

Further, the physico-chemical properties and rheological behaviour of rubber seed oil (RSO) and its derivative methyl esters (ROME) as well as ROME blends with diesel fuel (RDXX) were investigated. The viscosity behaviour of RSO, ROME and RDXX were found to be nearly Newtonian within the studied temperature range 25 °C–80 °C. The dynamic viscosity at 25 °C was found to be 25.58 mPa.s and 4.485 mPa.s for RSO and ROME, respectively. The engine performance test showed that maximum brake thermal efficiency (BTE) was achieved at 80% load with RD10 (28.36%) compared to neat diesel (24%) and a drastic improvement of overall 13% increase at all loads. However, emissions of CO, CO_2 and NO_x were reduced with the use of ROME blends.

Solid wastes generated during biodiesel feedstock preparation process comprise 40–48 wt% rubber seed shell (RSS) and 25–30 wt% rubber seed cake (RSC) was used to produce liquid fuel and bio-char. Active pyrolysis zones of RSC (175–589 °C) and RSS (265.2–530 °C) were broadly observed in three and two stages, respectively. Model-free kinetic analysis of TG data was performed using various methods. This part of work was further continued in a lab scale semi-batch pyrolysis reactor. The effects of pyrolysis temperatures (350 °C–600 °C) and heating rates (10 °C/min–40 °C/min) on product distribution (liquid, gas and bio-char) were investigated. The maximum yield of RSS pyrolytic liquid (46.14 wt%) and carbon-rich RSS bio-char (31.92 wt%) were obtained at 550 °C at a heating rate of 30 °C/min. While for RSC the maximum of pyrolytic liquid (48.25 wt%) and carbon-rich RSS bio-char (26.18 wt%) yield were obtained at 500 °C temperature at heating rate of 20 °C/min. The fuel characteristics of produced bio-char (from RSS) such as higher calorific value (34.5 MJ/kg),

higher fixed carbon (79.74 wt%), lower ash (1.87 wt%) and lower moisture content (2.11 wt%) were found better than that of RSC bio char. However, the liquid product (organic phase) obtained from pyrolysis of RSC showed much higher calorific value than RSS pyrolytic liquid. Further, the yield and quality of organic phase (bio-oil) during RSC pyrolysis was enhanced by co-pyrolysis process through addition of waste polystyrene. Value-added organic compounds such as acetic acid, phenolic compounds, amide compounds, creosol, pilocarpine, benzene and levoglucosan were identified in the pyrolytic liquid product. In depth analysis of physico-chemical-thermal properties of RSS and RSC obtained products (liquid and bio-char) using various analytical techniques suggested that both RSS and RSC can be considered as a suitable feedstock for the production of value added chemicals including fuel.

List of Tables

Chapter I

Chapter II

Chapter III

Chapter IV

Chapter V

Chapter VI

List of Figures

Chapter I

Chapter II

Chapter III

Chapter IV

Chapter V

Chapter VI

Abbreviations and Notations

AC –Ash content

ANOVA – Analysis of variance

AOCS –American oils chemists society

ASTM –American society for testing and materials

AV –Acid value

BC –Bio-char

BDXX –Blending of biodiesel with diesel

BET –Brunauer-Emmet-Teller

BP –Brake power

BSEC –Brake-specific energy consumption

BSFC –Brake-specific fuel consumption

BTE –Brake thermal efficiency

bTDC –Before top dead center

CCD –Central composite design

CHNS –Carbon hydrogen nitrogen sulfur

CIME –*Calophyllum inophyllum* oil methyl ester

CIO –*Calophyllum inophyllum* oil

CL –Catalyst loading

CMME –*Croton megalocarpus* oil methyl ester

CMO –*Croton megalocarpus* oil

COME –Coconut oil methyl ester

CPO –Crude *Ceiba pentandra* oil

CPOME –*Ceiba pentandra* oil methyl ester

CA –Crank angle

DI –Direct injection

DSC –Differential scanning calorimetry

DTG –Differential thermogravimetric

EDX –Energy dispersive X ray spectroscopy

EGT –Exhaust gas temperature

ERSO –Esterified rubber seed oil

FAME –Fatty acid methyl esters

FC –Fixed carbon

FESEM –Field emission electron scanning microscopy

FFA –Free fatty acid

FT-IR –Fourier transform infrared spectroscopy

GC-MS –Gas chromatography – Mass spectroscopy

HC –Hydrocarbon

HSD –High-speed diesel

IKP –Invariant kinetic parameters

IUPAC – International union of pure and applied chemistry

JCOME –Jatropha *curcas* oil methyl ester

MC –Moisture content

MR –Molar ratio

NAH –Nitric polycyclic aromatic hydrocarbon

NMR –Nuclear magnetic resonance

NREL –National renewable energy laboratory

PAH –Polycyclic aromatic hydrocarbon

POME –Palm oil methyl ester

RDXX –Rubber seed oil methyl ester−diesel blends

ROME –Rubber seed oil methyl ester

RSC –Rubber seed cake

RSC-BC –Rubber seed cake bio-char

RSM –Response surface methodology

RSO –Rubber seed oil

RSS –Rubber seed shell

RSS-BC –Rubber seed shell bio-char

SFC –Specific fuel consumption

TAG –Tiryglyceride

TG –Thermogravimetric

TGA –Thermogarvimetric analysis

THC –Total hydrocarbon

UC –Ultrasonic cleaner

UH –Ultrasonic horn

VM –Volatile matter

WPS –Waste polystyrene

XRD –X- ray diffraction

XX –Amount of ROME (by volume) blended with diesel

Notations

A – Pre-exponential factor (1/min)

D – Crystallite size (nm)

E – Activation energy (kJ/mol)

f(α) – Temperature-independent function of conversion or the reaction model

k – Flow consistency index obtained from power law model

k – Rate constant

k_{exp} – Average dynamic viscosity obtained from experiment

l –Full width at half maximum intensity (radian)

n – Order of reaction model

R – Gas constant (8.314 J/ mol. K)

R^2 – Correlation coefficient

t – Time (min)

T_o – Initial temperature for the main mass loss (°C)

T_f– Final temperature for the main mass loss (°C)

T_p or T_{max} – Temperature for maximum rate of mass loss (°C)

T50 – Temperature at which 50 wt% loss of sample (°C)

w_A – Mass of ash obtained after 3 h at 575 °C (g)

w_c – Mass of empty dried crucible after heated for 3 h at 105 °C

w_f – mass of residue obtained after 7 min at 950 °C (g)

w_{fr} – Mass of moisture free sample (g) after heated for 16 h at 105 °C

w_o – Mass of raw sample (g)

w_{OD}– Mass of oven dried sample (free MC) (g)

$wt\%$– Mass loss (%)

$wt\%_f$ – Mass loss at end of active pyrolysis (%)

$wt\%_t$ – Mass loss at time t (%)

$X\ (\%)$ – Conversion of RSO to ROME

X_E – Fractional conversion of FFA

α – TGA conversion of biomass (wt%)

β – Heating rate (°C/min)

θ –Half of the diffraction angle/Bragg angle

λ – Wave length of Cu-K_α (nm)

Units

vol/wt% –Percentage in volume (ml) per mass (g)

wt% –Weight percentage

% –Percentage

cSt –Centistoke

°C –Degree centigrade

cp –Centipoise

m.Pa.s –Millipascal second

mg KOH/g –Milligrams of KOH per gram

h –Hour

kHz –Kilo hertz

µl –Microliter

g –Gram

$gI_2/100$ g –Grams of iodine per 100 g

°C/min –Degree centigrade per minute

kg/m^3 –Kilogram per cubic meter

kg –Kilogram

m^3 –Cubic meter

min –Minute

ml/min –Milliliter per minute

mw –Milliwatt

MJ/kg –Mega joule per kilogram

nm –Nano meter

kJ/mol –Kilo joule per mole

Subscript

i – TGA conversion

j – Heating rate

k – TGA conversion function

o – Initial

f – Final

t –Time

CHAPTER I

Introduction and Literature Review

Motivation;

Current Biofuel Scenario;

Objectives;

Thesis Organization

Part of the Work Published As:

Reshad, A.S., Tiwari, P., Goud, V.V., 2016. Production of Biodiesel from Renewable Resources, In: Singh, R.S., Pandey, A., Gnansounou, E. (Editors), Biofuels: Production and future perspectives. Taylor & Francis Group, PP: 223–242.

Chapter I

Introduction and Literature Review

In this chapter, a brief discussion on alternative energy demands, biofuels and suitable techniques for production of biofuels from oilseeds are provided. The focus is also towards selection of suitable feedstock (i.e. non-edible feedstock) for the production of biodiesel and its sustainability for the future is discussed. The chapter elaborates the catalytic and non-catalytic transesterification processes for various feedstocks. Further, the chapter also emphasis on utilization of solid waste (by-product) generated during feedstock preparation for biodiesel synthesis (i.e. during oil extraction process) for value added chemical and fuel production. The current state of the art literature related to production of biofuels from oilseed is reviewed. Subsequently, the possible scope for further research directions and a research topic for the chosen field has been formulated. Finally, specific objectives of the thesis and its organization are summarized in this chapter.

1.1. Introduction

Excessive demand of fossil fuels and their limited availability impose scarcity of supplying energy for various needs, especially in developing countries. About 80% world energy consumption is dependent on ordinary fossil fuels [1, 2]. The growth of population, industrialization revolution, improved living standard, environmental concerns and sustainable development issues have made especial attention to search for an alternative sources of renewable energy [2-8]. On the other hand, the petrochemical age have resulted a

massive pollution on air, water and soil as well as emission of anthropogenic greenhouse gases (GHGs) cause irreversible climate change [1, 9]. It is well reported that massive pollution is related to excessive usages of fossil fuels [10, 11]. Both finite sources of fossil fuels and environment issues are major concerns to search for an alternative source of renewable energy [10, 12, 13]. Utilization of renewable energy resources for the production of biofuels is one way of partial substituting of fossil fuels as well as a significant reduction of emission of greenhouse gases to the atmosphere. Hence, significant attention to our energy utilization and reducing dependence on non-renewable energy sources is required for sustainable and carbon-neutral energy for the future. Meanwhile, effective utilization of renewable energy sources and technologies will be needed to overcome the challenges of fossil fuels. The use of biomass can play a major role in this manner [1, 2, 9]. The term biomass refers to all organic materials that obtained from plants (including woody material, grass, algae, trees and crops) through natural processes or by-product of human activities. It is a primary source of energy in which the energy of sun light is stored in the form of chemical bonds. Currently, the biomass source of energy contributes 10–14% of the world energy supply, but theoretically it has a potential to supply 100% of world energy supply [1, 2]. According to the report by the European Environment Agency (EEA, 2013), 20% of the final energy consumption has to be provided using renewable resources (i.e. biofuel) by 2020. Utilization of biomass would not only reduce our dependence on fossil energy sources, but also improve energy in a sustainable and carbon-neutral manner. But biomass utilization in the traditional way has negative effects. Most present-day production and use of biomass for energy are carried out in a very unsustainable manner with a great many negative environmental consequences [2, 8].

1.2. Biofuels

Biofuel is a generic name for solid, liquid or gaseous fuels that are not derived from petroleum–based fossil fuel or contain a proportion of non-fossil fuel. Biofuels are produced from biomass sources such as woody materials, corn, soybeans, flaxseed, rapeseed, sugarcane, bagasse, sorghum, rice husks, palm oil, sugar beet, raw sewage, food scraps, animal parts, agricultural waste, rubber seed, algae, etc [2]. Biomass can be converted into valuable chemicals and fuels such as biodiesel, bio-ethanol, bio-methanol, bio-oil, bio-char, syngas (CO, CO_2, CH_4, H_2), etc. Basically, there are three principal methods of conversion of solid biomass into value-added products: (1) physical-chemical conversion, (2) thermo-chemical conversion and (3) bio-chemical conversion (Fig. 1.1). Biological catalysts and organisms are used to produce energy rich products from biomass in the bio-chemical conversion process, while heat and chemical catalysts are used in the thermo-chemical conversion process to produce liquid, solid and gaseous fuels. The complete conversion of biomass into energy through bio-chemical technique is one major challenge. However, this limitation may be overcome by applying thermo-chemical technique [14]. With this regard, the present study is focused mainly on the production of biodiesel from non-edible resource and, bio-oil and bio-char from solid waste generated during the preparation of feedstock for biodiesel production through physical-chemical and thermo-chemical methods.

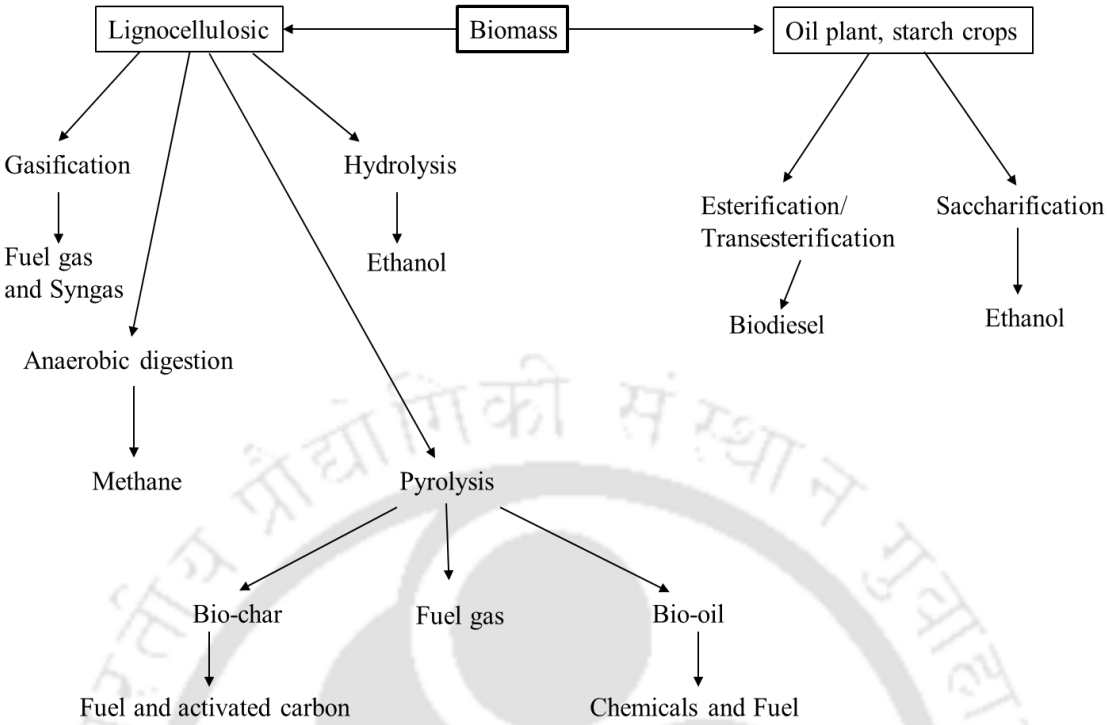

Fig. 1.1: Schematic of biomass conversion technologies

Biodiesel, an alternative fuel for the diesel engine is a promising, nontoxic, biodegradable fuel which can be produced by chemical transformation of triglyceride present in the seed oil or/and animal fats with a short chain of alcohol in the presence or absence of a catalyst [9, 15]. Chemically, it is a mixture of long chain fatty acid alkyl esters (FAAE) in the carbon range of C_{12}–C_{22} [16]. The most common fatty acid alkyl group present in the vegetable and algae oil, and a respective methyl esters are capric (C10:0), lauric (C12:0), palmitic (C16:0), palmitoleic (C16:1), stearic (C18:0), oleic (18:1), linoleic (C18:2), linolenic (C18:3), etc [11, 16]. Apart from that consumption of biodiesel contributes much less to global warming than fossil fuels. While biodiesel possesses advantages and benefits, there are some disadvantages and challenges that must be addressed. It has some higher cloud, pour point than petro diesel, thus restricting its use in low temperature environment [17, 18]. According to U.S. Energy Information Administration (EIA, 2012) worldwide consumption of biodiesel has been

exponentially increased from 605,000 to 17,606,000 gallon per day in the last decade (2000 to 2012) with the projected value of 71,230,000 gallons per day by 2015 [8, 19]. Therefore, several issues on feedstock and by-product utilizations need to be considered for sustainability of biodiesel for the future generation. Huge amount of solid by-product, 40–70 wt%, generates during feedstock preparation. The current state of the art mainly considers about the biodiesel production from edible feedstocks, instead of production of biodiesel from non-edible feedstocks and utilization of solid by-products for the synthesis another biofuel. The solid by-product has a potential to produce value added products such as bio-oil, bio-char, bio-methanol, bio-ethanol and CH_4 [20-22]. Currently, more than 95% biodiesel is being produced from edible feedstocks (first generation) which may also affects sustainability of biodiesel industries for the future [8, 23]. Recent studies reported that, the use of edible vegetable oils and animal fats for biodiesel production has been a great concern because they compete with food materials [24-26]. As the demand of vegetable oils for food has increased tremendously in recent years, it is difficult to elucidate the use of these oils as feedstock for biodiesel synthesis [25, 27]. And also excess use of edible oils for biofuel production leads to food versus fuel crisis. For example, India's vegetable oil import touched to 10.3 million tons in 2012 and was about 46% of vegetable oil for edible purpose [11, 28]. As a result, developing country like India cannot afford to use edible oil for biodiesel production. Hence, the problem of high feedstock cost as well as food versus fuel crisis for edible oil based biodiesel production can be minimized by the selection of non-edible materials (second generation). Therefore, non-edible renewable feedstocks such as oilseed plants of *Jatropha curcas L*. (Jatropha), *Ricinus communis* (Castor), *Hevea brasiliensis* (Rubber tree), *Pongamia pinnata L.* (Karanja), *Moringa oleifera*, *Calophyllum inophyllum L.* (Polanga), *Mesua ferrea*

(Nahor), etc. are considered as potential raw materials for the production of biodiesel in India [2, 12, 24-26].

Therefore, present research was intended to use rubber seed oil which is one of the promising non-edible vegetable oil feedstock for partial substituting edible oil like soybean oil, cotton oil, sesame oil, canola oil, coconut oil, etc. for biodiesel production (Table 1.1). Next section deals with the rubber seed scenario in India and around the World.

Table 1.1: Renewable sources for biodiesel production

Edible feedstock [4, 13, 29]

Common name	*Botanical name*	*Plant type*	*Plant part*	*Oil content seed(wt%)*
Soybean	*Glycine max*	Oilseed	Seed	15–22
Cotton	*Gossypium hirsutum*	–	Seed	20
Sesame	*Sesamum indicum*	Flowering plant	Seed	50
Canola	*Brassica campestris*	Flowering plant	Seed	40
Olive	*Olea europaea*	Small tree	Seed	20
Sunflower	*Helianthus annuus*	Flowering	–	44–50
Almond	*Prunus dulcis*	Tree	Seed	55
Corn	*Zeamays subsp. mays*	Flowering plant	Seed	10
Walnut	*Juglans regia*	Tree	Seed	60
Hazelnut	–	Tree	Seed	55
Rapeseed	*Brassica napus*	Flowering plant	Seed	35
Peanut	*Arachis hypogaea*	Herbaceous annual	Seed	36–56
Safflower	*Carthamus tinctorius*	Herbaceous, thistle-like annual plant	Seed	32
Coconut	*Cocos nucifera*	Tree	Seed	60–70

Table 1.1 (Continued) Renewable sources for biodiesel production

Non-edible feedstock [11-13, 24-28]

Common name	*Botanical name*	*Plant type*	*Plant type*	*Seed (wt%)*	*Kernel (wt%)*
Rubber	*Hevea brasiliensis*	Tree	Seed, kernel	40–60	40–50
Neem	*Azadirachata indica*	Tree	Seed, kernel	20–30	25–45
Milk weed	*Asclepias L.*	Herbaceous perennial	Seeds	20–25	–
Ethiopian mustard	*Brassica carinata*	Herbaceous annual	Seed, kernel	42	2.2–10.8
Desert date	*Balanites aegyptiaca*	Tree	Kernel	–	36–47
Annona Squamosa	*Annona squamosa*	Tree	Seed	15–20	–
Purging Croton	*Croton tiglium*	Herbaceous perennial	Seed, kernel	30–45	50–60
Cuphea	–	Herbaceous annual	Seed	20–38	–
Garcinia indica	*Vrikshamla*	Tree	Seed	45.5	–
Jatropha	*Jatropha curcas*	Tree	Seed, kernel	20–60	40–60
Sapindus	*Sapindus saponaria*	Tree	Seed	51.8	–
Ximenia	*Ximenia americana*	Tree	Kernel	–	49–61
Terminalia catappa	*Terminalia catappa*	Tree	Seed	49	–
Tung	*Vernicia fordii*	Tree	Seed	35–40	–
Linseed	*Linum usitatissimum*	Herbaceous annual	Seed	35–45	–

Table 1.1 (Continued) Renewable sources for biodiesel production

Common Name	*Botanical Name*	Plant type	Plant part	Seed (wt%)	Kernel(wt%)
Karanja	*Pongamia pinnata*	Tree	Seed, kernel	25–50	30–50
Castor	*Ricinus communis L.*	Tree	Seed	45–50	–
Kusum	*Schleichera oleosa*	Tree	Kernel	–	55–70
Mahua	*Madhuca longifolia*	Tree	Seed, kernel	35–50	50
Nahor	*Mesua ferrea*	Tree	Seed, kernel	58–75	–
Micro algae feedstock [16, 30, 31]				*Oil content (dry wt%)*	
Botryoccocus braunii				25–75	
Chlorella sp.				28–32	
Dunaliella primolecta				23	
Monallanthus salina				>20	
Nannochloposis sp.				31–68	
Neochloris oleoabundans				35–54	
Nizschia sp.				45–47	
Phaeodactylum tricornutum				20–30	
Oedogonium, Spirogyra sp				–	
Tetraselmis sueica				15–23	
Schizochytrium	*sp.*			50–77	

1.3. Rubber Seed Scenario in the World

Rubber tree (*Hevea brasiliensis*) belongs to the family of euphorbiaceous [24, 27]. It is originated from South America (Amazon) and cultivated as an industrial crop since its introduction to Southeast Asia in 1876. Globally, the rubber plantation area has increased in 1990s. Rubber trees growth is most rapid in tropical or subtropical climate and with monthly mean temperature about 27 or 28 °C. Rubber crop is famous for its common products; rubber wood and rubber latex. According to food and agriculture organization (FAO) report (2010) [32] the major natural rubber producer countries are Indonesia, Thailand, Malaysia, China, India, Nigeria, Viet Nam, Sri Lanka, etc. More than 92% of the world's rubber plantations is in Asia (Table 1.2). India is one of the top five countries in the world producing rubber seeds as a by-product from rubber tree (6%) (Fig. 1.2A). India was the third largest rubber producer in terms of yield hectogram per hectare next to Mexico and Côte d'Ivoire in 2013 [32]. Currently, rubber seed is getting more attention for production of biofuels due to huge rubber plantation (i.e. 10,107,419 Ha of rubber plantations in 2013) already exists, thus reduced the competition for land with vegetable crops [33, 34].

Rubber plantation has gained its popularity in India due to congenial agro-climate condition as well as its eco-friendly environment and great income for local society [35, 36]. In India, Tripura and Assam states are the main rubber tree producer states next to Kerala state (Fig. 1.2B). Rubber seed is a by-product of the rubber tree (Fig. 1.2). Rubber seed oil is virtually not used to maximum benefit commercially, probably because it is non-edible. But it has a potential to partially replace/substitute for edible oils such as soybean oil, sunflower oil, palm oil, coconut oil, etc. as a raw material for biodiesel production during periods of high

food sector demand. Rubber seed gives 40% to 50% of kernel by weight of non-edible oil (42–50 wt% of kernel) which is promising amount of oil for the production of biodiesel [35]. Rubber seeds are abundant in North-Eastern State of India and is generally considered as waste. The production rate of the seed and promising content of oil (1553.19 kg/Ha/yr) [34]; makes it a potential candidate for biodiesel production. Therefore, this thesis work has been focused to give an overview on utilization of non-edible oilseed such as rubber seed for production of biofuels.

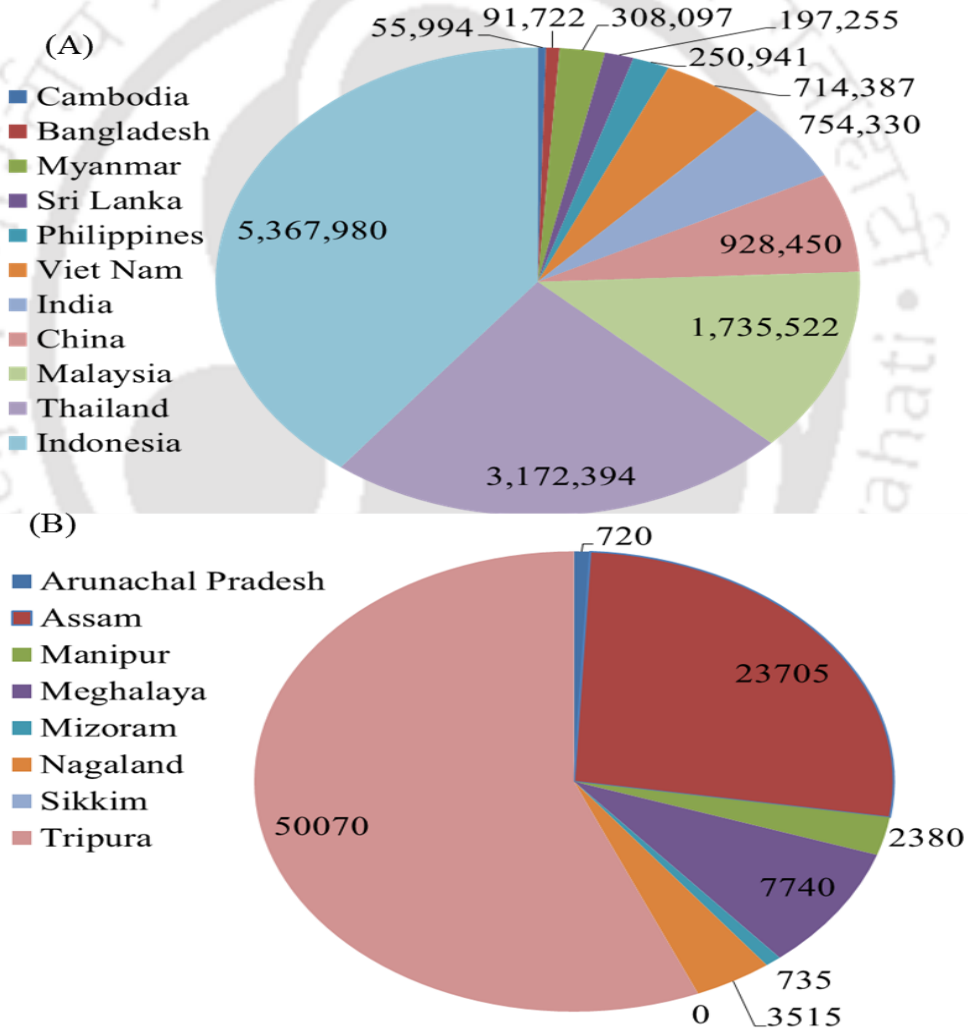

Fig. 1.2: (A) Rubber seed scenario in Asia (Ton) and (B) rubber plantation in north east India (Ha); *Source: http://thetripurafoundation.org/art-rubber-north-east-hopes-vs-concern*

Table 1.2: Rubber plantation scenario by country, 2013 (Global forest resources assessment 2010)

Country/region	Yield (1000 hectogram per hectare), 2013	Natural rubber, area harvested (1000 Ha), 2013	Estimated rubber seed (Ton) [34]
Bangladesh	1	60	93,180
Brazil	13.27	140	217,420
Burma	7.26	204	308,097
Cambodia	11.94	36	55,908
Cameron	10.18	55	85,415
Central Africa Republic	11.6	1.3	2,019
China	12.61	685.9	1,065,203
Congo	8.75	2.4	3,727
Cote d'Ivoire	21.45	135	209,655
Democratic Republic of the Congo	2.38	50.5	78,427
Dominican Republic	16.8	0.019	29.507
Ecuador	17.1	12	18,636
Gabon	14	15	23,295
Ghana	8	26.8	41,620
Guatemala	13.86	76	118,028
Guinea	14.44	10.8	16,772
India	20.4	485.7	754,330
Indonesia	8.74	3555.8	5,522,157
Liberia	8.29	76	118,028
Malaysia	7.82	1057.3	1,641,987
Mexico	25.4	20.2	31,371
Nigeria	4.16	345	535,785
Papua New Guinea	6.6	14.4	22,363
Philippines	6.01	184.9	287,150
Sri Lanka	9.57	136.2	211,519
Thailand	15.96	2420.8	3,759,502
Viet Nam	17.32	548.1	851,199

Source: Food and Agricultural Organization of the United Nations (FAO) [32]

1.4. Literature Review

In this section state of the art of research and experimental techniques related to production of biofuels and utilization of solid by-products are compiled.

1.4.1. Extraction of Vegetable Oil from Oilseed

Vegetable oil used for fatty acid alkyl ester (FAAE) production can be extracted from oilseed by different methods viz. solvent extraction, ultrasonic-assisted extractors, supercritical fluid extraction, hydraulic pressing and screw pressing (Table 1.3) [37-39]. The solvent extraction method is commonly used technique to extract vegetable oil from oil seed. In solvent extraction, both polar and non-polar components can be extracted using polar and non-polar solvents [40]. Hence, a suitable extracting solvent must be chosen for extraction of seed oil using Soxhlet extraction method. Hence, particle size has a important role to increase the extraction yield of vegetable oil [37]. Because internal diffusion of solvent through the plant material is the rate limiting step during for the extraction of oil from the grinded seeds. Ultrasonic-assisted extraction is based on the application of sound waves, having frequencies higher than the hearing limit of the human ear. Sound waves are mechanical vibrations which travels in a solid and liquid, involves expansion and compression cycles during travel in a medium and create micro bubbles and cavitation [37, 41]. Ultrasonic-assisted extraction facilitates release of intracellular material from the oilseed and can enhance mass transfer coefficient [41]. On the other hand, supercritical fluid extraction is a non-conventional extraction technique for oil extraction. Supercritical fluid offers the characteristics of both liquid and gases. The dissolving power of supercritical fluid solvent depends on its density,

which is one of the main advantages of supercritical extraction. The density of the fluid is highly adjustable by changing pressure and temperature [42]. However, the investment and operating cost for this technique is higher as compared to other methods. The comparison of various extraction techniques are presented in Table 1.3. By considering the advantages listed in Table 1.3, conventional extraction technique is used in this work and the details about the technique are discussed in chapter III.

Table 1.3: Advantage and disadvantage of different extraction techniques

EM	Soxhlet extraction	Ultrasonic	Supercritical fluid
Advantage	Simple technique Cheap Filtration is not required Solvent recovery is high Higher contact time of solid matrixes with fresh solvent	Simple technique Cheap Increase extraction yield Short extraction time	Fast extraction Filtration is not required Automated system
Disadvantage	Long extraction time Large amount of solvent is required Possibility of thermal decomposition of target compounds	Filtration is required Large solvent is required Solvent loss is higher Repeated extraction is needed Solid matrixes contact with solvent in mixture form	High investment cost High operating pressure Higher operating cost Mostly used for non-polar solute

EM: Extraction method, Sources: [37, 43]

In a solvent extraction technique via Soxhlet extractor, the parameters such as extraction time, amount of solute to solvent ratio, particle size, drying time, extraction temperature, and

solvent type affect the oil yield during the extraction process [12]. Design of experiment is a useful technique to prepare an experimental matrix within the range of process parameters to optimize process conditions [44].

Sayyar *et al.* [45] have obtained optimum oil yield from jatropha seed using hexane solvent at 8 h extraction time and 0.16 ratio of solute to solvent. They reported that optimum oil yield varies (46–47.3%) with the studied particle size range of 0.5–0.75 mm. Kostic *et al.* [46] have reported optimization of hemp seed oil extraction using response surface methodology (RSM) and artificial neural network-genetic algorithm (ANN-GA) techniques. They considered the effect of solvent to seed ratio (3:1, 6.5: 1 and 10:1 ml/g), extraction temperature (20, 45 and 70 °C) and extraction time (5, 10 and 15 min) on the oil yield of hemp seed for RSM technique, whereas 8 time levels were considered for the ANN model fitting. The optimum extraction conditions obtained from both the techniques, RSM and ANN-GA were found similar. They reported an optimum oil yield of 29.56% under extraction condition: solvent to seed ratio (10:1 (ml/g)) and extraction time (10 min) at near boiling temperature of solvent, hexane. Similar observations were also reported by Bokhari *et al.* [12] for RSO extraction. They performed RSM analysis on the extraction of RSO and obtained optimal oil yield (33.56%) with hexane as solvent at 37:1 ratio of solvent to solute (ml/g) and 4.5 h extraction time. RSM was also applied for the extraction of oil from neem seed using hexane solvent [47]. The optimal oil yield, 37.2% was reported at 6 h extraction time, ~8.3:1 ratio of solvent to solute (ml/g) and particle size of 0.4–0.7 mm.

1.4.2. Modification of Vegetable Oil

Oil extracted by any means cannot be used directly in the existing diesel engines due to high free fatty acids (FFA) content, low volatility, high viscosity, presence of moisture, and other impurities. The injection, atomization and combustion characteristics of vegetable oils in diesel engines are significantly different from those of a mineral diesel. The fuel properties of vegetable oils and mineral diesel are different with respect to viscosity, molecular weight, density, flash point, and cetane number [17, 48, 49]. Direct use of oil in the engine often results in short and long term operational problems. Plugging and gumming of filters, injectors, and engine knocking are the short-term engine problems. Coking of injectors, carbon deposits, failure of engine are the most probable long term problems [6, 50]. Therefore, modification of feedstock oil, physical and chemical transformation, is required through blending with diesel (dilution), pyrolysis (cracking), emulsification and transesterification. Transesterification has been demonstrated as the simplest and the most efficient route for biodiesel production at large scale [6, 7, 29, 51]. The summary of utilization of feedstock for various physical and chemical transformation processes are illustrated in Fig.1.3.

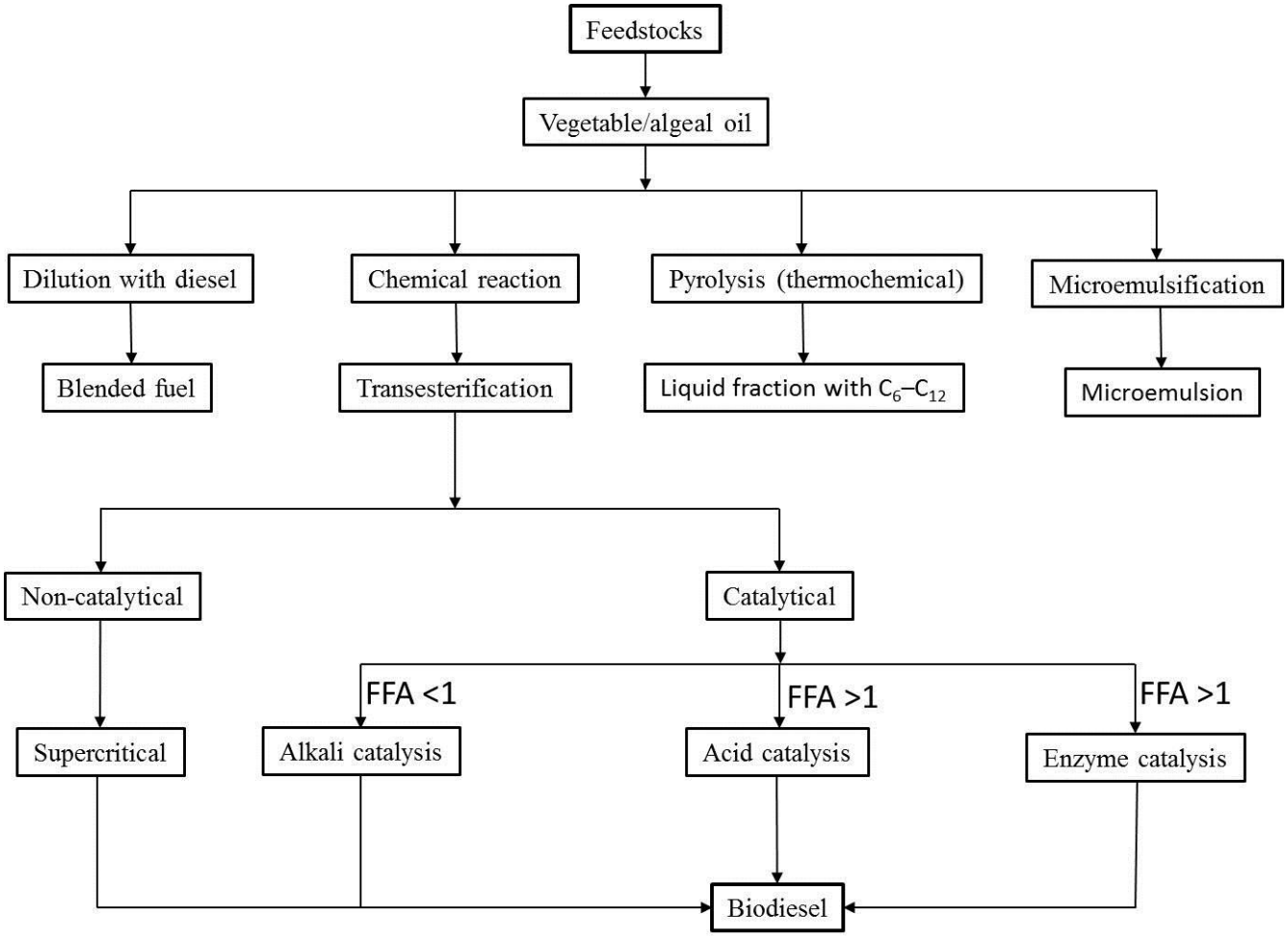

Fig. 1.3: A process chart for utilization of vegetable/algal oil as renewable energy source

1.4.2.1. Blending of Feedstock Oil with Diesel

Several studies have been reported on the effect of blending of vegetable oils with diesel. Adams *et al.* [52] have investigated the performance of Johon Deere 6-cylinder engine for a total of 600 h operated with blended fuel of soybean oil and diesel fuel. The results indicated lubricating oil thickening and potential gelling with 1:1 blend ratio while a blend of one-third soybean oil and two-third diesel (ratio of 1:2) suggested being suitable fuel ratio for agricultural machines during the shortage of diesel fuel. The comparative test of agricultural engine fuelled by refined palm oil and diesel fuel showed that the specific fuel consumption of engine was increased by 15–20% due to lower calorific value and incomplete combustion of palm oil [53]. Use of vegetable oil directly or its blend with diesel fuel have generally been considered to be unsatisfactory and impractical for diesel engine [52]. The high viscosity, free fatty acid content as well as gum formation can be reduced by other processes. A long-term evaluation of the engine using 100% crude vegetable oil was prematurely terminated as severe injector coking led to decrease in power output and thermal efficiency [54, 55].

1.4.2.2. Pyrolysis of Vegetable Oil

Pyrolysis or thermal cracking is a process of conversion of the feedstock (high molecular weight compounds) into the products (smaller compounds) by means of thermal energy (heat) in the absence of air or oxygen with/without the presence of catalyst. Thermo-chemical conversion of feedstock has become an alternative method for the synthesis of high grade biofuels (gasoline fraction with carbon chain C_6–C_{12}) [56]. The long chain of the feedstock is cleavages of chemical bond to yield small molecules [6, 26]. The mechanisms of thermal decomposition of triglycerides to several products are likely to be complex in nature because

of many structures and multiplicity of possible reactions pathways of mixed triglycerides. The pyrolytic products are primarily olefins, paraffins, carboxylic acids and aldehydes. The large variations in compounds are directly related to the type of vegetable oils and its origin.

During catalytic cracking of feedstock, catalyst has a significant role on the molecular distribution of the product [56-59]. Catalytic upgrading of the soybean pyrolytic product by HZSM-5 zeolite at 400 °C supported a partial deoxygenation [60]. Xu *et al.* [56] have investigated thermal and catalytic cracking of soybean and high acid value waste oil using Na_2CO_3 catalyst. About 70% yield of bio-oil was obtained at a reaction temperature of 450 °C with a heating rate of 5 °C/min. Furthermore, the undesired product of pyrolysis process, i.e., carboxylic acid converted into its corresponding esters by esterification process. In addition to liquid and gaseous products (i.e. CO, CO_2), considerable amounts of propane and butane were also produced.

1.4.2.3. Micro-emulsions

A high viscosity of the feedstock for diesel engine application can be solved by micro-emulsions with solvent or co surfactants such as methanol, ethanol, 1-butanol, hexanol, octanol [6]. Micro-emulsion is a colloidal equilibrium dispersion of two or more immiscible liquids, of which at least one is immiscible and dispersed into other. Micro-emulsions are the spontaneously formed system and have especial features i.e., thermodynamically stable. The formulation of emulsified vegetable oil fuel is a promising technique for solving high surface tension, high viscosity and also possible to reduce smoke, particulate matter, nitric oxide emission [61, 62]. Unlike thermal cracking and transesterification processes, no complex chemical reaction and by-product formation are involved during an emulsification of animal

fats and vegetable/algal oil [62]. Ternary phase equilibrium diagram and the plot of viscosity versus solvent fraction are often used to determine the emulsified fuel formulations. Water is one of the essential components used to prepare emulsified fuels. The presence of water in fuel can lead to corrosion of engine part. Hence, special attention is needed on water issue, mainly salt content [63-65].

1.4.2.4. Transesterification

Some of the problems encountered in diesel engines on the direct use of vegetable oils are associated with the polyunsaturation of a large triglyceride molecule and its higher molecular mass. These problems cannot be solved with the physical means as discussed in the previous section. Appropriate chemical means need to be employed to get vegetable oil derivatives which are low molecular mass fatty acid alkyl esters (FAAE) and possess properties similar to mineral diesel. Transesterification process is one of the most successful and promising processes to convert vegetable oil into cleaner and environmentally safe diesel fuel-like liquid (i.e. biodiesel). Chemically, natural oils and fats are made up mainly of triglycerides. These triglycerides when reacted chemically with a shorter chain of alcohols in the presence of a catalyst result in alkyl esters. Methanol and ethanol are the most widely used alcohols, because of their lower cost, higher polarity, and short-chain over other alcohols. If methanol/ethanol is used in this process it is called methanolysis/ethanolysis [66, 67]. Transesterification of triglycerides produces fatty acid alkyl esters and glycerol [6]. Diglycerides and monoglycerides are produced as an intermediates in this process. Overall three moles of monoalkyl esters are obtained from one mole of triglyceride. Due to the reversible nature of reaction, excess alcohol is used to shift the equilibrium reaction to the

forward direction. The equilibrium conversions of triglycerides during transesterification process are affected by various factors, namely, feedstock quality (like free fatty acid content, water content etc.), type of alcohol used, molar ratio of alcohol to triglyceride, type of catalyst, amount of catalyst, reaction temperature, stirring rate and reaction time [6, 7, 9, 13, 15, 50, 68, 69]. Transesterification process significantly reduces the viscosity of triglyceride without affecting the heating value of the original feedstock [6, 31]. Therefore, engine performance and emission characteristics of transesterified product give better results compared to original feedstock [6, 50, 70, 71]. Free fatty acid (FFA) content of feedstock is the most important parameter for the selection of synthesis route of FAAE (Fig. 1.3). The higher conversion of feedstock is not achieved if the oil contains higher amount of FFA >1% [6, 15, 72, 73]. The higher content of FFA leads to an increased acid value of the feedstock; that causes soap formation with alkaline (base) catalyst, thereby preventing separation of the biodiesel from the glycerol fraction and reduce the yield of biodiesel [6, 31]. Therefore, a two-step process is required for these kinds of feedstocks. Initially the FFA of these oils can be converted to fatty acid alkyl esters (FAAE) by an acid catalyzed pretreatment via esterification process (Eq. 1.1) followed by transesterification process (Eq. 1.2) to achieve higher conversion of triglyceride.

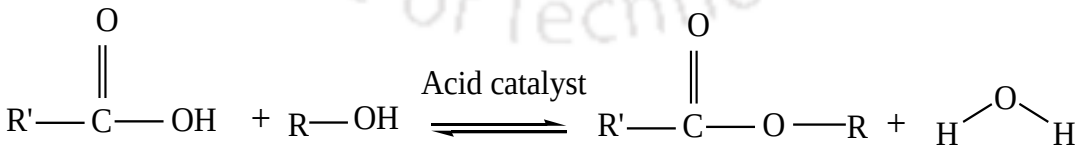

Free fatty acid (FFA) | Alcohol | Fatty acid alkyl ester (FAAE) | Water

(1.1)

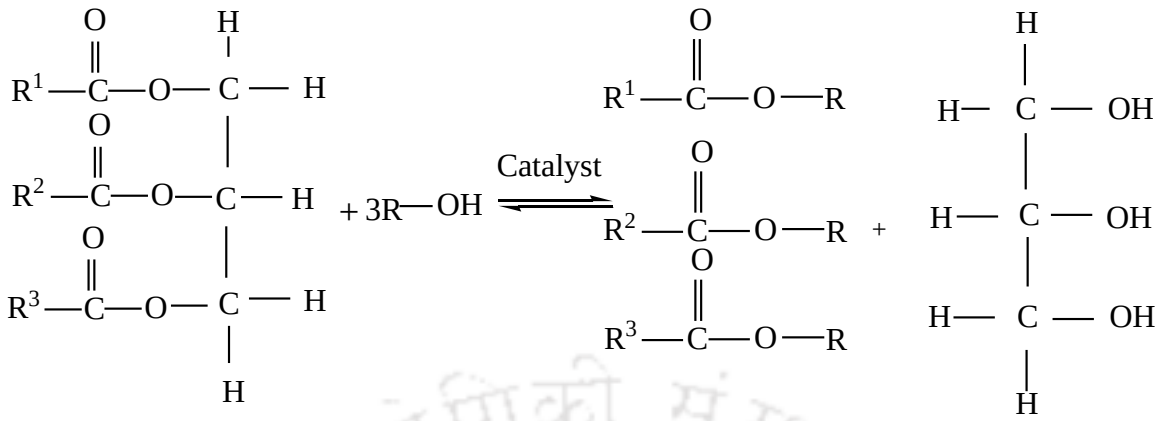

Triglyceride Alcohol Fatty acid alkyl ester (FAAE) Glycerol

(1.2)

Esterification (Eq.1.1) and transesterification (Eq.1. 2) reaction for high FFA vegetable/ algal oil, R': free fatty acid alkyl, R^1, R^2 and R^3 are triglyceride alkyl group and R: alcohol alkyl group**.**

1.5. Biodiesel Synthesis and Pyrolysis of Solid By-Products (Shell of Seed and Cake)

In this section state of the art of literature on production and up gradation of vegetable oil for production of biofuels and utilization of solid by-products is compiled. As mention in previous section, transesterification process and pyrolysis are the simplest techniques for the modification of vegetable oils for biodiesel production and for conversion of solid by-product into bio-oil and bio-char, respectively.

Vegetable oil and alcohol are immiscible in nature [74, 75]. So, both esterification and transesterification reactions are limited due to the high mass transfer resistance present primarily because of the poor diffusion process (physical step) [76]. This can be overcome by

employing an external force such as intensive agitation [51]. Mechanical stirring is the most common technique to increase the rate of transesterification reaction [6, 7, 77]. Constant vigorous agitation and high temperature are required because the reaction can take place only at the interfacial region between the reactant mixtures [78]. Correia et al. [79] have studied the transesterification of sunflower oil via mechanical stirring method and around 97.75% yield was obtained with a stirring speed of 1000 rpm for 4 h at a reaction temperature of 65 °C. While, for nahor oil conversion was reported to be 94% at 900 rpm for 4 h [80]. Mustata *et al.* [81] have also studied the optimization of methyl ester production from corn oil and summarized that around 99% conversion can be achieved at 500 rpm in 2 h duration using 3.6 wt% $Ba(OH)_2$. Waste cooking oil at a lower stirring rate (400 rpm) for 6 h resulted in 90.6% conversion [82].

In the conventional transesterification process, longer reaction time causes glycerol accumulation in the polar phase (alcohol) which makes catalyst separation difficult [51, 76, 78]. Therefore, different alternative techniques such as application of microwave (as an alternative energy source) and ultrasonication (using an ultrasound tool) have been employed to overcome the problems related to diffusion limitations [16, 76, 83]. In the Conventional heating process energy is transferred from the surface to the bulk by convection and conduction. This is an inefficient mode of heat transfer to reaction mixture and the vessel must be overheated to achieve the desired temperature. In contrast, microwave radiations supply heat directly and efficiently to the reacting mixtures [84, 85]. Several studies on intensification of transesterification via microwave and ultrasonication have been reported for a variety of feedstocks using various catalysts [29, 51, 68, 75, 78, 86]. A comparative study on the transesterification reaction of cotton seed oil using KOH catalyst (1.5 wt%) with 6:1

molar ratio of methanol to oil showed improved yield in a lesser duration in the case of microwave assisted process (92.4% in 7 min reaction time) than conventional process, 91.4% in 30 min reaction time [87]. Similarly, Encinar *et al.* [84] have reported that the use of microwave irradiation assisted transesterification of soybean oil yields highest conversion (99%).

Due to the immiscible nature of reactant compounds alcohol and triglycerides of vegetable/algal oil, a contact surface area between the reactants is only at the interface and hence causes a lower reaction rate. An ultrasonic phenomenon in a reactive solution increases the liquid-liquid interfacial area, which is important to enhance the rate of transesterification reaction. During ultrasonic irradiations vapour bubble in methanol and cavitation in vegetable oil are generated ultrasonically [76, 88]. Ultrasound application can be extended to a wider range of frequencies, but 20–60 kHz is the most commonly used frequency range [29, 86, 89]. Deng *et al.* [90] have studied ultrasonic assisted transesterification of jatropha *curcas L.* oil (5.25% FFA) and achieved 96.4% yield of biodiesel with total reaction time of 1.5 h using NaOH as catalyst. Georgogianni *et al.* [72] have achieved 98% yield of ethyl ester from sunflower oil within 40 min using ultrasonic-assisted (24 kHz) transesterification whereas stirring of a reaction mixture for 4 h resulted only 88% yield. Mostafaei *et al.* [74] have also reported an improvement in the conversion of waste cooking oil to methyl esters using ultrasonic approach (89% yield) compared to conventional stirrer technique (50% yield).

1.5.1. Catalytic and Non-catalytic Transesterification

Like other chemical reactions, catalyst has an important role to increase the rate of transesterification reaction and FAAE yield (biodiesel). Catalysts used in the

transesterification reaction can be classified as alkali, acid and biocatalyst (enzyme) [15, 91].

1.5.1.1. Acid Catalyzed Transesterification

The most common homogeneous acid catalysts used in the synthesis of biodiesel from higher free fatty acid content feedstock are sulphuric acid (H_2SO_4), hydrochloric acid (HCl), boron trifluoride (BF_3), phosphorous acid (H_3PO_3) and organic sulfonic acid. Acid catalyzed transesterification reaction requires the use of higher molar ratio of alcohol to oil in order to obtained improved product yield. However, the conversion of feedstock or yield of FAAE does not increase proportionally with molar ratio. Transesterification of soybean oil using sulfuric acid showed an improvement in the yield from 77% to 87.8% using methanol to oil ratio of 3.3:1 to 6:1; but with a much higher molar ratio (30:1) only moderate improvement in yield (98.4%) was achieved [92].

The rate of transesterification reaction using homogeneous acid catalyst is about 4000 times slower than alkali catalyst. Canakci and Gerpen [69] reported highest conversion of 95.1% with soybean oil via acid catalysis (3%) using reaction time of 96 h at 65 °C. However, Freedman *et al.* [15] have reported that the acid catalyst is more effective than alkali catalyst for feedstock containing higher free fatty acid, more than 1%. The overall FFA content of particular oil can be reduced by blending with oil containing less FFA. Khan *et al.* [93] have studied acid esterification of a blended feedstock of rubber seed oil (high FFA) and palm oil via sulphuric acid (0.5 wt%) for 3 h reaction time and achieved 95% reduction of free fatty acid. Sulphuric acid has been also used for esterification of high free fatty acid *Chlorella sp.* lipid and maximum 60% yield of methyl esters was observed with 3.5 wt% H_2SO_4 and, at stirring speed of 400 rpm and reaction time 2.5 h [94]. A better conversion of high free fatty

acid feedstock into its methyl esters was observed by homogeneous acid catalyst compare to a homogeneous alkali catalyst [31, 94]. The homogeneous acid catalyst can perform both esterification and transesterification reaction to produce corresponding alkyl esters and prevent saponification reaction. The high free fatty acid content of *Jatropha curcas* oil (21.5%) and waste cooking oil (21.84%) were reduced to less than 1% using homogeneous acid catalyst (H_2SO_4) and about 21.2% and 21.5% methyl ester yield were obtained during the esterification process, respectively [82, 95]. Many researchers suggested that around 1% (v/v) homogeneous acid catalyst should be used because a higher amount of acid may burn the feedstock and darken the products [50].

Heterogeneous acid catalysts are promising alternatives to replace strong homogeneous acids. The corrosion, environmental hazard posed by strong liquid acid and product purification problems can be improved by the uses of solid acid catalysts [92]. Sulphated zinc oxide, Zeolites, Heteropoly acids, functionalized zirconia and silica, tungsten oxides, sulphonated zirconia (SZ), Amberlyst115, Lewatit GF 101, sulphonated saccharides, nifion 1 resins, organosulphonic functionalized mesoporous silica are solid acid catalysts which have been used effectively in esterification of carboxylic acid as well as to obtain high conversion of triglycerides [92, 96-98]. An active solid catalyst (SO_4^{-2} –ZnO) for methyl ester synthesis from soybean oil under mild reaction conditions resulted 80.19% yield within 4 h [96]. However, the shortcoming of solid acid catalysts are; (1) complicated catalyst preparation, (2) energy intensive, (3) leaching of the catalyst can cause product contamination and side reaction, (4) low acid site, (5) low micro porosity, (6) diffusion limitation, (7) high temperature and a longer time for higher yield of products.

1.5.1.2. Alkali Transesterification

The most commonly adopted route for biodiesel production at industrial scale is based on homogenous alkali catalyzed transesterification using sodium hydroxide (NaOH) and potassium hydroxide (KOH) as catalysts. Many literatures have reported on parametric optimization of transesterification process using homogenous alkali catalysts. Keera *et al.* [99] have considered NaOH catalyst (0.5–1.5 wt%), molar ratio of methanol to oil (3:1–9:1), reaction time (1–3 h) and at constant reaction temperature, 60 °C as process parameters to optimize the biodiesel yield. The best yield, 90% and 98.5% from soybean and cotton seed oils, respectively, were obtained for 1 wt% NaOH, 6:1 molar ratio and 1 h reaction time [99]. Silva *et al.* [100] have applied response surface methodology (RSM) considering a wide range of process parameters and obtained optimum yield of 95% ethyl esters at a molar ratio of ethanol to soybean oil: 9:1 with catalyst loading of 1.7 wt% NaOH during 80 min reaction at 40 °C. Lueung and Guo [101] have studied characteristics and performance of sodium hydroxide (NaOH), potassium hydroxide (KOH), sodium methoxide (CH_3ONa) and potassium methoxide (CH_3OK) catalysts for alkaline-catalyzed transesterification of edible canola oil and used frying oil. Both CH_3ONa and CH_3OK showed higher yield of biodiesel compared to NaOH and KOH. Due to sensitiveness of free fatty acids and formation of water and soap during alkali catalyzed transesterification results in lower conversion of the triglyceride of vegetable oil [50, 101]. The formation of soap is not only lowers the conversion of the feedstock, but also makes purification of the final product difficult and cause emulsion formation. Separation of catalysts after transesterification reaction requires washing the final product with distilled water, which gives rise to the generation of waste water. Heterogeneous alkali catalyzed transesterification is included under green technology

due to; reusability of catalyst, relatively faster reaction rate than acid catalyzed transesterification, no water formation during the process and separation of biodiesel from glycerol is much easier [102]. The main drawbacks of heterogeneous catalysts are anhydrous condition, poisoning of the catalyst when exposed to ambient air, diffusion limitation, and low free fatty acid feedstock. Commonly used solid heterogeneous catalysts for transesterification reaction are CaO, ZnO, MgO, BaO, Na_3PO_4, CaMgO, CaZnO, tripotasium phosphate (K_3PO_4), trisodium phosphate (Na_3PO_4), disodium phosphate (Na_2HPO_4), dipotasium phosphate (K_2HPO_4), monosodium phosphate (NaH_2PO_4) and monopotasium phosphate (KH_2PO_4), magnesium-lanthanum mixed oxide (Mg/La), strontium-titanium mixed oxide (Sr-Ti), Calcium-zirconium mixed oxide (Ca-Zr), $Ca(OCH_2CH_3)_2$, KOH/NaX zeolite, calcium ethoxide, calcium methoxide, calcium glyceroxide, calcium hydroxide ($Ca(OH)_2$), barium hydroxide ($Ba(OH)_2$), etc.

Biodiesel production from kapok seed oil using two steps method; esterification (H_2SO_4) followed by transesterification (CaO) reaction showed that high FFA (9.32%) content of oil can be reduced to 1% by esterification reaction [103]. The optimum biodiesel of yield 88.57% was obtained at molar ratio: 15:1, reaction time: 1 h and reaction temperature: 60 °C. Catalyst, CaO has also been used for transesterification of several feedstocks such as soybean oil, *Jatropha curcas* oil, rapeseed oil and sunflower oil [31, 77, 92, 104]. Pukale *et al.* [86] have compared transesterification of waste cooking oil (WCO) using 2 wt% heterogeneous solid catalysts and their catalytic performance was obtained in the following order tripotasium phosphate (K_3PO_4) (70.5%)) > trisodium phosphate (Na_3PO_4) (63.1%) > disodium phosphate (Na_2HPO_4) (14.3%) and negligible conversion of WCO was observed in dipotasium phosphate (K_2HPO_4), monosodium phosphate (NaH_2PO_4) and monopotasium phosphate

(KH_2PO_4).

Mootabadi *et al.* [78] have studied catalytic performance of alkaline earth metal oxides (CaO, BaO and SrO) for transesterification of palm oil. The result shows that, under similar reaction condition, the catalytic activity was found in order of CaO < SrO < BaO. This is attributed to the difference in basic strength of the catalysts. Eggshell-derived CaO catalyst has also been used for the transesterification reaction of vegetable oils [79, 80, 89, 105, 106]. The eggshell (crushed) calcined at 600 °C – 900 °C for 2– 4 h found to contain more than 98% CaO. The use of such activated eggshell reported to yield biodiesel up to 90% – 97% [89, 107-109].

1.5.1.3. Enzyme Catalyzed Transesterification

Biocatalytic transesterification reaction is another alternative of chemical catalysts. Enzymes catalyzes both esterification and transesterification reaction. Lipase from *Pseudomonas flseudomona*, *Pseudomonas cepacia*, *Candida rugosa*, *Candida Antarctica*, *Rizhomucor miehei* and *Thermomyces lanuginosa* are the most extensively studied enzymes for biodiesel production [31, 110]. Transesterification reaction using lipase enzyme looks attractive and encouraging due to easy product separation, minimal generation of wastewater, less energy intensive, do not promote side reactions and more environmentally friendly [7, 8, 16, 31]. Although, the enzymatic transesterification process has some disadvantages (1) contamination of product with residual enzyme, (2) longer reaction time and (3) cost of the enzyme [31]. But, immobilization of the enzyme, addition of alcohol solvent (ethanol and methanol) has been proposed to improve the product and cost of catalysts [111]. Rodrigues *et al.* have found two-step ethanolysis as a very effective technique to avoid the negative effect

caused by ethanol, and reported 100% conversion of soybean oil in presence of n-hexane. A stepwise addition of ethanol could enhance conversion of fish oil up to 95% [112]. Raita *et al.* [113] have observed that operational stability of protein-coated microcrystals (PCMC-lipase) could be improved by introducing hydrophilic solvent *tert*-butanol and thus, allow recycling of the biocatalyst for at least 8 consecutive batches.

1.5.1.4. Non-catalytic Transesterification

Supercritical alcohol transesterification provides a new way to produce biodiesel from vegetable oils. Triglyceride and fatty acids of vegetable oil and short chain alcohols (ethanol and methanol) are immiscible in nature and, results incomplete transesterification reaction. Under supercritical conditions, short chain alcohols such as methanol and ethanol are hydrophobic and triglyceride dissolves well in them [110]. Hence, there is no issue of soap formation, catalyst efficiency and consumption as well as yield of biodiesel [16, 114]. Supercritical fluid has characteristics of both liquid (density) and gases. The dissolving capacity of supercritical solvent depends on its density, which is one of the main advantages of supercritical transesterification reaction. The density of a fluid is highly adjustable properties by changing its pressure and temperature [110]. However, the supercritical method requires high molar ratios of alcohol to oil and the use of high temperature and pressures to afford satisfactory conversion levels, leading to high operational cost and investment [16, 100]. Supercritical reaction using methanol achieved optimum conversion of palm oil (81.5%) at relatively lower reaction time compared to the supercritical ethanol process (79.2%) [115]. The conversion achieved by supercritical methanolysis is relatively higher than ethanolysis [67].

Table 1.4: The most commonly fatty acids found in vegetable oil

Chemical Name	Common name	Symbol	Chemical Formula	Number of Unsaturation and position
Hexadecenoic	Palmitoleic	C16:1	$C_{16}H_{30}O_2$	1, 9 cis
Octadecenoic	Petroselinic	C18:1	$C_{18}H_{34}O_2$	1, 6 cis
Octadecenoic	Oleic	C18:1	$C_{18}H_{34}O_2$	1, 9 cis
Octadecenoic	Elaidic	C18:1	$C_{18}H_{34}O_2$	1, 9 trans
Octadecenoic	Vaccenic	C18:1	$C_{18}H_{34}O_2$	1, 11 cis
Eicosenoic	Gadoleic	C20:1	$C_{20}H_{38}O_2$	1, 9 cis
Eicosenoic	Gondoic	C20:1	$C_{20}H_{38}O_2$	1, 11 cis
Docosenoic	Erucic	C22:1	$C_{22}H_{42}O_2$	1, 13 cis
Hexadecadienoic	Dienoic	C16:2	$C_{16}H_{28}O_2$	2, –
Octadecadienoic	Linoleic	C18:2	$C_{18}H_{32}O_2$	2, 9 and 12 cis
Octadecatrienoic	α-Linolenic	C18:3	$C_{18}H_{30}O_2$	3, 9, 12 and 15 cis
Octadecatrienoic	ϒ-Linolenic	C18:3	$C_{18}H_{30}O_2$	3, 6, 9 and 12 cis
Octadecatrienoic	Eleostearic	C18:3	$C_{18}H_{30}O_2$	3, 9 cis, 11 and 13 trans
Octadecatrienoic	Calendic	C18:3	$C_{18}H_{30}O_2$	3, 8 and 10 trans, 12 cis
Decanoic	Capric	C10:0	$C_{10}H_{20}O_2$	
Dodecanoic	Lauric	C12:0	$C_{12}H_{24}O_2$	
Tetradecanoic	Myristic	C14:0	$C_{14}H_{28}O_2$	
Hexadecanoic	Palmitic	C16:0	$C_{16}H_{32}O_2$	
Octadecanoic	Stearic	C18:0	$C_{18}H_{36}O_2$	
Eicosanoic	Arachidic	C20:0	$C_{20}H_{40}O_2$	
Docosanoic	Behenic	C22:0	$C_{22}H_{44}O_2$	
Tetracosanoic	Lignoceric	C24:0	$C_{24}H_{48}O_2$	
Docosanoic	Behenic	C22:0	$C_{22}H_{44}O_2$	
Tetracosanoic	Lignoceric	C24:0	$C_{24}H_{48}O_2$	

Sources: [6, 11, 16, 25, 116]

Table 1.5: Reduction in emissions of harmful gases using biodiesel

Emission type	100 % Biodiesel	20 % Biodiesel
Carbon Monoxide	- 43.2 %	-12.6 %
Hydrocarbons	- 56.3 %	- 11.0 %
Particulates	- 55.4 %	- 18.0 %
Nitrogen Oxides (NO_x)	+ 5.8 %	+ 1.2 %
Air Toxics	- 60 % – -90 %	- 12 % – -20 %
Mutagenicity	- 80 % – -90 %	- 20 %
Carbon Dioxide	- 78.3 %	- 15.7 %
Sulphur Oxide	-100 %	–
Methane	-51 %	–
Polycyclic Aromatic Hydrocarbons	-80 %	-75 %
Unburned Hydrocarbons	-67 %	–

Source: National Renewable Energy Laboratory (NREL) [70]

1.5.2. Thermo-Chemical Conversion of the Solid by-Products

Huge amount of solid wastes such as shell (during de-shelling of seed) and cake (by-product of oil extraction process) are generated during the preparation of feedstock for biodiesel production. For example, the solid waste produced during the synthesis of methyl ester from various feedstocks are as follows; rubber seed (60–70 wt%), castor oil (50–55 wt%) [11, 13], *Pongamia pinnata L.* (60–70 wt%) [24], Jatropha *curcas L.* oil (40–50 wt%) [24], *Sleichera triguga* (kusum) (30–45 wt%) [25], tung oil (60–65 wt%) [117], *Ximenia americana* (39–51 wt%) [13, 24]. The solid wastes, both cake and shell are a rich source of lignocellulose (more than 90 wt%) proportion than lipid (less than 5 wt%) [118, 119]. The solid waste can be exploited for the production of value added products through thermo-

chemical means [21, 120]. Thermo-chemical conversion processes commonly follow any of the three approaches such as combustion, gasification and pyrolysis. Combustion is a necessarily needs air (oxygen) to convert stored chemical energy in biomass to heat, mechanical and electrical energy. A biomass with moisture content less than 50 wt% can be combusted via various process equipment such as stove, furnace, boilers, steam turbines, etc [13]. Emissions and ash handling for the combustion process are cause for high process costs. Gasification is the conversion of solid biomass into the gaseous mixture at high temperature (800–1000 °C). Carbon dioxide (CO_2), carbon monoxide (CO), water (H_2O), methane (CH_4) and other hydrocarbon gases are main products of gasification process [2]. The derived gases can be used as feedstock for chemical synthesis and as fuel for the power generation. The applications of produced gas depend on its qualities such as heating value and product gas compositions.

Pyrolysis is the most promising thermo-chemical method to produce mainly liquid and solid fuel from the biomass in the slight amount or absence of oxygen [14]. It is a process in which thermal decomposition of the chemical constituent of the biomass such as hemicellulose, cellulose and lignin produces energy rich products. The thermal degradation of biomass using pyrolysis process leads to the formation of products in a three different phase (bio-char, pyrolysis oil and gas). In the pyrolysis process, the thermal decomposition of biomass components occurred in the temperature window of 350–800 °C [121]. Among all the three thermo-chemical processes for conversion of biomass in to energy, pyrolysis is the most promising and attractive thermo-chemical technique with a potential to convert cheap, local and abundant lignocellulosic biomass such as crops, grasses, waste agricultural biomass, waste industrial biomass and trees into a liquid and carbon-rich solid fuels [5, 21, 122]. The

liquid product has certain advantage such as easy storage, transportation and versatility in application such as boilers, turbines, combustion engine, feedstocks for chemicals synthesis, etc. The decomposition of biomass releases condensable and non-condensable gas-phase. The portion of condensable gas-phase collected as a viscous dark brown liquid, which is termed as bio-oil or pyrolytic oil. The remaining portion of solid (non-volatile) is bio-char. The yield of pyrolysis products depends on the operating condition and biomass properties such as heating rate, reactor configuration, temperature, pressure, flow rate of inert gas, particle size of biomass, moisture content of biomass, and the bio-chemical composition of biomass, etc [2, 5, 123]. The simplified biomass pyrolysis process can be represented by Fig. 1.4.

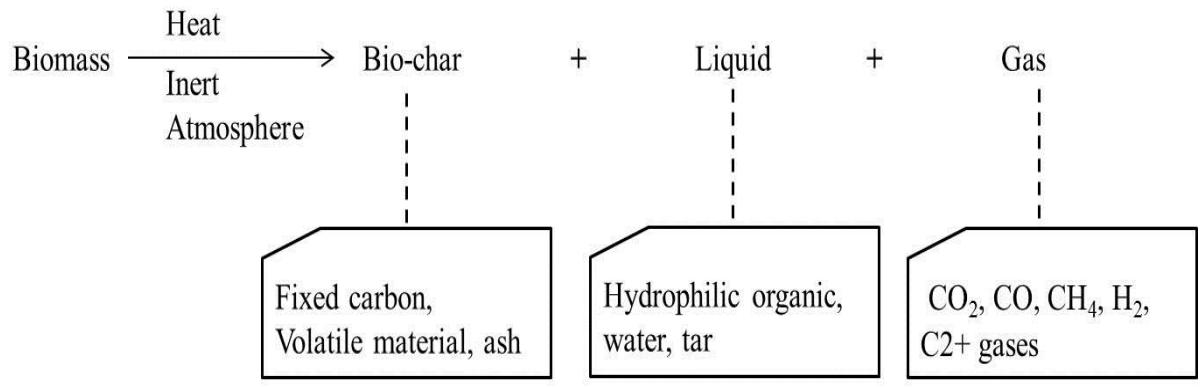

Fig. 1.4: Biomass pyrolysis process

Pyrolysis process is usually classified according to the mode of pyrolysis temperature, heating rate and residence time [5]; (1) slow pyrolysis and (2) fast or flash pyrolysis. Slow pyrolysis can be maintained at a low heating rate of 0.1–1 °C/min and pyrolysis temperature range of 400–600 °C for residence time of minutes to hours. In this case, the pyrolysis reaction occurs are always in equilibrium [123]. Heating rate and product residence time in the reactor are important since the presence of products influence both primary and secondary

reactions [5, 123]. The process is also used traditionally for charcoal production. But, charcoal production by slow pyrolysis process is energetically not efficient and increases polluting gases. Fast pyrolysis is a process that terminates secondary conversion of products by high heating rates. In this mode of pyrolysis, bio-oil yield is maximum at reaction conditions of dry biomass (< 12 wt% moisture), particle size 0.6–1.25 mm and vapour residence time of maximum 5 sec [123, 124]. Dickerson and Soria [5] have also reported that fast pyrolysis is promising to achieve high liquid yield through rapid heating rate of 10 to 1000 °C/sec and pyrolysis temperature range of 400–600 °C with short residence time of less than 2 sec.

Uzun *et al.* [124] have studied the effect of important parameters such as pyrolysis temperature (300, 400, 450, 500, 550 and 700 °C), particle size (0.224–0.425 mm, 0.425–0.85 mm, 0.85–1.25 mm and 1.25–1.8 mm), heating rate (5, 100, 300 and 700 °C/min) and sweeping gas velocity (50, 100, 200 and 400 cm^3/min) on oil yield during pyrolysis of soybean cake. Optimum oil yield of 42.83% was obtained at a heating rate (700 °C/min), temperature (550 °C), particle size (0.425–0.85 mm) with a sweeping gas velocity of 200 cm^3/min. They conclude that, pyrolysis yield and conversion efficiency depends mainly on pyrolysis temperature [124].

Sensoz and Angin [125] have investigated the effect of pyrolysis temperature (400, 450, 500 and 550 °C), heating rate (10, 30 and 50 °C/min), and a sweep gas flow rate (50, 100, 150 and 200 cm^3/min) on yield of pyrolysis products from safflower seed press cake using fixed-bed reactor. The highest liquid yield (36.1%) was obtained at pyrolysis temperature of 500 °C, a heating rate of 50 °C/min and a sweep gas flow rate of 100 cm^3/min. They conclude that employing higher heating rate of 50 °C/min result in increased bio-oil yield, probably due to

decrease in mass transfer limitation. They also report that pyrolysis temperature has more effect than heating rate on bio-oil yield and conversion efficiency [125].

The pyrolysis of de-oiled groundnut cake was studied by Agrawalla *et al.* [126] using a semi-batch reactor. The results showed that maximum liquid product (50 wt%) can be obtained at 450 °C pyrolysis temperature [126]. Singh and Shadangi [127] studied liquid fuel production from castor seeds by pyrolysis using a semi-batch reactor. TGA for castor seed at a heating rate of 20 °C/min in the presence of atmospheric air shows, active pyrolytic zone from 200–500 °C for maximum conversion of castor seed and the result showed that about 79.24% weight loss was observed in active pyrolytic zone (200–500 °C). They also reported that, yield of the liquid product increased with an increase in the pyrolysis temperature. But at higher temperature, 550 °C to 600 °C, the volumetric yield of liquid remains nearly constant. This was probably due to the formation of more amounts of non-condensable gases/volatiles at higher temperature. The maximum oil yield of 64.4% was obtained at pyrolysis temperature of 550 °C, residence time of 30 min with slow heating rate of 20 °C/min. The calorific value of pyrolytic products of castor seed; pyrolytic oil, bio-char was 35.509 MJ/kg and 28.963 MJ/kg, respectively [127].

Abnisa *et al.* [128] have studied the pyrolysis of palm shell waste using a fixed-bed reactor. They achieved maximum liquid product of 46.4 wt% with operating conditions of temperature (500 °C), N_2 flow rate (2000 ml/min), particle size (2 mm) and reaction time (1 h). The heating value of the liquid product obtained from pyrolysis of palm shell was less (11.94 MJ/kg) due to higher water content (53 wt%) [128]. Volli and Singh [122] also studied the pyrolysis of sesame (*sesamun indicum*), mustard (*Brassica napus*) and neem (*Azadirach indica*) de-oil cake in a semi-batch reactor. The pyrolysis experiments were conducted by

varying the pyrolysis temperature (350, 400, 450, 500, 550, 600 and 700 °C) at a constant heating rate of 25 °C/min. The maximum yield of liquid product was achieved at pyrolysis temperature of 550 °C for sesame cake (58.5%) and mustard cake (53.2%) and 400 °C for neem cake (40.2%). They concluded that, pyrolysis temperature has a major role on pyrolysis yield and conversion efficiency [122].

Chaiya, Reubroycharoen [120] reported production of bio-oil from para rubber seed using pyrolysis process. They studied that the effect of different parameters such as seed shell particle size (2.18 mm and 1.13 mm), pyrolysis temperature (300, 350, 400 and 450 °C) and nitrogen flow rate (50, 100 and 150 ml/min) on bio-oil yield. Their result showed the highest bio-oil yield (38.22%) for para rubber seed and (34.35%) for residue at pyrolysis temperature (450 °C), nitrogen flow rate (50 ml/min) and RSS particle size of (2.18 mm). The fuels analysis of bio-oil showed that the heating value of Para rubber residue bio-oil (37.76 MJ/kg) was higher than that of RSS bio-oil (22.11 MJ/kg) [120].

Angin [129] have investigated the effect of pyrolysis temperature and a heating rate on the yield of bio-char from safflower seed cake. The result showed that pyrolysis temperature has a significant effect on the yield of bio-char and its physico-chemical properties. The maximum calorific value of 30.27 MJ/kg for bio-char pyrolyzed at 600 °C temperature at a heating rate of 50 °C/min [129].

Ahmed *et al.* [20] have studied pyrolysis of palm kernel shell in a fixed-bed reactor; considering the effect of pyrolysis conditions: temperature (350, 400, 500 and 550 °C) and particle size (212 µm–300 µm, 300–600 µm, 600 µm–1.18 mm and 1.18 mm–2.36 mm) at a fixed heating rate of 50 °C/min. Their result showed that maximum bio-oil yield (38.40%) can

be achieved at 450 °C and particle size of 600 µm–1.18 mm. They also reported that, the obtained pyrolysis oil is highly oxygenated, containing a high fraction of phenol-based compounds [20].

Chutia *et al.* [130] have reported pyrolysis of *pongamia glabra* de-oiled cake at pyrolysis temperature ranging from 350 °C to 600 °C for a heating rate of 10, 20 and 40 °C /min using fixed-bed pyrolysis reactor. The liquid product achieved was 30.6 wt % at 500 °C pyrolysis temperature at a heating rate of 40 °C/min. The heating value of bio-char was 24.30 MJ/kg [130]. Further, *pongamia glabra* seed cover pyrolyzed over the temperature range of 350–650 °C and at a heating rate of 40 °C/min were also investigated by by Bordoloi *et al.* [131]. The study shows that, the yield of bio-oil was maximum at 550 °C (28.5 wt%), however, increased in the pyrolysis temperature to 650 °C decreased the bio-oil yield to 26.9 wt% and increased the gas yield from ~23 wt%–24.8 wt% [131]. The increase in gas yield is thought to occur mainly due to secondary cracking and decomposition of pyrolysis vapors and solid residue (bio-char) at higher temperature.

Similarly, Mohammed *et al.* [21] have reported pyrolysis of castor shell residue using a fixed bed pyrolyzer. In this study effect of different parameters such as pyrolysis temperature (400, 450, 500, 550 and 600 °C), particle size (< 0.25 mm, 0.2–0.3 mm, 0.3–0.5 mm and 0.5–1 mm) and a heating rate (10, 30, 50 and 70 °C/min) were considered to increase the liquid product yield. Increase in pyrolysis temperature from 400 °C to 600 °C, liquid and gas yield increased from 36.8 to 41 wt% and 30 to 35.5 wt%, respectively. This is probably due to more decomposition of castor shell at high temperature. They also observed that, at higher temperature beyond 600 °C; oil yield decreased while gas yield was increased. They stated that particle size has a significant effect on liquid product yield and experienced increased

yield as the particle size decrease and that attributed to larger temperature gradient inside larger particles. The liquid yield of 38 wt% obtained at a heating rate of 10 °C/min was increased to 41 wt% when a heating rate increased to 70 °C/min. This is because the heat and mass transfer barriers in the particles are less at higher heating rate. Finally, considering all parameters; maximum oil yield of 42 wt% was obtained at pyrolysis temperature of 550 °C, particle size of 0.5–1 mm and a heating rate of 70 °C/min. The calorific value of castor shell and bio-oil obtained at optimum condition was 18.9 MJ/kg and 35 MJ/kg, respectively. They concluded that obtained bio-oil can be used as fuel and chemical feedstock [21].

Hassan *et al.* [22] have studied rubber seed shell (RSS) and rubber seed kernel (RSK) as raw material for biofuel production. Their result shows that, the calorific value of RSK (27.5 MJ/kg) was higher than that of RSS (23.9 MJ/kg). This may be due to higher carbon content in RSK. They concluded that, RSK has a potential to use as a raw material for liquid biofuel production [22].

Sahu *et al.* [132] have studied utilization of palm oil sludge through pyrolysis for bio-oil and bio-char production. In their study, about 27.4% bio-oil and 49.9% bio-char was produced through a pyrolysis process at 550 °C with an actual heating rate of furnace 24 °C/min. The fuel properties of produced bio-oil was within the ASTM D7544-09 specification of fuel. They also reported that bio-char can be further utilized for removal of Cd^{+2} metal from waste water [132].

Brebu *et al.* [133] have investigated co-pyrolysis of pine cone (*pinus pinea L.*) with synthetic low density polyethylene (LDPE), polypropylene (PP) and polystyrene (PS) polymer. The pyrolysis temperature used during this process was 500 °C at a heating rate of

10 °C/min. Liquid yield was found to be varied from 47.5 to 69.7 wt%. The lowest liquid yield of 47.5 wt% was obtained when pine cone alone was used as raw material. However, by mixing the pine cone and polymers in the same weight ratio, the liquid yield obviously increased. Similarly, Brebu et al. [133] also stated that the energy contents of oils from the co-pyrolysis were higher than those produced by the pyrolysis of the pine cone alone.

Similarly, Abnisa *et al.* [134] also have explored the co-pyrolysis of palm shell with waste polystyrene (PS). In their study, palm shells were obtained from a local processing plant in Kuala Lumpur (Malaysia). The maximum liquid yield of 68.3 wt% was obtained by mixing 2:3 weight ratio of palm shell to PS at a temperature of 600 °C for 45 min duration. Further, co-pyrolysis of karanja and niger seed with polystyrene has been also investigated by Shadangi and Mohanty [135] using a semi-batch pyrolyzer. The oil yield was found to be the main product of the experiment and the yield was increased from 32.9 wt% to 57.81 wt% and 33.39 wt% to 57.94 wt% for karanja and niger seed, respectively up on mixing of PS by 50 wt% of seed. Furthermore, Shadangi and Mohanty [135] also reported that the energy contents, water content and viscosity of oil from the pyrolysis of mixed materials were improved as compared to oil produce by the pyrolysis of karanja and niger seed alone.

1.6. Summary

Currently, more than 95% of biodiesel has been predominantly produced from edible vegetable oils. However, continuous and large scale production of biodiesel from edible oils has recently been of great concern because they compete with food materials. Therefore, the uses of non-edible renewable resources are considered as a suitable option for sustainable

industrial production of biodiesel. The transesterification process is the simplest and commercialized process for the production of biodiesel from various vegetable oils. The rate of transesterification reaction is affected by various parameters such as (1) reaction time and temperature; (2) type and amount of alcohol and catalyst; (3) method of transesterification (conventional and ultrasonic technique); (4) amount of FFA in vegetable oil. Nature of free fatty acid and a fatty acid chain in feedstocks such as the degree of unsaturation and presence of the other functional group also strongly affect the properties of biodiesel produced in any of the techniques. Transesterification reaction does not change the fatty acid chain and degree of unsaturation. The most common carbon number of fatty acids of vegetable oils ranges between C_{10}–C_{24} (Table 1.4). The physico-chemical properties of feedstock, vegetable oils obtained from different origin, makes difference in the produced biodiesel. Even with similar feedstock material slight changes in physico-chemical properties of the product (FAAE) are due to genotype of the feedstocks and performance of transesterification reaction at different conditions. Biodiesel can be blended with petroleum-based diesel fuel for use in existing diesel engine. Considering engine performance and emissions characteristics several standard-setting organizations worldwide have adopted biodiesel specifications; D6751 (ASTM international), DIN5160611 (German authorities issued), EN14214 (Europe's Committee for Standardization). Biodiesel prepared from various renewable resources and processes should meet the international standard, ASTM D6751 [136]. The pure biodiesel and biodiesel blends can achieve a significant reduction in reactive hydrocarbons and carbon monoxide emissions when used in an unmodified diesel engine (Table 1.5). Most of the emissions reduce while using biodiesel with the exception of nitrogen oxides, which either remain the same or slightly increased. Moreover, due to certain other properties, like biodegradable nature, non-toxicity,

high flash point and higher cetane number, biodiesel is being viewed as a suitable alternative to mineral diesel.

Although biodiesel is a promising alternative fuel to diesel fuel; several issue such as feedstock and solid by-product utilization need to consider for its sustainability for the future. It was observed that 39–70 wt% of solid by-product (waste biomass) is generated during feedstock preparation for biodiesel synthesis which contain promising amount of hydrocarbon for the production of biofuel through pyrolysis process. Hence, utilization of solid by-product as biomass feedstock may offer more benefit and potency to reduce current environmental challenges, energy crisis as well as sustainability of biodiesel industries. Biomass pyrolysis seems to be a promising process for production of liquid and solid fuels (i.e. bio-oil and bio-char). Bio-oil from biomass (solid by-product) pyrolysis mainly consist of aromatic, aliphatic and naphthenic hydrocarbons, phenolic and oxygenated compounds. Bio-oil can be used as a substitute for fuels in motive energy production. Bio-oil has strategic values because of liquid product with higher calorific value, can be used as furnace oil, its handling and storage and also it can be upgraded to obtained light hydrocarbon for transportation fuel. The solid product of pyrolysis of biomass (i.e. bio-char) can be utilized as solid fuel and/or as feedstock for adsorbent like bio-activated carbon preparation for metal removal from water. Physical, chemical and thermal conditions for pyrolysis of biomass, such as reactor configuration, pyrolysis temperature, heating rate, particle size of biomass, residence time, gas flow rate, etc. are important parameters that affect product yield and composition.

1.7. Scope and Objectives of Research

Thus, based on the above brief discussions, it seems that there is a good scope to carry out further research on non-edible oil seeds to produce biodiesel, bio-oil and bio-char. With this basis rubber seed (*Hevea brasiliensis*) was considered as the feedstock in the present work which is rarely studied, abundantly available in India (North East and Kerala) and one of the promising non-edible oil feedstock for partial substitution of edible oil like soybean, cotton, sesame, canola, coconut oil, etc. Beside its non-edible nature, rubber plantations are already existing and thus eliminating competition for land space with vegetable crops. Therefore, this PhD thesis with title **"Utilization of Rubber Seeds for Biofuels Production",** targets the fulfillment of the following major objectives.

1. Extraction of rubber seed oil (RSO)
    i. Parameter optimization for extraction of rubber seed oil using response surface methodology (RSM)
    ii. Determination of physico-chemical properties of RSO for suitability of biodiesel feedstock
2. Synthesis of rubber seed oil methyl esters (ROME) using non-conventional catalysts
    i. Studies on catalytic performance of $Ba(OH)_2 \cdot 8H_2O$, Na_3PO_4, CaO, and waste egg shell based CaO for transesterification reaction
    ii. Comparison study on ROME synthesis through non-conventional techniques such as ultrasonic bath and ultrasonic horn
    iii. Optimization of reaction parameters such as reaction time, methanol to oil molar ratio and catalyst loading

iv. Kinetic study and thermal degradation behaviour for feedstock and its esters

3. Engine performance, emission characteristics and rheological study of ROME blends

4. Thermo-chemical conversion of solid by-products

i. Characterization of rubber seed shell (RSS) and rubber seed cake (RSC)

ii. Kinetic study and thermal degradation behaviour of RSS and RSC

iii. Lab scale pyrolysis of RSC and RSS

iv. Co-pyrolysis of RSC with waste polystyrene

v. Characterization of obtained products

1.8. Organization of the Thesis

The content of thesis is organized in seven chapters.

Chapter I provides an overview of the biofuel production with state of the art literature. This chapter also includes possible scope for further research, formulation of objectives and thesis organization.

Chapter II describes about material and methodology used for experiments in this thesis work. The aim of this chapter is to provide details of extraction of oil from oil seeds, esterification and transesterification reaction and pyrolysis process for bio-char and bio-oil productions from solid by-products. Further, this chapter emphasis on thermal degradation/decomposition of liquid products (RSO and ROME) and solid by-products (RSC and RSS) using non-isothermal TG analysis. This chapter also addresses various characterization techniques used for estimation of physico-chemical-thermal properties and quantification of the raw material and produced products.

Chapter III focuses on details of extraction of rubber seed oil using conventional technique (Soxhlet extractor). This chapter also describes the effect of particle size and organic solvents (polar and non-polar) on the yield of RSO. Further, the chapter presents application of response surface methodology for parameter optimization. The physico-chemical characterizations of extracted RSO for its suitability for biodiesel synthesis are briefly discussed.

Chapter IV deals on reduction of free fatty acid of RSO using H_2SO_4 and performance of heterogeneous catalysts (CaO, Na_3PO_4, egg shell based CaO and $Ba(OH)_2 \cdot 8H_2O$) for transesterification reaction of esterified rubber seed oil. This chapter also elaborates different non-conventional techniques used for transesterification reaction using selected heterogeneous catalysts. Chapter IV also describes in detail about optimization of parameter such as molar ratio, catalyst loading and reaction time for ultrasonic-assisted transesterification method using RSM. Further, the chapter elaborates comparison of physico-chemical properties of ROME obtained at optimum conditions with its original feedstock (RSO) and ASTM standard value for biodiesel to measure its suitability for fuel purpose. Further, the thermal stability and degradation kinetics along with activation energy and thermodynamic properties of RSO and its methyl esters under inert atmosphere are estimated. The chapter also describes qualitative analysis of evolved product gases during thermal decomposition of RSO and its methyl esters.

Chapter V provides rheological properties of RSO, ROME and blends (R5, R10 and R15)

and, comparison of important physico-chemical properties. Further, the chapter elaborates about the diesel engine performance and emission analysis of the blends with pure mineral diesel fuel.

Chapter VI summarizes characterization of solid by-products obtained during extraction process. Analogous study was carried out for solid by-product (RSC and RSS) like chapter IV. The chapter elaborates about utilization of solid by- products, RSC and RSS for the production of bio-oil, bio-char and gas using a semi-batch pyrolysis reactor. The effects of pyrolysis temperature and heating rates on product distribution and calorific value of the products are also discussed. Further, present co-pyrolysis of RSC with waste polystyrene.

Chapter VII presents conclusion drawn from the research work. It also provides possible direction and recommendation for future work based on the output of thesis work.

CHAPTER II

Materials and Methods

Materials;

Methods;

Procedures;

Physico-Chemical Characterizations of Feedstocks and Products

Chapter II

Materials and Methods

In this chapter, the details of experimental methods and procedure for the main processes; (1) extraction of rubber seed oil, fatty acid reduction by esterification process and transesterification process for esterified rubber seed oil (ERSO) and (2) thermo-chemical conversion of solid by-products are described. During extraction and transesterification process, response surface methodology (RSM) with central composite design (CCD) was applied for parameter optimization. This chapter also describes the thermal kinetic degradation/decomposition methods based on TGA results for liquid samples rubber seed oil (RSO) and rubber seed oil methyl esters (ROME) and solid samples rubber seed cake (RSC) and rubber seed shell (RSS), and lab scale pyrolysis of solid by-products (rubber seed cake and rubber seed shell) using semi-batch reactor. ^{1}H *NMR,* ^{13}C *NMR, GC-MS, TGA, and acid value are extensively used for evaluation of methyl ester formation during esterification and transesterification process and, pyrolytic product identification during thermo-chemical conversion process. Furthermore, physico-chemical characterization of the feedstocks and products for their suitability for respective application were elaborated in detail in this chapter. Further, the chapter elaborates about the solid samples characterization (solid catalyst, raw RSS and RSC, RSS bio-char and RSC bio-char) using XRD, FESEM-EDX and BET methods.*

2.1. Materials

Rubber seeds were collected from Assam, India. The rubber seeds were sun dried for 2 days and de-shelled manually for rubber seed kernels separation. Sulfuric acid (H_2SO_4) (Analytical Reagent grade (AR); 98%) and potassium hydroxide flakes (KOH), sodium hydroxide flakes (NaOH), barium hydroxide octahydrate ($Ba(OH)_2 \cdot 8H_2O$), tri-basic sodium phosphate (Na_3PO_4), calcium oxide (CaO), acetone ($(CH_3)_2CO$), hexane (C_6H_{14}), ethyl acetate ($C_4H_8O_2$), ethanol (C_2H_5OH), methanol (CH_3OH), sodium thiosulphate ($Na_2S_2O_3$), carbon tetrachloride (CCl_4), potassium iodide (KI), potassium bromide (KBr), deuterated chloroform ($CDCl_3$), starch powder, phenolphthalein indicator and Wijs' solution were procured from Alfa Aesar, Sigma-Aldrich and Merck India Pvt. Ltd.

2.2. Methods

2.2.1. Extraction Experiment

There are different techniques to extract the oil from seeds such as mechanical and chemical (solvent) extraction techniques (discussed in chapter I). The mostly widely used technique is chemical extraction by Soxhlet method. Soxhlet extractor with round-bottom flask with capacity of 500 ml was used (Fig. 2.1). The cylindrical Soxhlet extractor with capacity of 200 ml holding filter paper bag containing grinded rubber seed kernel (RSK) was placed onto the round-bottom flask containing the organic solvent. Top of the Soxhlet is connected with a condenser, operated by tap water together with ice. The solvent is heated with heating mantle to reflux. The solvent vapour moves up in a Soxhlet chamber through by-pass tube arm and the vapour cools dawn and condense and the solvent drips back into the

Soxhlet chamber. Condensed solvent floods into the chamber containing grinded rubber kernel seeds within filter paper bag. When the Soxhlet chamber is full, the chamber is automatically emptied through a siphoning action along a siphon tube, with the solvent running back, down into flask. This cycle is repeated according to the time allotted for extraction of the oil (2–12 h).

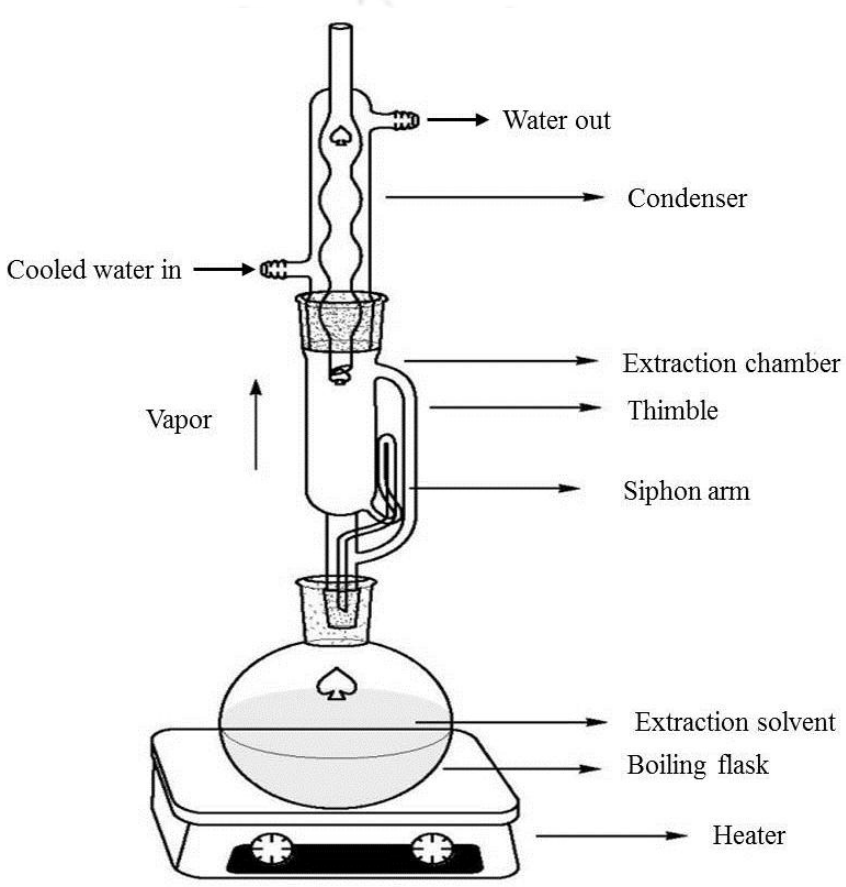

Fig. 2.1: Schematic of Soxhlet extractor

In this work, organic solvents such as hexane, methanol, ethyl acetate and mixture of ethyl acetate and water, extraction time (3, 4, 5, 6 and 8 h), average size of kernel (0.5, 1.00, 1.22, 2 and 3 mm) and kernel to solvent ratio (0.04, 0.06 and 0.08 g/ml) were studied to find the optimal condition for extraction of rubber seed oil. The extracted oil sample was obtained by separating the solvent using rotary vacuum evaporator (*Buchi, R-200, Germany*). The mixture

of oil and excess solvent was poured into a weighed conical flask. The flask was fitted to the rotary vacuum evaporator and immersed in the water. The temperature of the water bath was set slightly above the boiling point of the solvent. After recovery of the solvent, the heating system was switched off and the flask was removed and then left for 30 min to cool down. Finally, the flask was weighed and the concentrated extract was taken out from the flask. The percentage yield of extracts was calculated by Eq. 2.1.

$$Y = \frac{M_o}{M_k} \times 100 \qquad (2.1)$$

Where; M_o, M_k and Y, are mass of extracted oil (g), mass of kernel before oil extraction (g) and yield of RSO on the basis of extracted oil (%), respectively.

2.2.2. Chemical Modification of Rubber Seed Oil

2.2.2.1. Rubber Seed Oil Methyl Esters Synthesis

Esterification and transesterification reactions were conducted in a reactor of 60 ml and 100 ml (three necked round bottom flask) capacity equipped with a water and/or oil bath assembly to control the reaction temperature (30 °C and 65 °C). A probe type ultrasonic generator, with an operating frequency, amplitude and cycle maintained at 30 kHz, 80% and 1, respectively was used for mixing process.

Esterification reaction: The acid value (AV) or/and free fatty acid (FFA) content of vegetable oil determines the pathway of transesterification (i.e. either one step or two step process) for biodiesel synthesis [137]. The extracted RSO under optimum condition contents 12.12% free fatty acids. Therefore, it is required to perform acid treatment to reduce the FFA content prior to transesterification. The extracted RSO was heated at 100 °C for 10–15 min to remove the

impurities, if any. Three parameters; catalyst (H_2SO_4) loading (0.5–2 wt%), reaction time (30–150 min) and molar ratio (6:1–18:1) were considered as the effective parameters to reduce the acid value. A water bath was used to maintain the reaction temperature (30 °C) and absorb the heat generated due to exothermic nature of esterification reaction. After the esterification, reaction mixture was transferred into separating funnel and allowed to settle for 2 h. Two distinct layers were formed top layer, which consists of excess methanol and H_2SO_4 was removed and the bottom layer was then washed with hot millipore water (60–70 °C) to remove any impurities present in the esterified oil. The washed oil was then dried in rotavapor to evaporate the water/methanol, if any. Finally, the esterified rubber seed oil (ERSO) was analyzed for acid value by ASTM standard method and also the formation of methyl ester during esterification process was confirmed by ^{1}H NMR analysis [138, 139]. The conversion of FFA was calculated according to Eq. 2.2

$$X_E = 1 - \left(\frac{AV_t}{AV_0} \right) \quad (2.2)$$

Where; AV_0 *and* AV_t are acid value of initial and final esterified RSO (mg KOH/g sample), respectively. X_E is fractional reduction of FFA.

Transesterification: A known amount of ERSO, methanol (9:1) and catalyst (5 wt%) were added in to the glass reactor and the reaction mixture was stirred at 800 rpm (mechanical agitation) and 30 kHz (ultrasonic-assisted technique), and methyl ester formation was compared. Water bath was used to maintain the reaction mixture temperature to 30±2 °C. Ultrasonic-assisted technique (i.e. non-conventional method) for biodiesel synthesis using variety of catalysts such as $Ba(OH)_2{\cdot}8H_2O$, CaO, Na_3O_4 and egg shell based CaO was adopted and the conversion of esterified RSO to ROME was compared. Further, $Ba(OH)_2$

·$8H_2O$ catalyst was used to synthesis biodiesel (ROME) from ERSO via ultrasonic horn and ultrasonic cleaner (UH/UC) assisted transesterification reaction in a conical flask of 50 ml capacity and methyl ester formation for the two techniques were compared. UH operating with 100 W, 30±1 kHz working frequency, 1 cycle and 80% amplitude was fitted with piezoelectric transducer of 1 cm tip diameter (Fig. 2.2A). UH tip was immersed into the upper layer of interface of the reaction mixture to reduce possibility of vortex formation [140]. UC operating at 40±3 kHz working frequency and 300 W with piezoelectric transducer at bottom was used (Fig. 2.2B). Conical reactor was immersed in the ultrasonic cleaner/bath at the center position. Surrounding temperature was controlled with the help of water bath. Further, ultrasonic assisted transesterification at 30 °C temperature was studied in detail using $Ba(OH)_2·8H_2O$ (4–6 wt% of esterified oil), methanol reactant (6:1–9:1 molar ratio of methanol to ERSO) and for reaction time varying from 5–15 min. The overall product of transesterification was centrifuged to separate the solid catalyst. Methyl esters of rubber seed oil (ROME), excess methanol and bio-glycerol were separated by gravity settling. Methyl ester layer was washed (three times), and then dried with the help of rotavapor. The conversion of fatty acid alkyl groups of triglyceride presented in RSO sample into respective fatty acid methyl ester was confirmed and quantified by ^1H NMR spectroscopy methods. Extent of conversion of ERSO to ROME was compared for ultrasonic horn and ultrasonic cleaner assisted techniques. All the experiments were duplicated and average values are reported. ROME obtained under optimal condition was mixed with diesel and tested in diesel engine.

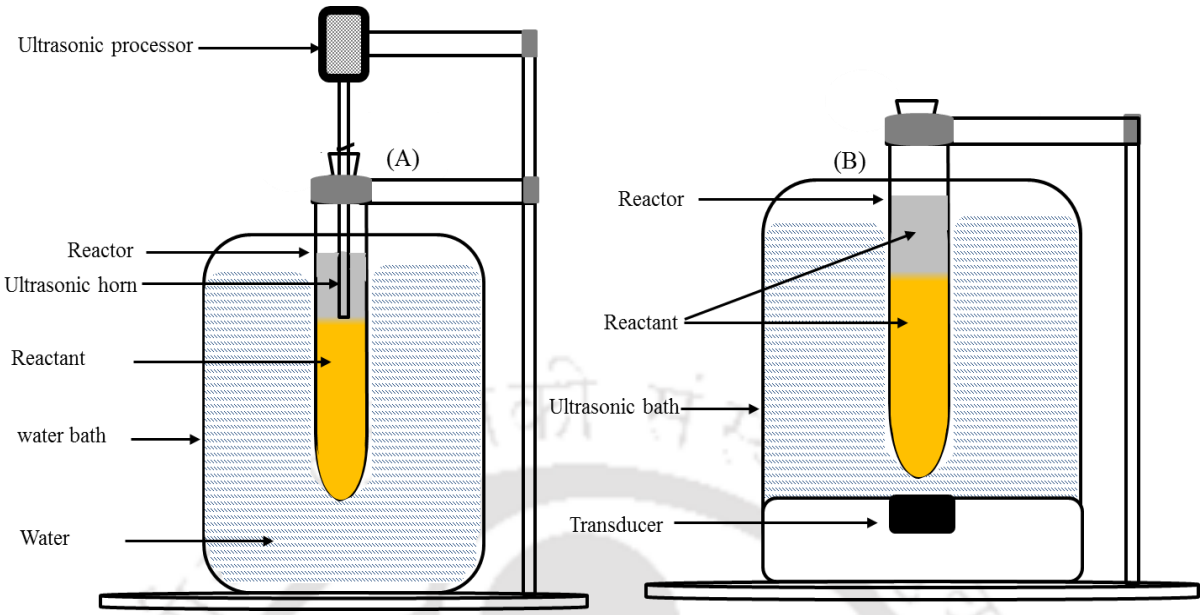

Fig. 2.2: Ultrasonic-assisted transesterification reactor configuration; (A) ultrasonic horn (UH) and (B) ultrasonic cleaner (UC)

Engine performance: ROME obtained under optimal condition was mixed with diesel using mechanical stirrer for 1 h to prepare homogeneous RDXX samples and tested in diesel engine [48, 141]. XX represents the amount of ROME (by volume) blended with diesel. Four samples labeled as RD0, RD5, RD10 and RD15 were prepared. Direct injection (DI) diesel engine consists of single cylinder, 4-stroke, water cooled, constant speed, naturally aspirated was used for engine performance analysis (Fig. 2.3). The detail specifications are listed in Table 2.1. The setup is coupled with eddy current dynamometer (*SAJ Make, Model AG10*) for loading which is applied by manually controlled knob of potentiometer and noted with the help of strain gauge type load cell (0–50 kg) on digital indicator. In cylinder combustion diagnostics, cylinder pressure measurement for each degree of crank rotation was done using piezo sensor for crank angle (CA) 360 degree incremental encoder with push-pull interface for crank angle measurement. The encoder operates on an electro-optical scanning principle. The transform of mechanical movements into electrical signals was acquired at time interval

of two-degree crank angle and logged using Engine Soft software. All prepared fuel samples (RD0, RD5, RD10 and RD15) were tested at constant speed of 1500±50 rpm with intake fuel pressure of 190 bar for the fixed compression ratio 17.5:1 with crank position at 23^{o} before top dead center (bTDC) under varying loads from 0% to 100% in steps of 20%. The engine jacket and exhaust gas calorimeter water flow rate were maintained constant at 300 lph and 100 lph, respectively. After the baseline assessment with diesel, the tests were performed for different fuel blends. The liquid fuels were supplied to the engine injection pump from the fuel tank under gravity feed. One minute fuel consumption measurements at a particular load were performed on a volumetric basis. Air consumption measurement was carried out by air-box method [142]. The coefficient of discharge of orifice meter was taken as 0.6.

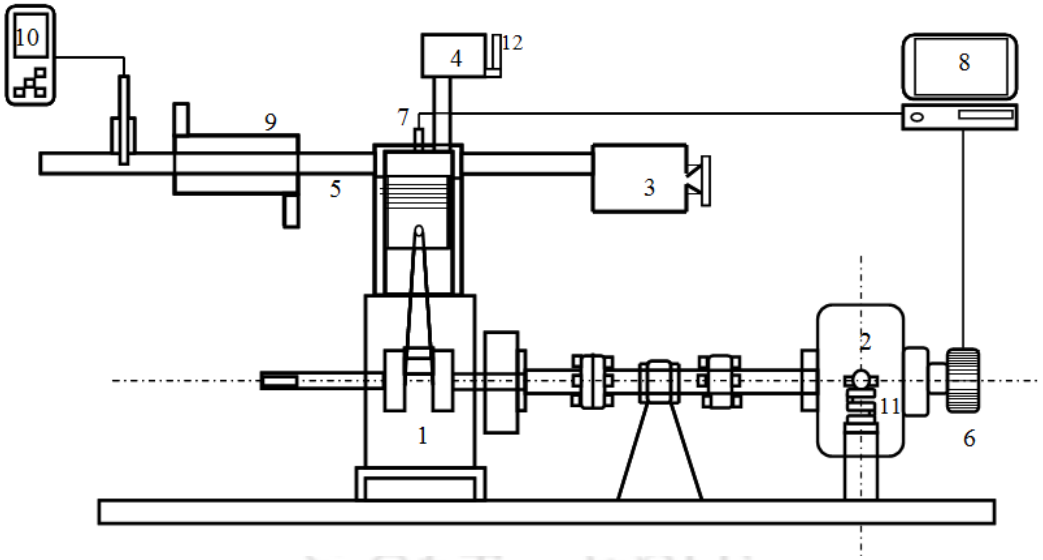

Fig. 2.3: Schematic of DI diesel engine test bench

Where: 1. Engine set up; 2. Eddy-current dynamometer; 3. Air box with orifice meter; 4. Fuel tank; 5. Exhaust gas line; 6.Crank angle encoder; 7. Cylinder pressure transducer with amplifier; 8. Computer system with Engine Soft Software; 9. Exhaust Gas calorimeter; 10. Exhaust Gas emission analyser; 11. Strain gauge type load cell; 12. Fuel measuring tube.

Table 2.1: Specification of diesel engine test bench and gas analyzer

Make and model	Kirloskar, Model TV1
Engine type	Single-cylinder, 4-stroke DI diesel engine
Rated power	5.2 kW (7 BHP) at1500 rpm
Type of cooling	Water cooled
Bore × Stroke	87.5 × 110 mm
Swept volume	0.661 L
Compression ratio	17.5:1
Speed	1500 rpm, constant
Injection timing	(diesel) 23°BTDC
Make, type of sensor and maximum pressure	PCB make, Piezo electric (15000 psi)
Resolution and response time	0.1 psi, 2 micro seconds
Crank angle sensor	360 degree encoder with a resolution of 2 degree

Specifications of exhaust gas analyzer[#]

Emission	O_2	CO	CO_2	NO	NO_2	HC	SO_2
Range[*]	25 vol%	10^4 ppm	50 vol%	3000 ppm	500 ppm	40,000ppm	5000 ppm

[*]*all of the emission values are started from zero,* [#] *Uncertainty ±5%*

2.2.3. Thermal Cracking of Solid Residue: Rubber Seed Shell and Rubber Seed Cake

Lab scale pyrolysis experiments of RSS and RSC were performed in a semi-batch pyrolyzer with continuous flow of nitrogen at 400 ml/min (Fig. 2.4). For each experiment 50 g of rubber seed shell (RSS) was placed inside stainless steel reactor. The reactor was heated externally by an electric furnace with PID controller to achieve pyrolysis temperature of 350 °C, 400 °C, 450 °C, 500 °C, 550 °C and 600 °C, at heating rates ranged between 10 °C/min–40 °C/min and then kept isothermal for 1 h. As the temperature of furnace raised dehydration, depolymerization, decomposition and fragmentation reactions of three key biomass building

blocks in rubber seed shell (RSS) or rubber seed cake (RSC): hemicellulose, cellulose and lignin were occurred and condensable and non-condensable gases were produced and then cooled using series condensers. Two condensers in series connected with flask (at average temperature of -2 °C) were assembled to collect condensable vapor in the flasks. The amounts of solid (bio-char) remained after pyrolysis process was also measured. The yield of non-condensable gaseous product was calculated from the material balance (Eq. 2.3). The individual experiment was duplicated and the average values were calculated.

$$Yield\ (wt\%) = \frac{W_f}{W_o} \times 100 \qquad (2.3)$$

Where: W_o and W_f are the initial and final weight (liquid, bio-char or gas) after reaction (g), respectively.

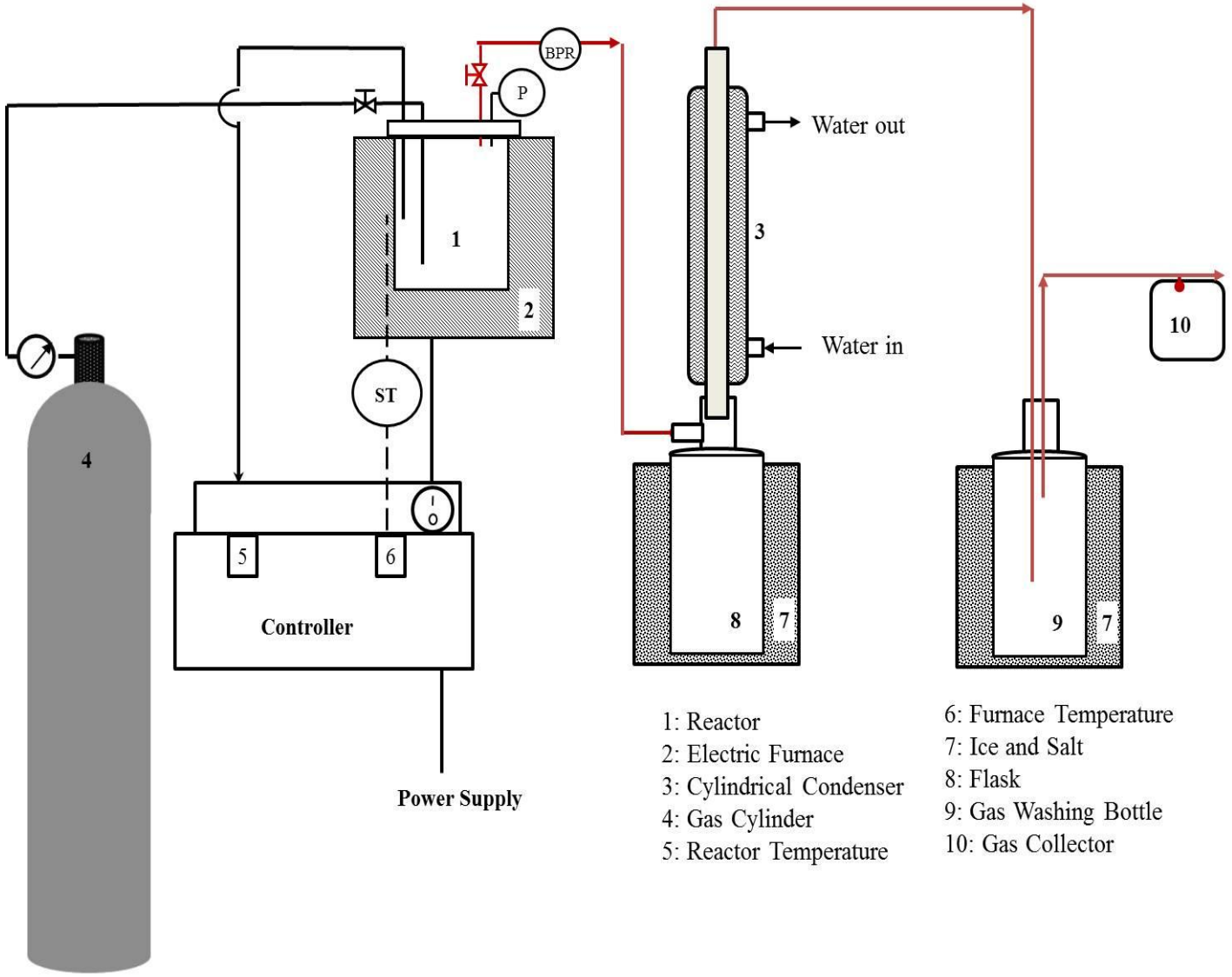

Fig. 2.4: Schematic diagram of pyrolysis set-up

2.2.4. Characterization of Raw Materials and Products

Proximate Analysis: This analysis is the most widely used method for solid and liquid fuels characterization such as moisture content (MC), ash content (AC), volatile matter (VM) and fixed carbon content (FC). The solid samples were prepared according to American Society for Testing and Materials (ASTM) and National Renewable Energy Laboratory (NREL) standards. For each analysis the crucible was dried at respective operating temperature (i.e. for moisture content at 105±1 °C, ash content at 575±25 °C and volatile matter at 950±25 °C) for 30 min and placed in a desiccator. For moisture determination, sample (~ 2 g) was placed in the dried crucible and then oven dried again for 16 h at 105±1 °C, MC is calculated using the following mass balance expression (Eq. 2.4) [143].

$$MC\ (wt\%) = \frac{\left(w_c + w_o\right) - \left(w_c + w_{fr}\right)}{w_o} \times 100 \qquad (2.4)$$

Where w_c, w_o and w_{fr} are the weight of empty crucible, raw sample and moisture free (oven dried) sample, respectively.

Further, moisture free sample (in dried crucible) was placed in muffle furnace at respective temperature for a specific duration to estimate ash content (180 min at 575±25 °C) and volatile matter (at 950±25 °C for 7 min). The ash content and volatile matter were estimated (on dry basis) using Eq. 2.5 and Eq. 2.6 [143], respectively. Fixed carbon content was calculated by the difference. Each sample was triplicated and the average values were calculated. However, the moisture content of the liquid sample (RSO, ROME and pyrolyltic oil) was measured using volumetric Karl Fisher Method (*Titrino 787 Karl Fisher from Metrohm*).

$$AC\ (wt\%) = \frac{w_A}{w_{OD}} \times 100 \qquad (2.5)$$

Where w_{OD} and w_A are weight of oven dried sample and ash obtained.

$$VM\ (wt\%) = \frac{w_{OD} - w_f}{w_{OD}} \times 100 \qquad (2.6)$$

Where: w_{OD} and w_f are weight of oven dried sample and residue obtained.

Ultimate Analysis: The elemental compositions such as carbon, oxygen, hydrogen, nitrogen and sulfur present in RSC and RSS samples were determined using CHNS Elemental Analyzer (*Eurovector/EA3000*). Approximately 1 mg sample was completely combusted in pure oxygen which resulted in different gases such as CO_2, H_2O, N_2 and SO_2. The analysis of these gases (mole counts) provides elemental compositions. The percentage of oxygen was calculated by difference (i.e. $O = 100 - (C + H + N + S)$)

Extractive Analysis for Rubber Seed Kernel (RSK) and Rubber Seed Shell (RSS): The extractives from RSK and RSS were extracted using hexane (non-polar) and ethanol (polar) as solvent using a Soxhlet method. Grinded and oven dried (105 °C for 3 h) RSS were placed in cellulose thimble bag and the bag was placed in a Soxhlet tube. About 300 ml solvent was taken in the round bottom flask of Soxhlet extractor. The extraction process was performed first by hexane to separate the class of compounds such as non-polar lipids, hydrocarbon compounds. The hexane raffinated biomass were dried at 60 °C for overnight to remove hexane and then extracted with ethanol to separate compounds such as chlorophylls, polar wax and other minor compounds. The extraction was counted for 8 h at boiling point of respective solvents. The yield of extractives (wt%) was calculated using the following expression (Eq. 2.7);

$$Yield\ (wt\%) = \frac{W_E}{W_{SS}} \times 100 \quad (2.7)$$

Where W_E and W_{SS} are weight of extractives (g) and oven dried solid sample (RSS or RSK) (g), respectively.

Extracted rubber oil, ROME, diesel and blended samples (RDXX) were characterized using standard procedures (ASTM/AOCS, etc.) to measure physico-chemical properties such as density, refractive index, calorific value, acid value, saponification value, iodine value, flash point, fire point, cold flow properties.

Acid value (AV): The amount of potassium hydroxide (KOH) in milligram required to neutralize a gram of sample is known as acid value. It measures the presence of free fatty acid in the sample. Free fatty acid percentage in the sample is approximately equal to half the acid value. American oils chemists society (AOCS) official method (Te TA-64, 1997) was used to estimate the acid value of RSO, ERSO and ROME. The acid value was calculated using the following expression (Eq. 2.8);

$$AV = \frac{N \times V \times 56.1}{M_s} \quad (2.8)$$

Where: *Av*, *N*, *V* and M_s are acid value (mg KOH/ g of sample), normality of NaOH (N), volume of titrant (ml) and mass of the sample (g), respectively.

Density: Density (ρ) is defined as mass of sample per unit volume and can be measured using specific gravity bottle as per ASTM D4052 method (Eq. 2.9). It is an important property for fuel since fuel injection operates on a volume metering system, as the fuel density increases, more fuel is injected by mass. With increase in density, viscosity also increases. Fuel with higher density causes an increase in particulate matter (PM) and NOx emission in

diesel engines [142, 144]. The density of rubber seed oil and its biodiesel were marginally higher than that of mineral diesel but within the prescribed limit of European standard (EN 14214-07) for fuel production and fuel application diesel engine.

$$\rho = \frac{Mass\ (kg)}{Volume\ (m^3)} \tag{2.9}$$

Viscosity: Viscosity is a very important flow property of fuel. The standard range of viscosity of fuel is 1.9–5 mm^2/sec in EN 14214 standard. The upper limit of viscosity ensures that fuel will flow readily during cold starting and a minimum limit is often specified to avoid the possibility of a serious power loss at high temperature. High viscosity leads to poorer atomization of the fuel spray and less accurate operation of the fuel injectors. The major disadvantage of using of vegetable oil directly as fuel in diesel engine is due to the high viscosity which may cause in long and short term problems to engine. In general, the viscosity of vegetable oil and biodiesel is higher than that of petroleum diesel. Further, rheology analysis of liquid samples are measured by using Interfacial Rheometer (*Anton-Paar Model: MCR 301*) by varying temperature from 25–80 °C and shear rate range of 5–300 1/sec. Thermostatic water bath was used to control the working temperature within the set point range ±0.1 °C. Diesel, methyl esters of RSO and three different blends (5 vol%, 10 vol% and 15 vol%) sample (approx. volume 2 ml) were stored in different Eppendorf tube and approximately 0.6 ml of sample were taken for the analysis. The Rheometer configuration used was cone and plate system with (a) measuring cone, *Model CP 50-1* (angle 0.994°), Dia.: 50 mm and (b) INSET I-PP 80/SS, Dia.: 80 mm; details was listed below. The cone gives torque by using air bearing system, clean and filtered air provided by air compressor (*Make : ANEST IWATA Motherson Limited, India ; Model : FS05*) with pressure ranges from 4–6 kg/cm^2. Minimum torque: 0.1 µNm; Maximum torque: 200 µNm; Torque resolution: 0.001

μNm; Torque accuracy max.: (0.2 μNm; 0.5%); Maximum rise of torque: 1500 Nm/sec; Power supply: 100–240 VAC; Frequency: 50–60 Hz; Maximum power consumption: 850 W; Fuses T10 AH. All rheological data was stored and extracted by Rheoplus V3.1 software. The sample temperature was maintained constant within ±0.1 °C by means of a water bath (*Escy Ic201, Escy Enterprises*) with Peltier temperature control which circulated water and through the jacket of the rheometer. All the measurements were performed in triplicate, and the average values are presented here. The maximum uncertainties of viscosity determinations were less than ±1%.

Flash and Fire Point: Flash point is the minimum temperature at which the fuel will ignite (flash) on application of an ignition source under specified conditions. Whereas fire point is the temperature at which the fuel vapors can burn continuously for more than 5 seconds when tested in flash point apparatus. The flash and fire points were estimated using Cleveland open cup apparatus following ASTM D56-16a standard.

Calorific (Heating) Value (CV): It is one of the most important properties of fuel and defined as the amount of heat released in one gram of samples undergoes complete combustion. A known amount of sample (0.5–1 g) was placed in the bomb calorimeter crucible. Fused wire was threaded through the electrode and the tip of wire was placed on sample surface and then kept in the bomb. The bomb was pressurized with pure oxygen and then placed in the calorimeter tank which was filled with 2 L distilled water. The bomb was fired after temperature reach constant and the raise temperature was recorded for CV calculation according to ASTMD2015-85.

2.2.4.1. Differential Scanning Calorimeter (DSC)

Low temperature properties of a fuel at which the sample begins to crystallize upon cooling, such as cloud (CP) and pour (PP) points, are important properties from engine performance point of view. Cloud point, which occurs at a higher temperature than the pour point, is the temperature at which a fatty material becomes cloudy due to the formation of crystals and solidification of saturates. These solids can clog fuel lines. The pour point is the temperature at which the amount of wax from solution is sufficient to gel the fuel; thus it is the lowest temperature at which the fuel can flow. The cloud and pour points of diesel are much lower than that of the vegetable oil derived biodiesel. DSC analysis helps to measure the phase change points of the sample using minimal sample amount (10 mg) as compared to ASTM method (~50–100 ml). DSC analysis was conducted on RSO, ROME, RDXX (~10 mg) using DSC1 stare system (*Metteler Toledo*) with aluminium crucible. Thermal program was set with heating rate of 5 °C/min for (1) heating from 25 °C to 50 °C and, holding for 10 min to homogenize and dissolve any waxy material present in the sample (2) cooling from 50 °C to -25 °C (3) followed by heating from -25 °C to 50 °C. DSC analysis was conducted for three cycles (repeated) with same sample and excellent reproducibility was observed.

2.2.4.2. Thermogravimetric Analysis (TGA)

Thermogravimetry (TG) technique provides a measurement of weight loss of the sample as a function of temperature and time. These techniques are used to continuously monitoring the physical and chemical changes of a sample which happen with increase or decrease in the temperature of the sample. Mass loss observed in the TGA can be directly related to the thermal stability as well as to volatility of the sample. Thermal stability behavior and thermal decomposition temperatures of liquid products (RSO and ROME) and solid samples (RSK,

RSS and RSC) were analyzed using TGA system (*Netzsch:STA449F3A00*). Non-isothermal TGA experiments of RSO, ROME, RSC, RSS and RSK (8–10 mg) were performed from ambient temperature to 800 °C at a heating rates of 2, 5, 10, 20, 30, 40 and 50 °C/min. Inert gas was used as purge gas (flow rate of 40 ml/min) as well as protective gas (flow rate of 20 ml/min). Further, the evolved gas products during thermal decomposition were continuously monitored and measured using Perkin-Elmer TGA and FT-IR coupled system. Gas transfer tube and gas cell were heated up to 250 °C to prevent condensation of the evolved products.

2.2.4.3. Nuclear Magnetic Resonance (NMR) Spectroscopy

To estimate the fatty acid compositions of RSO, ERSO and ROME samples, Nuclear Magnetic Resonance Spectroscopy (^{1}H NMR) (*Make: Bruker, 600MHz*) analyses were performed. Liquid sample of 10–30 µl was taken in a 5 mm NMR tube and mixed with 600µl deuterated chloroform ($CDCl_3$) solvent. The chemical shift peak of deuterated chloroform at 7.26 ppm was taken as internal reference. The proton shift peaks of methyl ester and methylene were taken at 3.65 ppm and 2.31 ppm, respectively. ^{1}H NMR profile for RSO showed no peak at 3.65 ppm. From NMR profiles of the samples fatty acid composition of oil [145] and RSO conversion [146] were estimated. The conversion of RSO was calculated using Eq. 2.10.

$$X\ (\%) = \frac{2 \times A_{ME}}{3 \times A_{\alpha-CH_2}} \times 100 \qquad (2.10)$$

Where X (%) is the percent formation of rubber oil methyl ester, A_{ME} is the integration value of methyl ester proton (peak area at 3.65 ppm in ^{1}H NMR) and $A_{\alpha\text{-}CH2}$ is the integration value of carbonyl methylene proton (peak area at 2.31 ppm in ^{1}H NMR). Further, the structural characterization by ^{1}H NMR for pyrolytic liquid sample was performed to obtained an

overview of the liquid product compositions.

2.2.4.4. Fourier Transform Infrared (FT-IR) Spectroscopy

Infrared spectra of the samples were measured using FT-IR analyzer instrument (*Shimandzu: IR Affinity*) with attenuated total reflection (ATR) using air as background for functional group identification. All the ATR spectra of the samples were collected in the range of 5000–600 cm^{-1} for 30 scan and with 4 cm^{-1} spectra resolution at room temperature. FT-IR spectrums of the samples were used for characteristic functional group identification.

2.2.4.5. Gas Chromatography-Mass Spectroscopy (GC-MS)

Gas chromatography (*Varian* 450-GC) coupled with mass spectrometry (*Varian* 240-MS) (GC-MS) was used to identify the chemical compositions present in the liquid sample. Capillary column (VF-5ms) of 50 m x 0.2 mm (0.33 μm film thickness) dimension was used. The oven was heated from ambient to 70 °C and kept at isothermal condition for 3min and, then heated up to 300 °C at a heating rate of 10 °C/min. The final temperature was maintained for 7 min. The ion source temperature was set at 300 °C; MS detector was operated in a scan mode in the range of 50–550 amu. The constituents of samples were identified by comparing the mass spectra with national institute of standards and technology (NIST) research library.

2.2.4.6. XRD, BET and FESEM-EDX for Solid Samples

Barium hydroxide octahydrate catalyst received in the pellet form was grinded and used directly for transesterification reaction. Further, the grinded catalyst was dried at 50 °C for 24 h and then calcined at several temperatures 200 °C, 400 °C and 800 °C for different time

period 4.5 h, 4.5 h and 4 h, respectively. The catalyst sampled freshly prepared, calcinated and collected after transesterification process were characterized using techniques; i.e. X-ray diffraction (XRD), field emission scanning electron microscopic (FESEM), Beruauer-Emmer-Teller (BET) and Fourier transform infrared spectroscopy (FT-IR).

X-ray diffraction (XRD): Powder X-ray diffraction analysis of catalyst was conducted using Bruker (*Model-D8- Advance*). Cu-K_α radiations were employed at ambient temperature to generate patterns from the sample. A range of two theta angle from 5–80^o with 0.04 step size and 2/min scanning speed was used. The samples were mounted on sample holder and, average crystallite size was determined via Debye-Scherrer equation (Eq. 2.11) [147].

$$D = \frac{0.9\,\lambda}{l \times \mathrm{Cos}\theta} \qquad (2.11)$$

Where: *D* is crystallite size (nm); λ is wave length of Cu-K_α (0.1541 nm); *l* is full width at half maximum intensity (radian); θ is half of the diffraction angle/Bragg angle.

Morphology and Energy Dispersive X-ray (EDX): Morphology of the solid samples was determined by field emission scanning electron microscopic (FESEM) analysis using Zeiss (*Model: Sigma*). The samples were sprayed on the carbon conductive tape which was attached with sample holder (stub) and gold coated to reduce charging, then image and elemental analysis were obtained using FESEM and FESEM-EDX, respectively.

Beruauer-Emmer-Teller (BET): The total surface area, pore volume, pore size and pore size distribution of the catalyst were calculated via Quantachrome (*Model: Autosorb-IQ MP*) using

nitrogen adsorption. BET method was used to calculate the total surface area, pore volume and actual pore size [148]. The particle size (nm) was calculated assuming the catalyst particle as sphere (Eq. 2.12) [149]. Further, the pore size distribution was determined by BJH (Barrett-Joyner-Halenda) method [150].

$$Dp = \frac{6 \times 10^3}{\rho \times S_A} \quad (2.12)$$

Where: ρ is density of sample, S_A is BET surface area (m^2/g)

Similar analysis such as XRD, FESEM and BET has been conducted for solid by-product (RSS and RSC) and bio-char obtained during thermal cracking of RSS and RSC.

2.2.5. Design of Experiment (DOE) for Parameter Optimization

DOE is a tool to develop an experimentation strategy that maximizes learning and understanding of the existing processes using minimum resources [44]. It ensures that all factors and their interactions are systematically investigated. RSM technique is used to find the optimize conditions when the number of factors are involved in the process and response is affected by them. CCD is the most popular RSM design that fit an empirical polynomial model based on three groups of design, fractional factorial points, axial points and center points. The total number of experiment required for 'n' numbers of independent parameters are $2^n + 2n + c$; c is number of center point experiments [151]. The distance of the star points from the center point is given by $\alpha=2^{n/4}$. The detail of RSM using CCD scheme can be found elsewhere [44]. Preliminary experiments for extraction and transesterification process were performed by conventional optimization approach (i.e. one parameter at time optimization) to choose and set the range of parameters. During extraction process, an experimental matrix was design schematically to screen the effect of organic solvent (polar and non-polar), particle

size of kernel, extraction time (3–12 and 40 h) and kernel to solvent ratio (0.04, 0.05, 0.064 and 0.08). The experiments were performed based on the screening criteria, for example, first set of the experiments were conducted with four solvents keeping other process parameters constant. Further experimental matrix was modified based on the response from previous set. Two independent parameters extraction time (B) and kernel to solvent ratio (C) were selected for RSM analysis. Similarly, transesterification reactions were conducted at different condition such as (1) for fixed reaction time (10 min) and varied catalyst loading (2 wt%–10 wt%) and molar ratio (3:1–13:1), (2) for fixed molar ratio (7.5:1) and varied time (5 min–50 min) and catalyst loading (2 wt%–10 wt%) and (3) for fixed catalysts loading (4 wt%) and varied reaction time (5 min–50 min) and molar ratio (3:1–13:1). Based on the preliminary experiments for the above two processes lower (-1) and upper limits (+1) were obtained for further optimization study using RSM (Table 2.2). However, optimization of pyrolysis process was carried out by one parameter at a time optimization approach.

Table 2.2: Independent parameters used for CCD in extraction and transesterification

Parameter	Unit	Symbol	Levels				
			$-\alpha$ ($-2^{n/4}$)	Low (-1)	Medium (0)	Higher (+1)	$+\alpha$ ($+2^{n/4}$)
Extraction							
Time	h	B	3	4	5	8	9
Ratio	g/ml	C	0.03	0.04	0.05	0.08	0.09
Transesterification							
Catalyst loading (wt/wt)	wt%	A	3.3	4	5	6	6.68
Time	min	B	1.59	5	10	15	18.41
Molar ratio (mole/mole)	–	C	4.98	6	7.5	9	10.02

$\pm\alpha$ is ±1.414 and ±1.682 for Extraction and transesterification process, respectively

2.2.6. Thermal Kinetic Models

Thermogravimetric analysis (TGA) under non-isothermal pyrolysis condition is an effective technique to deduce kinetic parameters of the process such as activation energy (*E*), pre-exponential factor (*A*) and order of reactions (*n*). TG monitors online mass change of a given material as a function of time and temperature. The shape of thermogravimetric curve helps predicting the reaction kinetic [152]. Mass loss rate data during thermal degradation of a sample can be used to acquire kinetics of the decomposition process using various mathematical models. Several model-fitting and model-free kinetic methods have been reported in the open literature to evaluate the kinetics of solid and liquid decomposition [24, 119, 152-157]. Invariant kinetic parameter (IKP) and Coats-Redfern (CR) methods are model-fitting methods. Model-free methods are Friedman (FRD), Flynn-Wall-Ozawa (FWO),

Kissinger-Akahira-Sunoes (KAS). These kinetic methods are more reliable and widely used to analysis the thermal decomposition data for different biomass and waste materials. The activation energy values (*E*) of the samples for thermal decomposition were calculated using model free and fitting approaches such as Friedman (FRD) [158], Flynn-Wall-Ozawa (FWO) [159], Kissinger (KM) [160], Coats-Redfern (MCR) [161], Modified Coats-Redfern (CR) [122] and Invariant kinetic parameter (IKP) [162]. The mathematical expressions for these methods are summarizes in Table 2.3. The conversion (α) at various thermal degradation temperatures/times was estimated from TGA at various heating rates (Eq. 2.13).

$$\alpha = \frac{(w_0 - w_t)}{(w_0 - w_f)} \tag{2.13}$$

Where: w_o, w_t and w_f are initial weight, weight left at time, t and weight left at end of time, respectively.

The fundamental expression for estimating kinetic parameters of decomposition process under non-isothermal condition considering Arrhenius temperature dependency can be written as (Eq. 2.14)

$$\frac{d\alpha}{f(\alpha)} = \frac{A}{\beta}\exp\left(-\frac{E_i}{RT}\right)dT \tag{2.14}$$

Where: β, $f(\alpha)$, A, E, T *and* R refer to heating rate (°C/min), the reaction mechanism model, pre-exponential factor (1/min), activation energy (J/mol), temperature (K) and gas constant (8.314 J/mol K), respectively.

Friedman model (FRD) is the first and general iso-conversional method on the basis of model free differential technique and obtained by taking natural logarithm of both sides of Eq. 2.14 [158] and becomes (Eq. 2.15)

$$\ln\left(\frac{d\alpha}{dt}\right)_{i,j} = \ln\left(f(\alpha)\cdot A\right) - \frac{E_i}{RT_{i,j}} \quad (2.15)$$

Where: *i*: conversion; j: heating rate

The aspects of Friedman [158] and Coats-Redfern [163] methods can be combined for estimation of kinetic parameters for multiple heating rate by Vyazovkin method can used as modified Coats-Redfern and the general expression for n^{th} order thermal decomposition of sample as follows (Eq. 2.16) [164-166]

$$\ln\left(\frac{\beta}{T^2}\right)_{i,j} = \ln\left(\frac{AR}{E\,g(\alpha)}\right)_{i,j} - \frac{E_i}{RT_{i,j}} \quad (2.16)$$

Where: g(α) is the integral form of the reaction model

Beside the differential method, the fundamental expression (Eq. 2.14) also used by integral method of Flynn-Wall-Ozawa model (Eq. 2.17) using Doyle approximation [159].

$$\ln \beta_{i,j} = C - 1.052\frac{E_i}{RT_{i,j}} \quad (2.17)$$

Kissinger proposed that the maximum rate occurs when $d(d\alpha/dt)/dt$ is zero. Therefore, the differentiation of fundamental Arrhenius expression (Eq. 2.14) for constant heating rate at which maximum rate occurs at peak temperature T_p is equal to zero. The simplified Kissinger model for first order thermal decomposition at peak temperature (T_p) can be expressed as follow (Eq. 2.18);

$$\ln\left(\frac{\beta}{T_P^2}\right)_j = \ln\left(\frac{AR}{E}\right) - \left(\frac{E}{R}\right)\left(\frac{1}{T_P}\right)_j \quad (2.18)$$

The plots of $ln(d\alpha/dt)_{i,j}$ versus $1/T_{i,j}$ (Eq. 2.15) (FRD), $ln(\beta_j/T^2_{i,j})$ versus $1/T_{i,j}$ (Eq. 2.16) (MCR), $ln(\beta_j)$ versus $1/T_{i,j}$ (Eq. 2.17) (FWO) and $\ln(\beta/T_p^2)$ versus $1/Tp_j$ *(Eq. 2.18) (KM)* were resulted a straight lines. The slopes and intercepts can be used to determine kinetic parameters

for respected methods.

Coats-Redfern method consider n^{th} order reaction model for studying non-isothermal kinetic decomposition using Taylor series expansion approximation. An assumption that $2RT/E$ is much lower than unity results the following expression (Eq. 2.19);

$$ln\frac{g(\alpha)}{T^2} = ln\frac{AR}{\beta E} - \frac{E}{RT} - \ln\left(1-\frac{2RT}{E}\right) \approx ln\frac{AR}{\beta E} - \frac{E}{RT} \quad (2.19)$$

Where $g(\alpha) = -\ln(1-\alpha)$ if $n=1$; and $g(\alpha) = \left(\left(1-\left((1-\alpha)^{(1-n)}\right)\right)/(1-n)\right)$ if $n \neq 1$

To construct the linear plot of $ln\frac{g(\alpha)}{T^2}$ versus $\frac{1}{T}$, several values of the order of reaction (n) within in the interval of [-10 10] were chosen to optimize the correlation coefficient (R^2). The best value of correlation coefficient ($R^2 \rightarrow 1$) ensures (within the range) the appropriate order of reaction. The activation energy and pre-exponential factor for each active pyrolysis stage were calculated from the slope and intercept of plots where maximum correlation coefficient (R^2) was obtained.

Further, the observations of Criado's master plot [167] are used in IKP method (Eq. 2.20–2.25) for thermal decomposition of the samples. In order to apply IKP technique for the decomposition kinetics of RSC and RSS, $\alpha=\alpha(T)$ curves for all respective heating rates were used. A set of various reaction model functions (Table 2.4) were considered for the interval of conversion at which the activation energy not changed significantly. The activation parameters for all the reaction models were calculated using differential method (Eq. 2.20) at each heating rate. The resulted linear relationship between LHS vs. reciprocal of temperature (K) for a specific model function $f(\alpha)$ provides $ln\ (A)$ and E values.

$$\ln\left(\frac{d\alpha}{dt}\right) - ln\left(f(\alpha)\right) = \ln A - \frac{E}{RT} \quad (2.20)$$

The obtained parameters were correlated through an apparent compensation effect (Eq. 2.21)

$$lnA = a + bE \quad (2.21)$$

Where: *a* and *b* are compensation constant; which are estimated from the intercept and slope of *lnA* vs *E*. The values *a* and *b* depend on heating rate. A plot of *lnA* vs *E* for different heating rates should intersect at true value of ln*A* and *E* [168, 169]. However, for RSS and RSC samples considered in this study, no single intersection point was found. Thus, true values of ln*A* and *E* (invariant activation parameters) were evaluated using super correlation (Eq. 2.22) [162, 168].

$$a = lnA_{inv} - bE_{inv} \quad (2.22)$$

To choose a reaction model which may help mechanism of the decomposition, the shape of *f(α)* vs. *α* obtained from IKP method and theoretical expression were compared [162]. Further, Sestak-Berggren (SB) model (Eq. 2.23) was applied with the activation energy obtained from IKP method over the conversion data obtained experimentally. The kinetic exponents, *m* and *n* are related through α_{max} (conversion at which *f(α)* is maximum) as,

$$s = \frac{m}{n} = \frac{\alpha_{max}}{1-\alpha_{max}} \quad (2.24)$$

Table 2.3: Kinetic method used for kinetic parameter evaluations

Method	Expression	Type	Plot	Result
FRD (Eq. 2.15)	$\ln\left(\frac{d\alpha}{dt}\right)_{i,j} = \ln Af(\alpha) - \frac{E_i}{RT_{i,j}}$	Differential	$\ln\left(\frac{d\alpha}{dt}\right)_{i,j}$ Vs. $\left(\frac{1}{T}\right)_{i,j}$	$Af(\alpha)_i$ and E_i
MCR (Eq. 2.16)	$\ln\left(\frac{\beta}{T^2}\right)_{i,j} = \ln\left(\frac{A\cdot R}{E\cdot g(\alpha)}\right)_{i,j} - \frac{E_i}{R\cdot T_{i,j}}$	Integral	$\ln\left(\frac{\beta}{T^2}\right)_{i,j}$ Vs. $\left(\frac{1}{T}\right)_{i,j}$	$\ln\left(\frac{A\cdot R}{E\cdot g(\alpha)}\right)_i$ and E_i
FWO (Eq. 2.17)	$ln\beta_{i,j} = C - 1.052\frac{E_i}{RT_{i,j}}$	Integral	$\ln\beta_{i,j}$ Vs. $\left(\frac{1}{T}\right)_{i,j}$	E_i
KM (Eq. 2.18)	$\ln\left(\frac{\beta}{T_P^2}\right) = \ln\left(\frac{AR}{E}\right) - \left(\frac{E}{R}\right)\left(\frac{1}{T_P}\right)$	Integral	$\ln\left(\frac{\beta}{T_P^2}\right)$ Vs. $\left(\frac{1}{Tp}\right)$	*E and A*
CR (Eq. 2.19)	$ln\frac{g(\alpha)}{T^2} = ln\frac{AR}{\beta E} - \frac{E}{RT} - \ln\left(1-\frac{2RT}{E}\right) \approx ln\frac{AR}{\beta E} - \frac{E}{RT}$ $g(\alpha) = -\ln(1-\alpha)$ if n=1 $g(\alpha) = \left(\left(1-\left((1-\alpha)^{(1-n)}\right)\right)/(1-n)\right)$ if n≠1	Integral	$\ln\frac{g(\alpha)}{T^2}$ Vs. $\frac{1}{T}$	E_j, n_j *and* A_j

Table 2.3 Continued…

IKP via SB (Eq. 2.20-2.25)	$\ln\left(\frac{d\alpha}{dt}\right)-ln\left(f(\alpha)\right)=\ln A-\frac{E}{RT}$ $lnA=a+bE$ $a=lnA_{inv}-b\,E_{inv}$ $f(\alpha)=\alpha^{m}(1-\alpha)^{n}$ $s=\frac{m}{n}=\frac{\alpha_{\max}}{1-\alpha_{\max}}$ $\ln\left(\frac{d\alpha}{dt}\exp\left(\frac{E}{RT}\right)\right)=\ln A+n\ ln(1-\alpha)$	Differential	$\ln\left(\frac{d\alpha}{dt}\right)-ln\left(f(\alpha)\right)$ Vs. $1/T$ ln*A* Vs. *E* *a* Vs. *b*	$E_{i,j,k}$, $lnA_{i,j,k,}$ *a*, *b*, E_{inv},, $lnA_{inv,}$ *n, and m*

i: conversion; j: heating rate and k: f(α)

Table 2.4: Reaction models for most common reaction

Kinetic model	Symbol	*f(α)*	*g(α)*
Power law	P1	$4\alpha^{3/4}$	$\alpha^{1/4}$
Power law	P2	$3\alpha^{2/3}$	$\alpha^{1/3}$
Power law	P3	$2\alpha^{1/2}$	$\alpha^{1/2}$
Power law	P4	$2/3\alpha^{-1/2}$	$\alpha^{3/2}$
Avrami– Erofeev	A2	$2(1-\alpha)[-\ln(1-\alpha)]^{1/2}$	$[-\ln(1-\alpha)]^{1/2}$
Avrami– Erofeev	A3	$3(1-\alpha)[-\ln(1-\alpha)]^{2/3}$	$[-\ln(1-\alpha)]^{1/3}$
Avrami–Erofeev	A4	$4(1-\alpha)[-\ln(1-\alpha)]^{3/4}$	$[-\ln(1-\alpha)]^{1/4}$
Phase boundary controlled (contracting area)	R2	$2(1-\alpha)^{1/2}$	$1-(1-\alpha)^{1/2}$
Phase boundary controlled (contracting volume)	R3	$3(1-\alpha)^{2/3}$	$1-(1-\alpha)^{1/3}$
First order	F1	$1-\alpha$	$-\ln(1-\alpha)$
Second order	F2	$(1-\alpha)^2$	$-(1-\alpha)^{-1}$
n^{th} order	Fn	$(1-\alpha)^n$	$1-(1-\alpha)^{1-n}/1-n$
1-D diffusion	D1	$1/2\alpha$	α^2
2-D diffusion (Valensi equation)	D2	$[-\ln(1-\alpha)]^{-1}$	$(1-\alpha)\ln(1-\alpha)+\alpha$
3-D diffusion (Jander equation)	D3	$3/2(1-\alpha)^{2/3}[1-(1-\alpha)^{1/3}]^{-1}$	$[1-(1-\alpha)^{1/3}]^2$
3-D diffusion (Ginstling-Brounshtein)	D4	$3/2[(1-\alpha)^{1/3}-1]^{-1}$	$(1-2\alpha/3)-(1-\alpha)^{2/3}$

The thermodynamic parameters (enthalpy (ΔH) (Eq. 2.26), Gibbs free energy (ΔG) and entropy (ΔS)) of the RSO and ROME samples were calculated at the point of the maximum mass conversions (i.e. mass conversions at the maximum peak temperatures) [170-172]. The value of pre-exponential factor (*A*) estimated by Eq. 2.27 was used to calculate ΔG (Eq. 2.28) and ΔS (Eq. 2.29) [173-175].

$$\Delta H = E - RT \tag{2.26}$$

$$A = \frac{\beta \cdot E}{R \cdot T^2} \cdot \exp\left(\frac{E}{RT}\right) \tag{2.27}$$

$$\Delta G = E + RT \ln\left(\frac{K_B \cdot T}{h \cdot A}\right) \tag{2.28}$$

$$\Delta S = \frac{\Delta H - \Delta G}{T} \tag{2.29}$$

Where K_B is Boltzmann constant (1.3806×10^{-23} m^2 kg s^{-2} K^{-1}) and *h* is Planck constant (6.6261×10^{-34} m^2 kg/ s).

Beside the values of activation energy and pre-exponential factor of thermal degradation, reaction order is also an important index. Avrami theory was applied to calculate the order of thermal degradation of both RSO and ROME at various temperatures using Eq. 2.30 [171, 172, 176]

$$\alpha = 1 - \exp\left(\frac{A \cdot \exp(-E/RT)}{\beta^n}\right) \tag{2.30}$$

Eq. 2.30 can be simplified to the following expression (Eq. 2.31);

$$\ln(-\ln(1-\alpha)) = \ln A - {}^{E}\!/_{RT} - n \ln \beta \tag{2.31}$$

At a particular degradation temperature, *T*, the points of *ln(-ln(1-α))* versus *lnβ* at various

heating rates could be fitted to a linear line. The reaction order can be calculated from the slope of the linear line.

CHAPTER III

Optimization of Process Parameters for Extraction of Oil from Rubber Seeds

Effect of Process Parameters on Extraction of RSO;

Optimization of RSO Extraction using RSM;

Physico-Chemical Characterization of Extracted RSO

Work Published As:

Reshad, A.S., Tiwari, P., Goud, V.V., 2015. Extraction of oil from rubber seeds for biodiesel application: Optimization of parameters. ***Fuel,*** 150, 636–64

Chapter III

Optimization of Process Parameters for Extraction of Oil from Rubber Seeds

This chapter addresses the extraction of oil from rubber seeds. The effects of process parameters such as extraction time, particle size, the amount of solvent per kernel for Soxhlet extractor are investigated. Further, application of design of experiment has been taken into consideration to prepare an experimental matrix using RSM followed by CCD. The interactive effect of two parameters together on the yield of RSO and optimization of process parameters are also presented in this chapter. Finally, the physico-chemical properties of RSO obtained under optimum condition are addressed for its suitability for biodiesel production.

3.1. Effect of Process Parameters

3.1.1. *Effect of Solvent Type*

Rubber seed kernels of 1 mm average particle size were extracted for 4 h using polar and non-polar solvents maintaining a solute-solvent ratio as 0.064. The oil yield obtained with non-polar solvent hexane was found to be maximum (46.01%) while the lowest value (32.67%) was obtained with polar solvent methanol (Fig. 3.1A). It is consistent with the results reported by Sayyar *et al.* [45]. The effect of non-polar solvent on yield mainly attributed due to the presence of non-polar long chain hydrocarbon in fatty acids of rubber seed oil [42, 177, 178].

3.1.2. *Effect of Particle Size*

The effect of particle size on oil yield using hexane solvent was investigated at two ratios (0.064 and 0.08) for different extraction time i.e. 4 and 8 h. Obtained oil yields are summarized in Fig. 3.1B. During long time extraction, the average particle (kernel) size larger than 2 mm resulted lower oil yield (31.6%), while particle size lower than 1.22 mm provided higher yield (~49%). The experiments conducted under similar conditions but for different time durations showed that the particle size influences the oil yield for short extraction time (~4 h) and observed to be decreasing with increased particle size. However, in case of long extraction time (>8 h) no significant change on oil yield were observed with particle size lower than 1.22 mm. The maximum oil yield (49.36%) was obtained with the average particle size of ~1 mm, extraction time 8 h and 0.08 solute to solvent ratio.

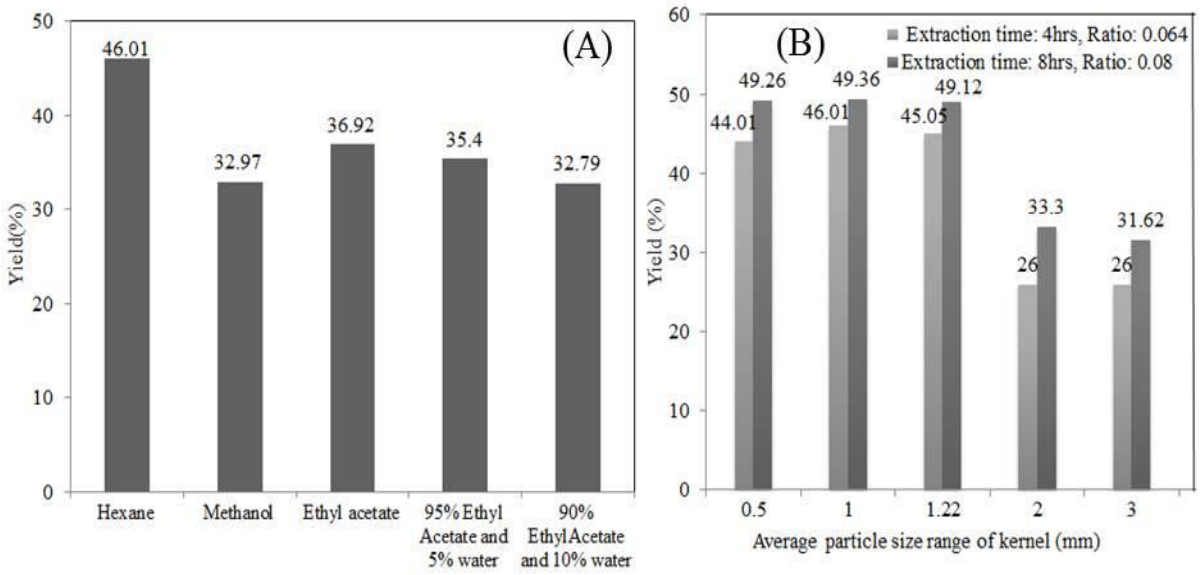

Fig. 3.1: (A) Effect of solvents on oil yield at the same extraction time of 4 h, 0.064 ratio of solute (g) to solvent (ml) and average kernel size range of 1 mm, (B) effect of particle size of kernel

3.1.3. *Effect of Solute to Solvent Ratio and Extraction Time*

Next set of extraction experiments were performed using hexane as solvent and kernel particle size of 1.22 mm to study the effect of extraction time and solute (g) to solvent (ml) ratio on oil yield. The obtained results are shown in Fig. 3.2. The maximum oil yield ~49% was obtained with 0.08 solute to solvent ratio. In general, the extraction yield should be higher at lower solute to solvent ratio. However, Mohamad *et al.* [179] studied the effect of solute to solvent ratio (0.03, 0.05 and 0.1) and reported the highest yield at an intermediate ratio of 0.05 and lowest yield at 0.03. This reverse trend of oil yield with respect to solute to solvent ratio may be due to the higher agglomeration of the kernel occurs at a low ratio. In the present study it was observed that the cake after extraction at a lower ratio showed relatively more agglomerated particles. Extraction experiments were also conducted for 12 h (0.08 g/ml ratio) and 40 h (0.18 g/ml ratio) using hexane solvent and the change in oil yield were found to be within 1.6%. In the literature the maximum extractable oil from the kernel (rubber seed) is reported to be 50% [12, 13, 24, 28]. Preliminary extraction data helped setting the range of parameters, a extraction time and ratio for DOE extraction study. Based on the obtained yields higher (+1) and lower (–1) bounds for extraction time (8 and 4 h) and ratio of kernel to solvent amount (0.08 and 0.04 g/ml) were considered to optimize the process yield (Table 3.1).

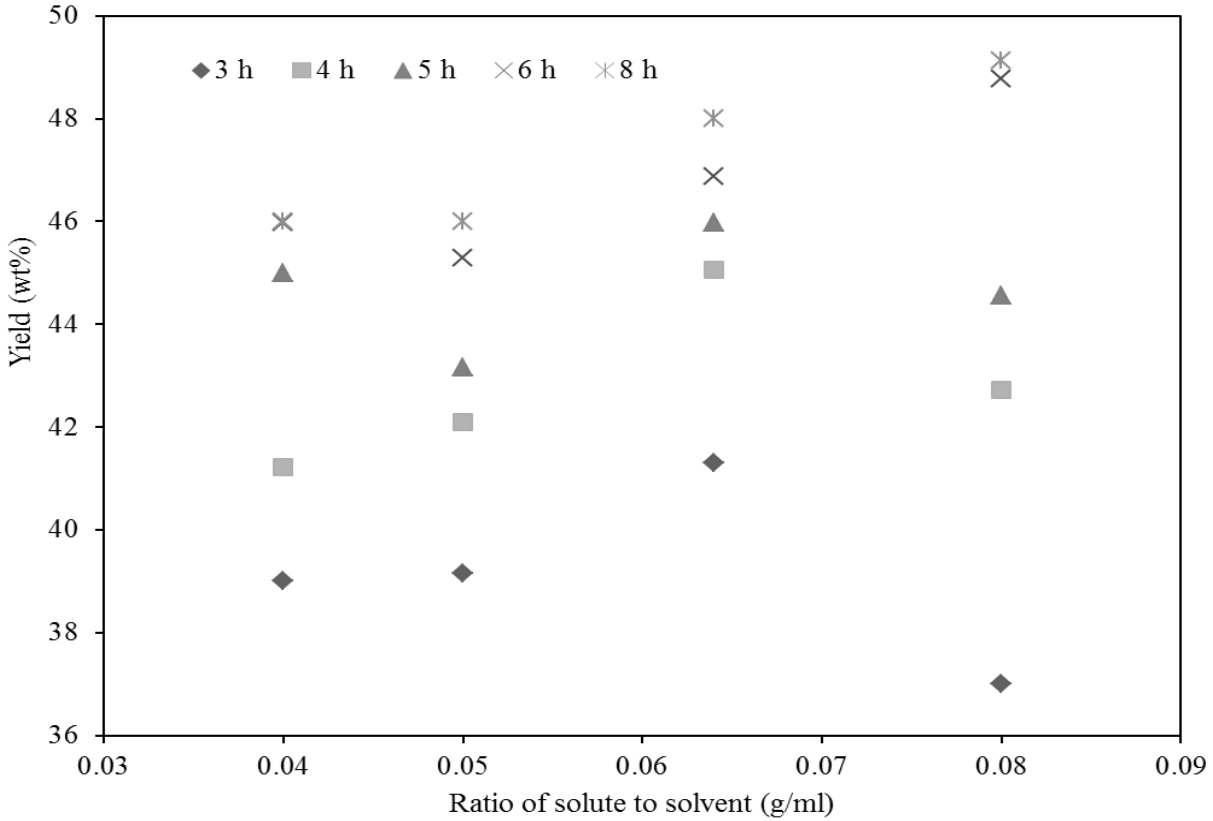

Fig. 3.2: Rubber seed oil yields at different solute to solvent ratios and extraction time using hexane as solvent with 1.22 mm particle size

Table 3.1: Experimental design matrix with code and actual level for interaction of the parameters and the responses obtained

Run	Code		Actual		Response		
	A: Time (h)	B: Ratio(g/ml)	t: Time (h)	R: Ratio(g/ml)	Actual Yield (%)	Model predicted Yield (%)	Residue
1	1.41	0.00	8.83	0.06	48.69	48.71	–0.02
2	0.00	0.00	6	0.06	42.55	42.55	0.00
3	0.00	0.00	6	0.06	42.55	42.55	0.00
4	–1.00	–1.00	4	0.04	41.23	42.08	–0.85
5	–1.41	0.00	3.17	0.06	41.1	40.78	0.32
6	1.00	–1.00	8	0.04	46.56	47.16	–0.6
7	1.00	1.00	8	0.08	49.12	48.57	0.55
8	0.00	0.00	6	0.06	42.55	42.55	0.00
9	0.00	–1.41	6	0.03	45.72	44.75	0.97
10	–1.00	1.00	4	0.08	42.73	42.43	0.3
11	0.00	0.00	6	0.06	42.55	42.55	0.00
12	0.00	1.41	6	0.09	45.33	46	–0.67
13	0.00	0.00	6	0.06	42.55	42.55	0.00

3.2. Optimization of Extraction Parameters by Response Surface Methodology

3.2.1. *Model Fitting and Analysis of Variance (ANOVA)*

To optimize the effect of extraction parameters on oil yield, RSM with CCD was used. The experimental range and model bound of the independent parameters studied are discussed in section 3.1.3. A 2^n factorial CCD model suggests conducting total 13 experiments, considering four axial, four factorial and five center points. The model predicted parameters and experimental generated data are shown in Table 3.1. The oil yield data obtained from the experiments are fitted to develop the model. The significance of each parameter was evaluated from the p-value by ANOVA, which reflects the strength of significances of the parameters. RSM suggested a quadratic model with F-value and p-value of 40.03 and 0.0001, respectively. Accordingly, the ANOVA of the suggested model was analyzed and presented in Table 3.2. The p-value was observed to be less than 0.0001; which signifies the reliability of the model. Similarly, smaller the p-value for the independent parameter, the more significant is the model response [44, 93]. The suggested model's p-value (<0.0001) is less than F-value which is significant and thus acceptable. The quadratic polynomial equations were generated to predict the oil yield using the design of experiment by code (Eq. 3.1) and in the form of actual parameters (Eq. 3.2). There was a good agreement observed between the calculated and experimental data.

$$\text{Yield}_{\text{Code}}\ (\%) = 42.55 + 2.81A + 0.44B + 0.26AB + 1.1A^2 + 1.41B^2 \quad (3.1)$$

$$\text{Yield}_{\text{Actual}}\ (\%) = 57.78912 - 2.28663t - 441.572R + 6.625Rt + 0.27438t^2 + 3531.25R^2 \quad (3.2)$$

Where: A (time (h)) and B (solute to solvent ratio (g/ml)) are parameters in DOE code.

Similarly, t (time (h)) and R (solute to solvent ratio (g/ml)) are actual parameters in the model to predict the oil yield.

Table 3.2: Analysis of variance for the response surface suggested model (i.e. quadratic model)

Source	Sum of squares	Degree of freedom	Mean square	F value	p-value
Model	84.62	5	16.92	40.03	<0.0001
A-Time	63.02	1	63.02	149.05	<0.0001
B-Ratio	1.54	1	1.54	3.64	0.0981
AB	0.28	1	0.28	0.66	0.4419
A^2	8.38	1	8.38	19.82	0.003
B^2	13.88	1	13.88	32.82	0.0007
Residual	2.96	7	0.42		
Lack of Fit	2.96	3	0.99		
Pure error	0.000	4	0.00		
Corrected	87.58	12			
Standard deviations = 0.65		Mean = 44.09	Coefficient of variation (%)= 1.47	R^2 = 0.966	Adj R^2 = 0.942

According to Table 3.2, all the parameters were found to be significant for the objective function i.e. yield. But, the significant strength varies for all the parameters. The p-value for parameter 'time' was observed to be less than 0.0001, which makes it most significant variable. The interaction of both the parameters was observed to be less significant. The coefficient of variation (%CV=1.47) indicates that the results of the quadratic model are reliable. Statistically estimated R^2 value for fitted model determines the quality of the model. The obtained value (R^2=0.966) indicates that 96.6% of the experimental results confirm

consistency with the data predicted by the suggested model (Eq. 3.1 and Eq. 3.2).

The relationship between studied process variables and resulted response function are shown in Fig. 3.3A. The oil yield was increased with an increase in the extraction time for all ratios. The ratio has less impact on the oil yield after 6 h extraction time. The oil yield data obtained from experiments were compared with RSM predicted yields and resultant values are summarized in Table 3.1. The residue values for each case were found to be less than unity which also indicates that R^2 value for the model is close to one. Fig. 3.3B shows the effect of extraction time and solute to solvent ratio on oil yield for fixed size of a kernel, 1.22 mm. It can be observed that, the oil yield increased significantly with the extraction time. This may be because of the more interaction between solute and solvent. On the other hand, oil yield decreased with an increase in the ratio initially and then increases at a higher ratio. The trend agrees well with experimental results (Fig. 3.2).

3.2.2. *Process Optimization*

Using the design of expert 7.0.0 software the optimal values for the obtained regression model (Eq. 3.1) for selected variables were determined by numerical method. The model was employed by setting parameters in the range (Table 3.1) with the goal of maximizing oil yield. The model predicted optimal (maximum) oil yield, 48.57% at 8 h extraction time and 0.08 kernel (g) to solvent (ml) ratio with a desirability of 0.931 of the variables. The experimental oil yield at optimal condition, 49.12%, is close to the model predicted value (within 1.11% error values).

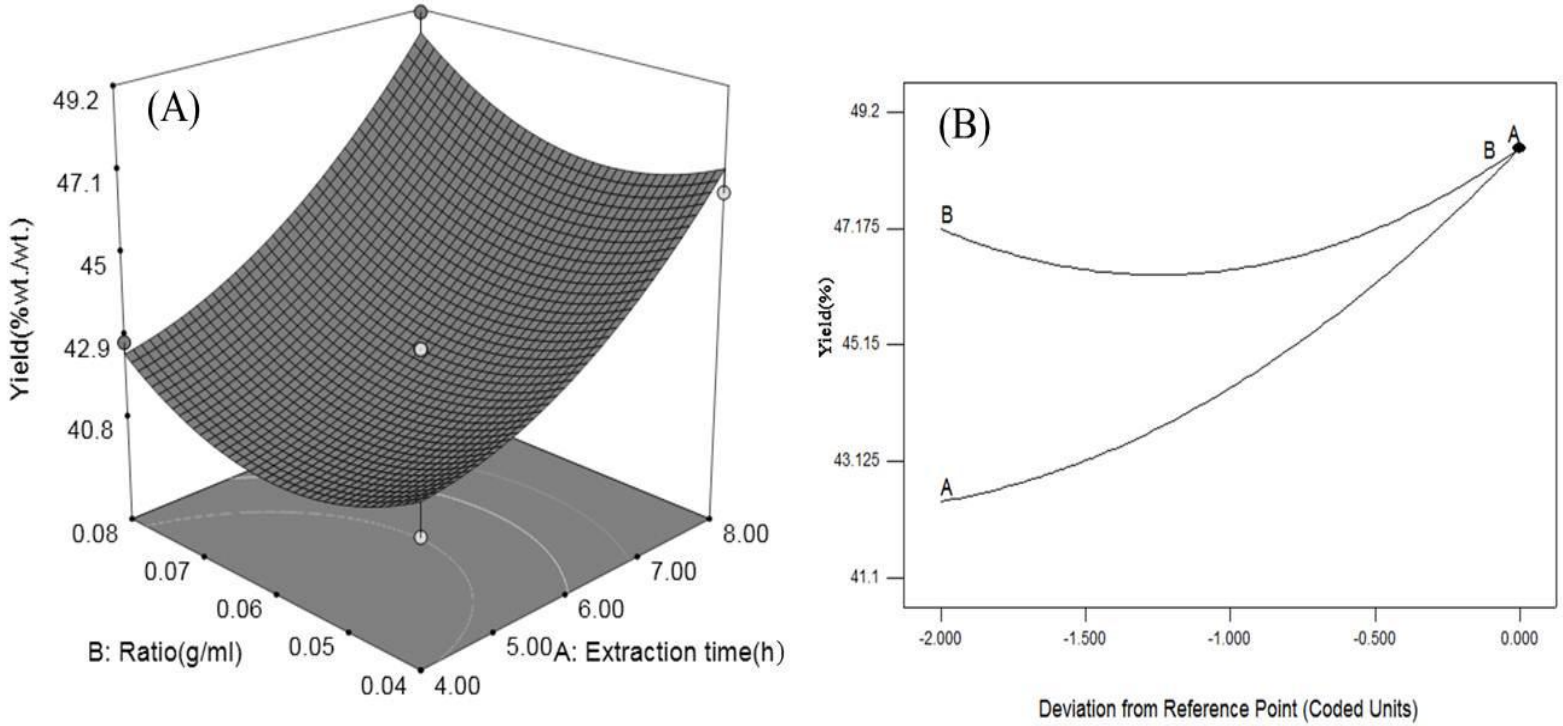

Fig. 3.3: Effect of extraction process parameters, extraction time and solute to solvent ratio (combined) on oil yield for 1.22 mm particle size sample. (A) 3D view with contour plot (B) deviation from reference point

3.3. Characterization of Rubber Seed Oil (RSO)

3.3.1. *Physico-Chemical Properties of RSO*

RSO obtained at optimum extraction condition was characterized for various physico-chemical properties using standard methods. The methods used and the values obtained are summarized in Table 3.3. The oil obtained using hexane as solvent appeared to be golden yellowish color whereas in case of methanol and ethyl acetate solvents the oil color was different (i.e. dark brown). Specific gravity of RSO was found to be 0.91 which indicates that the oil is lighter than water. Refractive index (RI) of the RSO was found to be 1.47 at temperature 22.8 °C which falls within the refractive index range reported in the literature for organic oil (i.e. 1.3–1.6) [180]. Dynamic viscosity of RSO at 24 °C was measured by interfacial rheometer and the kinematic viscosity was found to be 30 cSt which is lower compared to *Jatropha curcas* L. oil [181], but higher compared to conventional diesel (<5 cSt). The acid value of the extracted RSO was found to be 24 mg of KOH/ g of oil which is higher than the acid value of Crude *Pangium edule* oil (19.62 mg of KOH/g of oil) [141], *Ceiba Pentandra* oil (15.3 mg of KOH/g of oil) [182], *Croton megalocarpus* (10.52 mg of KOH/g of oil) [17] and *Jatropha curcas* L. oil (2.24 mg of KOH/g of oil) [181]. Free fatty acid content of RSO was obtained as 12.12% which is lower than some of the seed oils such as *Jatropha curcas* L. oil (14%) [25], palm oil (13%) [93], etc. Iodine value determines the unsaturation content in the form of double bonds and also measures the oxidation stability of oil. The iodine value, 113 g I_2/g oil was estimated by Wij's method, which falls in the range of semi-drying oils. Higher iodine value of RSO oil might be due to higher unsaturated fatty acid content in the oil as observed in ^{1}H NMR and ^{13}C NMR analysis.

Table 3.3: Comparison of physico-chemical properties of different seed oil with rubber seed oil

Properties	Rubber seed [this study]	CP[#] [182]	JCL[##] [181]	CPE[*] [141]	CM[**] [17]	Testing methods
Colour	Golden yellowish	Yellow	–	–	–	
Density, kg/m^3 at 24°C	910	905.2[1]	857.45	897.6[1]	909.4[1]	ASTM(D854-10)
Kinematic Viscosity, cSt at 24°C	30	34.456[1]	77.4[1]	27.17[1]	30.195[1]	ASTM(D445)
Oil content, %wt./wt.	40–50	–	–	–	40–45	AOAS
Cloud point, °C	3	–	11	–6	–8	ASTM(D97)
Pour point, °C	–1.5	–	4	–10	–8	ASTM(D97)
Acid value, mg of KOH/g of oil	24	15.3	2.24	19.62	10.52	AOCS(Te 1a-64)
Saponfication Value , mg of KOH/g of oil	235.28	224	–	–	–	AOCS(Te 1a-64)
Iodine value	113	98	87.56	–	–	Wijs(IID7)
Ester value, mg of KOH/g of oil	211.01	–	–	–	–	AOCS(Te 1a-64)
Free fatty acid, %	12.12	7.69	–	–	–	AOCS(Te 1a-64)
Calorific value, MJ/Kg	39.34	–	39.8	39.52	39.198	
Refractive index	1.47	1.4705	–	1.4682	–	

[1]measured at 40°C, [##]Jatropha curcas L. oil, [#]Ceiba Pentandra oil, [*]Crude Pangium edule oil, [**]Croton megalocarpu

3.3.2. *^{1}H and ^{13}C NMR Analysis of RSO*

Fatty acid compositions of oil extracted from rubber seed was determined by ^{1}H NMR spectroscopy. Identified peaks (1–10) in NMR spectra (Fig. 3.4) are used to determine linolenic (Ln), linoleic (L), oliec (O) and saturated (S) fatty acid content in the RSO. The peak assignment was done based on Table 3.4 and used to identify functional groups of fatty acid present in RSO (Fig. 3.4). The percentages of fatty acids were obtained by Eq. 3.3–3.6 [146]. A, 1; B, 2; C, 5; D, 6 and E, 7 are the areas of the peaks with chemical shift in ppm (Fig. 3.4).

$$Ln\ (\%) = 100 \times \left(\frac{B}{A+B} \right) \tag{3.3}$$

$$L\ (\%) = 100 \times \left(\frac{E}{D} - 2\frac{B}{A+B} \right) \tag{3.4}$$

$$O\ (\%) = 100 \times \left(\frac{\mathrm{C}}{2\mathrm{D}} - \frac{\mathrm{E}}{\mathrm{D}} - 2\frac{\mathrm{B}}{\mathrm{A+B}} \right) \tag{3.5}$$

$$S\ (\%) = 100 \times \left(1 - \frac{C}{2D} \right) \tag{3.6}$$

Where: A, methyl hydrogen atoms of saturated oleic and plus linoleic acyl groups; B, methyl hydrogen atoms of linolenic acyl groups; C, methylenic hydrogen atoms in position α in relation to one double bond (also named allylic protons); D, methylenic hydrogen atoms in α position, in relation to the carboxyl group; and E, methylenic hydrogen atoms in α position with respect to two double bonds, also named bis-allylic Protons.

Table 3.4: ^{1}H NMR spectra peak identifications

Peak	Chemical shift (ppm)	Functional groups
1	0.82–0.94	—CH_3 (terminal methyl proton (saturated, oleic and linoleic)
2	0.94–1.03	—CH_3 (terminal methyl protons (linolenic))
3	1.20–1.43	—$(CH_2)_n$— (methylene protons (saturated))
4	1.55–1.69	—OCO—CH_2—CH_2— (β–methylene protons (carbonyl))
5	1.93–2.13	—CH_2—CH=CH— (allyl methylene protons)
6	2.25–2.36	—OCO—CH_2— (α–methylene protons)
7	2.73–2.87	=HC—CH_2—CH= (divinyl methylene protons)
8	4.10–4.35	—CH_2OCORs (methylene protons (glyceryl)) or triglyceride moiety
9	5.25–5.29	CHOCORs (proton on carbon atom 2 of glyceryl group)
10	5.29–5.43	—CH=CH— (olefinic proton)

^{1}H NMR analysis showed that RSO contains saturated, monounsaturated and polyunsaturated fatty acids (Table 3.5). The unsaturated fatty acids such as linoleic (polyunsaturated), linolenic (polyunsaturated) and oleic (monounsaturated) acids were found to be 39.86%, 13.17% and 27.06%, respectively with balance 19.91% as saturated acid. There are significant differences in fatty acid compositions of RSO compared to the reported value [183-187] (Table 3.5). This variation is attributed to genotype of the seed. ^{1}H NMR analysis of the oils produced from various particle sizes showed no significant variation in the fatty acid compositions. The variation in the compositions from the average values for linoleic, linolenic and oleic acid were observed to be 1.4%, 4.3% and 3.8%, respectively. The data show that linoleic acid is the predominant fatty acid in RSO. The high unsaturated fatty acid content of RSO contributes to its low temperature properties [13, 188]. Due to the low profile of oleic acid (27.06%) RSO has less nutritional quality compared to olive (64.6–84.4%), canola (60–75%) and nusun (43.1–71.8%) oils

[13, 188]. The concentration of linolenic and linoleic acid in RSO is within the range of European standard for biodiesel production [187]. It was clearly observed that, the resonances in the aromatic region (6.8–8.8 ppm) were not present. Further, the ^{13}C NMR spectra of RSO analysis provide a clear difference between the characteristic signal of acid and glycerol ester moiety (Fig. 3.5). The carbonyl (–C=O) signal for free fatty acids appeared at 179 ppm (i. e. carbonyl of free fatty acids (C=O)) in ^{13}C NMR, whereas ester signal in triglycerides appeared at 172–174 ppm chemical shift (i. e. carbonyl of triglycerides (C=O)). The glyceride backbone of triglycerides was clearly observed at 69 ppm (H–C–O–) and 62 ppm (CH_2–C–O–). Further, the characteristic signal of each functional group such as carbon–carbon single and double bond due to saturated and unsaturated fatty acids of triglycerides were found between 20–33.6 ppm and 123–133 ppm, respectively. The terminal of $–CH_3$ for free fatty acid and triglycerides clearly appeared at 14 ppm in ^{13}C NMR (Fig. 3.5). Structural and chemical changes up on the chemical modification of the extracted rubber seed oil are discussed in chapter IV.

Table 3.5: Fatty acid compositions of oil extracted from rubber seed at optimum condition

		Percentage (mean ±standard deviation)				
			Reference			
Fatty acid	Structure ($C_{N:M}$)[2]	In this study	[184]	[183]	[186]	[189]
Linoleic acid	18:2	39.86± 1.31	31.5	37.03± 2.3	50.9	–
Linolenic acid	18:3	13.17± 0.89	19.6	20.35± 1.8	2.5	32.3
Oleic acid	18:1	27.06± 0.64	27.6	23.34± 2.6	32.6	49.9
Saturated acid	N:0	19.91± 0.68	21.6	18.75± 2.2	14	17.7

[2] *N and M are number of carbon and double bond respectively. a carbon with m 'zero' double bond are saturated fatty acid, one double bond are monounsaturated fatty acid and two and more are polyunsaturated fatty acid.*

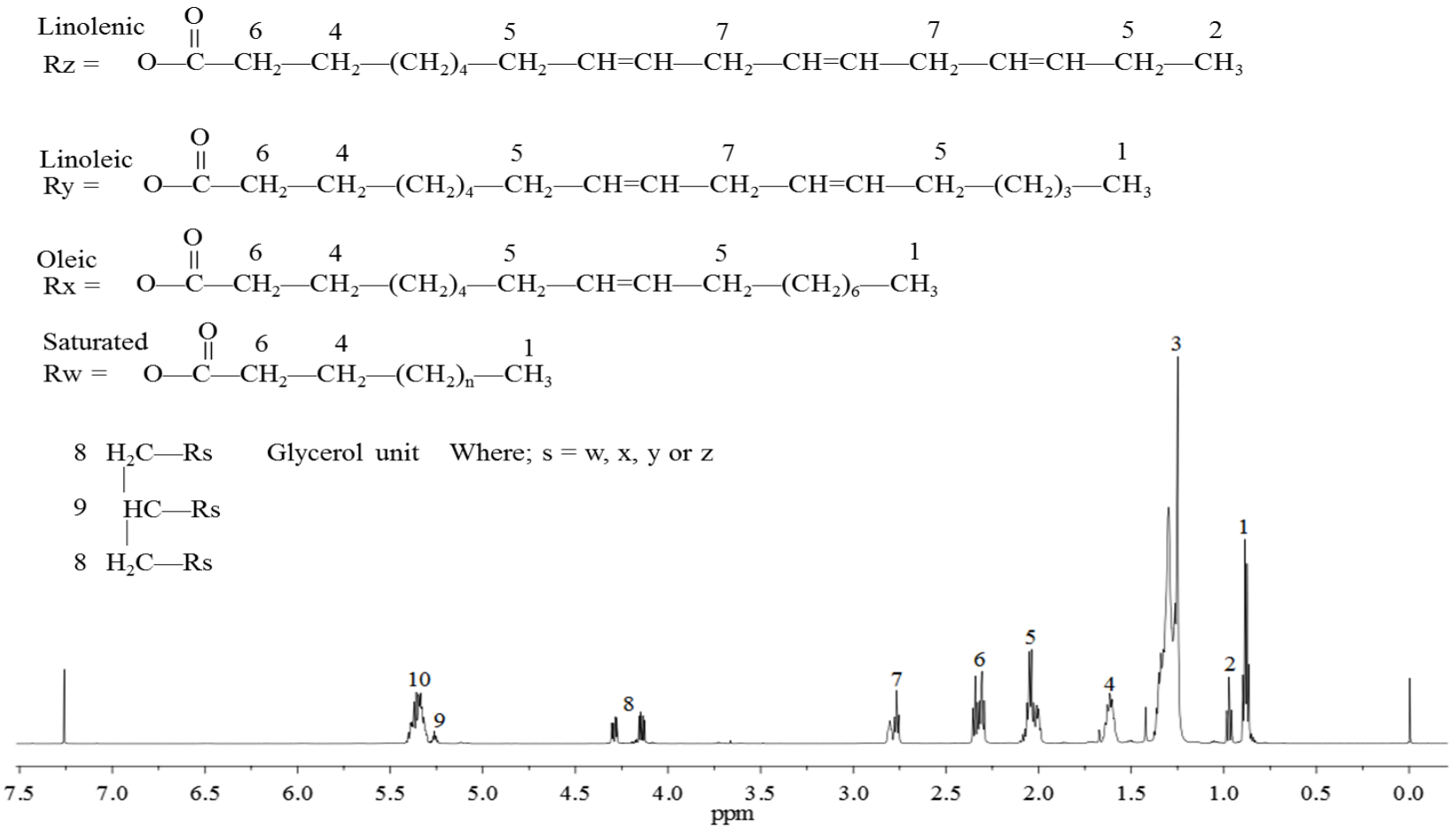

Fig. 3.4: ^{1}H NMR of spectrum of rubber seed oil

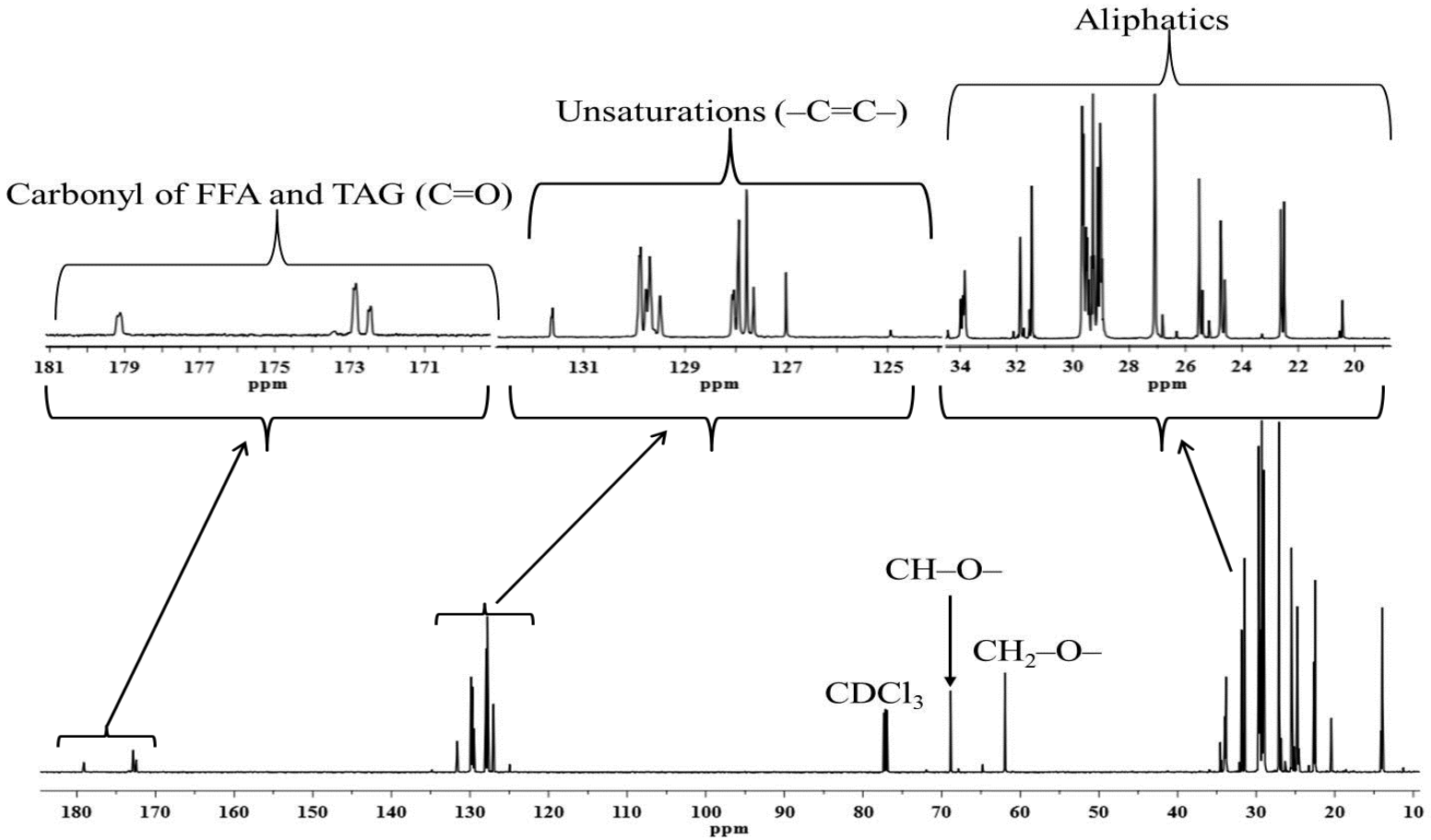

Fig. 3.5: ^{13}C NMR spectrum of rubber seed oil

3.3.3. *Comparison of Cold Flow Properties with DSC*

The saturated fatty acid content in oil are responsible for its poor cold flow property; more the saturated fatty acid content poorer its cold flow properties [185, 190]. The obtained DSC profile for RSO is shown in Fig. 3.6. The crystallization point of the sample was used to estimate the pour point on DSC curve (Fig. 3.6). There were two exothermic peaks at -10.45 °C and 14.7 °C in the DSC curve associated with change in phase from liquid to solid during cooling of the sample from 30 °C to -30 °C at heating rate of 5 °C/min. This reveals the presence of saturated and unsaturated fatty acids (FFA) in RSO. The pour point of RSO was found to be 2.13 ± 0.23 °C. Pour point value of oil sample obtained in the present study using DSC were then compared with those of Borugadda *et al.* [190], who reported pour point of waste cooking oil is poor (–7 °C) compared to canola oil (–18 °C) and castor (–22 °C). This trend is due to the presence of more saturated fatty acids in the waste cooking oil (18.27%) compared to canola (7.37%) and castor oil (3.2%). Thus, the poor pour point of rubber seed oil could attributed to the presence of 19.91% saturated fatty acids in its composition (**Table 3.5**).

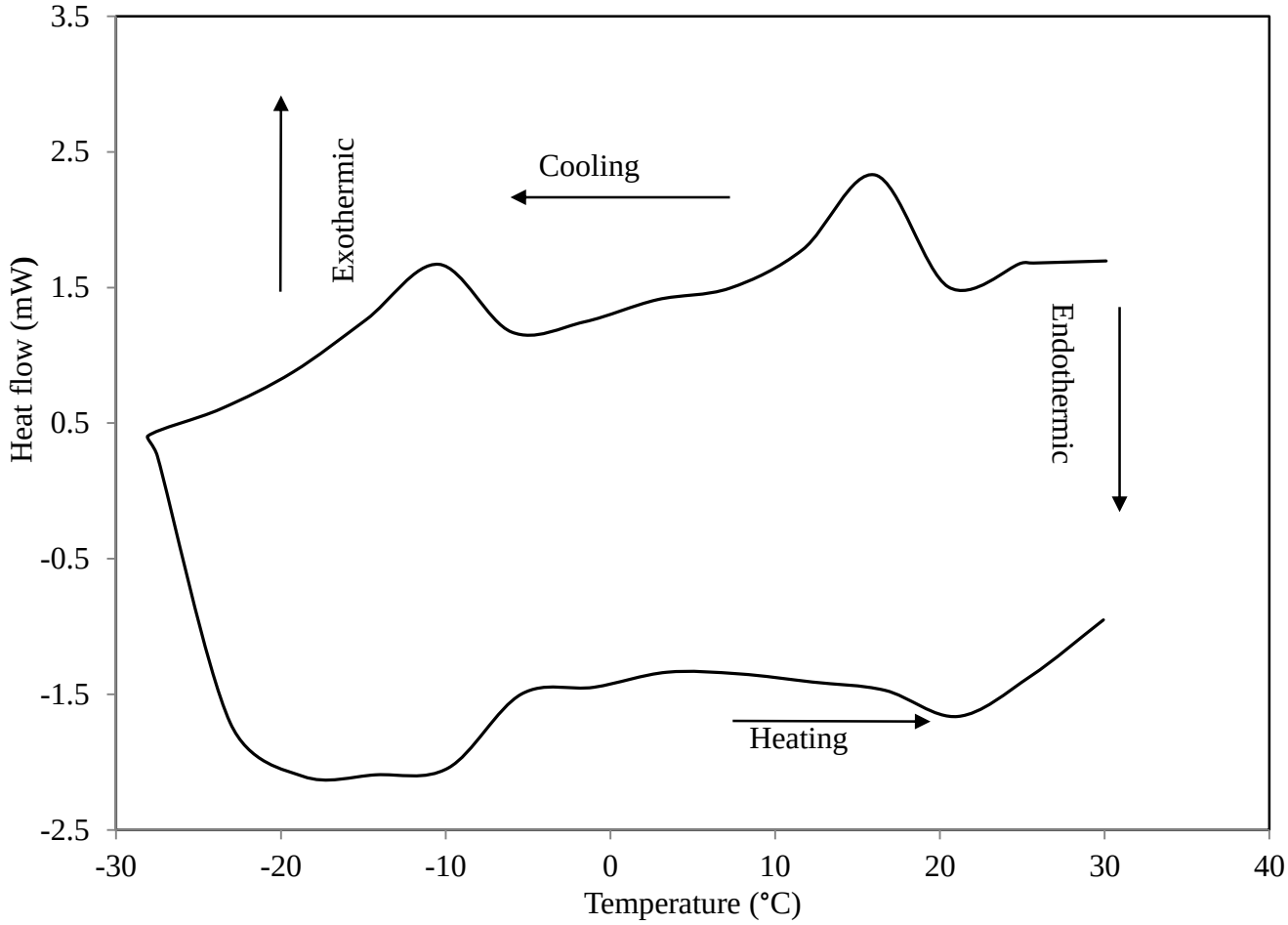

Fig. 3.6: DSC profile of rubber seed oil obtained at optimum condition at 5 °C/min under inert atmosphere

3.3.4. FT-IR Analysis of the Extracted Oil, Kernel and Cake

FT-IR analysis of the samples (oil, kernel and cake) revealed (Fig. 3.7) three infra-red regions, hydrogen stretching, double bound and finger print in each spectra. The main peak and their functional group identification are presented in Table 3.6. Similar data (peak observations) reported in literature for various vegetable oils [191-193]. In Fig. 3.7, the signals specific to –CH, $–CH_2$ and $–CH_3$ groups of fatty acid chain are obtained at 3013, 2926 and 2856 cm^{-1}. From the oil and kernel spectra it can be observed that all the identified peaks of kernel are present in oil. The identified functional groups were also observed in ^{1}HNMR analysis (Table 3.4). Similarly, the composition of cake and kernel spectra showed that cake content all identified peaks of a kernel except the hydrogen bond stretching (–OH). This may be due to the extraction of fatty acids from kernel during oil extraction. Therefore, rubber seed cake contains hydrocarbon and can be used as a feedstock for the production of solid and bio-oil fuels, detail investigation is conducted and presented in chapter VI.

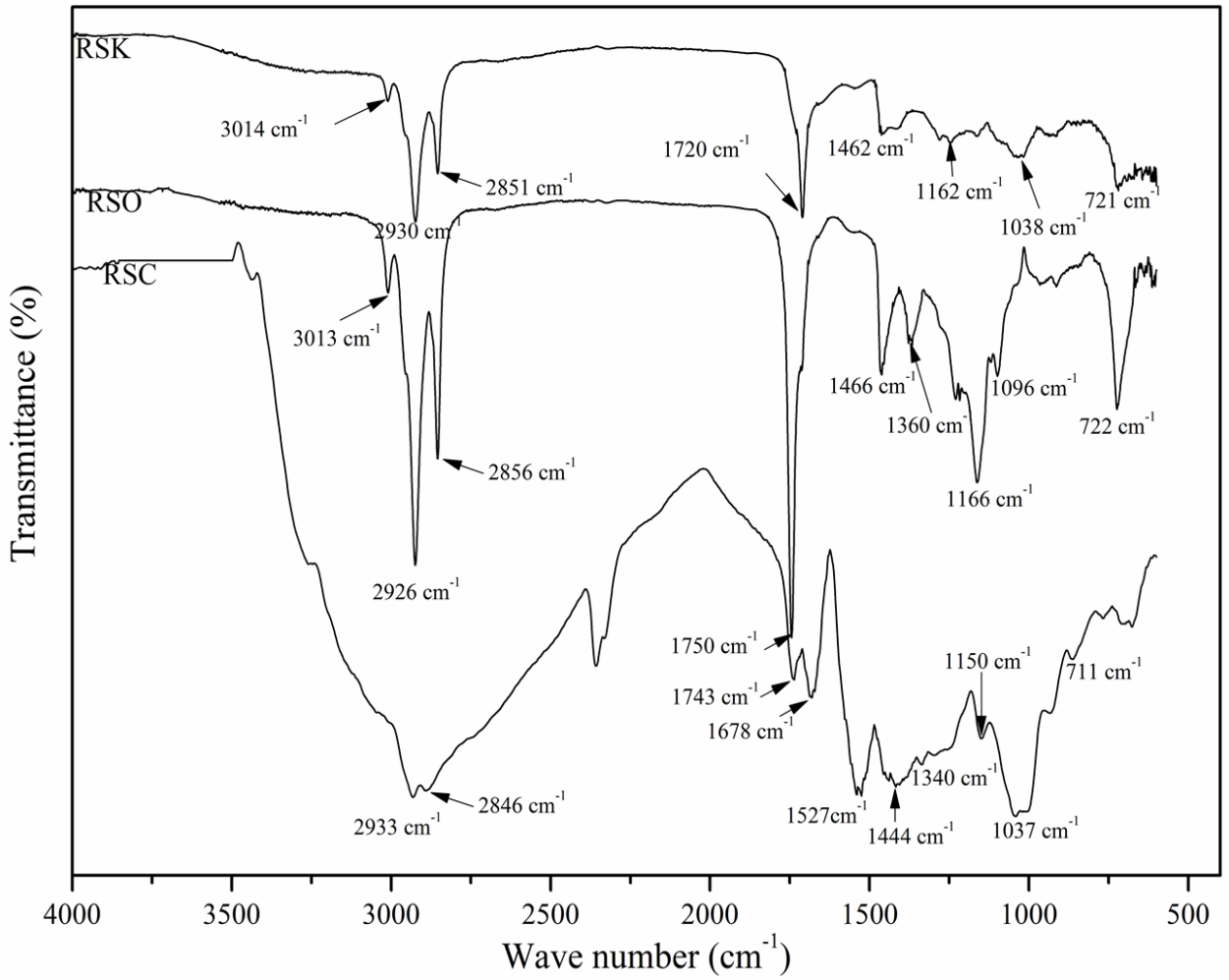

Fig. 3.7: FT-IR spectra of rubber seed oil, kernel and cake

Table 3.6: FT-IR spectra evaluation of extracted oil, cake and kernel

Functional group	Peak (cm^{-1})			Remarks		
	Kernel	Oil	Cake	Kernel	Oil	Cake
Hydrogen stretching	3014	3013	–	$–CH_3$ terminal	$–CH_3$ terminal	–
	2930	2926	2933	–OH of fatty acids, H–C–H asymmetric and symmetric stretch	–OH of fatty acids, H–C–H asymmetric and symmetric stretch	H–C–H asymmetric and symmetric stretch, aliphatic
	2930, 2852	2926, 2856	2933, 2846	Unsaturated –CH, Symmetric and asymmetric stretching vibration shoulder of the aliphatic CH_2 group	Unsaturated –CH, Symmetric and asymmetric stretching vibration shoulder of the aliphatic CH_3 group	
	2852	2856	2846	Saturated –CH	Saturated –CH	Saturated –CH
Double bound stretching and bending	2848, 1720	2856, 1750	2846 1743	Ester carbonyl functional group, fatty acid shoulder C=O of fatty acid C=C stretching vibration	Ester carbonyl functional group, fatty acid shoulder, C=O stretch of fatty acid C=C stretching vibration	Ester carbonyl functional group, fatty acid shoulder C=O carbonyl stretch
	1462	1466	1444	Bending vibration of the CH_2 and CH_3 of aliphatic group C=C bending vibration(aliphatic)	Bending vibration of the CH_2 and CH_3 of aliphatic group C=C bending vibration(aliphatic)	Bending vibration of the CH_2 and CH_3 of aliphatic group
	1375	1360	1340	Bending vibration of CH_2	Bending vibration of CH_2	Bending vibration of CH_2
	1162	1166	1150	Stretching vibration of the = C–O–C ester groups	Stretching vibration of the = C–O–C ester groups	Stretching vibration of the =C–O–C ester groups
Finger print region	1038	1096	1037	C–O stretching	Overlapping of the CH_2 rocking vibration and the out-of-plane vibration of cis-disubstituted olefins	C–O stretching

3.4. Summary

Rubber seed comprises of 40–48 wt% shell and 52–60 wt% kernel of seed was subjected for oil extraction study. RSO was extracted from rubber kernel using Soxhlet extraction technique. The yield of RSO was affected by particle size, extraction time, type and amount of solvent used during extraction process. About 96.6% of experimental results were explained by the model equation (Eq.3.2) which revealed that the actual and predicted values are in good agreement within 5% error. The maximum yield of RSO was found to be 49.36 wt%. The higher yield of RSO was obtained in case of non-polar solvent (hexane); the effect of non-polar solvent on yield is attributed to the presence of fatty acids of non-polar long chain of hydrocarbon in the rubber seed kernel. Linoleic acid (39.86%) was the most abundant in RSO. Physico-chemical properties revealed that the RSO is promising to substitute edible vegetable oil such as soybean, coconut oil, sunflower for biodiesel production. However, from the physico-chemical properties of RSO, it is observed that, some of the properties such as FFA, viscosity, cloud point, pour point are essential and need to improve for fuel application in the existing diesel engine via esterification and transesterification reaction. Therefore, chapter IV and V deal about the synthesis of rubber seed oil methyl esters through ultrasonic technique, rheological and also the engine performance test for blend of ROME with diesel fuel. Furthermore, thermal conversions of rubber seed shell (RSS) and rubber seed cake (RSC) were essential for complete utilization of rubber seed for biofuels production. Hence, the solid by-products were subjected to thermal cracking for biofuel production through semi-batch pyrolysis process and, the detailed is presented in chapter VI.

CHAPTER IV

Rubber Seed Oil Methyl Esters Synthesis: Process Parameter Optimization, Physico-Chemical Characterization and Thermal Degradation Kinetics

Reduction of FFA of RSO;

Heterogeneous Catalyst Performance;

Synthesis and Parameter Optimization for Transesterification Process;

Physico-Chemical-Thermal Characterization of RSO and ROME

Part of the work published:

Reshad, A.S., Deoashish P. Panjiara D., Tiwari, P., Goud, V.V., 2017. Two-step Process for Production of Methyl Ester from Rubber Seed Oil using Barium Hydroxide Octahydrate Catalyst: Process Optimization. ***J Clean Prod,*** 142, 3490–3499

Chapter IV

Rubber Seed Oil methyl Esters Synthesis: Process Parameter Optimization, Physico-Chemical Characterization and Thermal Degradation Kinetics

This chapter focused on chemical modification of non-edible rubber seed oil (RSO) extracted under optimal conditions (discussed in chapter III) to synthesize rubber seed oil methyl esters (ROME). The high FFA content of RSO was reduced during esterification reaction prior to transesterification using an ultrasonic (non-conventional) and mechanical stirring (conventional) techniques. Esterification process parameters such as catalyst (H_2SO_4) concentration, time and methanol to oil molar ratio (MR) has been investigated using ultrasonic technique. This chapter also elaborates the catalytic performance of $Ba(OH)_2{\cdot}8H_2O$, Na_3PO_4, commercial CaO and waste egg shell base CaO for transesterification of esterified rubber seed oil and screening of the catalyst based on the conversion of rubber seed oil to rubber seed oil methyl esters. Furthermore, the effect of transesterification process parameters on the formation of rubber seed oil methyl esters have been also investigated in detail using response surface methodology (RSM) with central composite design (CCD). A model to predict the response was formulated and validated by analysis of variance (ANOVA). A methyl esters produced at optimum transesterification condition using an ultrasonic technique was characterized and compared with American Society for Testing and Materials (ASTM) biodiesel standards. Additionally, thermal stability and decomposition kinetics for the produced oil (RSO) and methyl ester (ROME) are also discussed in this chapter.

4.1. Reduction of FFA Content (Esterification Process)

The acid value of the feedstock oil determines the pathway of transesterification (i.e. either one step or two step process [137, 194]. As mentioned in the previous chapter (chapter III), the acid value of extracted rubber seed oil (RSO) under optimum condition was found to be 24 mg of KOH/g (i.e.12.12% FFA contents). Therefore, acid treatment of RSO was performed to reduce the acid value (i.e. FFA content) prior to transesterification. Conventional stirring technique was used to reduce the acid value (AV) of RSO using H_2SO_4 catalyst. The FFA content of RSO was decreased from 24 mg of KOH/g to 1.5 mg of KOH/g in 3.5 h esterification reaction time, stirring speed of 600 rpm and 65 °C using mechanical stirring technique. However, an ultrasonic assisted process increased the rate of esterification of oil and also reduced the reaction time to ~2.5 h. Ultrasonic cavitation formation is an effective mean to achieve a better mixing compared to conventional processes [194]. Further, acid treatment of the extracted oil for acid value reduction was performed based on one parameter optimization technique using ultrasonic method at ambient condition [93, 103]. Three parameters; esterification time, catalyst loading and methanol to oil molar ratio were studied at a constant reaction temperature (ambient condition) (30 °C) using a conventional optimization technique with objective function as minimization of acid value/FFA content. Esterification reaction is a reversible reaction, and excess alcohol is required to enhance the progress of reaction in the forward direction. According to the reported literature for various feedstocks (varying % FFA) the maximum reduction of acid value/FFA content can be achieved with the molar ratio in the range of 6:1 to 30:1 [31, 194, 195]. By considering the reported values, molar ratios in the range of 6:1 to 18:1 were chosen. The effect of a molar ratio (6:1 to 18:1) on the rate of acid esterification reaction (Fig. 4.1A) showed that at 15:1

MR, the minimum acid value of 2 mg KOH/g (i. e. 91.67% conversion of FFA) can be achieved. The increase in acid value beyond 15:1 MR may be the result of water produced during the reaction that prevents further reaction or support reverse reaction and also act as a barrier for the reduction of acid value [7, 31]. The amount of acid catalyst used for the esterification process also affects the acid value of the product. Thus, the acid value of extracted oil was reduced to 2 mgKOH/g by varying the catalyst loading from 0.5 to1.5 wt% during esterification reaction (Fig. 4.1B). Further increased in the catalyst concentration to 2 wt% showed a slight increase in the acid value due to the fact that high acid concentration favors reversible reaction and triglyceride molecule hydrolyzed to form FFAs and low molecular weight alcohols [90]. Fig. 4.1C shows the effect of reaction time (varying from 30–150 min) on acid value.

A major reduction in the acid value (2 mg KOH/g) was achieved within 2 h of esterification reaction time. Performing the reaction for a longer duration does not reveal any significant improvement. Overall, considering the cost factor and time associate with the process, 91.67% reduction of acid value (acid value = 2 mg KOH/g) can be achieved by following optimum conditions; duration of 2 h, catalyst loading (H_2SO_4) of 1.5 wt% of RSO and 15:1 MR. The esterified oil obtained under this condition was used for the transesterification process. ^{1}H NMR analysis of the esterified oil obtained at optimum condition found to contain 17.65% transesterified product (ROME) (Fig. 4.2). The characteristic peak of the methyl ester was clearly observed at 3.7 ppm chemical shift. The signatures of NMR spectra revealed that 80–85% of fatty acids are unsaturated fatty acids. Similar to acid value, no substantial change in ROME yield was obtained with increased esterification time.

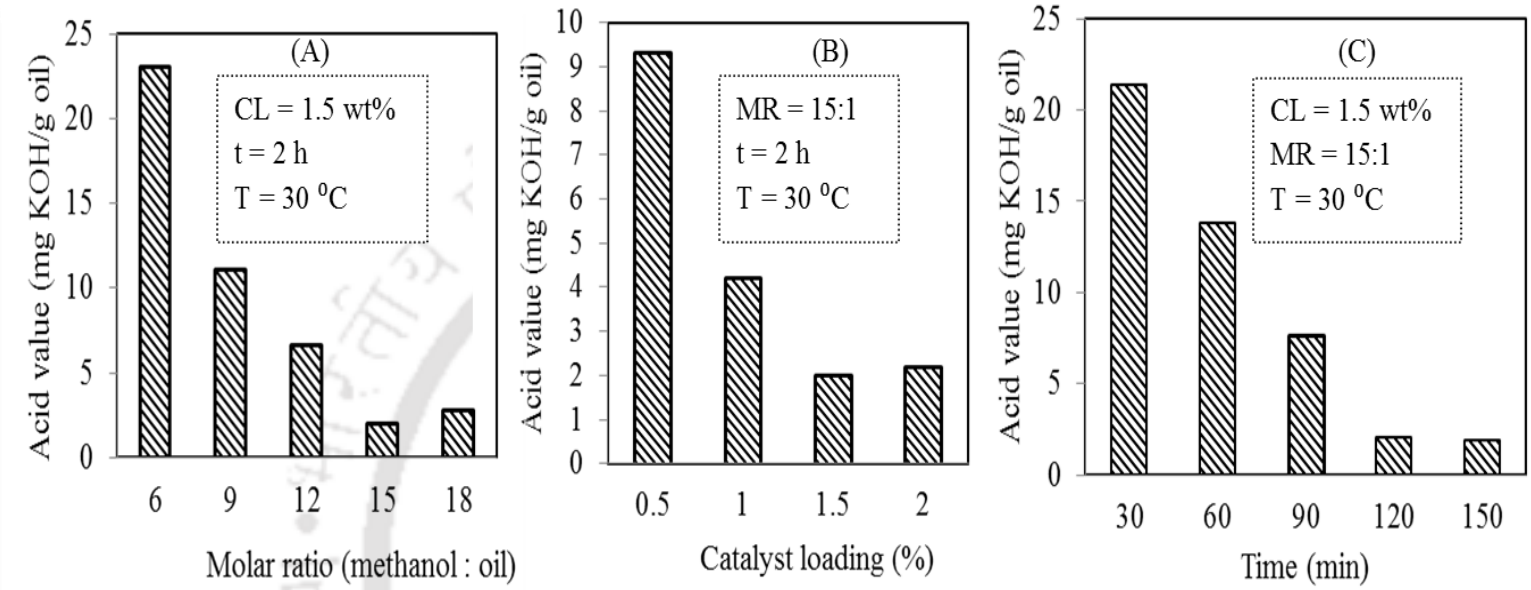

Fig. 4.1: Effect of process parameters on esterification (A): methanol to oil molar ratio, (B): catalyst loading and (C) reaction time. *Maximum reduction in FFA (~ 92% conversion) is achieved at operating condition, CL= 1.5 wt% H_2SO_4 , MR = 15:1, t = 2 h and T= 30 ℃.*

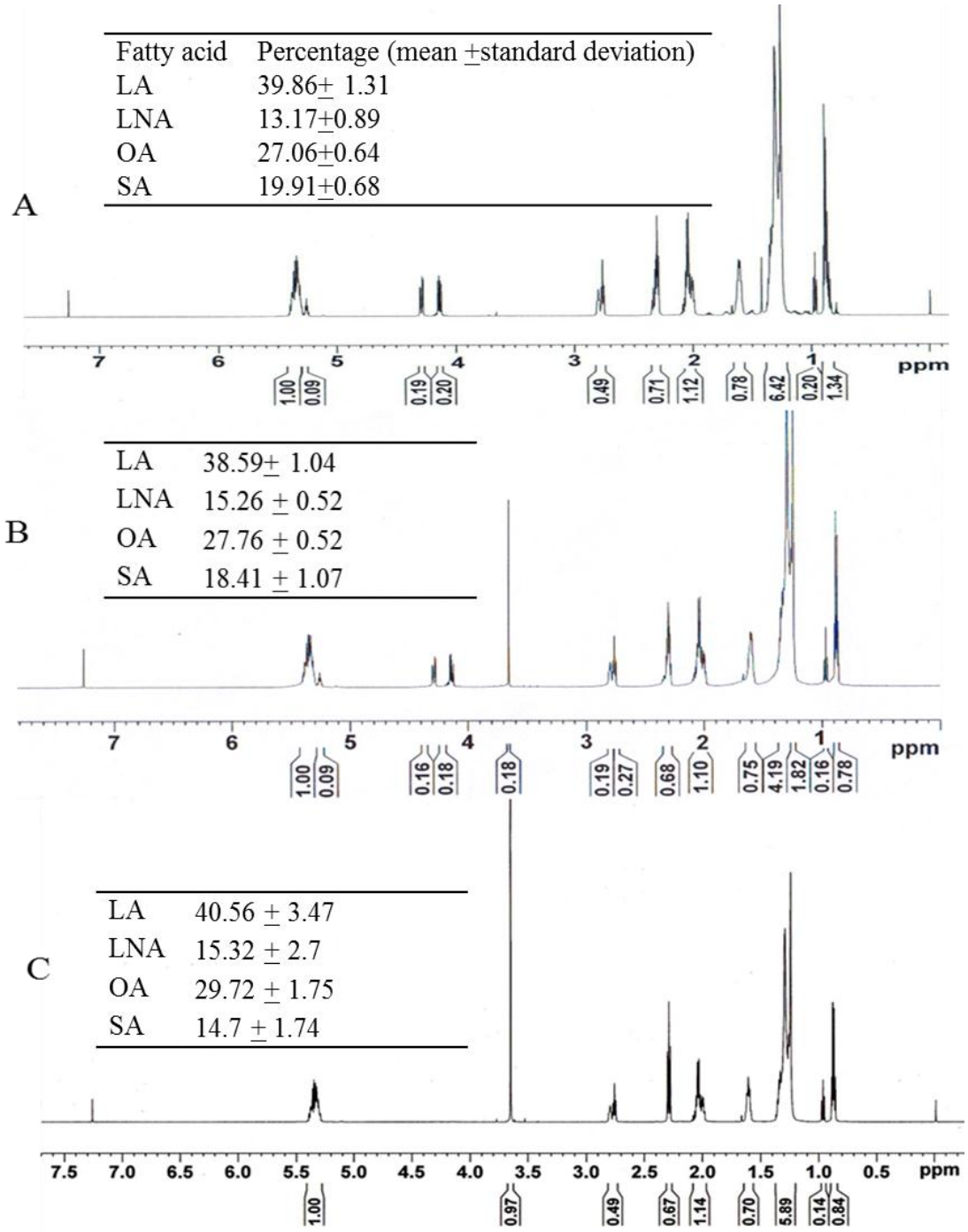

Fig. 4.2: ^{1}H NMR profile of (A) rubber seed oil (RSO), (B) esterified rubber seed oil (ERSO), (C) rubber seed oil methyl esters (ROME). LA: *Linoleic acid, LNA: Linolenic acid, OA: Oleic acid and SA: Saturated acid*

4.2. Characterization of Catalyst and its Activity for Transesterification Process

N_2 adsorption–desorption isotherm of catalysts ($Ba(OH)_2 \cdot 8H_2O$, Na_3PO_4, CaO and calcinated egg shell) are displayed in Fig. 4.3. Based on the IUPAC classification, the adsorption–desorption curve of all samples were found to be typical type II pattern which is a characteristic of a nonporous or macroporous material. It can be seen from Table 4.1 that, the higher total pore volume was found to be 0.055 cm^3/g for barium hydroxide octahydrate whereas, the lower total pore volume was for sodium triphosphate (0.011 cm^3/g). The pore diameters of $Ba(OH)_2 \cdot 8H_2O$, Na_3PO_4, CaO and calcinated egg shell were obtained as 41.98, 10.26, 15.51 and 10.86 nm, respectively (Table 4.1). Hence, all the catalyst could be defined as mesoporous catalyst since the pore diameter of each catalyst was between 2 nm (micropore) and 50 nm (macropore). From BET results, it was predicted that egg shell had low pores on the surface. However, the pore nature of the sample (egg shell) was increased from 0.0069 cm^3/g to 0.012 cm^3/g upon calcination process. On the other hand, large pores (0.055 cm^3/g) of $Ba(OH)_2 \cdot 8H_2O$ are favorable to be used in the liquid–solid heterogeneous phase reactions due to the enough interfacial area for reaction [196]. The Field emission electron scanning microscopy (FESEM) morphologies of $Ba(OH)_2 \cdot 8H_2O$, Na_3PO_4, CaO and calcinated egg shell catalysts are shown in Fig. 4.4. In the outer surface of $Ba(OH)_2 \cdot 8H_2O$ (Fig. 4.4A) and CaO (Fig. 4.4C), porous structure were observed; but the outer surface of Na_3PO_4 (Fig. 4.4B) and calcinated egg shell (CL-egg shell) (Fig. 4.4D) showed negligible pores. These results are in well agreement with that obtained by BET analysis (Table 2.1). The $Ba(OH)_2 \cdot 8H_2O$ sample was composed of cross-linked pores and particles. The basicity of the catalyst was found to be 10.3 mmol HCl/g for $Ba(OH)_2 \cdot 8H_2O$, 4.95 mmol HCl for Na_3PO_4, 23.07 mmol HCl/g for CaO and 23.3 mmol HCl/g for calcinated egg shell.

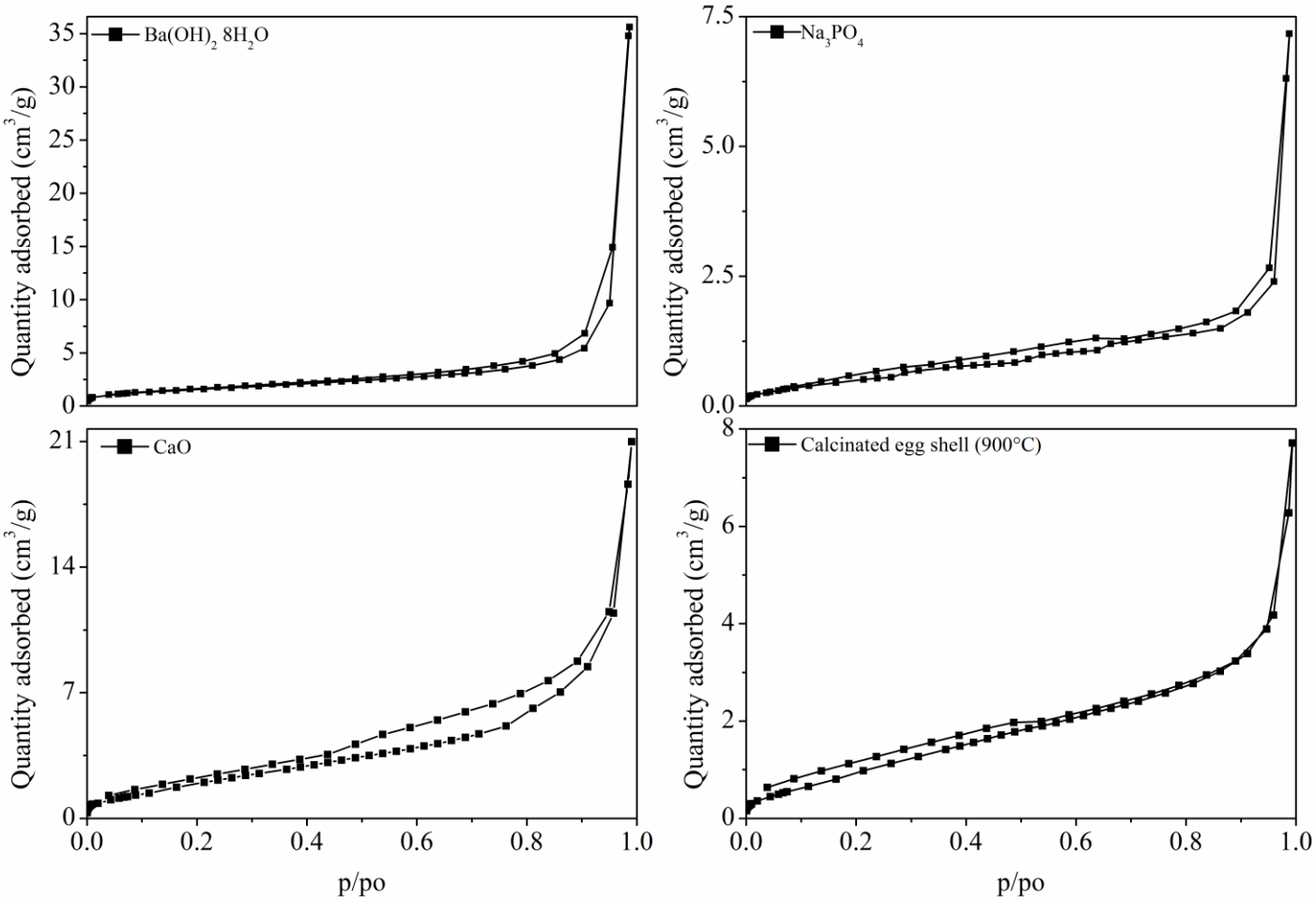

Fig. 4.3: N_2 adsorption/desorption plots for different heterogeneous catalysts

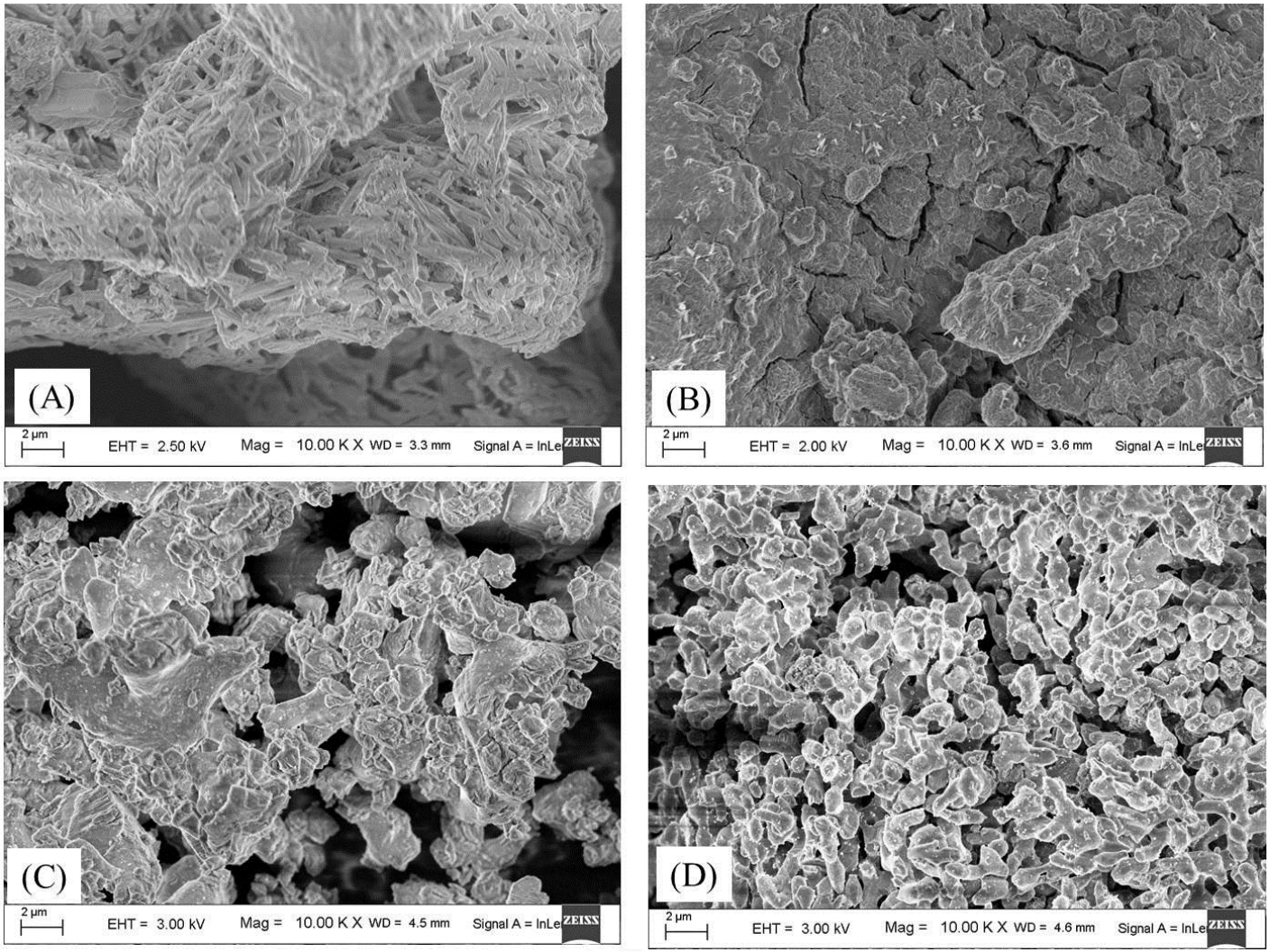

Fig. 4.4: FESEM micrograph of (A) $Ba(OH)_2 \cdot 8H_2O$, (B) Na_3PO_4, (C) CaO and (D) calcinated egg shell at 900 °C for 4 h

Table 4.1: Structural and textural properties of barium hydroxide octahydrated ($Ba(OH)_2 \cdot 8H_2O$), sodium triphosphate (Na_3PO_4), calcium oxide (CaO) and egg shell

Properties	$Ba(OH)_2 \cdot 8H_2O$	Na_3PO_4	CaO	CL-egg shell*	NCL-egg shell**
BET (m^2/g)	5.76	2.16	8.39	4.41	1.65
TVP (cm^3/g)	0.055	0.011	0.032	0.012	0.0069
APD (nm)	41.98	10.26	15.51	10.86	16.79

*APD: average pore diameter, TVP: total pore volume, *calcinated egg shell (calcinated at 900 °C for 4 h), **non-calcinated egg shell*

The comparison of the catalytic performance of $Ba(OH)_2 \cdot 8H_2O$, Na_3PO_4, CaO and calcinated egg shell for transesterification reaction was tested at various reaction time (5–180 min) and constant catalyst loading of 5wt% catalyst (weight to ERSO) with a molar ratio of methanol to ERSO 9:1 using an ultrasonic horn technique and is shown in Fig. 4.5. The catalytic activities were compared based on FAME yield from transesterification reaction. It can be noticed that there is a clear difference in FAME yield for these catalysts. Fig. 4.5 shows that the conversion of ERSO in to FAME over the catalyst was near to 96% in the case of $Ba(OH)_2 \cdot 8H_2O$ within 15 min, while 3 h reaction time showed 97, 97.98 and 92.59% of FAME in the case of CaO, calcinated egg shell and Na_3PO_4, respectively. Although there was a drop in the surface area in $Ba(OH)_2 \cdot 8H_2O$ as compared to CaO, barium (Ba) compounds could generate the catalytic activities for the transesterification reaction. It can be concluded that, only larger surface area of the catalyst cannot cause the great enhancement in the conversion of triglyceride of vegetable oil, but both higher surface area and porous nature of the catalyst greatly promote the diffusion of oil to the catalyst surface and/or pore and then enhance the internal diffusion since a typical triglyceride molecule of vegetable oil has pore

diameter of ~5.8 nm [197]. The trend in FAME yield was not concurrent with basicity of the catalyst. As can be seen, CaO (23.07 mmol HCl/g) and calcinated egg shell (23.3 mmol HCl/g) exhibited the highest basicity, but the rate of transesterification reaction for ERSO was slow as compared to $Ba(OH)_2 \cdot 8H_2O$. The higher yield of FAME over $Ba(OH)_2 \cdot 8H_2O$ can be attributed to the presence of water molecules, which probably increases the reaction rates for the formation of more methoxide anions [196]. It can be seen that $Ba(OH)_2 \cdot 8H_2O$ has the largest pore diameter (Table 4.1) and it can accommodate a large triglyceride molecule easily. As a result, the faster rate of transesterification reaction was observed for $Ba(OH)_2 \cdot 8H_2O$ catalyst (Fig. 4.5). Thus, based on the highest total pore volume, average pore diameter and activity (transesterification reaction), $Ba(OH)_2 \cdot 8H_2O$ catalysts was selected to further study in detail and the effect of various reaction parameters on conversion of ERSO and physico-chemical properties were also considered.

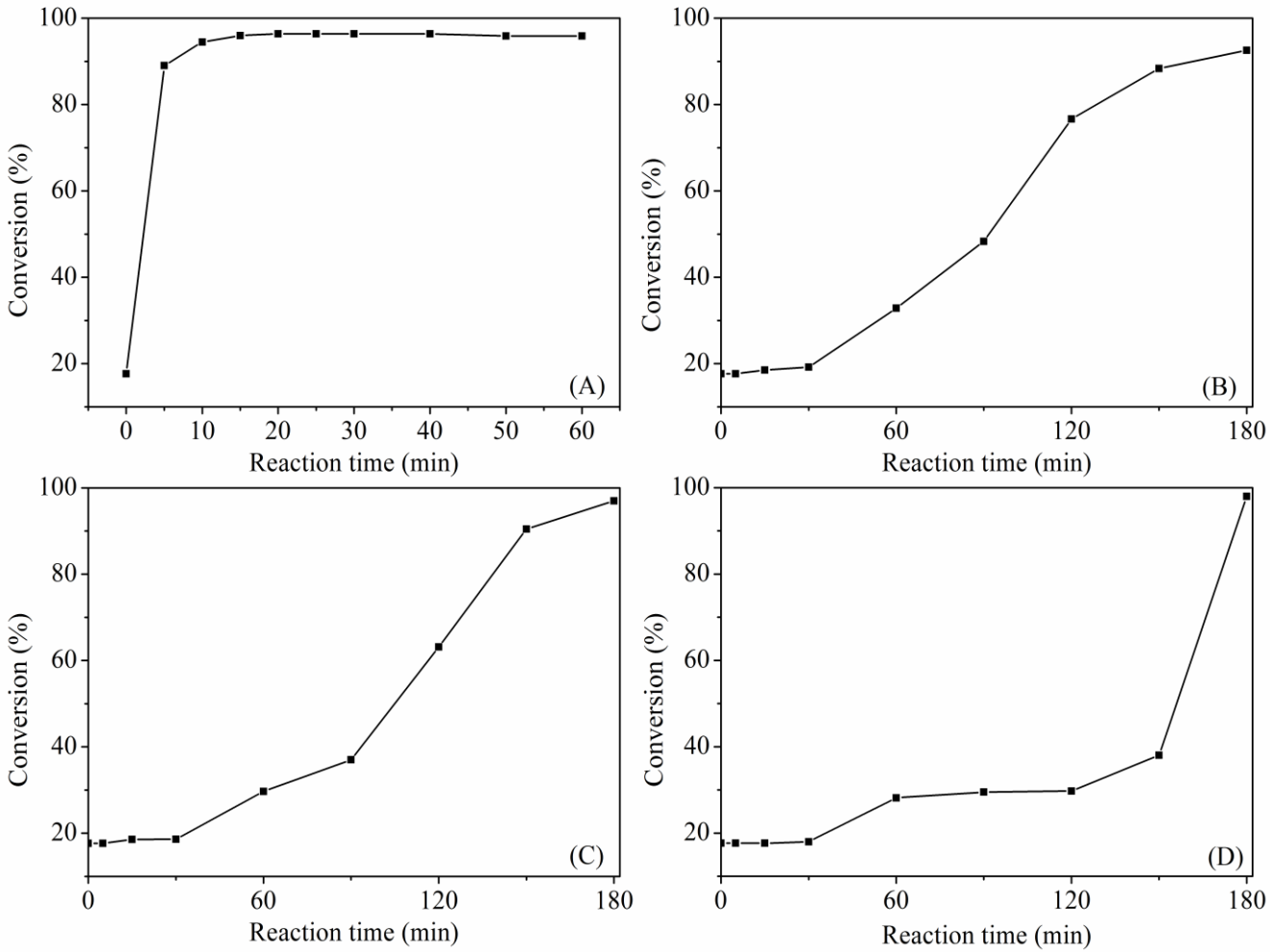

Fig. 4.5: Comparison of catalyst performance for transesterification reaction of ERSO (A) $Ba(OH)_2 \cdot 8H_2O$, (B) Na_3PO_4, (C) CaO and (D) CL-Egg shell

4.2.1. Effect of Calcination on Characteristic of $Ba(OH)_2$ $8H_2O$ and its Activity

TGA of the fresh catalyst ($Ba(OH)_2 \cdot 8H_2O$) was performed within the temperature range of 30 to 800 °C at a heating rate of 20 °C/min under an inert atmosphere and presented in Fig. A4.1. Two thermal events were identified for the overall mass loss of 13 wt%. The first mass loss of 7.75 wt%, took place between 115–200 °C mainly attributed to dehydration of $Ba(OH)_2 \cdot 8H_2O$ to $Ba(OH)_2$. The second event which begins at 200 °C ends at around 800 °C encountered mass loss of 5.25 wt%, which could be due to the decomposition of $Ba(OH)_2$ [198]. On the basis of TGA results, catalyst calcinations temperature range was fixed. The catalyst was calcinated at 200 °C for 4.5 h, 400 °C for 4.5 h and 800 °C for 4 h. The basicity of the catalyst was measured using titration method and for fresh catalyst it was found to be 10.3 mmol HCl/g. After calcinations at 200 °C and 400 °C, basicity was found to be increased slightly to 10.97 mmol HCl/g and 11.1 mmol HCl/g, respectively. However, with an increase in the calcination temperature to 800 °C, basicity reduced to 9.77 mmol HCl/g.

XRD patterns of $Ba(OH) \cdot 8H_2O$ catalysts calcinated at various temperatures are depicted in Fig. A4.2. Maximum intensity for the catalysts were obtained at 2θ degree of 15.25^o (non-calcinated), 19.25^o (200 °C), 18.86^o (400 °C) and 29.63^o (800 °C) (Fig. A4.2). As can be seen from the XRD pattern of the samples, calcination temperature has a significant impact on both the crystallite size and crystal phase. The crystallite size of the samples can be calculated using Debye-Scherrer's equation (Eq. 2.11) [149]. It was observed that crystallite size decreases as the calcination temperature increases, except for 800 °C temperature. This could be due to the microcrystalline structure and sintering of the fine particles of the sample at 800 °C calcination temperature, and also due to the crystal growth effect which further lowers the surface area. On the other hand, broadening of peaks could be another reason for a smaller

crystallite size of these samples at 200 and 400 °C calcination temperatures. At higher calcination temperature catalyst becomes hard, and methanol starved inside the catalyst during transesterification reaction ultimately reduces ROME yield. Similar results have been also obtained regarding the particle size reduction in nitrogen sorption analysis. Hence, instead of increase in the contact surface area of reactants and catalyst molecules, it is reduced due to a hard crystal of the catalyst (i.e. a crystal of catalyst having less crystallite size (Table 4.2)). Thus, in addition to the surface area of catalyst, crystal thickness and catalytic activities are interrelated for transesterification reaction. FESEM analysis of the catalyst calcinated at various temperatures showed an irregular shape of the catalyst particle. As the calcination temperature increases, a condensed mass of the catalyst appeared. As it can be seen from Fig. 4.6 (A–D) that the catalyst morphology changed, as the calcination temperature increased from 200 °C to 800 °C. The non-calcinated $Ba(OH)_2 \cdot 8H_2O$ has more numbers of non-structured pores compared to calcinated one. Low pore morphology of calcinated $Ba(OH)_2 \cdot 8H_2O$ is attributed to the blocking of non-structured pores by sintering and agglomeration of particles of the catalyst. As evident from the FESEM image (Fig. 4.6), the formation of cracks was observed on the surface of the catalyst with an increase in the calcination temperature from 200 °C to 400 °C. However, on contrary to this result, when calcinated at 800 °C, morphology of the sample changed and compacted to microporous nature. The smooth surface morphology resulted in a lower surface area and pore volume (Fig. 4.6D). The crystallite index obtained from the study revealed that catalyst crystals are polycrystalline [147]. As noted earlier, the catalytic performance reduced due to sintering effect (Table 4.3) and this has also been confirmed by BET results [199].

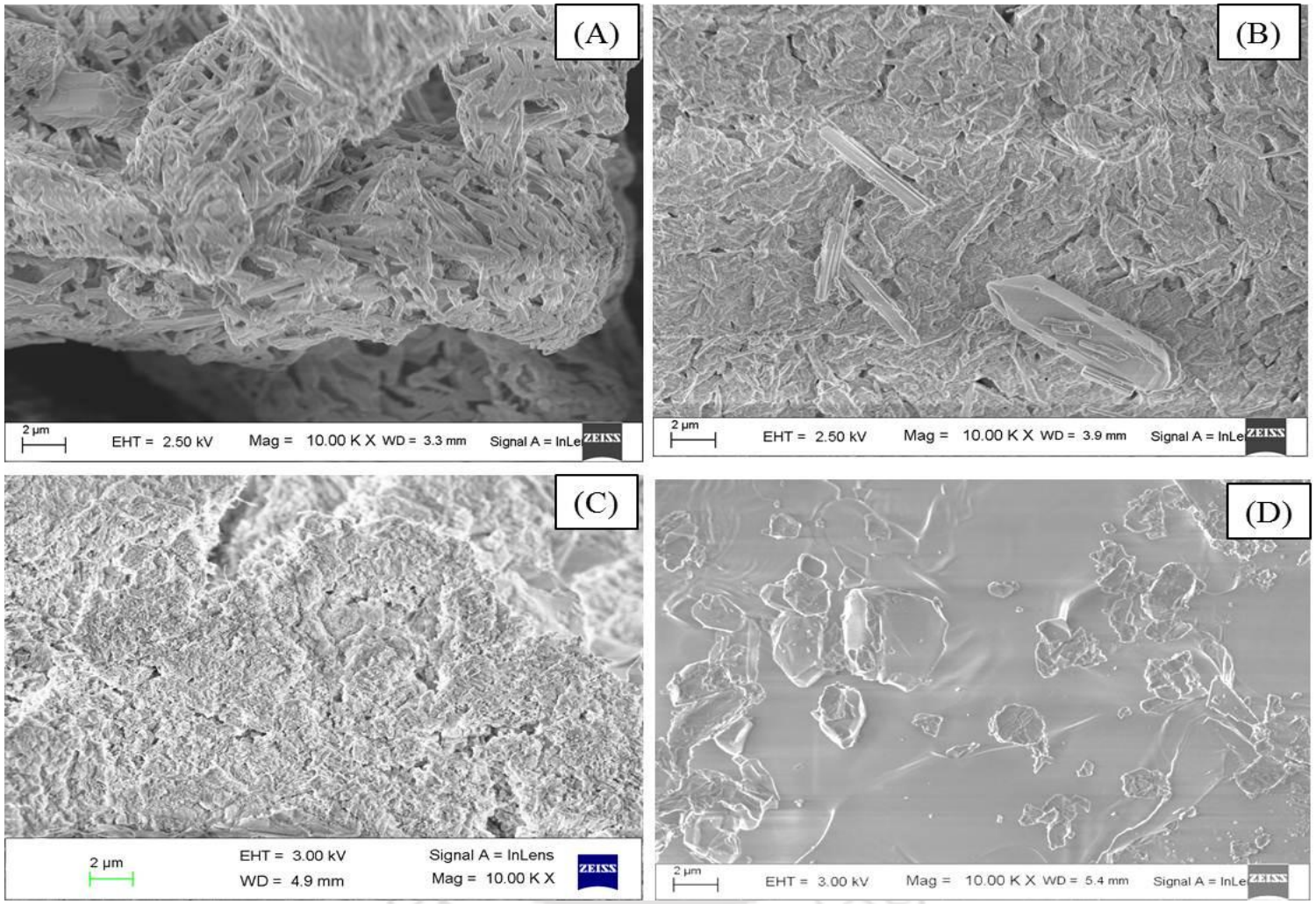

Fig. 4.6: FESEM micrograph of $Ba(OH)_2 \cdot 8H_2O$ at several thermal treatments (A): Non-calcinated (B): calcinated at 200 °C, (C): calcinated at 400 °C and (D): calcinated at 800 °C

Table 4.2: Characterization of $Ba(OH)_2 \cdot 8H_2O$ heterogeneous catalyst

Calcination		BET surface area(m^2/g)	TPV (cm^3/g)	APD (nm)	[a]Particle size(nm)	[b]Crystallite size(nm)
Temp (°C)	Time (h)					
NCL[**]	–	5.76	0.055	41.98	477.81	32
200	4.5	3.54	0.026	27.8	777.48	17
400	4.5	7.56	0.041	21.7	364.06	16
800	4	1.00	0.0037	14.82	2752.29	33
NCL-15[#]	–	4.3	0.0029	2.66	640.06	–

APD: average pore diameter, TVP:total pore volume, [a]S_{BET} method, [b]crystallite size calculated by Debye-Scherrer formula (XRD), [**] Non-calcinated catalyst (fresh), [#]Non-calcinated catalyst after 15 min transterification reaction

Nitrogen adsorption isotherms, quantity of gas adsorbed and desorbed on the catalyst are shown in Fig. 4.7. Multiple points BET surface area of $Ba(OH)_2 \cdot 8H_2O$ catalyst was found to be lower than other heterogeneous catalysts viz. strontium oxide (SrO), calcium oxide (CaO), magnesium oxide (MgO), CaO-MgO and iron (III) oxide (Fe_2O_3) [148, 200]. Isotherm shape depends on the catalyst porous texture. According to IUPAC classification, the adsorption isotherms of the samples were found to be of type II (Fig. 4.7). At 400 °C calcination temperature, the BET surface area of the catalyst sample was improved. This attributed to the lower particle size (Table 4.3) and formation of cracks on the catalyst surface at 400 °C (Fig. 4.6). Beyond 400 °C calcinations temperature, catalyst morphology totally changed and the porous structure was blocked due to the sintering effect. However, a low conversion was

obtained compared to non-calcinated $Ba(OH)_2 \cdot 8H_2O$ catalyst, which may be due to lower crystallite size, pore diameter and total pore volume. But, it should be noted that in this study catalyst calcinated at 400 °C showed a significantly higher conversion of ERSO to ROME compared to 800 °C. This could be due to the better surface properties of catalyst calcinated at 400 °C. Apart from that, Brunauer-Emmet-Teller (BET) surface area per gram of the catalyst, the amount of gas adsorbed and desorbed were found to be less for the sample calcinated at 800 °C compared to other calcinated conditions. This is because of coalescence and agglomeration of the catalyst particles which in turn lowers the catalysts surface area (1.0 m^2/g) at 800 °C [149, 150]. The total pore volume (TPV) of prepared catalyst, obtained by Barrett-Joyner-Halenda (BJH) method (Table 4.2), showed significant effect on TPV of calcinated catalyst. Thus, at higher calcination temperature fine particles of the catalyst sintered in the pores and ultimately blocked the pores, which reduces the average pore diameter of the sample from 41.98 nm to 27.8 nm (200 °C), 21.7 nm (400 °C) and 14.82 nm (800 °C) (Table 4.2). Furthermore, the total pore volume of the catalyst reduced from 0.055 cm^3/g to 0.026 cm^3/g (200 °C), 0.041 cm^3/g (400°C) and 0.0037 cm^3/g (800 °C) during the calcination process. These results attributed to the formation of aggregates or cluster agglomerates of fine particles during heating of samples [199]. This caused to reduce the ERSO conversion in the following order; non-calcinated (96%) > calcinated at 200 °C (94.83%) > calcinated at 400 °C (92.96%) > calcinated at 800 °C (19.05%). As summarized in Table 4.2, the total surface area has less contribution compared to total pore volume for overall catalytic activity in the transesterification reaction by ultrasonic technique. A better conversion during transesterification reaction can be achieved with non-calcinated $Ba(OH)_2 \cdot 8H_2O$ compared to calcinated (Table 4.3). The BJH plot showed mesoporous nature

of $Ba(OH)_2 \cdot 8H_2O$ at all calcination conditions used in this study. Thus, the diffusion limitation is not expected during the transesterification of ERSO. Hence, a non-calcinated catalyst which showed good conversion was selected for further experiments and for optimization of transesterification process parameters, and also studied catalyst reusability. BET surface area and total pore volume of the catalyst (i.e. non-calcinated) obtained after 15 min transesterification reaction were found to be decreased from 5.76 m^2/g to 4.3 m^2/g and 0.055 cm^3/g to 0.0029 cm^3/g, respectively. This may be due to changes in the surface characteristics and the blockage of catalyst pores during the reaction (also observed in FT-IR analysis shown in Fig. A4.3). FT-IR spectrum of used catalyst (after 15 min of reaction) appeared quite different from that of fresh catalyst. Since the conversion of ERSO (triglyceride of RSO) (96%) was high at 15 min reaction time, it is possible that the by-product glycerol reacts with the catalyst and forms some barium compound [77, 201]. Fig. A4.3 clearly shows new characteristic bands at 3682 cm^{-1}, 3008 cm^{-1}, 2916 cm^{-1}, 2846 cm^{-1}, 2725 cm^{-1}, 2023 cm^{-1}, 1892 cm^{-1}, 1963 cm^{-1}, 1700 cm^{-1}, 1325 cm^{-1}, 1286 cm^{-1}, 1234 cm^{-1}, 1180 cm^{-1}, 927 cm^{-1}, 887 cm^{-1} and 850 cm^{-1} signifies the presence of glycoxide compounds of catalyst [77]. As a result, the active surface of the catalyst gets occupied by glycerol and reduces $Ba(OH)_2 \cdot 8H_2O$ catalytic activity.

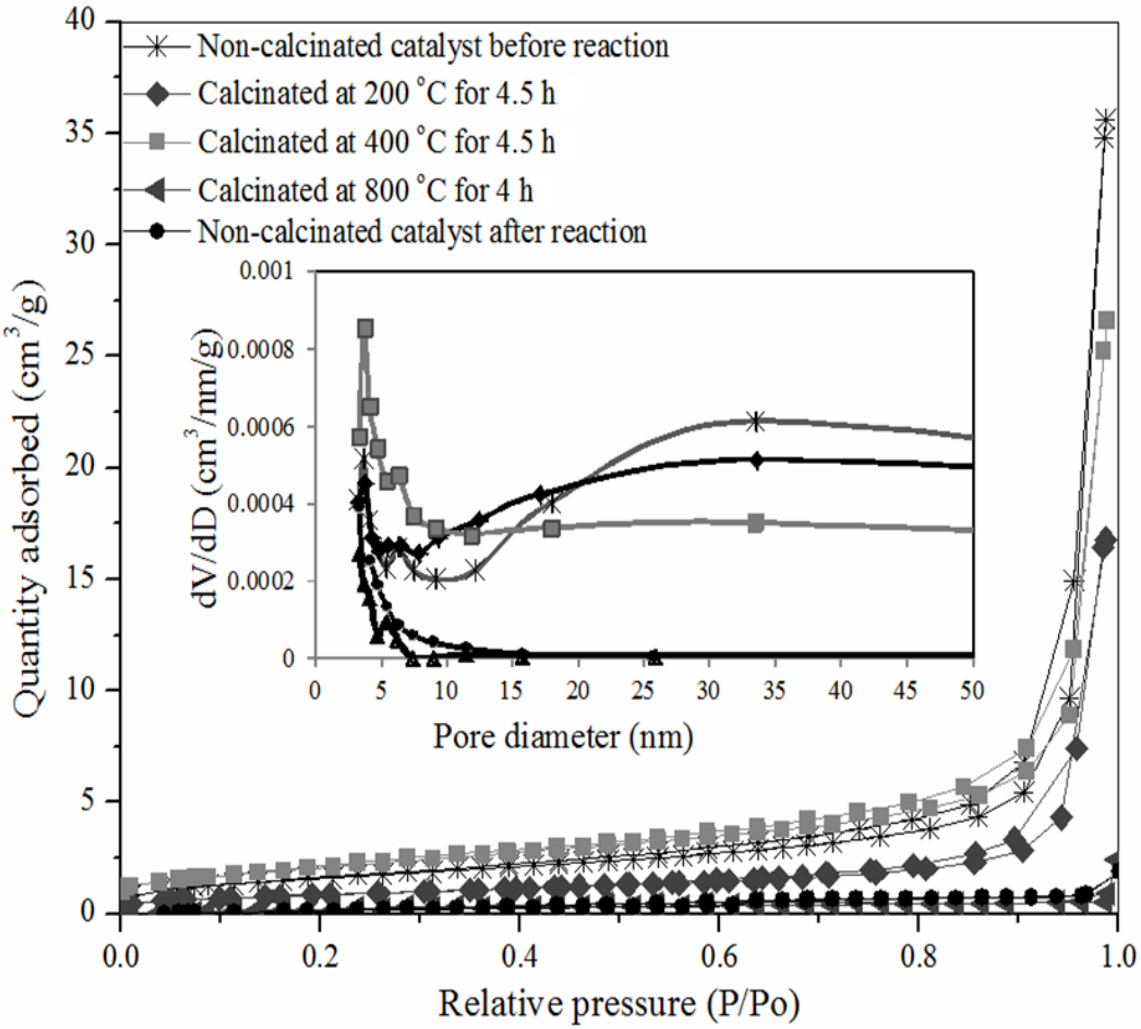

Fig. 4.7: Nitrogen adsorption-desorption isotherm and BJH plots (inside) of the $Ba(OH)_2 \cdot 8H_2O$ samples calcinated at various temperatures.

(BJH plots show the mesopore nature of catalyst; the desorption curve does not retrace the adsorption curve. Increase in calcination temperature favors coalescence and agglomeration of the catalyst particles and BET surface area decreases. Transesterification reduces BET surface area of catalyst due to blocking of the pores of the catalyst by bioglycerol produced. This was also observed by FT-IR analysis)

4.3. Synthesis of ROME (Transesterification)

Vegetable oil and alcohol phases are immiscible in a transesterification system. The high mass transfer resistance between the two phases in both esterification and transesterification reaction becomes a significant factor that affects the reaction rate [74, 75]. Thus, the improvement in the reaction rate through intensive mechanical agitation supports to reduce the mass resistance between the reactants. In the present study, esterified rubber seed oil (ERSO) obtained after acid catalyzed esterification found to contain 17.65% transesterified product (ROME) (section 4.1) along with triglycerides, and we have included this value while calculating the methyl esters formation (ROME) during transesterification steps. Further, transesterification of ERSO using a mechanical stirrer method (800 rpm) found to give only 44.44% and 44.8% ERSO conversion in 1 and 2 h reaction time, respectively. The yield obtained seems to be very less, but analogous to the result reported by with different feedstock (Table 4.3).

4.4. Ultrasonic-Assisted Transesterification: Comparison of Non-Conventional Technique

Ultrasonic mixing (ultrasonic horn (UH) and ultrasonic cleaner (UC)) helps to increase the liquid –liquid interfacial area through the formation of vapor bubbles of methanol and cavitations bubbles of feedstock (esterified oil), and increases the reaction efficiency [78]. In the present work, UH and UC assisted experiments were performed/compared with MR from 3:1 to 13:1 with 1.5 increments, catalyst loading from 2–10 wt% for the reaction duration of 5–50 min. The effect of process parameters on conversion of ERSO (triglycerides of RSO) is summarized in Fig. 4.8. UH provided better conversion compared to UC under similar

conditions. However, at later stage the conversion of ERSO were found to be similar. Fig. 4.8A shows the effect of MR on ERSO conversion at constant catalyst concentration (4 wt%) and reaction time (10 min). RSO conversion was increased from 45% to 94.5% (UH) and 40.82% to 90.9% (UC) with an increase in the MR from 3:1 to 7.5:1. Further increase in MR slightly decreased the conversion. The results were attributed to higher cavitational intensity of methanol in the reaction mixture which may directly shift the equilibrium of reversible reaction towards the product [76, 88, 140]. Further, an excess amount of methanol beyond the optimum enhances the mixing of glycerol and ROME which also makes alcohol recovery difficult [51, 140]. In order to study the effect of reaction time, experiments were performed under 4 wt% $Ba(OH)_2 \cdot 8H_2O$ catalyst loading and optimum MR (7.5:1) (Fig. 4. 8B). The higher conversion of ERSO was obtained by UH within short reaction time (10 min) with the optimum value of 94.5%, whereas UC requires more than 50 min to achieve the same conversion. The reaction for longer time had shown no significant improvement in the conversion of ERSO. Fig. 4.8C shows that an increase in the catalyst loading from 2 wt% to 5 wt% results significant improvement in the conversion, in both reactor configurations, from 85.44% to 96.01% (UH) and 73.8% to 92.93% (UC). In UH, the catalyst is directly exposed to ultrasonic irradiation which enhances the catalyst break up by the energy released from the bubbles created by cavitation collapsing and gives a larger surface of the catalyst [76]. Further, increase in the catalyst loading, first showed a slight increase in the conversion then the found to be decreased. This was attributed to higher catalyst loading, the slurry becomes too viscous, giving rise to problem of mixing [140, 202]. The reaction mixture in UH is directly exposed to the ultrasonic irradiation whereas in the case of UC, the mixing of the reacting mixture is limited due to indirect transmission of the vibrations to the system [76,

203]. The overall higher conversion of RSO (96.01%) was obtained using a UH reactor configuration at MR of 7.5 to 1 with 5 wt% loading of a catalyst in 10 min reaction time. Furthermore, the interactive effects of individual parameter were optimized using RSM and discussed in detailed in section 4.5. A few experiments were also carried out with used catalyst (recycling) to measure the effect of used catalyst performance on overall conversion. The conversion achieved in a first recycling of the processed catalyst was found to be only ~22 %, whereas, 20% make up with fresh catalyst (20% fresh plus 80% used catalyst) resulted ~92% conversion. The continuous deterioration of the catalyst in the process may not support its reusability [29, 149].

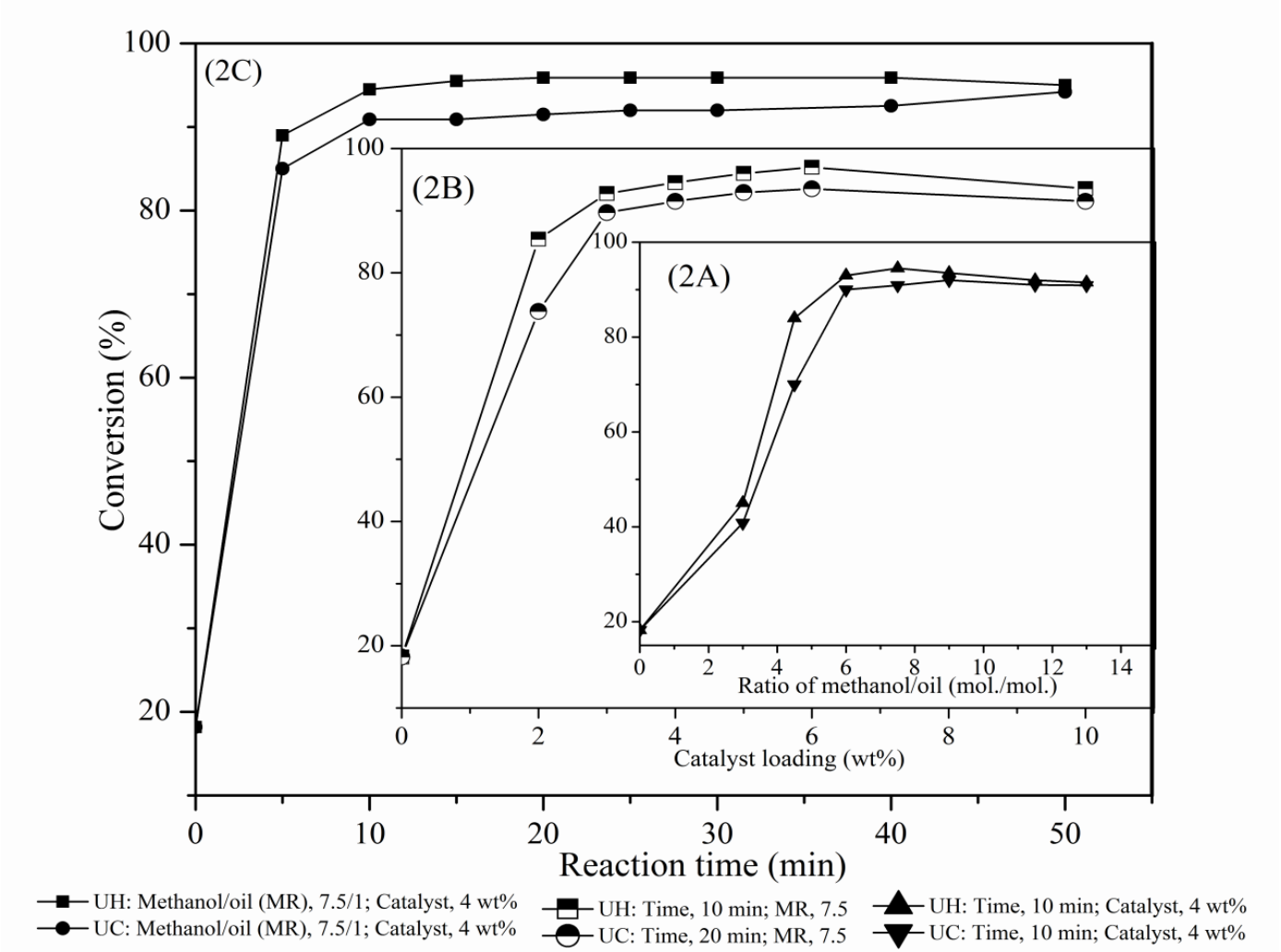

Fig. 4.8: Effect of process parameters on ERSO conversion (A) molar ratio of methanol to oil, (B) reaction time and (C) catalyst loading.

Table 4.3: Comparison of the performance of heterogeneous catalysts for transesterification reaction of ERSO

Oil	Catalyst				Time (h)	MR Ratio	Reaction Temp (°C)	Conversion (%)		Reference
	Non-calcinated	calcinated		wt%				Method		
		Temp (°C)	Time(h)					UL[a]	MS[b]	
Palm		500	3	3(CaO)	1	9	65 ± 2	77.3	5.5	[78]
		500	3	3(BaO)	1	9	65 ± 2	95.2	67.3	
		500	3	3(SrO)	1	9	65 ± 2	95.2	48.2	
RSO		700	7	5(CaO)	4	5	65	–	96.9	[116]
Corn		200	5	3.6($Ba(OH)_2$	~2	11.32	33	–	99.79	[81]
Sesame		200	10	1.79($Ba(OH)_2$	0.67	6.69	32	98.6	–	[204]
WCPO[#]		650	5	2.7(Sr/ZrO_2)	1.45	29	115.5	–	79.7	[75]
Rubber[*]	NCL[c]	–	–	5($Br(OH)_2 \cdot 8H_2O$)	0.25	9	30±1	96	–	Present study
	NCL-NCL-15	–	–	5(1:4,NCL:NCL-15)[d]	0.25	9	30±1	92	–	
	NCL-15	–	–	5($Br(OH)_2 \cdot 8H_2O$)	0.25	9	30±1	22.22	–	
	NCL	–	–	5($Br(OH)_2 \cdot 8H_2O$)	1	9	30±1	–	44.44	
	NCL	–	–		2	9	30±1	–	44.8	
		200	4.5	5($Br(OH)_2 \cdot 8H_2O$)	0.25	9	30±1	94.83	–	
		400	4.5					92.96	–	
		800	4					19.05	–	

[*]Esterified rubber seed oil, [#]Waste cooking palm oil, [a] and [b] are ultrasonic technique and mechanical stirrer methods, [c] Non-calcinated heterogeneous catalyst , NCL-15: non-calcinated catalyst after 15 min transesterification reaction, [d] 1% fresh and 4% NCL-15 $Br(OH)_2$ $8H_2O$

4.5. Process Optimization

4.5.1. *ANOVA Analysis and Model Fitting*

Among the models that fitted to the response such as linear, two factor interactions (2FI), quadratic and cubic polynomial models; the quadratic model was selected as a best fit model for ERSO transesterification reaction within the range of lower and upper limit of parameters. This model equation was suggested by design expert software are shown Table 4.4.

Table 4.4: Sequential model sum of squares

Source	Sum of squares	DF	Mean square	F value	p-value prob>F	
Mean vs Total	1.783E+005	1	1.783E+005			
Linear vs Mean	67	3	22.33	12.01	0.0002	
2FI vs Linear	4.73	3	1.58	0.82	0.5061	
Quadratic vs 2FI	21.71	3	7.24	21.82	<0.0001	Suggested
Cubic vs quadratic	1.8	4	0.45	1.78	0.2514	
Residual	1.52	6	0.25	–	–	
Total	1.784E+005	20	8921.86	–	–	

DF: degree of freedom

The results obtained from transesterification reaction using central composite design (CCD) design technique and the values predicted by the quadratic model are summarized in Table 4.5. Among the models fitted to the response, the quadratic model was selected as it was found to be one of the best fitted model and highly significant for the response ($P<0.05$). ANOVA analysis was performed to measure significance of the model and process parameters. The resulted second order model equation which is able to relate the

response and process parameters was obtained (Eq. 4.1). Model equation based on coded values of parameters (-1, 0 and +1) was also generated (Eq. 4.2).

$$X_A = 37.83 + 7.45A + 2.15B + 6.06C - 0.06AB + 9.17\times10^{-3}AC - 0.10BC - 0.62A^2 - 0.04B^2 - 0.30C^2 \quad (4.1)$$

$$X_C = 95.98 + 0.8a + 1.87b + 0.89c - 0.29ab + 0.014ac - 0.71bc - 0.61a^2 - 0.97b^2 - 0.68c^2 \quad (4.2)$$

where: *A*, *B*, *C* are actual values for catalyst loading, time and methanol/oil molar ratio, respectively and X_A (%) is conversion predicted using actual values of the parameters. a, b and c are code values (-1, 0 and +1) for catalyst loading, time and methanol/oil molar ratio, respectively and X_C is conversion predicted using coded values of parameters.

Table 4.5: Central composite design (CCD) arrangements and response for transesterification of esterified RSO

Catalyst loading (wt%) (A*)	Time(min) (B#)	Methanol/Oil MR (C**)	Conversion value (%)	
			Experimental (*X*)	Predicted (X_A)
4	5	6	89	89.17
6	5	6	92	91.31
4	15	6	95	94.91
6	15	6	96.3	95.90
4	5	9	92.5	92.35
6	5	9	95	94.54
4	15	9	95.09	95.22
6	15	9	97	96.28
3.31	10	7.5	93.2	92.89
6.68	10	7.5	94.5	95.58
5	1.59	7.5	89.7	90.10
5	18.40	7.5	96	96.38
5	10	4.98	92.22	92.55
5	10	10.02	95.09	95.54
5	10	7.5	96	95.98
5	10	7.5	96	95.98
5	10	7.5	96	95.98
5	10	7.5	96	95.98
5	10	7.5	96	95.98
5	10	7.5	96	95.98

*NB: Low, medium and high levels for each parameter are *4, 5 and 6; #5, 10 and 15; **6, 7.5 and 9*

Statistical analysis obtained from ANOVA for response surface using a quadratic model is shown in Table 4.6. The value of P (<0.0001) indicates that the model is statistically significant at 99% confidence level [205]. The average residual values and the leverage were found to be less than 0.3 and 0.5, respectively; this means the predicted value of the response by the model are almost same as experimentally obtained values for the response (Table 4.5 and Fig. 4.9A. The significance of the independent parameters can be analyzed by p-values. ANOVA suggested that all the independent parameters considered are significant in order of time (0.0001) > ratio (0.0002) > catalyst loading (0.0005) along with BC, A^2, B^2 and C^2 terms. A term with positive coefficient in the predicted model (Eq. 4.2) indicates an interacting effect favors to the response, whereas the negative coefficients indicate incompatible [206]. The fitted model indicates that, positive coefficient terms *a*, *b*, *c* and *ac* (interaction of catalyst loading and molar ratio) affects the response linearly. On the other hand, the terms such as *ab* (interaction of catalyst loading and reaction time), *bc* (interaction of reaction time and molar ratio), a^2, b^2 and c^2 have negative effects on the response [200]. The relation between actual and predicted values of conversion (%) is presented in Fig. 4.9A. The closer the regression coefficient R^2 (0.966) value to unity, the better the empirical model fits the actual data. Therefore, it was clearly observed that, 96.6% of the experimental results agrees with the model predicted data and, indicates that the model developed for the transesterification reaction of ERSO is reliable.

Table 4.6: ANOVA analysis of the quadratic model and comparison of model predicted and experimental response at optimum conditions

Source	Sum of squares	Df	Mean of square	F-value	p-value >F
Model	93.45	9	10.38	31.31	<0.0001
A-Catalyst	8.69	1	8.69	26.21	0.0005
B-Time	47.29	1	47.29	143.39	<0.0001
C- Ratio	10.75	1	10.75	32.41	0.0002
AB	0.66	1	0.66	1.98	0.1901
AC	1.513E-003	1	1.513E-003	4.56E-003	0.9475
BC	4.08	1	4.08	12.29	0.0057
A^2	5.45	1	5.45	16.42	0.0023
B^2	13.51	1	13.51	40.74	0.0001
C^2	6.74	1	6.74	20.31	0.0011
R-Squared =0.966			Adj R-Squared = 0.935		

Optimum condition				
	Catalyst loading (wt%)	Reaction time (min)	MR (mol. mol^{-1})	Conversion (%)
Criteria	In range*	In range#	In range**	maximize
Predicted	5.38	13.19	8.09	96.95
Actual	5.38	13.20	8.09	97.00

**[4, 6], #[5, 15] and **[6, 9]. The experiment conducted at optimum conditions shows a good agreement with predicted yield (0.05% error). All the independent parameters were found to be significant in order of time (0.0001) > molar ratio (0.0002) > catalyst loading (0.0005). Predicted conversions are agreed with the experimental conversion (R^2 = 96.83).*

4.5.2. ROME Yield and Process Parameters

The process variables such as, reaction time, molar ratio and catalyst loading were numerically optimized by using RSM for the desired output response (conversion of RSO to ROME). The variables were set in the range (Table 4.5) between the lower and upper bound to obtain the maximum conversion. Based on the fitted model, 20 solutions with three variables were generated using RSM. The optimum conversion of 96.92% was predicted by the model with a desirability of 1.00 at 5.38% catalyst loading, 13.19 min reaction time and 8.09:1 molar ratio. The optimum results predicted by the model have been verified by conducting the experiment under the optimum condition (Table 4.6). The deviation between experimental and model predicted value was only 0.05%. Therefore, it can be established that the fitted model is reliable and significant to predicate the response (% conversion).

Three-dimension surface plot representing the response as a function of two independent factors and their interaction within experimental range of considered values are depicted in Fig. 4.9B–D. These plots are the essential graphical representation of the regression equation (Eq. 4.1). Fig. 4.9B shows the effect of catalyst loading and reaction time on the response, while setting the other parameter, molar ratio at optimum condition (8.09:1). At lower catalyst loading, the ROME yield was found to be increased with sn increase in the reaction time. This was also observed in experimental analysis (Table 4.5). With an increase in the catalysts concentration, from 4 wt% to 6 wt%, the conversion increased gradually. The effect of molar ratio, reaction time and their interaction on the response at constant catalyst loading (i.e. 5.38 wt%) is presented in Fig. 4.9C. At a lower molar ratio (6:1), the conversion of RSO increased with reaction time up to 13 min and beyond this time period no significant change was observed in the conversion. Similar observation has been reported by Tang *et al.* [196] for soybean and rapeseed oil. In

general, the conversion of esterified rubber seed oil into methyl ester initially increased with an increase in the molar ratio and reaction time and then decreased. Similarly, the effect of molar ratio and catalyst loading is shown in Fig. 4.9D. At lower catalyst loading, increased molar ratio up to 9:1 favored the forward reaction (i.e. rubber oil methyl ester), and further increase in the molar ratio showed a slight decreased in the conversion; this could be due to the fact that excess methanol in reaction mixture increases mixing of glycerol (by product) with catalyst. Since the transesterification reaction is reversible in nature, so excess alcohol is required to ensure higher conversion of triglycerides, but a very high molar ratio is undesirable [207]. Similarly, the increase in the catalyst loading supports forward reaction, but excess catalyst loading caused saponification reaction of triglycerides to form soap which decreases triglyceride conversion to methyl esters [207].

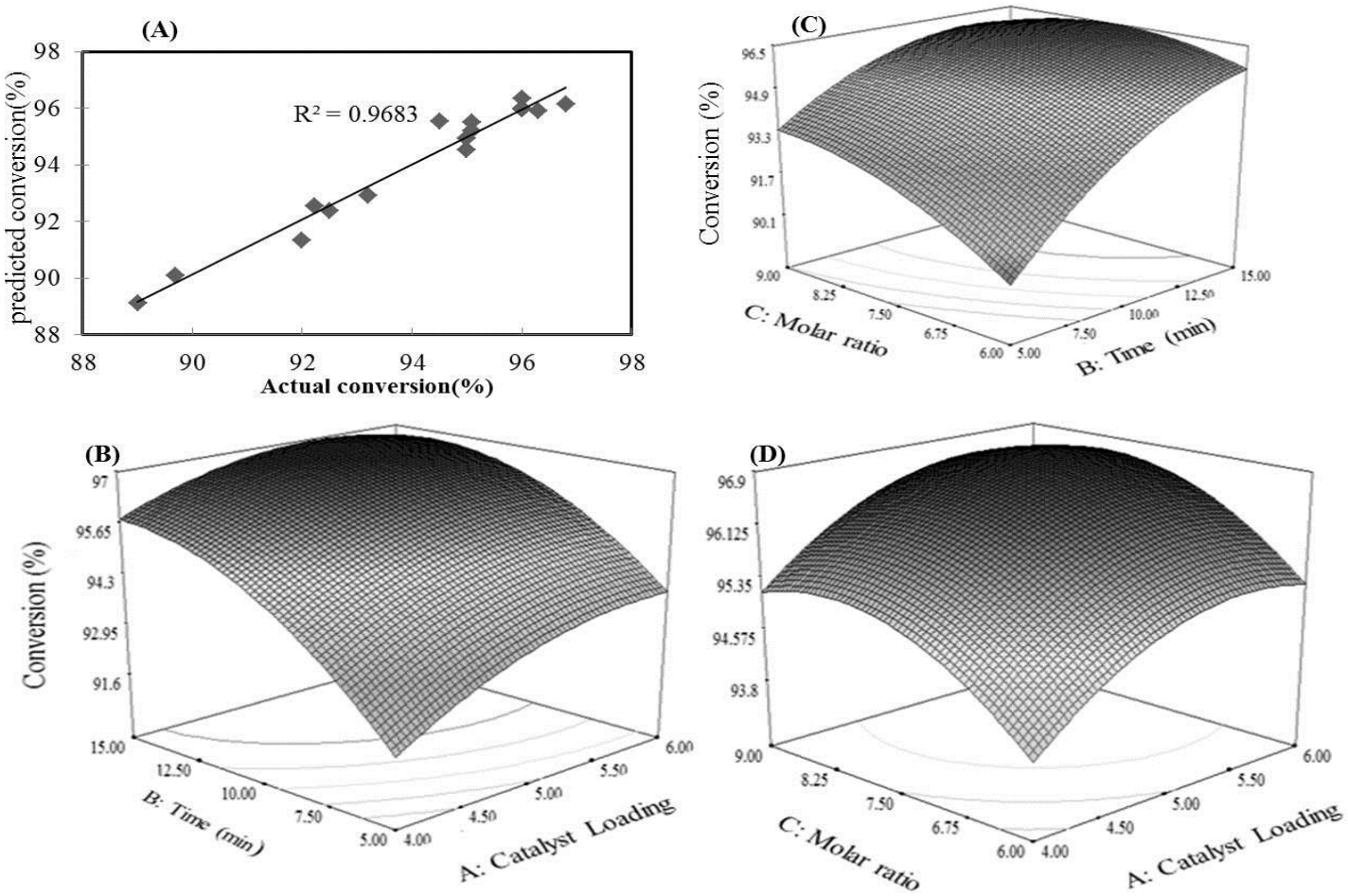

Fig. 4.9: Response surface plot showing the effect of ; (A) actual and model predicted RSO conversion comparison, (B) reaction time(min) and catalyst loading, (C) methanol/oil molar ratio and time(min), (D) methanol/oil molar ratio and catalyst loading.

4.6. Physico-Chemical Properties of RSO and ROME

Physico-chemical characteristics of the samples, extracted RSO and ROME obtained under optimum process conditions were estimated as per ASTM standard methods and obtained values are presented in Table 4.7. A significant reduction in specific gravity was found during the transesterification, from 0.91 (RSO) to 0.883 (ROME). Viscosity of the oil increases with an increase in molecular weight and decreases with an increase in unsaturation level and temperature [185, 208]. Dynamic viscosity of the sample was measured using interfacial rheometer at a constant share rate of 100/sec. The kinematic viscosity of the samples at 24 °C were found to be 30 mm^2/sec (RSO) and 5.82 mm^2/sec (ROME). The value obtained for RSO was much higher compared to conventional diesel, whereas of ROME, it is within the range of ASTM biodiesel standards (Table 4.7). The calorific value of the sample was measured using bomb colorimeter. The obtained values were almost similar, 39.34 MJ/kg (RSO) and 39.53 MJ/kg (ROME). During the esterification acid value reduced from 24 mg KOH/g (RSO) to 2 mg KOH/g (ERSO). The acid value of the final product (ROME) was found to be 0.4 mgKOH/g. The flow characteristics of samples have been observed under low temperature (Fig. A4.4). The obtained cloud point values of RSO and ROME were 3 °C and 2.5 °C, respectively. Differential scanning calorimeter analysis has also been performed to scan the thermal profiles of the samples, and the phase transition points are used to estimate pour points.

Table 4.7: Physico-chemical properties of rubber seed oil (RSO) and its methyl esters (ROME)

Properties	Unit	RSO	ROME[α]	Biodiesel[#]	Diesel[$]
SG at 24 °C	–	0.91	0.883	0.86–0.9[*]	0.846[*]
Kinematic Viscosity at 24 °C	mm^2/sec	30	5.82	1.9–6[*]	1.9–4.1[*]
Kinematic Viscosity at 40 °C	mm^2/sec	13.13	3.81	1.9–6	1.9–4.1
Calorific value	MJ/kg	39.34	39.53	35 min	45.62–46.48
Iodine Value	g I_2/100g	113	114	120 max	N/A
Acid Value	mg KOH/g oil	24	0.4	0.5 max	0.35
Saponification value	mg KOH/g oil	235.28	190	N/S	N/A
RI at 24 °C	–	1.47	1.45	N/S	N/S
Cloud point	°C	3	2.5	(-3) –12	(-15) –5
Pour point	°C	2[**]	-3[**]	(-15) –10	-40
Cetane No.	–	44	49.9	47 min	40 min
Moisture content	%	0.27	0.33	0.05 max	0.05 max
Flash point	^oC	273	131	130 min	52 – 96
Fire point	^oC	282	146	N/S	N/S

*[α]Rubber seed oil methyl ester, *measured at 40 ^oC, [#]Standards ASTM test methods, [$]Fossil fuel, [**]DSC method, RI: Refractive index, SG: Specific Gravity, N/S: not specified, N/A: not applicable*

Fig. 4.2A–C shows ^{1}H NMR spectra of virgin RSO, the product of esterification reaction (ERSO) and the final product after transesterification (ROME), respectively. In the ^{1}H NMR spectra, the peak at 3.7 ppm corresponds to the characteristic peak of FAME. In RSO, (Fig. 4.2A) the peak corresponds to methyl ester protons of biodiesel is absent while in ERSO it is evident only to a small extent (Fig. 4.2B). The presence of a prominent methyl ester proton peak at 3.7 ppm in the transesterified product (ROME) confirms the progress of transesterification with the formation of large quantities of fatty acid methyl esters (FAME). All three samples were comprised of saturated, monounsaturated and polyunsaturated fatty acid alkyl groups, in oil (RSO) sample it is in the form of fatty acid alkyl groups of triglycerides, in methyl esters (ROME) it is fatty acid alkyl groups of methyl esters, and in the esterified sample it is the mixture of both and mixture depends on the degree of esterification [209]. However, both fatty acid alkyl groups of triglycerides and esters can be seen in esterified RSO. Unsaturated fatty acids/esters such as linoleic (polyunsaturated), linolenic (polyunsaturated) and oleic (monounsaturated) have been identified in all the samples (Fig. 4.2). The comparison of esterification and transesterification product samples showed that all types of alkyl groups of fatty acid present in the original RSO triglyceride contributes to the processes; only slight decrease in saturated acid content was observed in a ROME sample (14.7 %) compared to its virgin RSO sample (19.9%). The ^{13}C NMR spectra of rubber seed oil and its methyl esters (biodiesel) are depicted in Fig. 4.10 and Fig. 4.11, respectively. The signal at 69 ppm and 62 ppm in ^{13}C NMR spectrum of rubber seed oil are due to the carbonyl methylene groups (69 ppm (H–C–O–) and 62 ppm (CH_2–C–O–)) (Fig. 4.10) while the signal is absent in the biodiesel (ROME) (Fig. 4.11). It can be clearly seen that the glyceride backbone of triglyceride is totally absent in the ROME sample. The methoxy carbon of methyl esters of rubber seed oil methyl esters illustrates the signal at 51.49 ppm.

The unsaturation signal (–C=C–) obtained between 133–120 ppm in ^{13}C NMR are due to the presence of linoleic (polyunsaturated), linolenic (polyunsaturated) and oleic (monounsaturated) fatty acids and ester in RSO (Fig. 4.10) and ROME (Fig. 4.11), respectively.

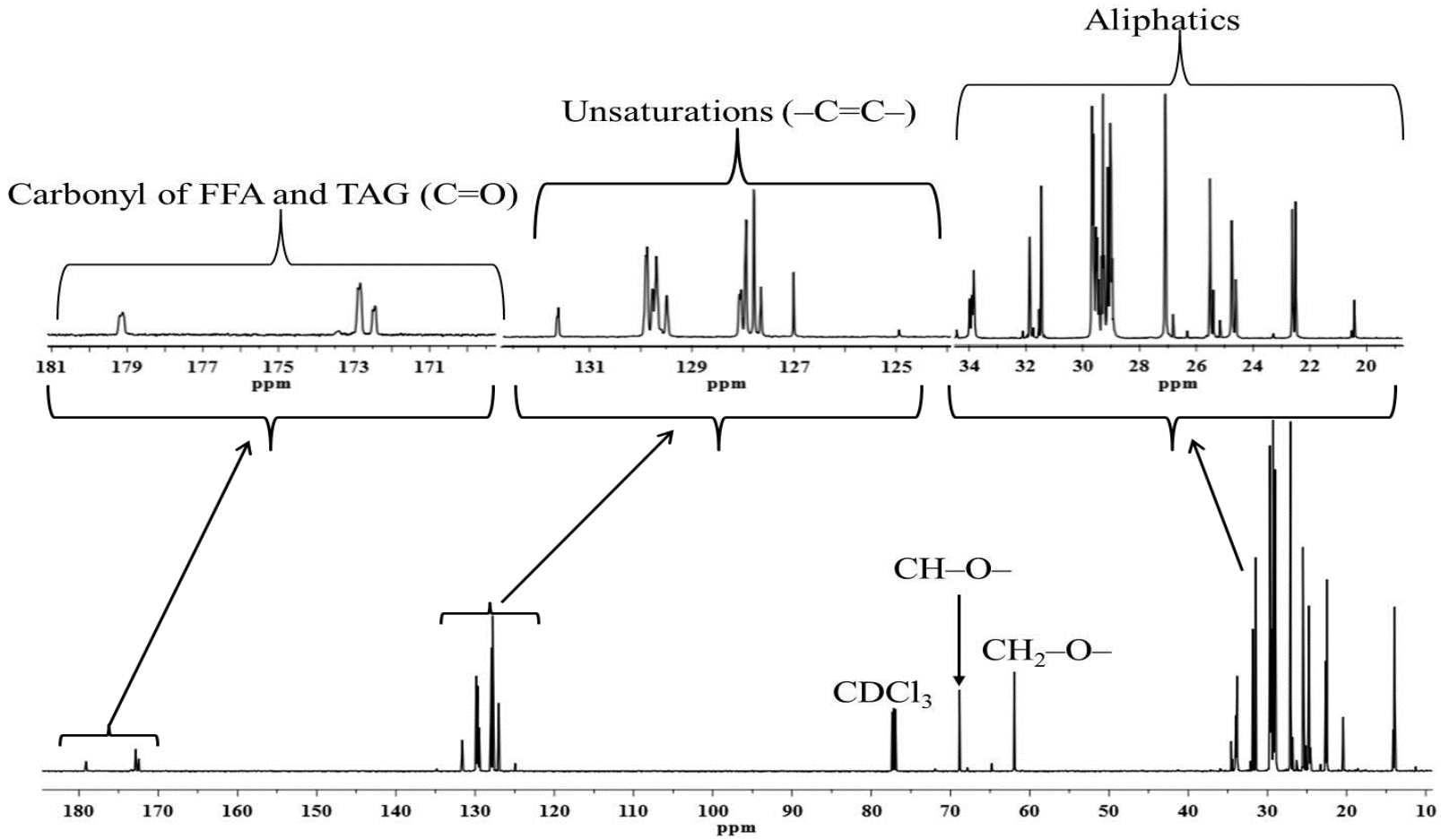

Fig. 4.10: ^{13}C NMR spectrum for rubber seed oil

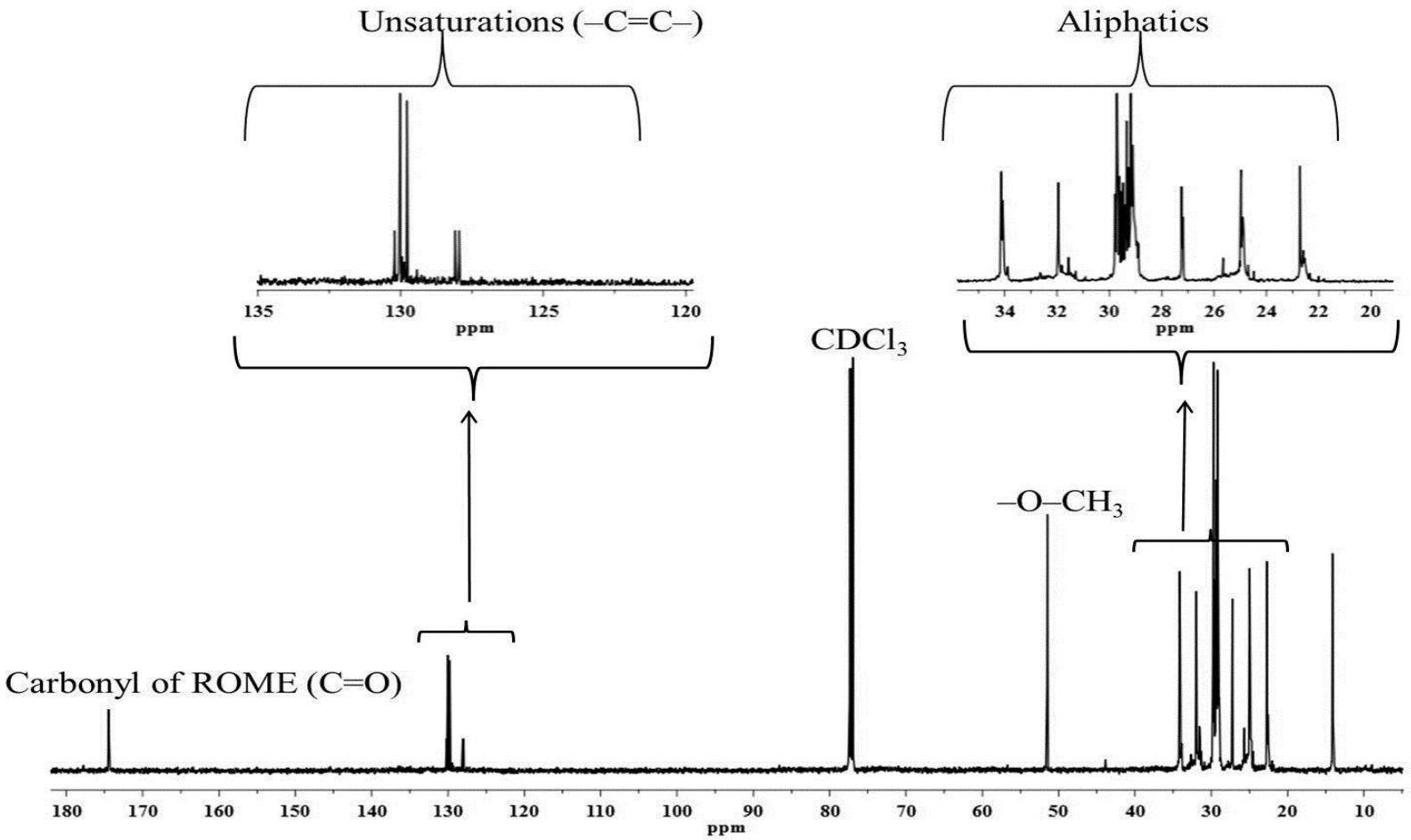

Fig. 4.11: ^{13}C NMR spectrum for rubber seed oil methyl esters

4.7. Thermal Degradation Kinetic Study of Rubber Seed Oil and its Methyl Esters

4.7.1. TG Analysis at Various Heating Rates

The thermal decomposition behavior of both, RSO and ROME samples was investigated by using thermogravimetric analysis technique. TGA and DTG profiles of RSO and ROME at various heating rates are shown Fig. 4.12. Volatilization occurs during early stage, when the lighter components evolved. During decomposition, the heavier components break to low molecular weight components. Further, the evolved products, low molecular weight components during decomposition go through the volatilization process. Thus, in active thermal degradation stage both the phenomena take place. A change in the slope of TG profile was considered as the beginning of new stage. Hence, thermal decomposition profiles of ROME and RSO can broadly be classified in three stages (Fig. 4.12). However, for kinetic analysis only active thermal decomposition temperature ranges were considered. The main (active) thermal decomposition of ROME sample at different heating rates (10, 20, 30, 40 and 50 °C/min) occurred in a single stage, that describes the volatilization and decomposition. However, the two-stage thermal decomposition was observed for RSO sample (Table 4.8). The first stage (RSO-I) showed the presence of higher free fatty acid in the sample. In addition to free fatty acid decomposition, mass loss of moisture and degradation of light volatile compounds also takes place within this stage. The active decomposition of RSO in the second stage (RSO-II) is due to degradation and volatilization of triglyceride (Fig. 4.12). At a heating rate of 20 °C/min, the thermal decomposition of RSO and its methyl ester (ROME) occurred in the temperature range of 242–480 °C (95.7 wt%) and 165–456 °C (97.2 wt%), respectively. The active thermal decomposition and volatilization of the RSO sample were started (242 °C) and completed (480 °C) at higher temperature as compared to its methyl

ester (ROME) (i.e. 165 °C for started and 456 °C for complete active thermal decomposition). This is because RSO has higher molecular weight and stronger intermolecular force (higher viscosity) as compared to ROME. The onset temperature values for palm oil methyl ester (164.5 °C), peanut oil methyl ester (155.8 °C), waste cooking oil methyl ester (142.2 °C) were almost similar to ROME (165 °C) as reported by Li *et al.* [171]. It can be seen from Fig. 4.12A–D that, onset temperature and the temperature at which rate of mass loss is maximum (T_{max}) were shifted to higher temperature with increased heating rate. This is due to low heat distribution (heat transfer limitation) at higher heating rate in both RSO and ROME samples [165, 171, 210]. With respect to heat transfer phenomenon, the initial thermal degradation temperature values for rubber seed oil in first stage (RSO-I) and second stage (RSO-II), and for rubber seed oil methyl esters (ROME) were shifted from 223 °C to 264 °C, 253 °C to 295 °C and 120 °C to 193 °C as the heating rate increased from 10 °C/min to 50 °C/min, respectively (Table 4.8). Furthermore, the values of peak temperature, T_{max} were also changed from 271 °C to 328 °C, 416 °C to 446 °C and 250 °C to 287.9 °C for thermal degradation of RSO-I, RSO-II and ROME, respectively. Similarly, some other parameters such as T_o and w_{max} values were also increased (Table 4.9). From Fig. 4.12 (B and D), it can also be clearly observed that the heating rate has a significant effect on the rate of thermal degradation of the samples.

Table 4.8: TG characteristic properties for active pyrolysis stage of RSO and ROME

Sample	Properties	Heating rate (°C/min)									
		10		20		30		40		50	
	Stage	I	II	I	II	I	II	I	II	I	II
RSO	T_o, °C	223	353	242	373	249	382	253	384	264	395
	T_f, °C	309	471	334	480.0	345.6	483	350	487	365	488
	Δwt, %	20	69.5	20	69.5	20	69.5	20	69.5	20	69.5
	T_{max}, °C	271	416	296	424	310	438	318	443	328	446
	w_{max},%/min	3.26	12.1	5.9	35.2	8.8	44.6	11.7	60	13.6	76.7
ROME	T_o, °C	120	–	165	–	172	–	181	–	193	–
	T_f, °C	407	–	456	–	470	–	474	–	480	–
	Δwt, %	97.2	–	97.2	–	97.2	–	97.2	–	97.2	–
	T_{max}, °C	250	–	268.5	–	277.5	–	283.5	–	287.9	–
	w_{max},%/min	15.9	–	29.1	–	41.4	–	55.2	–	76.2	–

T_o: Initial temperature for the main mass loss (°C), T_f: Final temperature for the main mass loss (°C), T_{max}: Temperature for maximum rate of mass loss (°C), Δwt: change of mass loss and w_{max}: maximum mass loss rate (%/min)

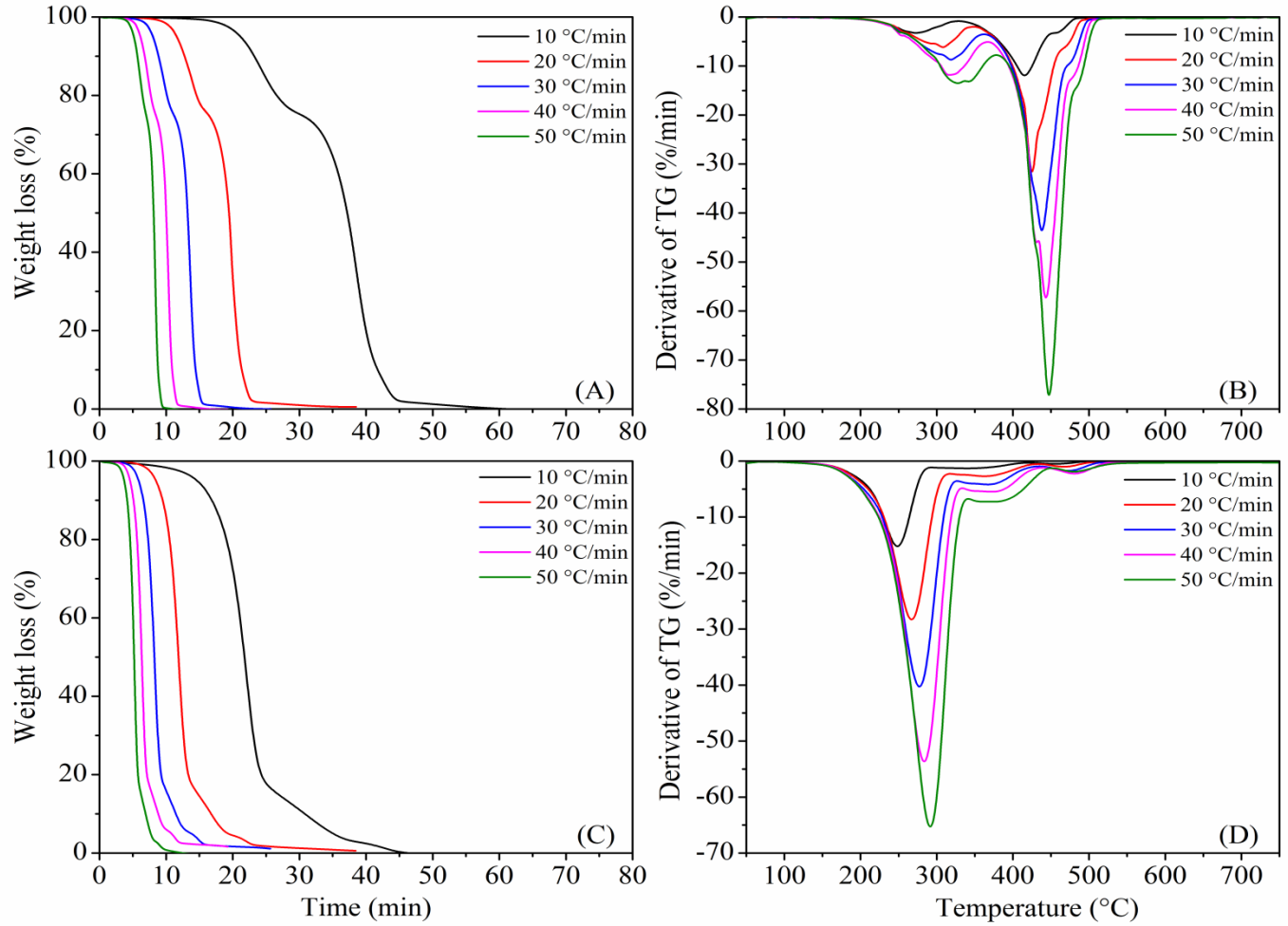

Fig. 4.12: TGA and DTG profiles (A, B) for RSO and (C, D) for ROME samples

4.7.2. Fourier Transform Infrared (FT-IR) Analysis for Evolved Products

Fig. 4.13 show FT-IR plot of evolved products at various mass loss temperatures during thermal volatilization and decomposition of RSO and its methyl esters at a heating rate of 40 °C/min. FT-IR profiles for RSO and ROME were found to be almost similar. However, the absorbance peak corresponding to gaseous and liquid water molecules can be seen only for RSO thermal degradation at 3500–3950 cm^{-1} and 3400–3500 cm^{-1}, respectively [211]. This may be because only oxygen-containing groups in ROME (i.e. $R1COOR_2$) decomposed to C=O– and C–O [171, 212]. The characteristics infrared absorption peaks for volatile components functional group were clearly shown in Fig. 4.13. Symmetric and asymmetric stretching vibrations of –CH– and, –CH3 asymmetric deformation vibration in the range of wave number, 3000–2700 cm^{-1} and 1475–1000 cm^{-1}, respectively revealed the presence of alkanes in the evolved products during thermal degradation of RSO and ROME. Carbonyl groups of aldehydes and ketones were also observed as H–C=O– and –C=O– in plane bending vibrations at 1720–1740 cm^{-1} and 1735–1750 cm^{-1} (Fig. 4.13), respectively. Furthermore, C–O–C (stretching vibration at 1000–1300 cm^{-1}), C=O (bending vibration at 2250–2400 cm^{-1} and 580–730 cm^{-1}), C=O (stretching vibration at 2000–2250 cm^{-1}) and C–O (stretching vibration at 2200–2100 cm^{-1}) were observed in evolved gas (Fig. 4.13) [213].

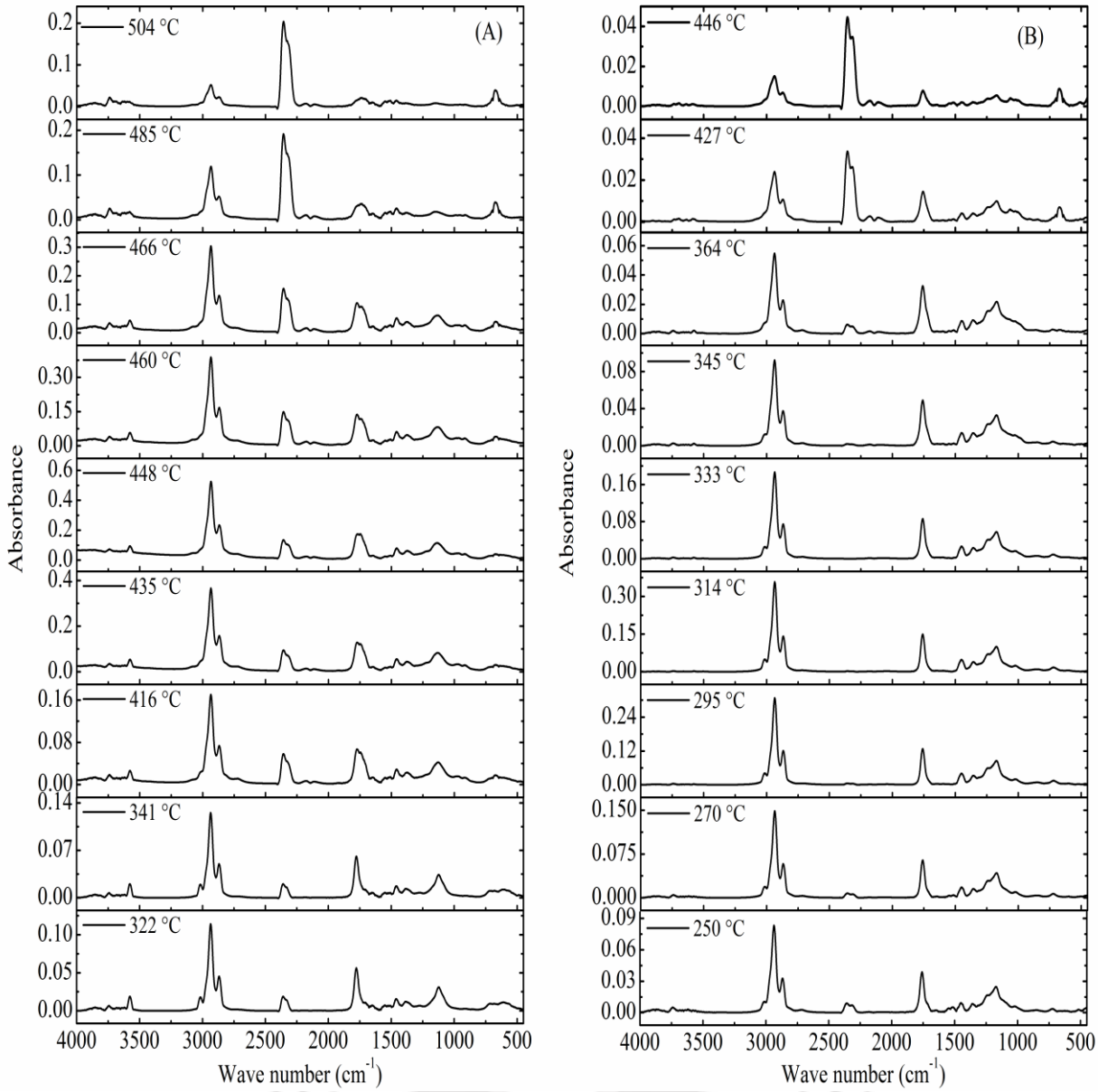

Fig. 4.13: FT-IR spectra for evolved products during thermal decomposition of (A) RSO and (B) ROME at heating rate of 40 °C/min

Taking the absorbance of identified volatile components such as alkanes, alkenes, aldehydes, ketones, ethers and CO_2, the intensity of evolved compounds with increasing thermal decomposition temperature is presented in Fig. 4.14. As the thermal decomposition temperature increased, ether and aldehydes were formed due to de-oxygenation of ester [212]. Presence of CO_2 in the evolved product revealed that the de-carboxylation of ester and triglyceride occurred during the thermal decomposition of ROME and RSO [171]. It can be seen from Fig. 4.14 that the maximum absorbance characteristic peaks for alkenes, alkanes, aldehydes and ether occurred at same temperature (448 °C) and, for ketones and CO_2 at temperature of 536 °C during thermal degradation of RSO. Similarly, during the thermal degradation of ROME, the maximum rate of alkenes, alkanes, aldehydes and ether production occurred at temperature of 307 °C while for ketones and CO_2, the maximum rate values were found at 571 °C. As can be observed in TGA profiles (Fig. 4.12) and FTIR spectra (Fig. 4.13), beyond 500 °C, the mass loss during thermal decomposition of ROME (1.44 wt%) and RSO (1.19 wt%) is mainly due to the formation of CO_2 and ketone (Fig. 4.14). Taking the Lambert-Beer law into consideration, the concentrations of alkanes in evolved products were found maximum during thermal decomposition RSO and ROM [212, 213]. The appearance of absorbance profile with temperature (Fig. 4.14) was similar to that of the DTG curve (Fig. 4.12).

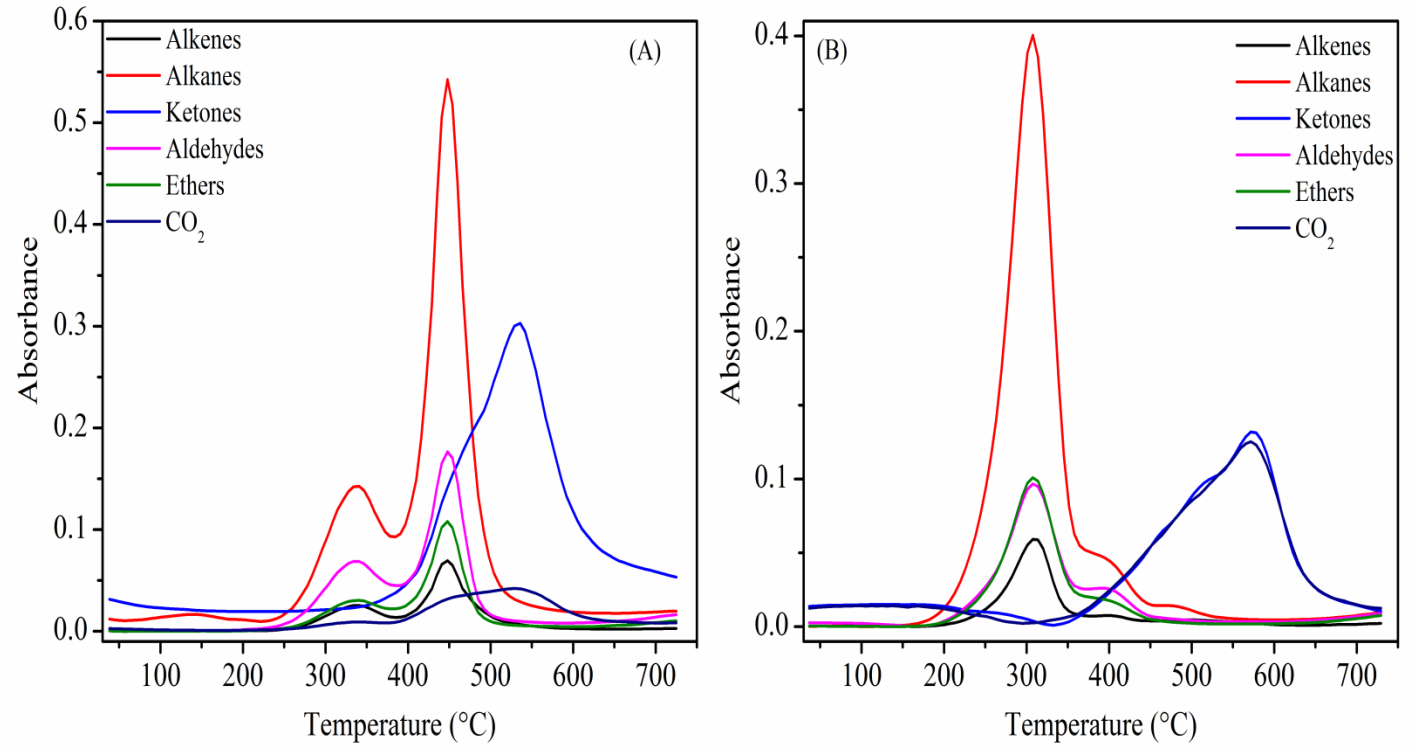

Fig. 4.14: Formation of evolved products during thermal decomposition of (A) RSO and (B) ROME at heating rate of 40 °C/min.

4.7.3. Kinetic Parameter Calculation

It can be seen from Fig. 4.15 that the degree of conversion of both the sample were greatly varied with temperature and heating rate. To estimate the dependency of activation energy on temperature and degree of conversion during the active decomposition (pyrolysis) process, nine conversions fraction from 0.1 to 0.9 with increment of 0.1 were selected at all heating rates. Based on FRD, FWO and MCR isoconversional methods, the activation energies (*E*) for selected conversions were calculated from the slopes of linear regression (Fig. 16–18).

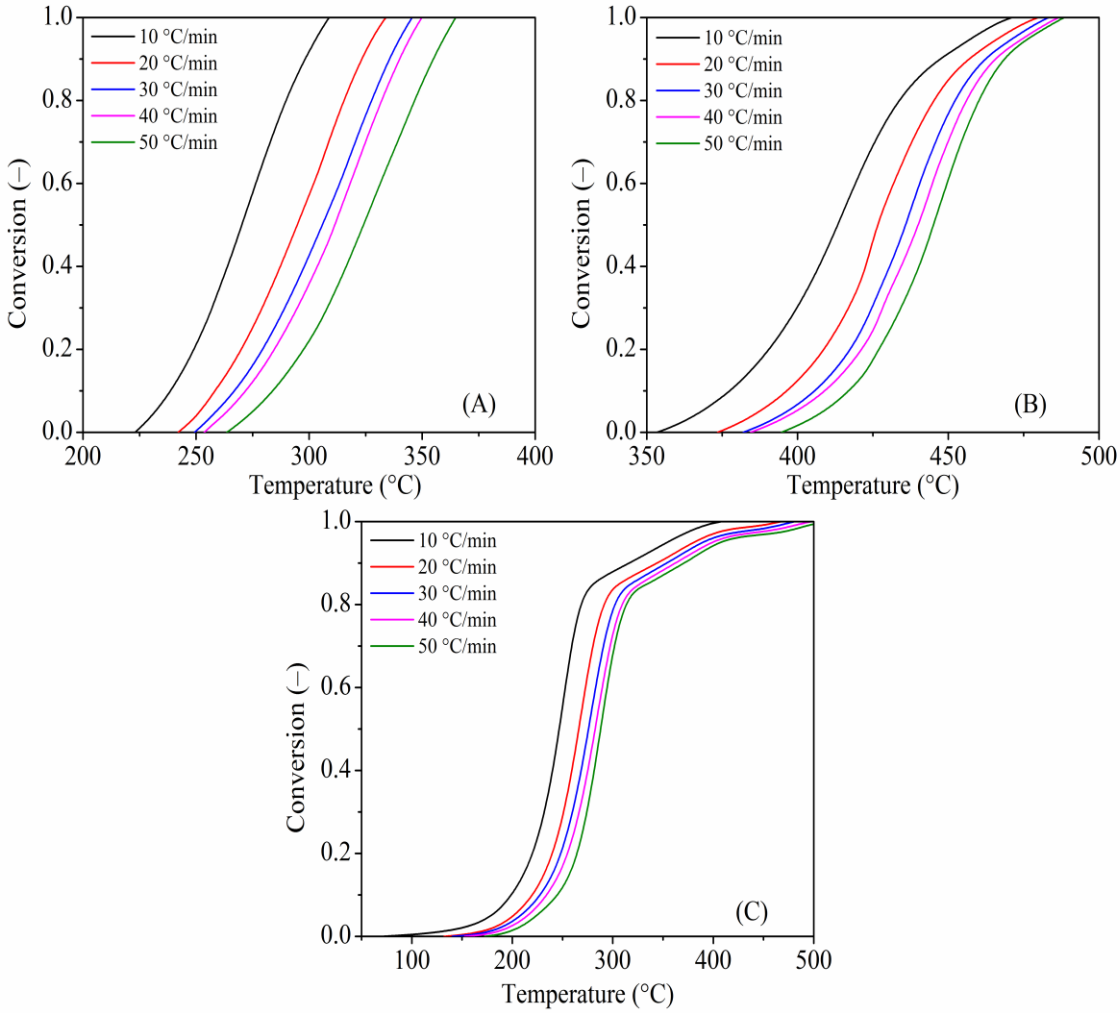

Fig. 4.15: TGA mass conversion for (A) RSO-I, (B) RSO-II and (C) ROME samples.

The deduced regression lines for RSO-I, RSO-II and ROME are presented in Fig. 16–18 and the values of activation energies (*E*) are summarized in Table 4.8. Parallel lines shown in Fig. 5–7 indicate that, the values of activation energy (*E*) for thermal degradation of the samples (RSO and ROME) for free fatty acids (RSO-I), triglycerides (RSO-II) and fatty acid methyl esters (ROME) in the respective sample follow the same reaction rate or intensity. In other words, the values of activation energy (*E*) obtained at different degree of conversions and temperatures were almost similar for RSO-I and ROME. This suggest that a single mechanism or unification of multiple reactions mechanism was followed in the active thermal degradation of RSO-I and ROME [171, 214]. However, the for RSO-II, fitted lines at different conversion were not purely parallel to each other's and this shows the change in activation energy at different degree of conversions due to multiple and parallel reactions during thermal decomposition of triglycerides of RSO. The change in the slope values of the lines at different conversion show that the rates of thermal decomposition differ due to multiple reactions occurring. For this reason, the higher values of activation energies were found at later stage of conversion (α=0.9). The values of R^2 were found to be more than 0.99 for the selected conversions (0.1 to 0.9) which show the fitness of the methods considered, FRD, FWO and MCR.

The activation energy (*E*) for RSO-I and RSO-II varies from 69.8–92.7 kJ/mol and 144–433.3 kJ/mol, respectively. The difference in activation energy at lower (α = 0.1) and higher (α = 0.9) degree of conversion for RSO-II reveal incomplete decomposition of free fatty acids in the first stage. Further, it also suggests that the thermal decomposition of RSO samples is a complex reaction which involves several parallel, competitive and consecutive types of

reactions. Activation energy (*E*) is the critical energy barrier to be overcome to generate a chemical reaction and also it represent the minimum energy required to break the chemical bond between atoms [176]. Hence, the higher values of activation energy for RSO-II as compared to RSO-I indicate that more difficult reactions have taken place during secondary stage (RSO-II). This may be due to higher free fatty acid content in RSO sample. Considering the three methods (FRD, FWO and MCR), the overall average activation energy (*E*) for the thermal decomposition of RSO was found to be 167.8 kJ/mol (FRD), 144.85 kJ/mol (FWO) and 142.05 kJ/mol (MCR). The obtained overall average activation energy for RSO thermal decomposition are in good agreement with sunflower oil (170–210 kJ/mol) [172], soybean (146.6–160.2 kJ/mol) [214], karanja seed oil (156.5–160.7 kJ/mol) [214] and mustard seed oil (142.4–148.1 kJ/mol) [214]. Fig. 4.17C shows the linear plot for Kissinger method for thermal decomposition of RSO at different active thermal degradation stages. As it was found in FRD, FWO and MCR methods, the activation energy for the primary stage (RSO-I) was also lower than that of the secondary stage (RSO-II) in KM. From the results it is clear that the obtained values of activation energy (*E*) (67.89 kJ/mol, RSO-I; 183.85 kJ/mol, RSO-II) by Kissinger method are lower than that of obtained by FRD (76.7 kJ/mol, RSO-I; 258.9 kJ/mol, RSO-II), FWO (80.9 kJ/mol, RSO-I; 208.8 kJ/mol, RSO-II) and MCR (75.8 kJ/mol, RSO-I; 208.3 kJ/mol, RSO-II) methods.

Table 4.9: The values of activation energy deduced from FRD, FWO and MCR methods

			Activation Energy (kJ/mol) at Conversion (%)*									Average
Biomass	Stage	Method #	10	20	30	40	50	60	70	80	90	
RSO	I	FRD	72.8	70.7	69.8	73.5	74.1	75.2	77.72	83.7	92.7	76.7
		FWO	83.8	81.6	80.2	79.6	79.4	79.5	79.9	81.1	83.7	80.9
		MCR	79.3	76.8	75.2	74.4	74.1	74.1	74.3	75.5	78.1	75.8
	II	FRD	164.2	196.9	220.7	212.1	231.2	261.1	283.1	328.6	433.3	258.9
		FWO	147.8	162.8	177.9	188.9	197.2	209.4	225.4	250.9	319.2	208.8
		MCR	144	160	176.3	187.3	196	209.5	225.3	252.1	324.1	208.3
ROME	I	FRD	71.8	89.6	93.9	93.3	90.9	87.1	83.9	78.2	100.9	87.7
		FWO	70.5	78.4	84.6	88.1	89.9	90.4	90.1	88.1	89.7	85.5
		MCR	65.9	74.0	80.3	83.8	85.6	86.1	85.5	83.3	84.2	80.9

* *Stage by stage conversion (α) of active pyrolysis of the samples, # average R^2 was found to be ~0.994 and overall average activation energy (E) for RSO decomposition was found to be 167.8 kJ/mol (FRD), 144.9 kJ/mol (FWO) and 152.5 kJ/mol (MCR)*

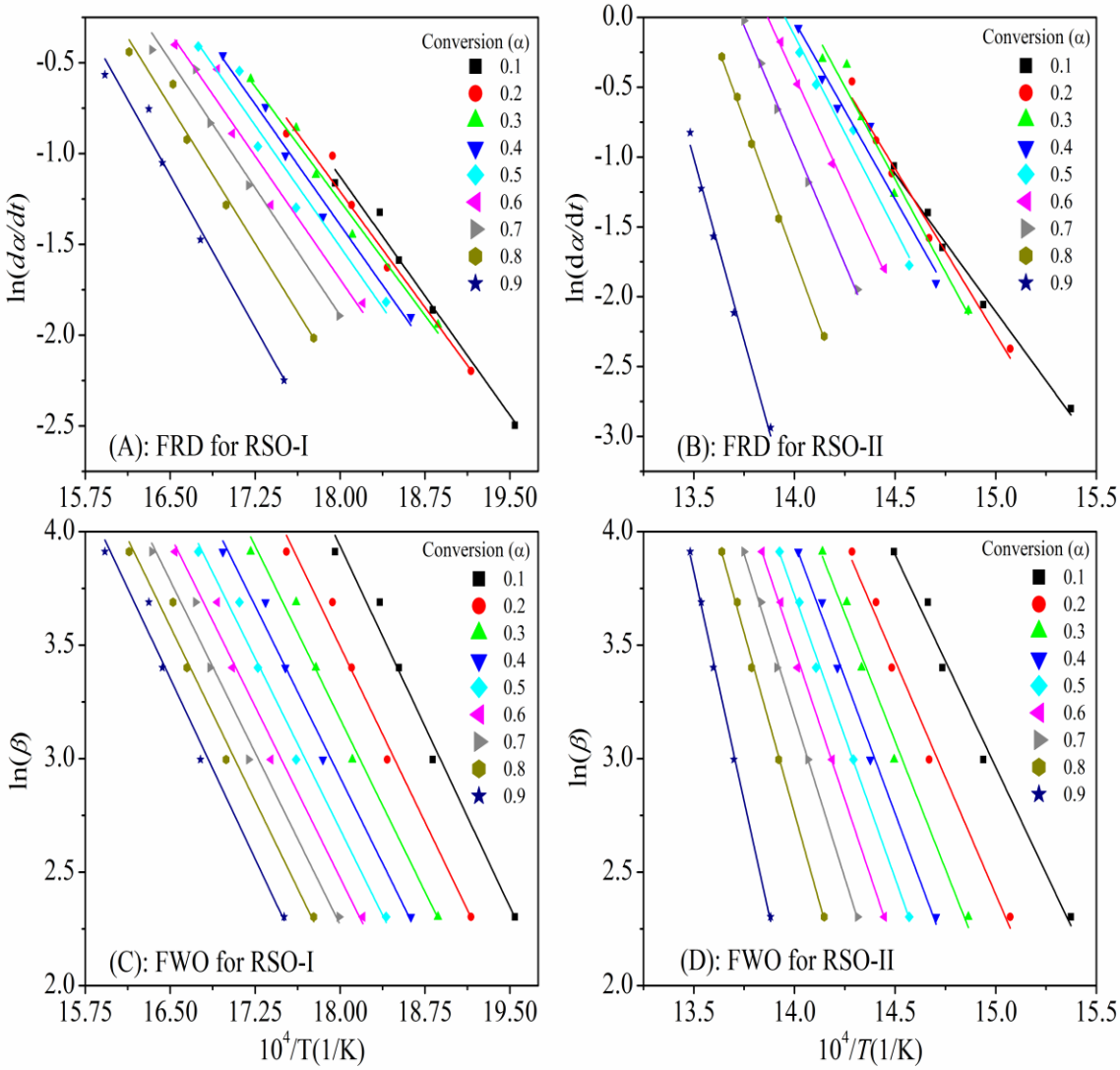

Fig. 4.16: Regression plots based on (A) FRD for RSO-I, (B) FRD for RSO-II, (C) FWO for RSO-I and (D) FWO for RSO-II

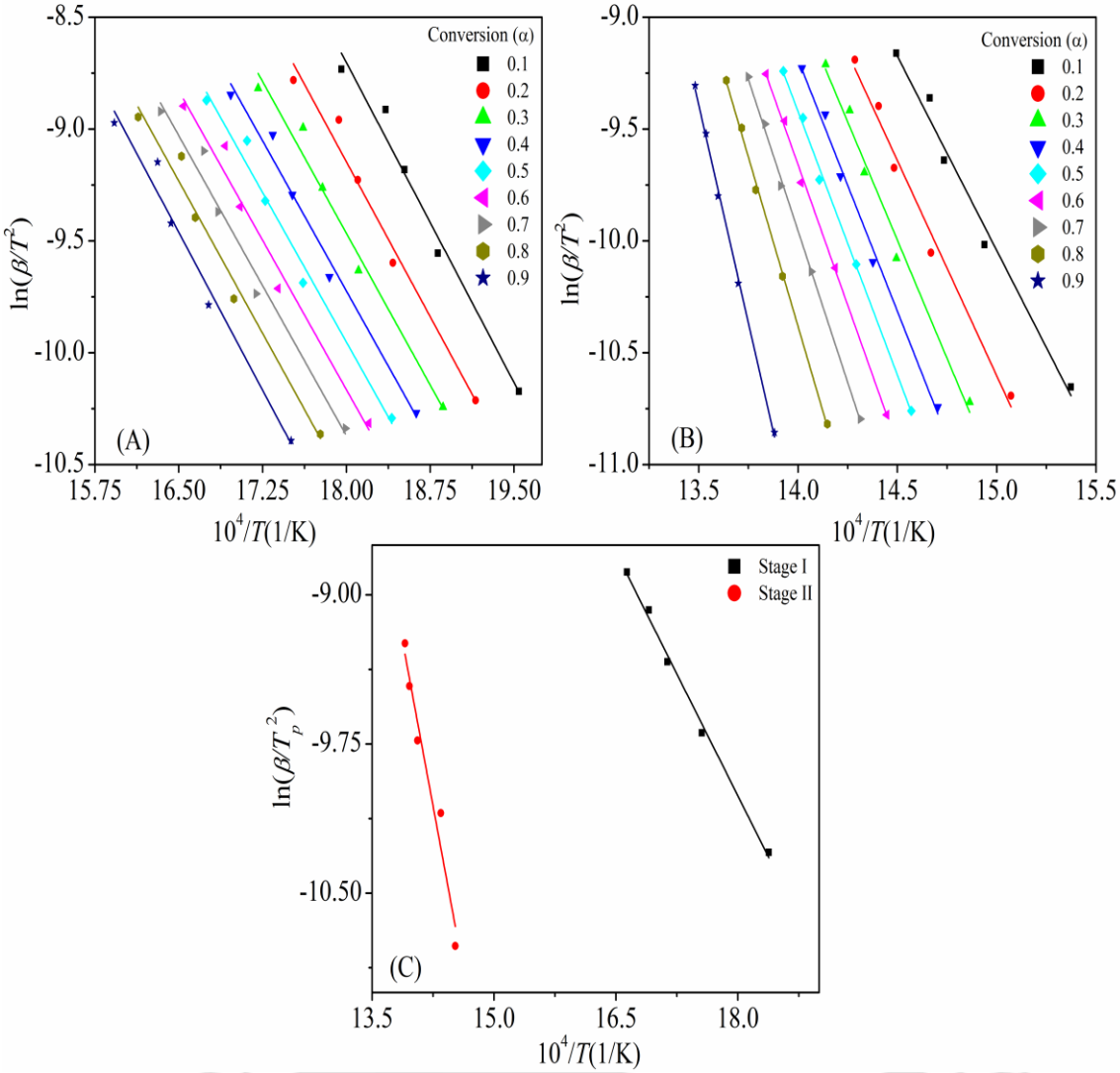

Fig. 4.17: Regression plots based on (A) MCR for RSO-I, (B) MCR for RSO-II and (C) KM for RSO-I and RSO-II.

Table 4.9 demonstrates that the average values of activation energy (*E*) of ROME were estimated as 87.7 kJ/mol, 85.5 kJ/mol and 80.9 kJ/mol calculated using FRD, FWO and MCR approaches, respectively. The values are lower than that of RSO-II. Higher molecular weight of triglycerides of RSO-II require high energy for thermal decomposition and volatilization [172]. The differences in the values of activation energy (*E*) of RSO and ROME revealed that

decomposition or volatilization mechanism of the samples occur in different manner, and RSO was chemically modified through transesterification process (Table 4.9). However, the activation energy range for first stage decomposition of RSO was found to be similar with ROME thermal degradation for 5–12% difference. Fig. 4.18D shows the fitness of Kissinger method for ROME thermal decomposition and the activation energy was found to be 92.5 kJ/mol. Considering all the above methods, the average activation energy for ROME was obtained as 86.65 kJ/mol. The calculated average activation energy is in good agreement with for sunflower oil methyl ester [172]. However, it is higher than peanut oil methyl ester (49.71 kJ/mol), waste cooking oil methyl ester (50.07 kJ/mol) and palm oil methyl ester (54.09 kJ/mol) [171]. This may be due to the difference in the physico-chemical-thermal properties of the parent feedstocks and produced biodiesels.

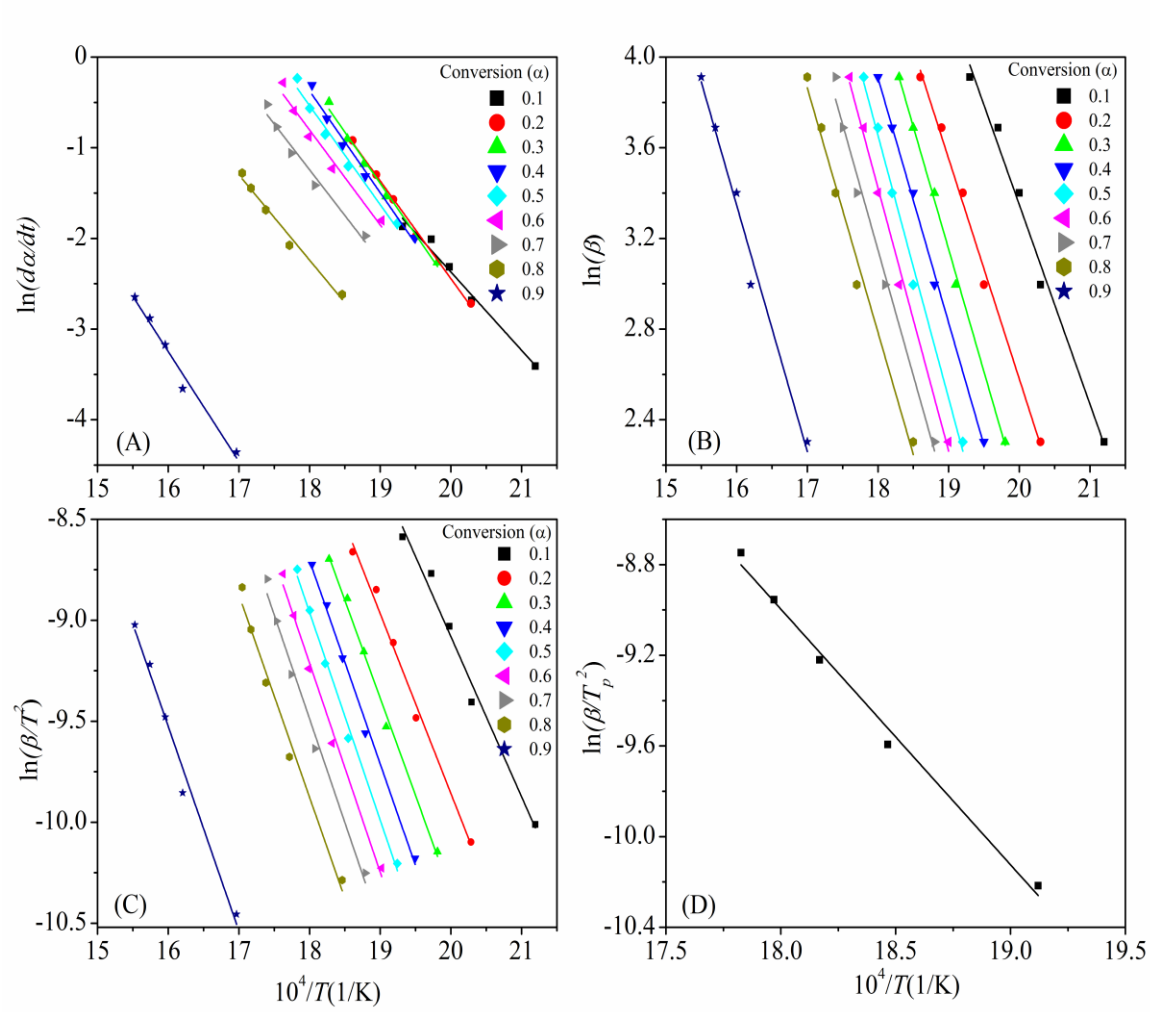

Fig. 4.18: Regression plots based on (A) FRD, (B) FWO, (C) MCR and (D) KM for ROME thermal degradation

4.7.3.1. Variation of Order of Reaction for RSO and its Methyl Ester

On the basis of reported literature by Gai *et al.* [176] and Li *et al.* [171], the dependency of order of reaction (*n*) on the temperature was investigated. Most of the investigations assumed zero-order or first-order reaction [214]. In the present study, the order of reaction (*n*) for the thermal degradation of RSO and ROME were evaluated through the Avrami theory. The regression plots of RSO (stage I and II) and ROME are shown in Fig. 4.19A–C and the calculated values of order of reaction for the thermal degradation of samples are presented in

Table 4.10. Based on the R^2 values (Table 4.10), the Avrami theory is suitable and well fitted to estimate *n* for the thermal degradation of RSO and ROME. As the decomposition temperature increased from 267 °C to 307 °C (within stage I), the reaction order of RSO first decreases from 1.59 to 1.26 and then increase to 1.42. Further increasing the decomposition temperature from 402 °C to 457 °C (within stage II), the value of *n* decreased from 1.41 to 0.38. The average order of reaction for RSO-I (1.37) was found higher than that of RSO-II (0.92). The values of *n* for sunflower oil reported Santos *et al.* [172] vary in the range of 0.95 to 1.82. Similarly, for overall decomposition of RSO, the n value is within the range 0.39 to 1.59. Varying decomposition temperature for ROME, the reaction order (*n*) initially increased from 0.92 (227 °C) to 1.10 (257 °C) and then decreased to 0.19 (317 °C). Li *et al.* [171] and Santos *et al.* [172] reported that the values of order reactions (*n*) varied from 1.6 to 1.68 (269 °C–277 °C), 1.77 to 1.95 (257 °C–277 °C), 0.71 to 1.13 (257 °C–277 °C) and 0.69 to 1.89 for peanut oil, palm oil, waste cooking oil and sunflower methyl esters, respectively. Similarly, the order of reaction (*n*) was found to be varied from 0.96 to 1.1 (237 °C–267 °C) for ROME thermal degradation. Furthermore, the average value of order of reaction (*n*) for ROME (0.69) is in good agreement with the results reported in the literature such as waste cooking oil (0.88), soybean (0.5), higuereta (0.7), babassu (1.4) and palm (0.4) oil ethyl esters thermal decomposition [215, 216].

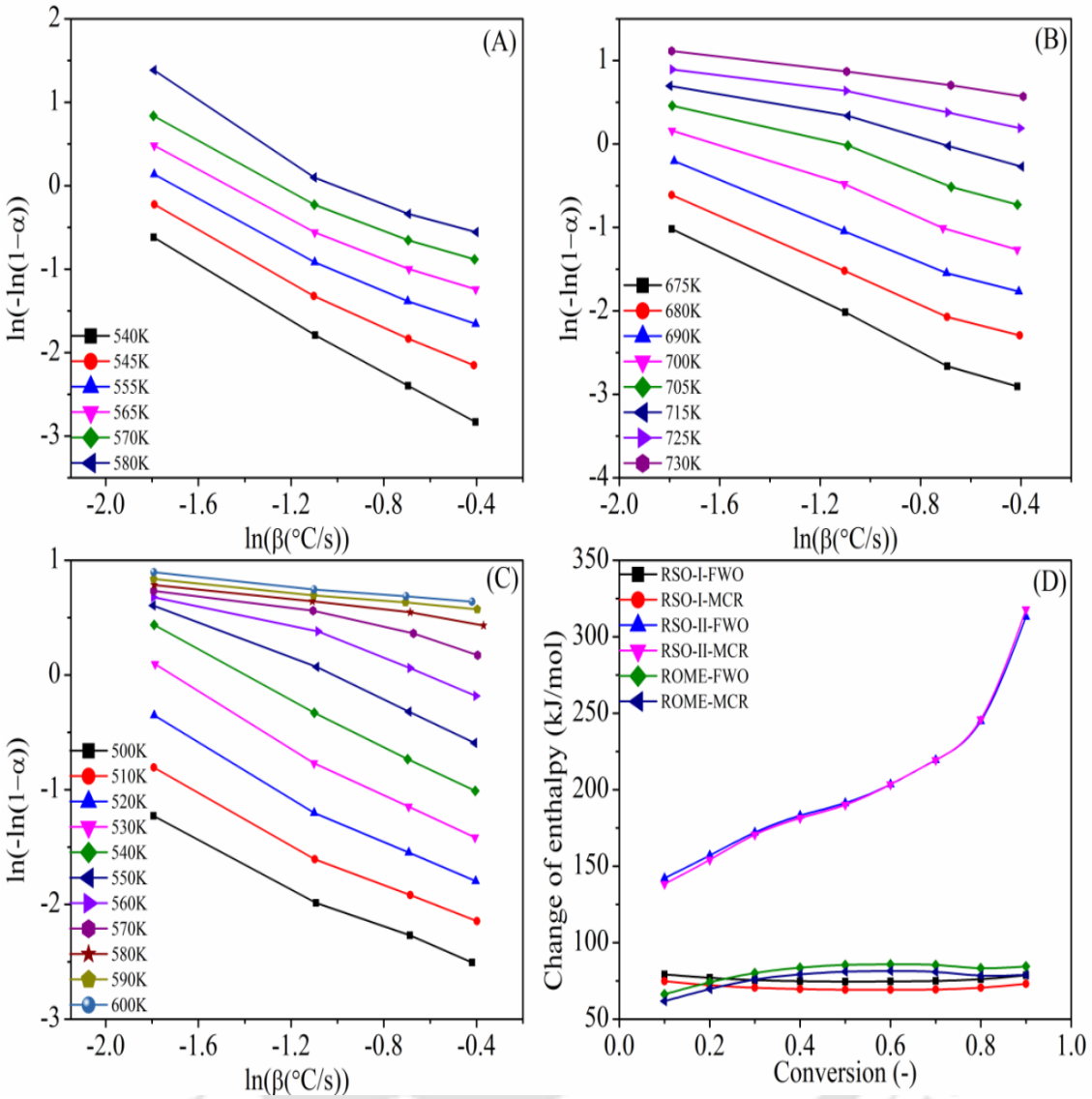

Fig. 4.19: Regression plots to order of reaction proposed by Avrami theory for (A) RSO-I, (B) RSO-II and (C) ROME; (D) enthalpy change for RSO and ROME based on FRD and MCR methods.

Table 4.10: The value of reaction order for thermal decomposition of RSO and ROME calculated using Avrami theory

RSO-I			RSO-II			ROME		
Temp (°C)	n	R^2	Temp (°C)	n	R^2	Temp (°C)	n	R^2
267	1.59	0.99	402	1.41	0.99	227	0.92	0.99
272	1.41	0.99	407	1.24	0.99	237	0.96	0.99
282	1.31	0.99	417	1.16	0.99	247	1.04	0.99
292	1.26	0.99	427	1.06	0.99	257	1.10	0.99
297	1.26	0.98	432	0.88	0.99	267	1.05	0.99
307	1.42	0.98	442	0.69	0.98	277	0.86	0.99
			452	0.50	0.98	287	0.61	0.98
			457	0.38	0.99	297	0.39	0.98
						307	0.24	0.98
						317	0.19	0.99
						327	0.19	0.99
Average (n)	1.37			0.92			0.69	

4.7.4. Thermodynamic Parameter Calculation for RSO and its Methyl Esters

In addition to the activation energy and order of reaction, some of the important thermodynamic parameters (ΔH, ΔG and ΔS) for thermal decomposition of RSO and its biodiesel were calculated using Eq. 2.26–29. It can be seen from Fig. 4.19D that all the calculated ΔH values are positives; thermal decomposition of RSO and ROME within active degradation stages is endothermic process. Due to high molecular weight of triglyceride of vegetable oil as compared to that of fatty acid alkyl esters, ΔH for vegetable oil is higher than that of biodiesel [212], similar to *E* values. The value of ΔH calculated by FWO and MCR method for RSO thermal decomposition within the conversion interval of 0.1 to 0.9 fractions was higher than that of ROME. The values of ΔH by FWO and FRD were found within the range of 69.27–79.34 kJ/mol (RSO-I), 138.39–318.01 kJ/mol (RSO-II) and 61.76–84.52 kJ/mol (ROME). From the study it was clear that the change of ΔH for RSO was wider compared to that of ROME, indicates that its thermal decomposition is also more complex than that of its biodiesel [212, 215]. The average value of ΔH was found to be 146.26 kJ/mol and 78.69 kJ/mol for RSO and ROME, respectively. Li *et al.*[212] evaluated the average values of ΔH for thermal decomposition of peanut oil (118.54 kJ/mol) and its biodiesel (48.08 kJ/mol) applying different methods. Oliveira *et al.* [215] reported ΔH values of for palm (90.53 kJ/mol) and babassu (80.38 kJ/mol) oil biodiesel. Additionally, ΔS and ΔG at T_o and T_{max} for RSO and ROME are evaluated and are presented in Table 4.11. The negative values of ΔS and positive values of ΔG confirm that the thermal decomposition of both the samples are non-spontaneous process [170, 171, 212, 215]. This was expected since the samples were subjected to forced thermal decomposition by non-isothermal conditions. The absolute values of ΔS indicate that higher energy is required to reduce the degree of disorder at T_o as

compared to disorder degree at T_{max} for RSO-I, RSO-II and ROME (Table 4.11). The higher value of ΔG reveals lower favorability of a reaction [170, 171, 212, 217, 218]. The favorability order for thermal degradation process of RSO and ROME were found to be 145.01–201.37 kJ/mol and 115.73–152.19 kJ/mol, respectively. Higher value of ΔG for RSO indicates that larger amount of heat is required for thermal decomposition as compared its biodiesel, which is similar with the average values activation energy (*E*).

Table 4.11: Thermodynamic parameters of RSO and ROME samples at T_o and T_{max} for heating rate of 10 °C/min

Sample	Temp(°C)	Log A(1/sec)	ΔH (kJ/mol)	ΔG (kJ/mol)	ΔS (kJ/mol K)
	T_o =223	4.89	+63.75	+145.01	-163.82
RSO-I	T_{max} =271	5.67	+78.02	+159.41	-149.62
	T_o =353	7.46	+122.33	+195.35	-116.64
RSO-II	T_{max} =416	11.83	+178.11	+201.37	-33.76
	T_o =120	1.01	+22.89	+115.73	-236.22
ROME	T_{max} =250	7.2	+89.44	+152.19	-119.97

4.8. Summary

In the present work series of chemical modifications viz. esterification and transesterification was carried out for free fatty acid and triglyceride present in the rubber seed oil. Optimization studies of ultrasonic assisted conversion of RSO to ERSO during esterification process and ERSO to ROME during transesterification process was conducted at 30 °C. Three process parameters; catalyst loading, reaction time and molar ratio of methanol to oil were studied for both the processes. The esterification process with homogeneous acid catalyst was able to reduce acid value of RSO from 24 to 2 mg KOH/g and esterified oil was found to contain 17.65% transesterified product (ROME). The BET result show that the total pore volume, average pore size was in the following order; $Ba(OH)_2 \cdot 8H_2O$ > CL-egg shell > CaO > Na_3PO_4. Under similar transesterification condition, the catalytic activity of $Ba(OH)_2 \cdot 8H_2O$ was much better than the other tested catalysts. XRD analysis confirms that calcination temperature had a significant impact on both the crystallite size and crystal phase. The lower conversion of ERSO in case of a calcinated $Ba(OH)_2 \cdot 8H_2O$ catalyst compared to non-calcinated, may be due to lower crystallite size, pore diameter and total pore volume. The catalyst calcination temperature of, 400 °C showed significantly higher conversion for ERSO compared to 800 °C. This could be due to the better surface properties of catalyst calcinated at 400 °C. The results of transesterification process revealed that calcination reduced the catalytic activity of $Ba(OH)_2 \cdot 8H_2O$ and, caused lesser conversion in the following order; non-calcinated (97%) > calcinated at 200 °C (94.83%) > calcinated at 400 °C (92.96%) > calcinated at 800 °C (19.05%).

Non-conventional techniques (ultrasonic-assisted), such as an ultrasonic horn (UH) and ultrasonic cleaner (UC) enhance the rate of transesterification reaction as compared to

conventional transesterification (mechanical stirring technique) with similar reaction parameter. Therefore, a detailed study is required to address the issues of heterogeneous base catalysts in terms of their ability to tolerate the higher acid value of feedstock, stability, durability, reusability and leaching of the catalyst. For ultrasonic-assisted transesterification (ultrasonic horn reactor configuration) process with $Ba(OH)_2 \cdot 8H_2O$ catalyst, the optimum values of parameters for the highest conversion (97%) of transesterification have been determined as follows: 13.20 min at 5.38 wt% catalyst loading and 8.01:1 molar ratio using response surface methodology (RSM) with central composite design (CCD). The developed second-order model equation could able to predict response function based on the input parameters. The model can be employed for a large scale synthesis of methyl ester to predict the conversion of RSO, before carrying out heterogeneous base catalyzed transesterification to save time and maximize RSO conversion at various conditions within the range studied.

The present chapter also summarizes the thermal stability and decomposition of RSO and its methyl esters (ROME) under an inert atmosphere. The thermal stability of RSO was greater than that of its biodiesel. The rate of maximum weight loss (w_{max}) was increased from 12.1 wt%/min to 76.7 wt%/min (RSO) and 15.9 %/min to 76.2 wt%/min (ROME) as the heating rate increased from 10 °C/min to 50 °C/min. Similarly, the active thermal degradation temperature range was also shifted from 223 °C–471 °C to 264 °C–488 °C (RSO) and 120 °C–407 °C to 193 °C–480 °C (ROME). The activation energy (E) and enthalpy (ΔH) of RSO calculated by several methods (FRD, FWO, MCR and KM) were greater than that of ROME and the positive values of ΔH reveals that thermal decomposition of RSO and ROME is an endothermic reaction. The average order of reaction obtained using Avrami theory was found to be 1.14 and 0.69 for RSO and ROME, respectively. The order of thermal decomposition

favorability (ΔG) for RSO and ROME was 145.01–201.37 kJ/mol and 115.73–152.19 kJ/mol, respectively. Furthermore, the positive value of ΔG and the negative value of ΔS at initial (T_o) and maximum (T_{max}) indicates that thermal decomposition of RSO and ROME is a non-spontaneous process. Lesser average activation energy (E) and enthalpy (ΔH) of ROME is an indication of better combustion properties than that of RSO. Alkanes, alkenes, aldehydes, ketones, ethers, water, carbon dioxide and carbon monoxide detected in the evolved products during TGA-FT-IR. However, the absorbance of water was not detected in ROME which shows the quality of produced ester from RSO.

Finally, the prepared ROME was characterized as per ASTM standard methods and found suitable for blending with diesel and/or direct uses in engine. Hence, further detail investigation are incorporated in the next chapter (chapter V) to addresses the suitability of produced biodiesel in an existing diesel engine.

CHAPTER V

Estimation of Rheological Properties (RSO, ROME and blend), Engine Performance and Emission Characteristics of ROME with Diesel Blends

Physico-Chemical Properties Blends;

Rheological Behaviour;

Engine Test for Blends

Part of the Work Published:

Reshad *et al.* (2015), Rubber Seed Oil Methyl Ester Synthesis, Engine Performance and Emission Characteristics of Blends, **Energy & Fuels** 2015, 29 (8), 5136–5144.

Chapter V

Estimation of Rheological Properties (RSO, ROME and blend), Engine Performance and Emission Characteristics for ROME with Diesel Blends

This chapter is focused to evaluate the rheological (viscosity, shear stress, shear rate) properties and compare the physico-chemical properties of rubber seed oil (RSO), rubber seed oil methyl ester (ROME) and its blend with diesel fuel. Flow behaviour of oil (RSO), methyl ester (ROME) and blend of methyl esters with diesel fuel were investigated and tried to fit with Power Law rheological model. Further, the chapter elaborates about the engine performance and emission characteristics of blends with diesel fuel.

5.1. Physico-Chemical Properties of RSO, ROME, Diesel and Blends

The physico-chemical properties of RSO and ROME are discussed at more length in chapter III and IV. The physico-chemical characteristics of RSO, ROME and ROME-diesel blends were estimated as per ASTM standard methods and are presented in Table 5.1. The quality of oil can be expressed in terms of physico-chemical properties, for example, the acid value of the oil determines the process of transesterification [137]. The acid value of RSO was found to be 24 mg KOH/g. The acid value of RSO was also higher than crude *pangium edule* oil (19.62 mg KOH/g of oil) [141] and crude *ceiba pentandra* oil (16.8 mg KOH/g of oil) [139]. The acid value of methyl esters viz. ROME was found to be 0.4 and it was higher than *jatropha curcas* methyl ester (0.28 mg KOH/g of oil) and palm oil methyl ester (0.08 mg KOH/g of oil) [181]. The specific gravity value of tested oil was found to be 0.91 (RSO) and the value was decreased after

transesterification reaction and obtained results are 0.883 (ROME). Similarly, kinematic viscosity (40 °C) of RSO (13.13 mm^2/sec) was reduced to 3.81 mm^2/sec (ROME) through a transesterification process which was within the range of ASTM standard of biodiesel. Calorific values of produced oils, methyl esters and blends were measured using oxygen bomb calorimeter and the obtained results were within ASTM standards. The energy content of both oil and methyl esters; RSO (39.34 MJ/kg) and ROME (39.53 MJ/kg were comparable with diesel (44.29 MJ/kg). Flow characteristic of the samples was observed under low temperature using differential scanning calorimeter (DSC). The phase transition point from DSC profile was used to estimate the cloud and pour point. The obtained results for the RSO and its methyl esters are presented in Table 5.1. Flash point and fire point are important properties of fuel to measure flammability of fuel, safer storage and use in the transportation sector [54, 219]. The flash point of the produced methyl esters was comparatively higher than diesel fuel which show that biodiesel is safer for storage.

Table 5.1: Comparisons of important physico-chemical properties of various vegetable oils, FAME and blends of FAME with diesel

Oil	Fuel	Density (Kg/m^3)	Specific gravity	Cloud point, ^0C	Pour point, ^0C	Flash Point, ^0C	Fire point, ^0C	Kinematic viscosity,mm^2/sec	Calorific value, MJ/kg	Ref.
	D ASTM	864	0.846	–35–15	–15–5	52–96	N/D	1.9–4	42–46	
	B-ASTM	860–900	0.86–0.9	–3–12	–15–10	100–170min	N/D	1.9–6	35min	
Rubber seed	RSO	911	0.8991	6.5	2.13	273	282	30	39.34	In this study
	ROME	883	0.8705	4	-3	131	146	3.81	39.53	
	RD15	861.2	0.8518	6	1.5	69	85	2.16	41.4	
	RD10	854.5	0.846	6	1.5	67	82	2.12	42.1	
	RD5	854.1	0.846	7	2	66	67	2.1	42.8	
	RD0	852.5	0.8408	7	2.5	60	66	1.98	44.29	
CP[£]	CPO	905.2	N/S	N/S	N/S	N/S	N/S	34.45	N/S	Silitonga *et al.*[28]
	CPOME	876.9	N/S	3	2.8	156.5	N/S	4.61	40.293	
	CPOME50	864.5	N/S	2.5	2	94.5	N/S	4.02	40.591	
	CPOME30	855	N/S	2	2	85.5	N/S	3.66	42.858	
	CPOME20	854	N/S	1.6	0	82.5	N/S	3.58	43.15	
	CPOME10	851.3	N/S	1	0	81.5	N/S	3.51	44.474	
JC[€]	JCOME	864	N/S	5.8	3	160.5	N/S	4.48	40.224	
	JCOME50	860.6	N/S	N/S	N/S	94.5	N/S	4.12	42.117	
	JCOME30	851.2	N/S	N/S	N/S	84.5	N/S	4.02	43.859	
	JCOME20	845.2	N/S	N/S	N/S	82.5	N/S	3.75	44.249	
	JCOME10	839.9	N/S	N/S	N/S	82.5	N/S	3.61	45.25	

CPO: crude *ceiba pentandra*, CPOME, JCOME: *ceiba pentandra* oil, Jatropha *curcas* oil methyl esters, [£] *ceiba pentandra* oil, [€] Jatropha *curcas* oil

Continued…..

Palm	POME	875	N/S	10.5	10.5	156.5	N/S	4.45	40.151	Silitonga *et al.*[28]
	POME50	858.1	N/S	N/S	N/S	92.5	N/S	3.89	40.146	
	POME30	857.9	N/S	N/S	N/S	83.5	N/S	3.64	40.901	
	POME20	854	N/S	N/S	N/S	77.5	N/S	3.58	42.483	
	POME10	844	N/S	N/S	N/S	75.5	N/S	3.51	44.913	
	Diesel	839	N/S	2	1	71.5	N/S	2.91	45.825	
CMO[#]	CMME	869.7	N/S	–4	–3	178.5	N/S	4.0565	39.534	Atabani *et al.*[17]
	CMME20	835.6	N/S	5	0	86.5	N/S	3.5023	44.23	
	CMME10	831.2	N/S	6	0	83.5	N/S	3.4675	44.90	
	CMME0	827.2	N/S	8	0	68.5	N/S	3.2333	45.304	
CIO[*]	CIME	877.4	N/S	10	11	93.5	N/S	5.7499	39.273	
	CIME20	843.3	N/S	8	1	73.5	N/S	3.6105	44.065	
	CIME10	838.8	N/S	8	1	72.5	N/S	3.4066	44.578	
Coconut	COME	866.4	N/S	0	–4	120.5	N/S	4.607	38.006	
	COME20	841.3	N/S	7	–15	76.5	N/S	3.3427	43.748	
	COME5	838.1	N/S	7	0	74.5	N/S	3.7862	44.532	
	Diesel	827.2	N/S	8	0	68.5	N/S	3.2333	45.304	
Pangium edule	PEME	871	N/S	–6	–4	N/D	N/S	5.2296	39.625	Atabani *et al.*[141]
	PEME20	843.2	N/S	6	–3	79.5	N/S	3.5278	44.082	
	PEME15	842.2	N/S	6	0	76.5	N/S	3.4481	44.412	
	PEME10	840.4	N/S	8	0	74.5	N/S	3.3467	44.634	
	PEME5	838.5	N/S	7	0	73.5	N/S	3.2759	44.907	
	PEME0	827.2	N/S	8	0	68.5	N/S	3.2333	45.272	

POME, CMME, CIME, COME and PEME: Palm oil, *Croton megalocarpus*, *Calophyllum inophyllum*, Coconut and *Pangium edule* methyl esters respectively. [#]*Croton megalocarpus* oil, [*]*Calophyllum inophyllum* oil

5.2. Rheological Properties

Internal flow property of methyl esters is important fuel property which depends on the fatty acid composition of parent oil. It is one of the important characteristics and should be within pre-established limits. The viscous property of vegetable oil and biodiesel exerts a great influence on the fluid dynamic properties of fuel such as fuel circulation and fuel injection during the engine operation [220]. The dynamic viscosity of RSO and its methyl esters shows approximately a similar flow pattern within shear rate range of 5–300 1/sec which could be characterized by nearly constant dynamic viscosity. Similar observation for WCO and its methyl esters was reported by Borugadda and Goud [221]. Further, the plots of shear stress versus shear rate at 25 °C shows a straight line with R^2 greater than 0.999 for all tested samples (Fig. 5.1A). Furthermore, flow behaviours of the tested samples were analyzed using power law model (Eq. 5.1) [222].

$$\tau = k\gamma^n \tag{5.1}$$

Where, τ is a shear stress (Pa), γ is shear rate (1/sec), n and k are the power law coefficients and they can represent resistance to the flow of the fluid. k is a flow consistency index (Pa. s^n) and n is called as a non-Newtonian flow behaviour index (dimensionless), n and k value were estimated from the linearization of a power law equation. Plots of $\ln\gamma$ vs. $\ln\tau$ should be a straight line with slope n and intercept, $\ln k$ (Eq. 5.2).

$$\ln\tau = \ln k + n\ln\gamma \tag{5.2}$$

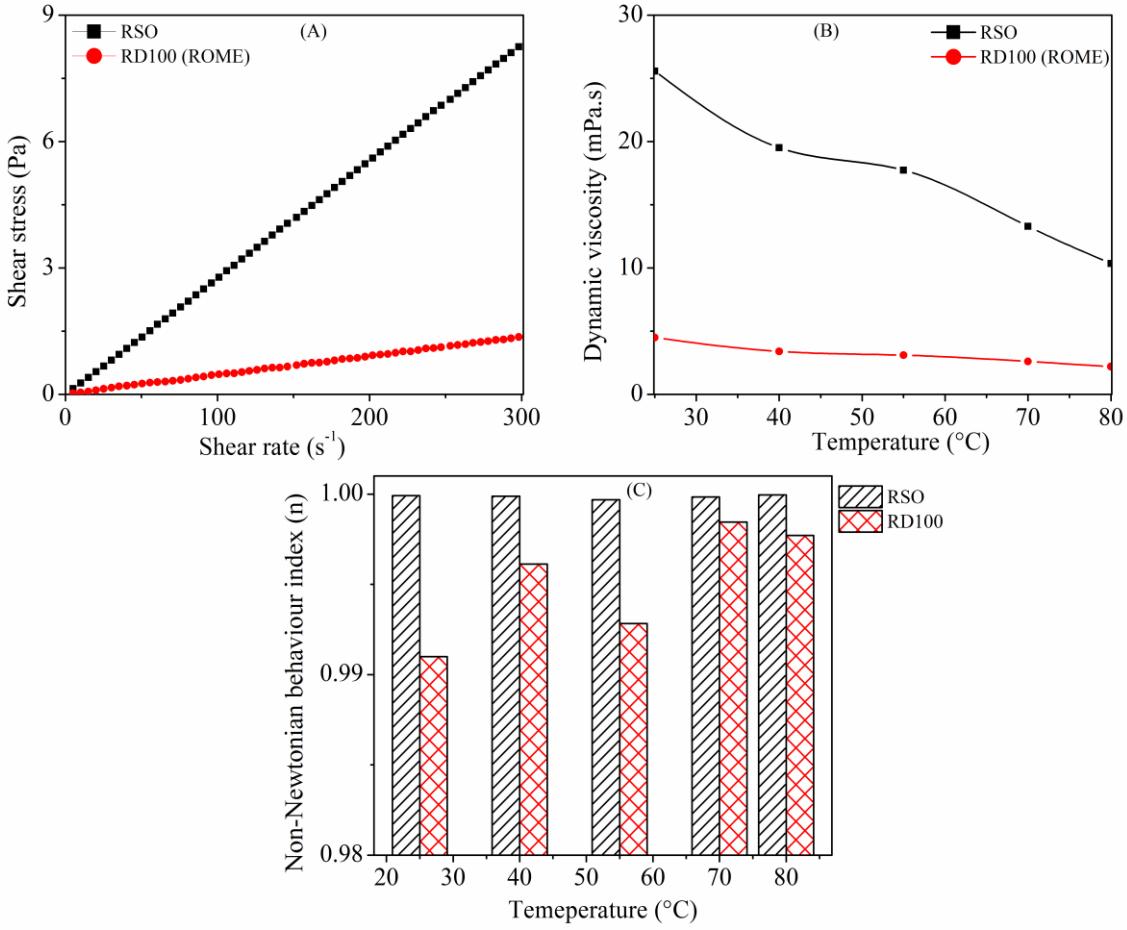

Fig. 5.1: (A) Plot of shear stress versus shear rate of samples at 25 °C and (B) effect of temperature on dynamic viscosity and (C) effect of temperature on flow index (n)

5.2.1. Viscosity Behaviour of RSO, ROME and Diesel

The rheological properties of RSO, ROME and diesel at 25 °C, 40 °C, 55 °C, 70 °C and 80 °C are presented in Fig. 5.1 and 5.2. The higher deviation of non-Newtonian flow behaviour index (n) value from unity (1), the higher deviation of the fluid from Newtonian behaviour [220, 223]. Non-Newtonian flow behaviour index (n) for RSO and diesel were found to be approximately unity (1) and also the variation of dynamic viscosity with shear rate for particular temperature was less than 1% which describes Newtonian fluid behaviour [49]. Similarly, Maskan *et al.* [224] and Gloria, Aguilera [225] reported that other vegetable oils showed Newtonian flow behaviour due to the long chain molecule of oils. Average dynamic viscosity obtained from experiment and power law model (i.e. flow consistency index or viscosity) were found to be in good agreement and shown in Table 5.2. The flow consistency index (mPa.s^n) of RSO was found to be 25.58 mPa.s^n. The chain length of fatty acids of triglyceride and unsaturation of RSO is the primary cause of the higher viscosity. It was found that viscosity increases with the chain length of fatty acids of triglyceride and decreases with an increase in the unsaturation. So it can be stated that viscosity is a function of dimension of molecules and orientation [226]. The flow behaviour results revealed that RSO has higher viscosity than that of diesel fuel. As a result, direct use of RSO as diesel engine fuel is not practical and can cause a short and long term problem to engine operations such as plugging and gumming of filters, injectors and engine knocking, coking of injectors, carbon deposits, and a failure of an engine [6, 50].

Table 5.2: Rheological properties (k, k_{exp} and n) values of RSO, ROME and its blends with diesel at 25 °C

	RSO	ROME	RD15	RD10	RD5	Diesel
Shear rate (1/sec)	5–300	5–300	5–300	5–300	5–300	5–300
k ($mPa.s^n$)	25.58	4.48	2.80	2.50	1.93	1.72
k_{exp} (mPa.s)	27.49	4.64	2.99	2.59	2.27	1.95
n (–)	0.9999	0.9910	0.9909	0.9988	0.9991	1.005
R^2	0.999	0.997	0.999	0.9967	0.999	0.999

k_{exp}: average dynamic viscosity obtained from experiment, k: flow consistency index obtained from a power law model, RDXX (XX vol% of ROME in diesel)

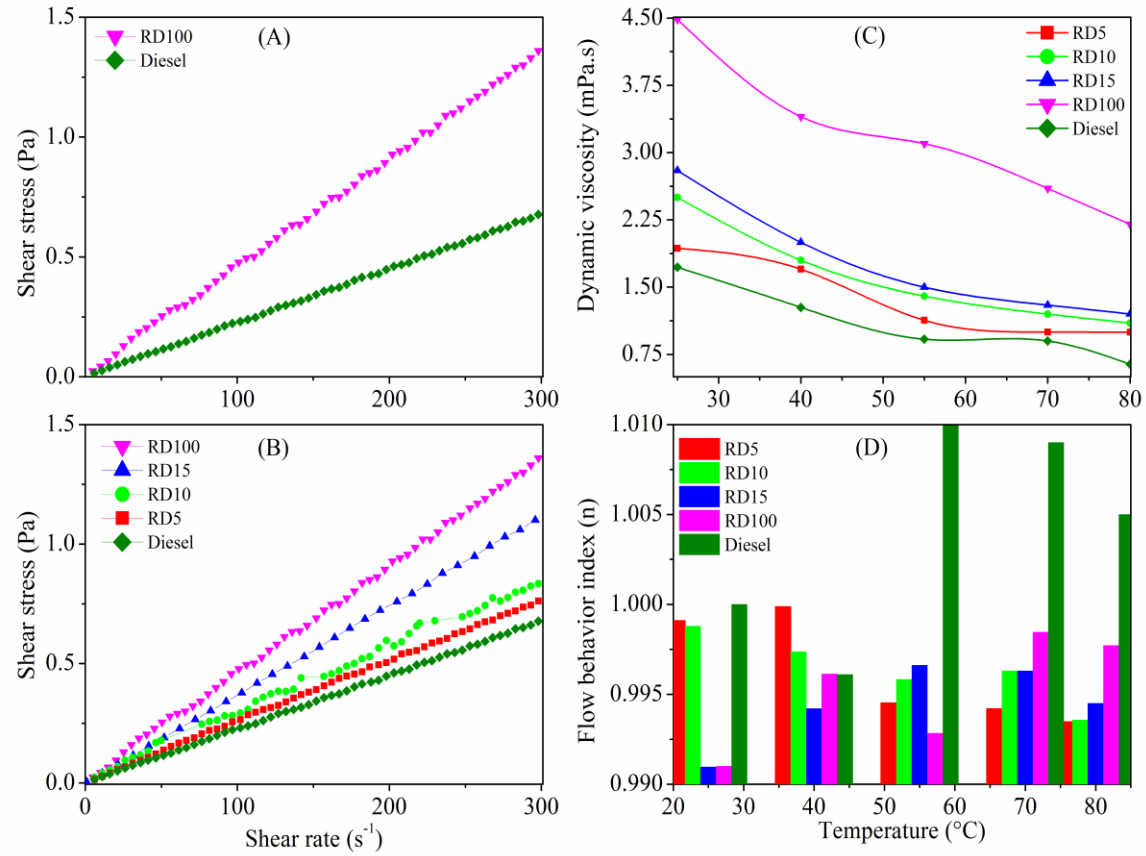

Fig. 5.2: Plot of shear stress versus shear rate at 25 °C: (A) for ROME (RD100) and diesel (B) for blend and (C) effect of temperature on dynamic viscosity (k), (D) effect of temperature on flow index (n)

Chemical modification of vegetable oil by esterification and transesterification reaction is one of the ways to reduce the viscosity and improve the other physico-chemical properties of vegetable oils (Table 5.1). Therefore, methyl esters (biodiesel) obtained from RSO found to have lower viscosity than the raw oil. This is due to the reduction of high molecular weight esters of glycerol present in oil samples into straight chain methyl esters by the transesterification process. In the present work methyl esters content of transesterified RSO was found to be greater than 90%. The rheological behaviours of ROME at varies

temperatures are presented in Fig. 5.1B and Fig. 5.1C. From the graph it can be observed that shear stress is directly proportional to shear rate with intercept near to zero (0) and, R^2 close to unity (1) for ROME. Non-Newtonian flow behaviour indexes for the methyl esters are presented in Fig. 5.2D. It is seen that flow behaviour indexes (n) are very close to unity (1) for ROME and a similar result was found for the parent feedstock (RSO) (Fig. 5.1C). The non-Newtonian flow behaviour index of unity (1) indicates the Newtonian behaviour of the sample. Dynamic viscosity of methyl esters obtained by a power law model agrees well with experimental results. A similar observation has also been seen for methyl esters blends with diesel fuel (Table 5.2). From Table 5.2, it can be also seen that 82.15% viscosity reduction was obtained for ROME as compared to RSO at 25 °C. However, the obtained dynamic viscosity of all the produced methyl ester are higher as compared to diesel fuel. Thus, the blends of ROME with diesel fuel at different proportion are considered for further flow behaviour study.

Blending of methyl ester in right proportion with diesel fuel results in reduced environmental problems and smooth engine operation [18, 227, 228]. Rheological behaviour of ROME-diesel blends at various proportions such as 5, 10, and 15 vol% were investigated. The rheological behaviour of diesel does not change after blending of ROME at shear rate range of 5–300 1/sec. Power law model also showed good fit for blend with R^2 value close to unity (1) (Table 5.2 and Fig. 5.2D). Non-Newtonian flow behaviour indexes (n) for 5, 10, and 15 vol% blend were obtained in Newtonian range. It can be seen from Fig. 5.2 (B–C) that blending of 5–15 vol% of ROME in diesel found to reduce its dynamic viscosity compared to native methyl esters (ROME). The dynamic viscosity of blends was found to be increased with higher methyl esters content for all tested proportion of methyl esters. This attributed to

molecular mass, intermolecular force and its polarity [6, 208, 229, 230]. The dynamic viscosity measurements in the preset are found to be in good agreement with literature reported data [208, 229].

5.2.2. Effect of Temperature on Viscosity of Tested Samples

Flow behaviours of RSO was also observed as a function of temperature (Fig. 5.1B). As it can be seen from Fig. 5.1B and Fig. 5.2C, all tested samples exhibits a similar viscosity pattern over the temperature range of 25 °C to 80 °C, and found to decrease non-linearly with increased temperature. This mainly attributed to decreased in intermolecular interaction with increase temperature. Dynamic viscosity of RSO was found to decrease from 25.58 mPa.s to 10.36 mPa.s with an increase in temperature from 25 °C to 80 °C. The changes in dynamic viscosity refer to the flow behaviour of RSO are dependent on temperature. As temperature increased from 25 °C to 80 °C, the dynamic viscosity of ROME and diesel fuel decreased from 4.485 mPa.s and from 1.72 mPa.s to 2.2 mPa.s and 0.641 mPa.s, respectively. The flow behaviour of the blend (5 vol%, 10 vol% and 15 vol%) are found same as that of the tested diesel fuel for the temperature range of 25 °C–80 °C. The dynamic viscosity of blended fuels also showed non-linear behaviour with respect to temperature. At 80 °C the dynamic viscosity of methyl esters blend (10 vol% and 5 vol%) were comparable with the dynamic viscosity of diesel fuel (Fig. 5.2 (B–C)). Similar trend was observed for other oils such as canola, corn, olive, peanut, soybean, egusi and sunflower oils [49, 231, 232].

5.3. Performance of DI Engine

Engine performance parameters such as brake power (BP), brake thermal efficiency

(BTE), specific fuel consumption (SFC), volumetric efficiency (η_{vol}) and exhaust gas temperature were estimated. The complete combustion analysis including heat release rate, maximum peak pressure, ignition delay, combustion duration and characterization of emissions were also studied. The performance analysis was conducted on the constant speed 1500±50 rpm engine which resulted in a linear relationship between the brake power obtained and load applied (Fig. 5.3A) [233, 234]. The brake specific fuel consumption (BSFC) was evaluated from the mass of the fuel consumed per unit brake power (Fig. 5.3B). As the brake power produced increased with an increase in load, the mass of fuel consumption also increased, but this increase was substantially lower than that of the increase of brake power. This is because the increase in load on the engine reduces BSFC [228]. No substantial change in BSFC for all RDXX sample with respect to diesel fuel was observed at 20% load. At 40% load, 11% reduction in BSFC was observed. This reduction of BSFC was continuous with a rise in load. At maximum load BSFC for blend showed little increase by 2% than that of diesel fuel. Overall 5% reduction in BSFC was obtained with various blends. RD10 was found to be the most suitable composition for lowest BSFC having 393 g/kW-hr which was 13% lower than that of diesel fuel throughout the load range. Similar observation was found by Mahanta *et al.* [235]. The calorific value of RDXX blend was lower as compared to diesel fuel but more oxygenated compared to diesel fuel which improves the combustion quality and improved BSFC [228, 236-238].

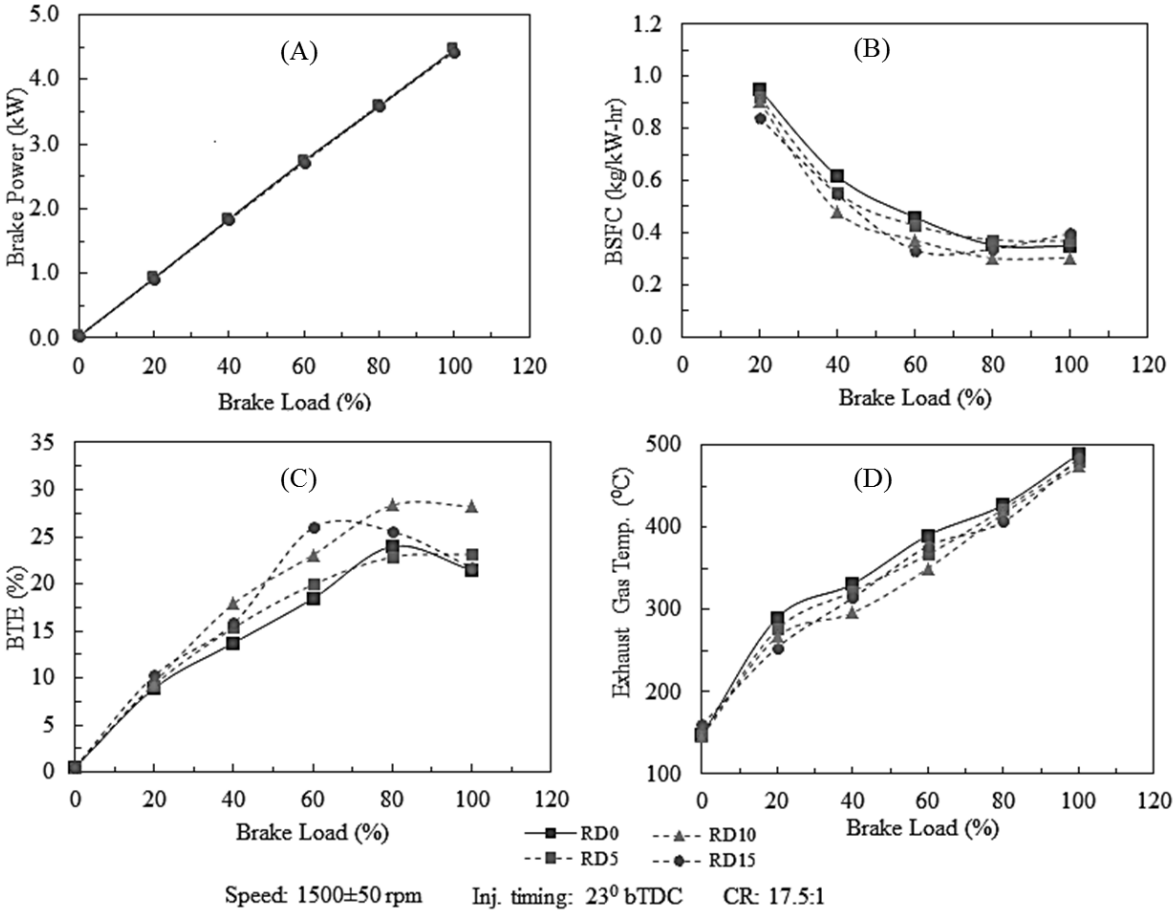

Fig. 5.3: Engine performance analysis (A) brake power variation with load, (B) brake specific fuel consumption variation with load, (C) brake thermal efficiency variation with load and (D) exhaust gas temperature variation with load

The brake thermal efficiency at 20% brake load showed rise of 7% and 15% for RD10 and RD15, respectively over baseline diesel fuel (Fig. 5.3C). The rise in BTE continued with a rise in load showing a maximum 32% rise for RD10 at 100% load with the overall increase of 13% using various blends combustion for the complete range of load. At 80% load, the maximum BTE of 28.36% was obtained for RD10 among all the tested fuels which was 23% higher than that of diesel fuel at same load conditions. This happened due to more oxygenated biodiesel fuel supply during the combustion process and additionally the lubricity property of

biodiesel help to improve the efficiency [228]. A remarkable decrease in exhaust gas temperature (EGT) was observed over the complete load range when the engine was run with RDXX (Fig. 5.3D). The lower calorific value, poor atomization rate and poor volatility of biodiesel blend produces lesser temperature at the end of combustion [55, 239]. At 20% load, the EGT recorded was 267 °C and 254 °C for RD10 and RD15, respectively which was correspondingly 8% and 12% decrease compared to diesel fuel (290 °C). Reductions in EGT for RD10 and RD15 at full load were found to be 3% and 1%, respectively. The overall 6% and 4% reduction in EGT was observed with the use of RD10 and RD15 blends, respectively. For RD5, no remarkable improvement was observed.

The comparison of pressure-crank angle variation for each of the tested fuel modes are shown in Fig. 5.4A for different engine loads. The combustion was smooth with no sign of misfire (knocking). Biodiesel blends produced maximum pressure of 77.16 bar, 75 bar and 75.29 bar at RD5, RD10 and RD15, respectively which was 72.50 bar with diesel fuel. A rise of average 4% in the maximum pressure for biodiesel blends was observed due to lower compressibility of biodiesel which helps the fuel pumped quickly, higher sound velocity for the supply of fuel towards injector and higher viscosity which reduces leakage in the injector [240]. The trend of increase in pressure under biodiesel blends was mild up to 40% load and found to be less than that of diesel fuel (Fig. 5.4B). Beyond 40% load condition, these trends showed intense degree of pressure rise at a higher temperature operating zone. The cylinder pressure showed substantial increase for all biodiesel blend fuels with respect to diesel fuel due to rise in a load on the engine, more force was required on the piston to produce the power. This force was in the form of cylinder pressure acting on the cross section area of the piston [142].

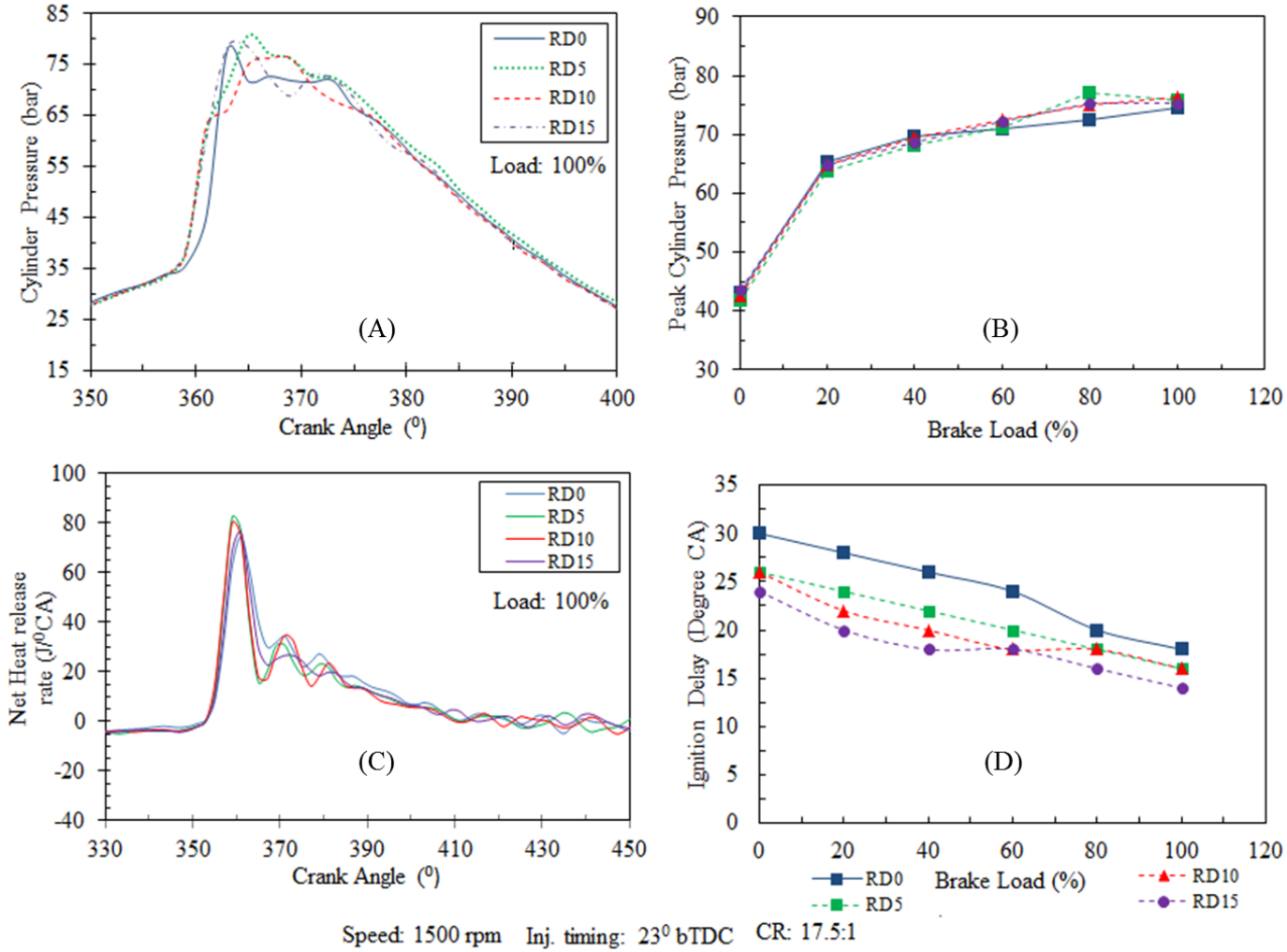

Fig. 5.4: Combustion analysis; (A) cylinder pressure variation with crank angle, (B) peak cylinder pressure variation with load, (C) net heat release rate variation with crank angle and (D) ignition delay variation with load

The net heat release rates are shown in Fig. 5.4C. At a low combustion temperature condition of up to 40% load, the reduction in heat release rate was only 12% with respect to diesel fuel. As load increased, the heat release rate was improved at 100% load and a maximum heat release rate of 82.323 J/^{0}CA, 80.100 J/^{0}CA, and 76.540 J/^{0}CA was found for RD5, RD10 and RD15, respectively as compared to 74.472 J/^{0}CA for diesel mode. As the combustion in all cases was performed at fixed injection timing 23^0 bTDC and the maximum heat release rate was found to be at around 359 ^{0}CA in all cases. The micro-explosion [234] small ignition delay responsible for the rise in cylinder pressure which ultimately results in the net heat released by the biodiesel blend fuel air mixture was more than that of diesel fuel combustion. Fig. 5.4D shows that the increase in both load and ROME concentration (RDXX) reduces ignition delay. With the increase in proportion of ROME in blend, the large amount of heat was absorbed to evaporate the fuel during combustion which reduces the engine temperature and ultimately raises the ignition delay. Rao *et al.* [144] reported a contradictory behavior stating that the oxygen content in the biodiesel improves ignition ability which is responsible for ignition delay. Based on the data collected, the computed performance parameter uncertainties are estimated and summarized in Table 5.3.

Table 5.3: Uncertainty associated with computed parameters

Computed parameters	Uncertainty
Brake power	± 0.9%
Brake thermal efficiency	± 1.52%
Brake specific fuel consumption	± 1.14%
Net heat release rate	± 1.6%
Ignition delay	± 0.2%
Emissions	± 5%

5.4. Emission Analysis

The emission of various gases by combustion of blends is shown in Fig. 5.5. From no load to full load CO emissions for biodiesel blends was found lower by 32%, 30% and 35% for RD5, RD10 and RD15, respectively (Fig. 5.5A). Supplying a rich mixture to the engine at low load (temperature inside cylinder is less) and high load (requires more power) conditions causes incomplete combustion and releases more amount of CO [235]. At on load variation, 30% (average) drop in CO emissions was achieved with biodiesel blend than diesel. The higher oxygen content in the biodiesel increases the combustion efficiency by reducing loss of chemical energy unused in the engine [55, 235]. NOx emission increases with an increase in load on the engine because the temperature of combustion increases and also more fuel get supplied to the engine [241]. Up to 60% load conditions, NO_X emissions produced by biodiesel blend were found to be lower by 23%, 28% and 35% for RD5, RD10 and RD15, respectively (Fig. 5.5B). This is attributed to the higher content of oxygen and absence of aromatics in biodiesel [242]. At maximum load, NOx emission rise of 23%, 17% and 20% for RD5, RD10 and RD15, respectively with respect to diesel was obtained. This is due to rise in exhaust gas temperature at high load (Fig. 5.3D).

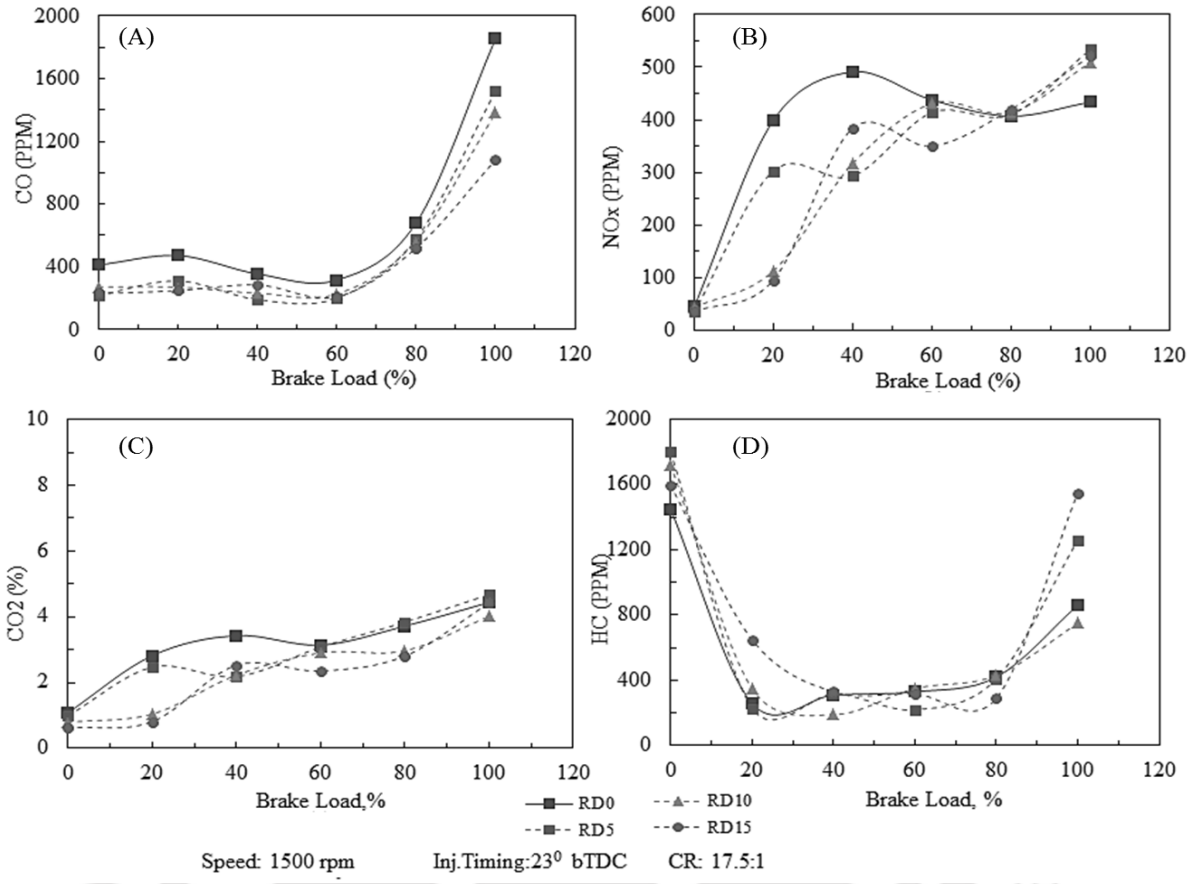

Fig. 5.5: Emission analysis with different blends (RDXX) at various loads; (A) CO emission, (B) NO_X emission, (C) CO_2 emission and (D) HC emission

Fig. 5.5C shows that diesel fuel produced more CO_2 at all loads than blends. Up to 60% load, CO_2 produced from RD0, RD5, RD10 and RD15 blends was 2.61%, 2.18%, 1.74% and 1.58%, respectively which increased to 2.69%, 2.67%, 2.18% and 2.20%, respectively with an increase in the load from 80 to 100%. This higher value of CO_2 emission by diesel was probably due to higher content of carbon in the diesel fuel compared to ROME (Table 5.1) [18, 54, 242]. In biodiesel blend hydrogen to carbon ratio is more than that of a diesel fuel which causes the lesser percent of CO_2 emission [54]. HC emission changes in descending and ascending order of the load as shown in Fig. 5.5D. HC emissions for biodiesel blend

found to be higher, especially during a low load and maximum load conditions. For the load condition from 40 to 80% the emissions for biodiesel blend were nearly equal or lower than that of diesel fuel. During low load condition, due to higher viscosity of biodiesel and a lower combustion temperature inside the cylinder fuel doesn't burn completely. Also at maximum load condition more fuel supplied to the engine is responsible for rising HC [243].

5.5. Summary

In this chapter, the physico-chemical properties and rheological behaviour of rubber seed oil (RSO) and its derivative methyl esters as well as blends with diesel fuel were investigated. Rheological properties of the sample were measured at a temperature from 25–80°C and shear rate from 5–300 1/sec. Similarly, rheological behaviour of produced rubber seed oil based methyl ester (ROME) and its blends (5 vol%, 10 vol% and 15 vol%) with diesel fuel were also studied. Chemical modification of the oil sample by transesterification was found to be decreasing rheological properties (viscosity). The power law model was used to investigate the flow behaviour of all the tested samples. The viscosity behaviour of oils (RSO), methyl ester (ROME) and ROME blend with diesel fuel were found to be nearly Newtonian behaviour. The dynamic viscosity of RSO was found to be 25.58 mPa. The dynamic viscosity of tested samples were found to be fatty acids chain length and temperature dependent. The estimated physico-chemical properties of ROME and its various blending with diesel (RDXX) were fulfilling the American Society for Testing and Materials (ASTM) standards. Maximum brake thermal efficiency (BTE) was achieved at 80% load with RD10 (28.36%) compared to neat diesel (24%) and a drastic improvement of overall 13% increase at all loads. Maximum

exhaust gas temperatures for biodiesel blends were found to be lower than neat diesel with a rise in pressure by about 4% which ultimately shows a slight improvement in the net heat release rate. The emissions of CO, CO_2 and NO_X were reduced with the use of ROME blends.

CHAPTER VI

Thermal Decomposition Kinetics and Production of Biofuel from Solid Waste (By-product) through Pyrolysis Process

Characterization of RSS and RSC;

Thermal Decomposition Kinetics;

Effect of Pyrolysis Temperature on Product Distribution;

Effect of Heating Rate on Product Distribution;

Co-pyrolysis of RSC and WPS

Characterization of Pyrolytic Products

Part of the Work Published and submitted to:

Reshad, A.S., Tiwari, P., Goud, V.V., 2017 Thermal Decomposition and Kinetics of Residual Rubber Seed Cake and Shell, **J. Thermal Analysis and Calorimetry** (DOI 10.1007/s10973-017-6136-4)

Chapter VI

Thermal Decomposition Kinetics and Production of Biofuel from Solid Waste (By-product) through Pyrolysis Process

This chapter is divided into three main sections such as characterization of RSS and RSC, kinetic parameters calculation for RSS and RSC thermal decomposition and pyrolysis of RSS and RSC in semi-batch reactor. Initially, the solid by-products (RSS and RSC) were characterized; further the non-isothermal decomposition kinetics at various heating rates is studied. The pyrolysis of RSS and RSC using a semi-batch reactor are investigated in detail. The effects of pyrolysis temperatures and heating rates on product distribution and calorific value of produced bio-char are also discussed in detail. The bio-oil yield and quality are enhanced through co-pyrolysis with waste polystyrene. Further, compositional analyses of the liquid and solid products are also investigated. For this purpose, Fourier transform infrared (FT-IR), proton Nuclear Magnetic Resonance (^{1}H NMR), gas chromatography with mass spectroscopy (GC-MS), thermogravimetric analysis (TGA), field emission scanning electron microscope (FESEM) with energy dispersive X-ray (EDX), ultimate analysis (CHNSO), proximate analysis, X-ray powder diffraction (XRD) are considered.

6.1. Characteristics of RSC and RSS

The solid wastes, both cake and shell are rich sources of lignocellulose (more than 90 wt%) than lipid (less than 5 wt%) [118, 119]. The solid waste can be exploited for the production of value added products through thermo-chemical means [21, 120]. The data

obtained from proximate, ultimate and calorific value analysis along with TGA based chemical compositions for RSC and RSS samples are summarized in Table 6.1. The total hydrocarbon contents (C and H) for RSK and RSC were found to be 62.962 wt% and 52.42 wt%, respectively. The value of hydrocarbon was measured as 58.47 wt% for RSS. The comparison of atomic ratios, H/C and O/C, on Van Krevelen diagram for different oil seeds [123, 127, 244, 245] and oil seed shells [128, 245, 246] with respective calorific values are summarized in Fig. 6.1. The molar ratios, H/C and O/C of RSK and RSC were found to be 1.843 and 0.452 for RSK, and 1.695 and 0.59 for RSC (Table 6.1) which fall within lignocellulosic biomass. Similarly, the molar ratios, H/C and O/C of RSS were measured as 1.485 and 0.551, respectively (Table 6.1) which fall within biomass region on Van Krevelen diagram. The ratios are consistent with carbon atom that is essentially saturated (due to the predominance of cellulosic material). RSS sample shown significant presence of moisture content (10.14 wt%) which may be responsible for slightly lower calorific value of the sample compared to RSC [143, 247]. The properties of parent material (RSK); carbon content (54.58 wt%) and calorific value (27.53 MJ/kg) may contributing for higher calorific value of RSC. Thus, calorific value obtained for RSC (19.58 MJ/kg) sample was found less compared to RSK (27.53 MJ/kg). This is due to the presence of higher extractive component in RSK (57.41 wt%). The calorific value of RSC (19.45 MJ/kg) was approximately close to the calorific value of rapeseed cake (19.49 MJ/kg) [248], sesame seed cake (19.78 MJ/kg) [122] and neem seed cake (18.2 MJ/kg) [122]. Similarly, the calorific value of RSS (18.93 MJ/kg) was equal to other seed shells reported in literature; palm seed shell (11 wt% moisture content) (18.85 MJ/kg) [128], castor seed shell (18.8 MJ/kg) [21]. The obtained ash content of RSC (6.64 wt%) was found to be lower than *Jatropha curcas L.* oil cake (8.07 wt%),

Pongamia pinnata oil cake (10.17 wt%) and *Mudhuca Indica* oil cake (14.63 wt%) [156]. Similarly, the ash content of shell (RSS) sample (0.24 wt%,) was found to be lower than pistachio shell (0.41 wt%) [153], M-RSS (Malaysia origin rubber seed shell) (3.81 wt%) [155] and palm kernel shell (11.08 wt%) [118].

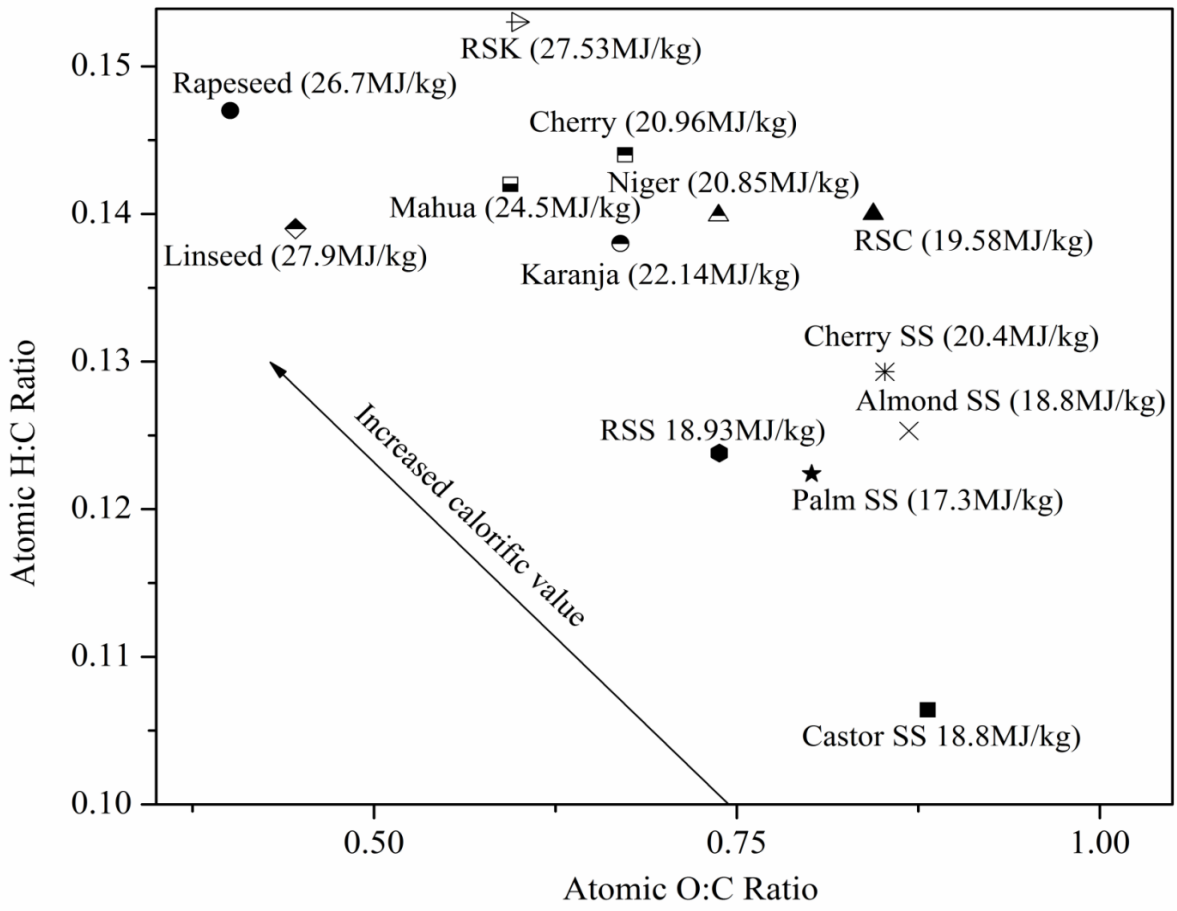

Fig. 6.1: Van Krevelen diagram for RSK, RSS, RSC and, other oil seeds and shells with calorific values

Table 6.1: Proximate, ultimate and compositional analysis of rubber seed shell and rubber seed cake

	RSK	RSC[(a)]			RSS[(b)]
Proximate					
Moisture content	8.49±0.16	2.58±0.06			10.10±0.12
Volatile matter [ζ]	90.98±0.12	82.85±0.51			76.36±0.71
Ash content [ζ]	3.79±0.09	6.64±0.11			0.24±0.04
Fixed carbon [ζ]	5.23±0.24	10.51±0.89			23.4±0.75
Residual mass[(c)]	2.98±0.15	5.6±0.89			0.8±0.05
HHV (MJ/kg)	27.53±0.25	19.58±0.22			18.93 ±0.13
Ultimate					
C	54.581	45.98			52.03
H	8.381	6.44			6.44
S	–	–			–
N	4.127	8.59			3.13
O[(d)]	32.911	38.99			38.4
Composition estimation using TGA					
Biomass	RSC	RSS	PC [152]	MSC [152]	JC[152]
Hemicellulose (250–350 °C)	29	31.92	–	–	–
Cellulose (350–500 °C)	27.32	30.01	13.24	27.99	15.31
Lignin (>500 °C)	20.3	25.39	18.45	14.91	23.79
VM and moisture[(d)]	23.37	12.68	68.31*	57.1*	60.9*
Extractive analysis (g of extractives per 100g of sample)	7.75 ±0.3	3.71 ±0.27	–	–	–

*[ζ] mass (%) in dry basis (moisture free), VM: Volatile matter, HHV: High heating value, [(a)]Rubber seed kernel after RSO extraction and evaporation of solvent used for RSO extraction, [(b)] Sun dried rubber seed shell [(c)] Residual mass at 800°C during TGA at rate of 10 °C/min under N_2 atmosphere, [(d)]Calculated by difference, *Including hemicellulose, PC, MSC and JC are pongamia, madhuca and jatropha oil cake, respectively.*

FESEM-EDX analysis (for inorganic elements) and XRD pattern (for crystallinity index) of RSS and RSC, and the obtained results are shown in Fig. 6.2 and Fig. 6.3, respectively. The biomass crystallinity depends on the content of extractives, wax, fatty acids, etc. RSS sample contains low amount of extractive, 3.53 wt% (Table 6.1) which resulted in lower value of crystallinity index (38.6%) compared to mahua seed (45.07%), niger seed (46.7%) and linseed (44.19%) [244]. Due to low moisture content [249], volatile matter and high calorific values [154] of RSS and RSC, these feedstocks are still suitable for bio-oil and bio-char productions [250]. The changes happened in solid phase (Fig. 6.2) during the pyrolysis of RSS and RSC samples are discussed in section 6.4 and 6.5.

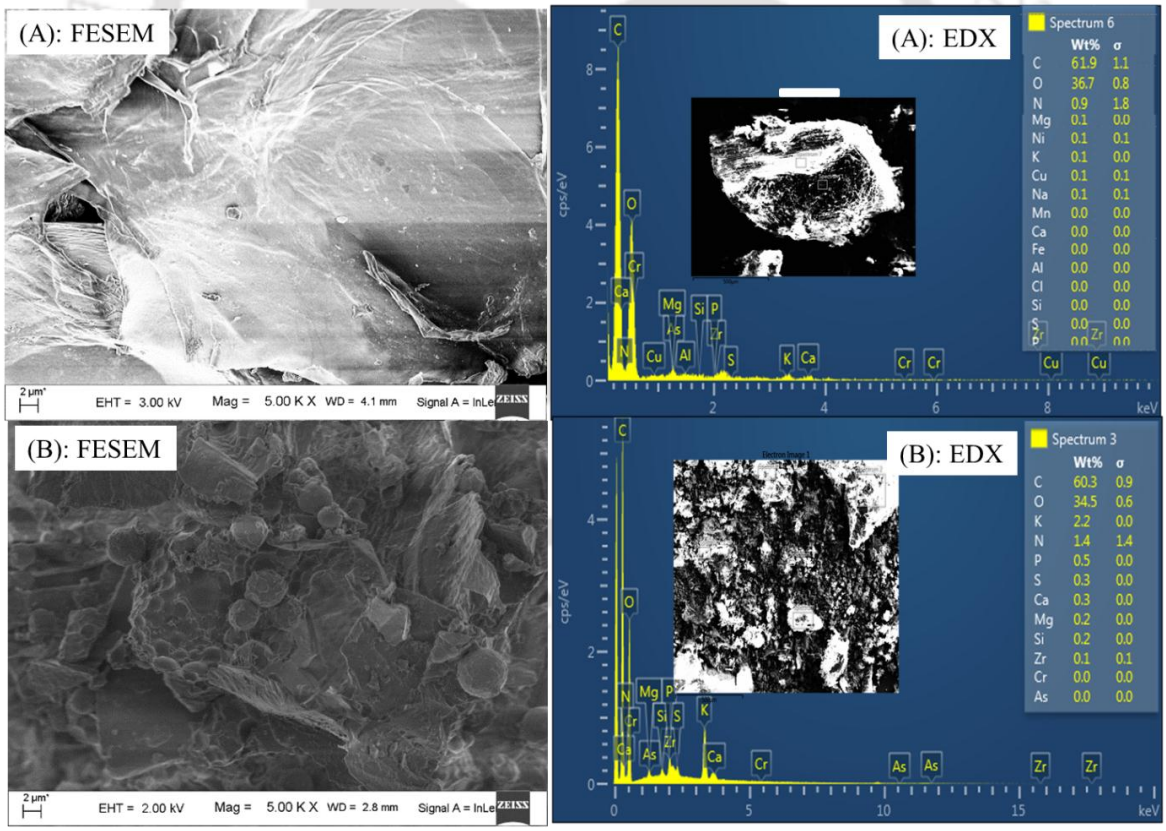

Fig. 6.2: FESEM-EDX analysis of (A) RSS and (B) RSC samples

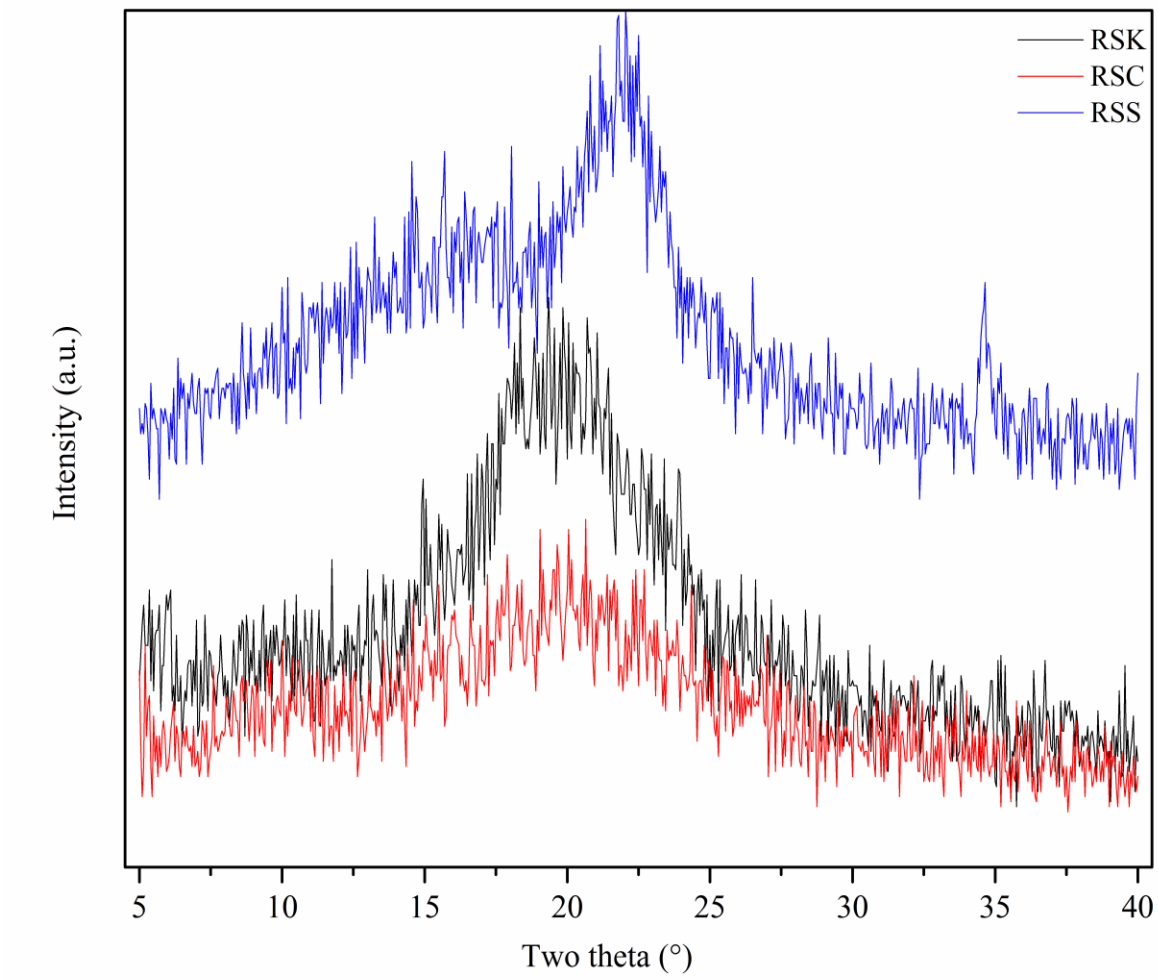

Fig. 6.3: XRD patterns for raw RSK, RSC and RSS samples

6.1.1. Thermogravimatric Analysis (TGA) for RSC and RSS

The thermal decomposition profiles of RSC and RSS are shown in Fig. 6.4. Every single slope change on a TG profile indicates the beginning of new stage [119, 156]. In the present study, thermal decomposition of the samples are classified as early (<200 °C) and active pyrolysis stages (Fig. 6.4). Early stage decomposition happens primarily due to water evaporation and, excluded for kinetic analysis. Active pyrolysis stage was subjected for kinetic analysis. Therefore, overall 4 stages were found for both the samples, RSC and RSS.

Active pyrolysis stages for RSC (stage II, III and IV) and RSS (stage IIa, IIb and III) were selected for kinetic analysis. The two split peaks of RSS (stage IIa and IIb), obtained within narrow temperature range of 265.2–341.79 °C and 341.79–391 °C were considered as single stage (stage II) for kinetic analysis. The mass fractions of RSC (~56 wt%) and RSS (~62 wt%) decomposed between 250 °C and 500 °C at heating rate of 10 °C/min were attributed to the degradation of hemicellulose, cellulose and other hydrocarbon compounds [13, 156, 251]. Higher decomposition of RSS than RSC is due to the higher amount of hemicellulose and cellulose present in RSS (Table 6.1). The rate of decomposition depends on the heating rates, and as the heating rate increases from 2 °C/min to 10 °C/min, all the peaks can clearly be distinguished (Fig. 6.4). From TG and its corresponding derivative of thermogravimetric (DTG) curve, the decomposition occurring in various stages can be established. For example, at heating rate of 10 °C/min, early decomposition (stage I) happened within the temperature range of 30–140 °C, and mass losses of RSS and RSC were found to be 7.03 wt% and 4.84 wt%, respectively. This mass loss attributed to physically absorbed water and volatile compound evaporation presented in the samples [252]. The active pyrolysis of RSC was mainly occurred in three stages; 175 to 357 °C (stage II), 367 to 492 °C (stage III) and 495 °C to 589 °C (stage IV) with overall mass loss of 83.26%. The thermal decomposition profile of RSS showed mainly two stage active pyrolysis (overall 79.21% mass loss); 265.2 to 391 °C (stage II) and 457.3 to 556.6 °C (stage III). The characteristic properties of TG profiles such as starting temperature (T_o), ending temperature (T_f), the temperature at which maximum mass loss rate occurred (T_{max}) and maximum mass loss rate (W_{max}) for active pyrolysis stages for all heating rates are summarized in Table 6.2. As heating rate increased from 2 °C/min to 10 °C/min the entire characteristic temperatures were shifted towards higher value of

temperature. This may be due to the duration (time-temperature relation) the material was exposed at different heating rates, which ultimately helped improving the effective heat transfer to inner portion of both RSC and RSS particle at lower heating rate [119, 152, 153, 155, 156]. The DTG curves at heating rate of 10 °C/min showed the maximum rate of mass loss at different stages for RSC; 3.74 wt%/min (stage II), 2.66 wt%/min (stage III) and 2.64 wt%/min (stage IV) at 287.8 °C, 410.4 °C and 548.8 °C, respectively. For RSS, these values were found to be 4.72 wt%/min (stage IIa), 5.66 wt%/min (stage IIb) and 6.22 wt%/min (stage III) at 310.8 °C, 361.4 °C and 530 °C, respectively. Temperature values at which 50% mass loss occurred (T_{50}) were found to be 367.54 °C and 361.84 °C for RSC and RSS, respectively. The value of R_{50} which measure the reactivity of biomass at its T_{50}, for RSS (5.66 wt%/min) was found to be higher than that for RSC (1.87 wt%/min). This is due to high hemicellulose content in RSS sample [249]. The obtained R_{50} values are within the range of reported results; between 1.5 wt%/min to 3.25 wt%/min at T_{50} temperature interval of 355 °C to 410 °C for different feedstock such as oil palm shell, oil palm frond, rice husk and paddy straw [253].

Table 6.2: TG characteristic properties for active pyrolysis stage of rubber seed shell and rubber seed cake samples

Biomass	Properties	β, °C/min								
		2			5			10		
		II	III	IV	II	III	IV	II	III	IV
RSC	T_o, °C	155	362	473	162	365	473	175	367	495
	T_f, °C	355	469	575	357	471	578	357	492	589
	Δwt, %	46.69	23.55	22.33	44.93	22.65	20.11	40.79	23.31	19.16
	T_{max}, °C	270.3	395.7	509.8	279.8	407.6	537.8	287.8	410.4	548.8
	w_{max}, %/min	1.88	1.47	1.67	2	1.45	1.42	3.74	2.66	2.64
RSS	T_o, °C	240	395.5	–	250.6	406	–	265.2	457.3	–
	T_f, °C	355.5	491.5	–	370.4	524.9	–	391	556.6	–
	Δwt, %	43.41	37.14	–	44.37	38.56	–	45.62	33.92	–
	T_{max}, °C	302.5	462.7	–	318.1	492.3	–	361.4	530	–
	w_{max}, %/min	1.25	2.31	–	2.52	2.47	–	5.66	6.22	–

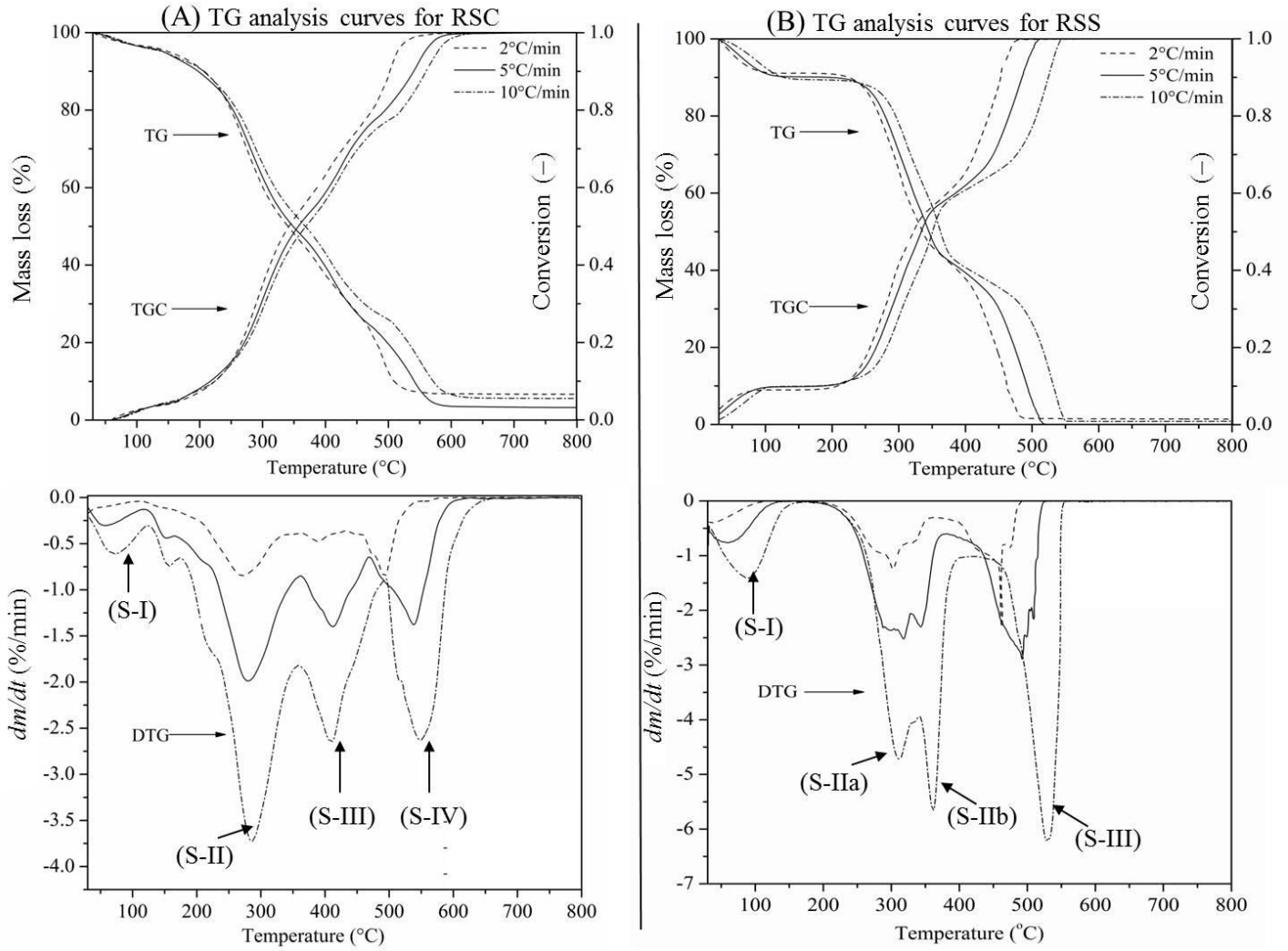

Fig. 6.4: TG profile of (A) RSC and (B) RSS obtained at different heating rates and mass loss used to generate the conversion profiles

6.1.2. Fourier Transforms Infrared (FT-IR) Analysis of Evolved Products from TGA

The gaseous products evolved during TG analysis of RSS and RSC samples were scanned using attached FT-IR unit at each degree temperature interval. FT-IR spectra of evolved gas products obtained at 50% weight loss for RSC and RSS, which represent the main decomposition, are presented in Fig. 6.5. The gaseous products such as CO_2, CO, CH_4, H_2O, ketones aldehydes, acids and other hydrocarbon were identified by their prominent characteristic bands (Table 6.3). The three substances corresponding to characteristic absorbance peaks at 2358, 1796 and 1180 cm^{-1} were dominant volatile components. CO_2 was formed via the decarboxylation reaction as well as due to the breakage of carbonyl groups which resulted in C=O stretching vibration band between 2400–2250 cm^{-1} [254]. Further, the C–H stretching band between 3060–2700 cm^{-1} indicates formation of CH_4 due to decomposition of methoxy ($–OCH_3$), methyl ($–CH_3$) and methylene ($–CH_2–$) group under high temperature [255]. The adsorption bands of H_2O at 4000–3400 cm^{-1} exist over entire temperature range, 167–699 °C, due to polycondensation of hydroxyl groups in the remained solid phase. The formation of organic acid was evidenced by the strong bands at 1786–1747, 1133 and 640 cm^{-1} [255]. The most significant band, O–H at 1300–01200 cm^{-1}, primarily corresponds to the phenolic compounds. The C–O stretching at 2250–2000 cm^{-1} was observed due to the presence of CO in the evolved gas. This result can be attributed to breakage of ether bonds [254].

Table 6.3: FT-IR analysis of evolved products during thermal decomposition of rubber seed shell and rubber seed cake

Species	Wavenumber (cm^{-1})	Functional groups	Vibrations
H_2O	4000–3400	O–H	Stretching
CH_4	3060–2700	C–H	Stretching
CO_2	2400–2250	C=O	Stretching
CO	2250–2000	C–O	Stretching
Aldehydes, Ketone and acids	1900–1650	C=O	Stretching
Aromatics	1690–1450	C=C	Stretching
Alkane, Alcohol, Phenol, ethers	1475–1000	C–O, C–C	Stretching
CO_2	700–580	C=O	Bending
Fingerprint region	1460–1000		
Alkanes	1396	C–C, C–H	Stretching
Alcohols	1172	C–O	Stretching
Phenols	1338	C–O	Stretching
Ethers	1264	C–O	Stretching

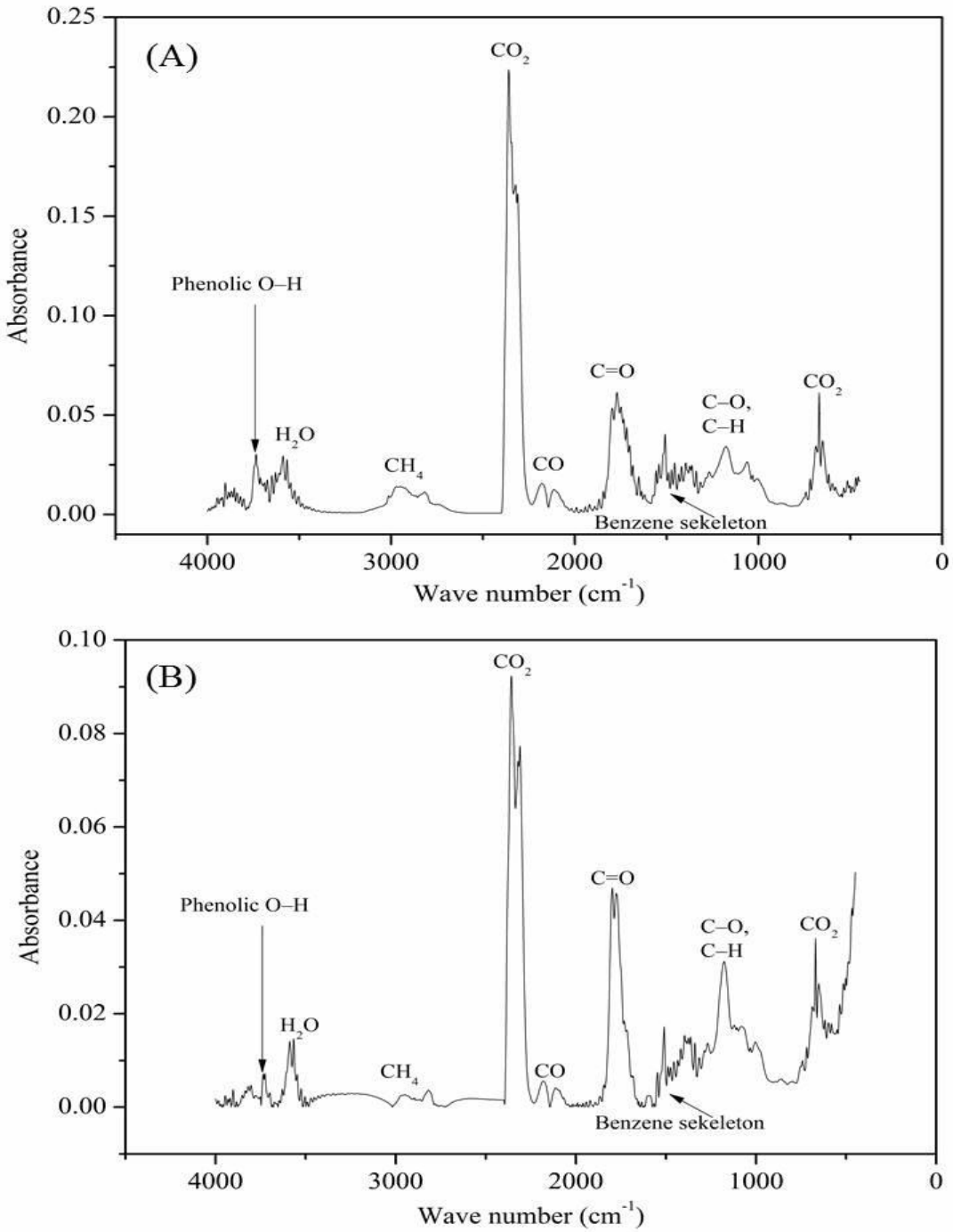

Fig. 6.5: FT-IR spectra of evolved gas products at 50 wt% loss for (A) RSC and (B) RSS

6.2. Kinetic Parameters Calculation

Initial attempts to estimate the kinetic parameters for RSC and RSS samples, considering the entire active pyrolysis occurring in single stage, in the temperature range of 200 °C to 551 °C for RSC and 197 °C to 530 °C for RSS samples, showed much variation in the values of activation energy estimated. The variation can be attributed to multi-step reaction mechanism occurs during the decomposition of RSC (stage II, III and IV) and RSS (stage II and III), as also revealed in TG profiles [152, 156, 157, 256]. It was observed that the mass loss in stage IIa and IIb of RSS was found to be 26.94 wt% and 18.38 wt% within narrow temperature range of 265.2–341.79 °C (i.e. ~77 °C temperature change) and 341.79–391 °C (i.e. ~49 °C temperature change), respectively. By considering the temperature change for thermal decomposition of RSS in stage IIa and IIb, the two stages were merged as single stage (stage II) for kinetic analysis. Therefore, the active pyrolysis zones of RSC and RSS were broadly classified into three and two stages, respectively as described by Chutia *et al.* [119] and Acikalin [153] for TG kinetic analyses of *Mesua ferrea L.* deoiled cake and pistachio shell, respectively. The mass loss data obtained from TG was used to construct the conversion profiles, and various kinetic models were employed to deduce the kinetic parameter for each stage. Fig. 6.6 and Fig. 6.7 show the plots for RSC and RSS samples, respectively, using Friedman (FRD) and Flynn-Wall-Ozawa (FWO) methods. The dependency of the activation energy (E) on the extent of conversion (α) for the decomposition of RSC and RSS was estimated from the slope of both FRD (Fig. 6.6A and Fig. 6.7A) and FWO (Fig. 6.6B and Fig. 6.7B) plots and summarized in Table 6.4.

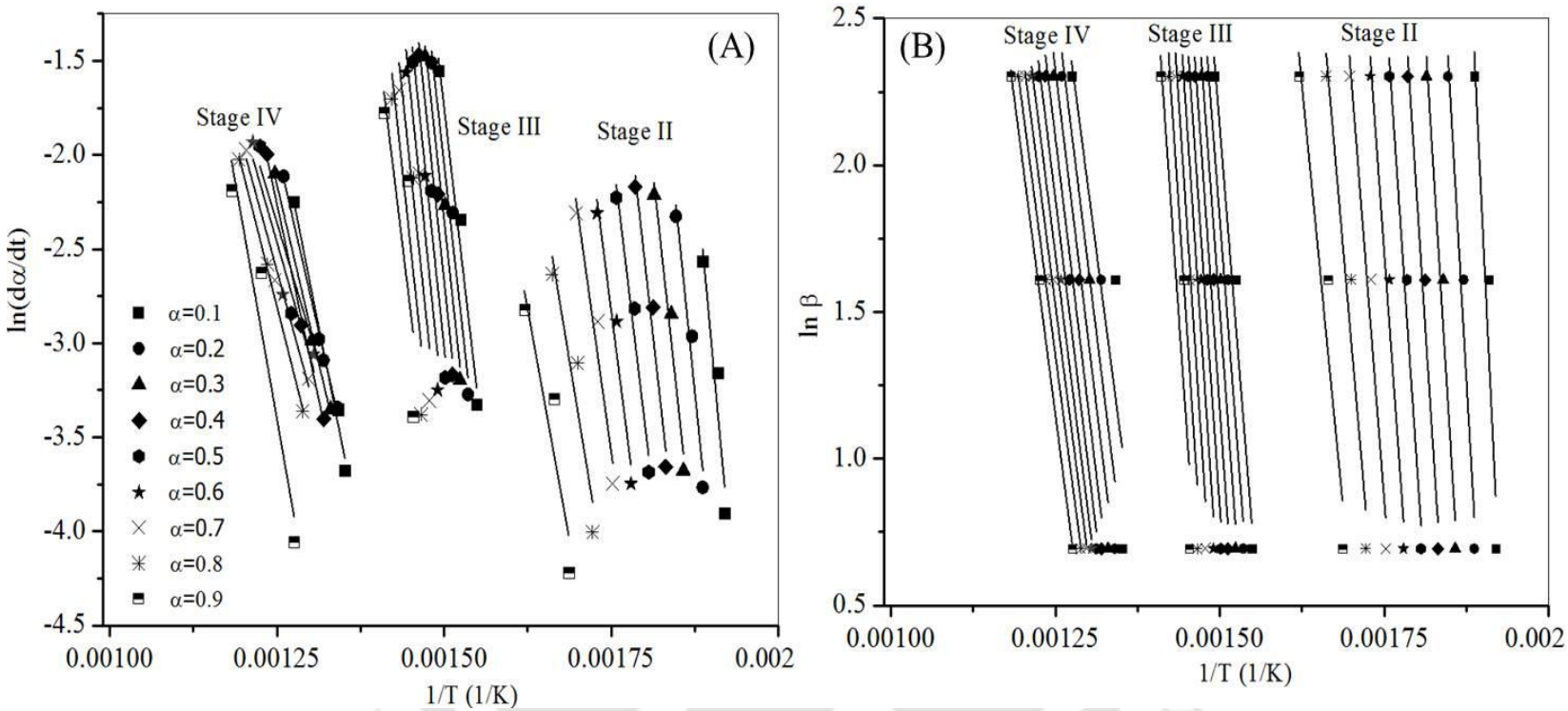

Fig. 6.6: Plots for (A) FRD and (B) FWO methods used to deduce the kinetic parameter for RSC thermal decomposition process

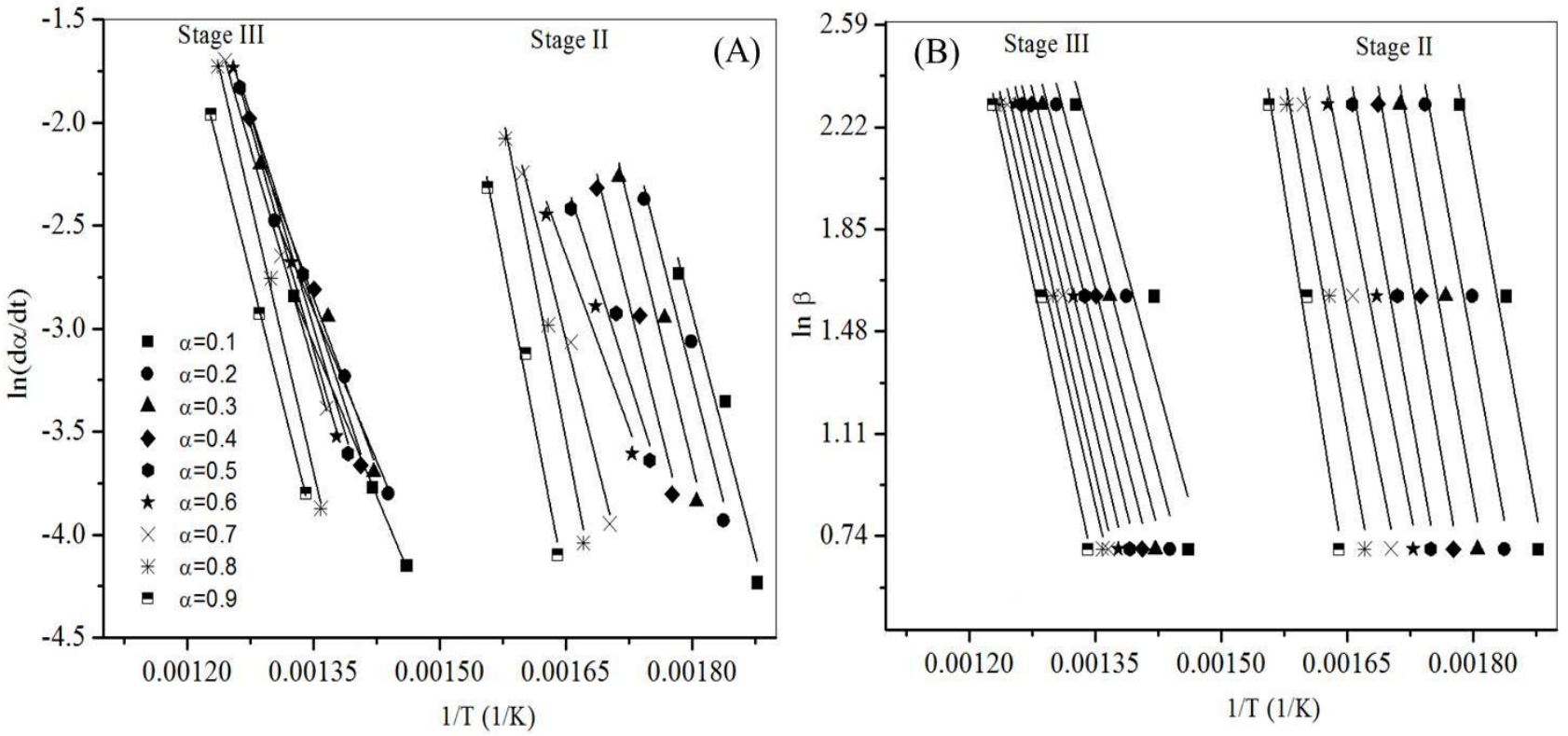

Fig. 6.7: Plots for (A) FRD and (B) FWO methods used to deduce the kinetic parameter for RSS decomposition process

Table 6.4: The values of activation energy obtained for active pyrolysis stages of RSS and RSC sample using various methods

			Conversion (%)* (activation energy (KJ/mol) at different conversion)								
Biomass	Stage	Method	0.1	0.2	0.3	0.4	0.5	0.6	0.7	0.8	0.9
RSC	II	FRD	321.5	292.7	273.0	265.9	247.0	230.9	202.9	180.0	162.8
		FWO	366.6	310.3	285.1	273.4	259.8	246.6	226.2	204.3	181.9
	III	FRD	254.6	264.7	271.4	276.9	279.0	284.9	300.1	300.9	293.4
		FWO	219.3	229.1	240.8	249.4	255.2	262.5	278.5	281.9	285.8
	IV	FRD	150.9	128.8	125.9	138.1	98.4	102.7	107.7	116.9	167.9
		FWO	139.3	143.1	145.3	145.9	143.9	139.7	136.5	133.6	136.3
RSS	II	FRD	129.8	134.7	139.3	136.0	107.0	92.8	135.1	174.4	175.7
		FWO	132.6	131.9	135.1	140.2	134.1	122.9	121.0	135.7	150.7
	III	FRD	88.6	91.5	92.4	94.6	97.3	102.4	104.9	103.5	112.6
		FWO	81.6	80.9	91.1	107.9	114.0	120.8	116.9	145.2	135.5

* *Stage by stage conversion of active pyrolysis of the samples*

The activation energy difference for stage II, III and IV of RSC obtained by Friedman and Flynn-Wall-Ozawa methods found to be varied from 7.5 kJ/mol–45 kJ/mol, 7.9 kJ/mol –35.3 kJ/mol and 7.8 kJ/mol–45.5 kJ/mol with average residual value of 19.7 kJ/mol, 24.8 kJ/mol and 14 kJ/mol, respectively. Similarly, for stage II and III of RSS difference in activation energy varied between 1.4 kJ/mol–41.7 kJ/mol and 2.8 kJ/mol–38.74 kJ/mol with average residual value of 2.31 kJ/mol and 11.374 kJ/mol with Friedman and FWO methods, respectively. It was also observed that no significant changes occurred in the values of activation energy during different stages of RSC and RSS decomposition: 0.2–0.6 (RSC, stage II), 0.1–0.9 (RSC, stage III), 0.1–0.9 (RSC, stage IV), 0.1–0.9 (RSS, stage II) and 0.1–0.9 (RSS, stage III) (Fig. 6.8). Fig. 6.8A shows the variation of activation energy (*E*) with degree of conversion in each stage considering FRD and FWO kinetics methods. The variation in *E* values signifies the presence of various complex reactions during decomposition of the samples [257-259]. Furthermore, the maximum rate of thermal decomposition of RSC at II stage (3.74 wt%/min) was higher as compare to stage III (2.66 wt%/min) and IV (2.64 wt%/min) and may resulted more reactions with more unstable intermediates and lower activation energies within stage II [257, 259]. Hence, the significant change in activation energy values at different conversions and stages indicates the RSC decomposition process proceeds via multi-step reaction. Kissinger plots for both the materials considering different stage decomposition are shown in Fig. 6.9. The values of activation energy obtained for different stages were found to be 224.19 kJ/mol (RSC, stage II), 367.37 kJ/mol (RSC, stage III), 196.36 kJ/mol (RSC, stage IV), 102.87 kJ/mol (RSS, stage II) and 101.57 kJ/mol (RSS, stage III). Lower values of activation energy within stage II infer that the degradation may occur at faster rate as compared to III. The variations of activation energy

values at different conversion and/or stage for RSC signifies that the decomposition process proceed via multi-step and parallel competitive reaction. However, due to the complexity of these materials and their by-products, it is difficult to estimate the detail reaction mechanism during degradation of samples. A decomposition study on targeting the intermediate products will be required to deduce such detailed information. Considering similar active decomposition stages for RSC and RSS samples (i.e. two stages), the average activation energy (295.78 kJ/mol) for combined stage (II and III) was found to be higher as compared to stage IV (196.36 kJ/mol) of RSC sample in Kissinger method (KM). Similar observation has been found for thermal decomposition for RSS in all used kinetic methods. However, the change was minimal in the RSS sample. Even though KM is simple to be applied to determine the single value of activation energy, it fails to explain the overall trends due to the fact that only single conversion data are used (T_{max}). Moreover, the values of activation energy obtained from KM deviate significantly from the average values obtained from FRD and FWO methods for active pyrolysis stages.

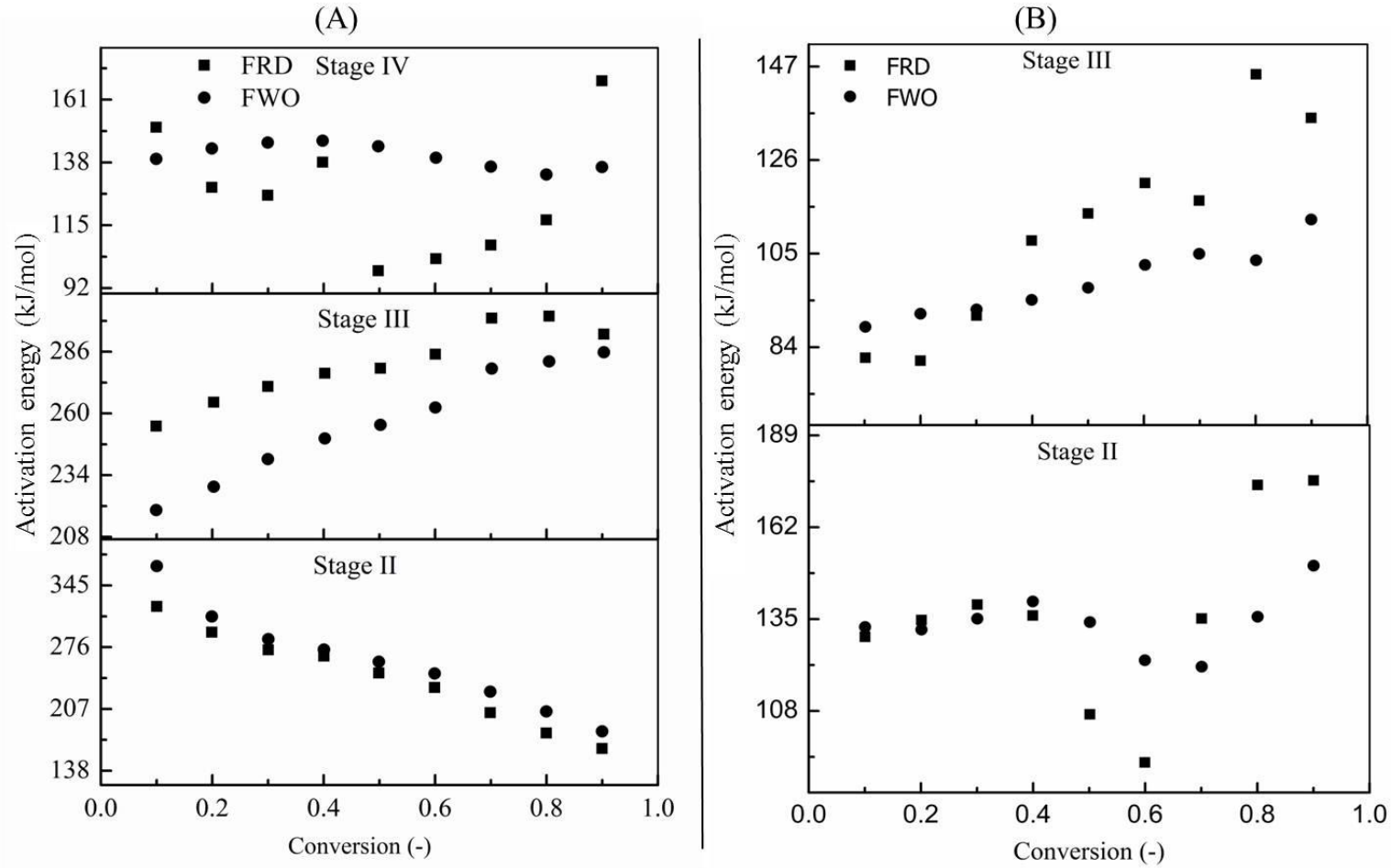

Fig. 6.8: Distribution of activation energy (A) RSC and (B) RSS using FRD and FWO

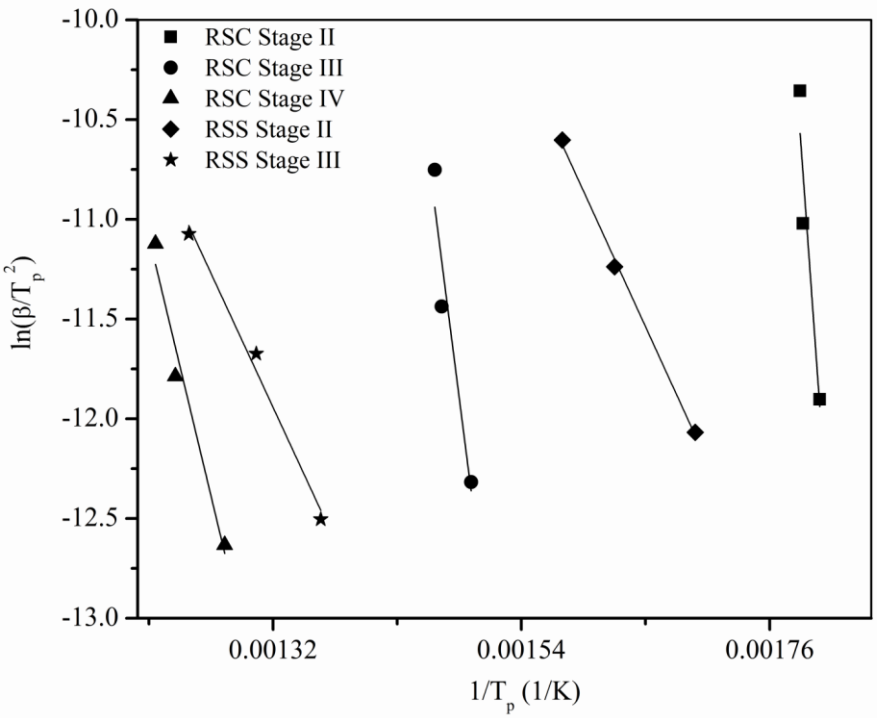

Fig. 6.9: Plots obtained by Kissinger method for determination of activation energy for decomposition of RSC and RSS samples

According to Coats-Redfern (CR) method, the kinetic exponent (*n*) at which the plot of $ln\,{g(\alpha)}/{T^2}$ versus ${1}/{T}$ results in straight line has been considered as suitable kinetic [119, 153]. Therefore, several values of kinetic exponents (*n*) were arbitrarily chosen in the range of -10 – 10 to construct the CR plots for each stage and, correlation coefficients (R^2) were estimated. The obtained correlation coefficient (R^2) with order of reaction for all active pyrolysis stages of RSC and RSS are depicted in Fig. 6.10 (A–C) and Fig. 6.11 (A–B), respectively. The value of *n* for which R^2 is maximum, is considered as the best choice. Coats-Redfern plots for RSC and RSS are presented in Fig. 6.10D and Fig. 6.11C, respectively. The average order of reaction obtained by Coats-Redfern method was found to be 1.63 (stage II), 1.82 (stage III) and 1.58 (stage IV) for RSC thermal decomposition and, 1.58 (stage II) and 1.55 (stage III) for RSS thermal decomposition. The values of kinetic triplet calculated on the basis of Coats-

Redfern method are given in Table 6.5. The heating rate and composition of biomass showed immense influence on activation energy and pre-exponential factor in all active pyrolysis stages (Table 6.5). In active pyrolysis stages of RSC and RSS, the obtained activation energy and pre-exponential factor values for each stage exhibited a similar trend: increase with stages (II to III).

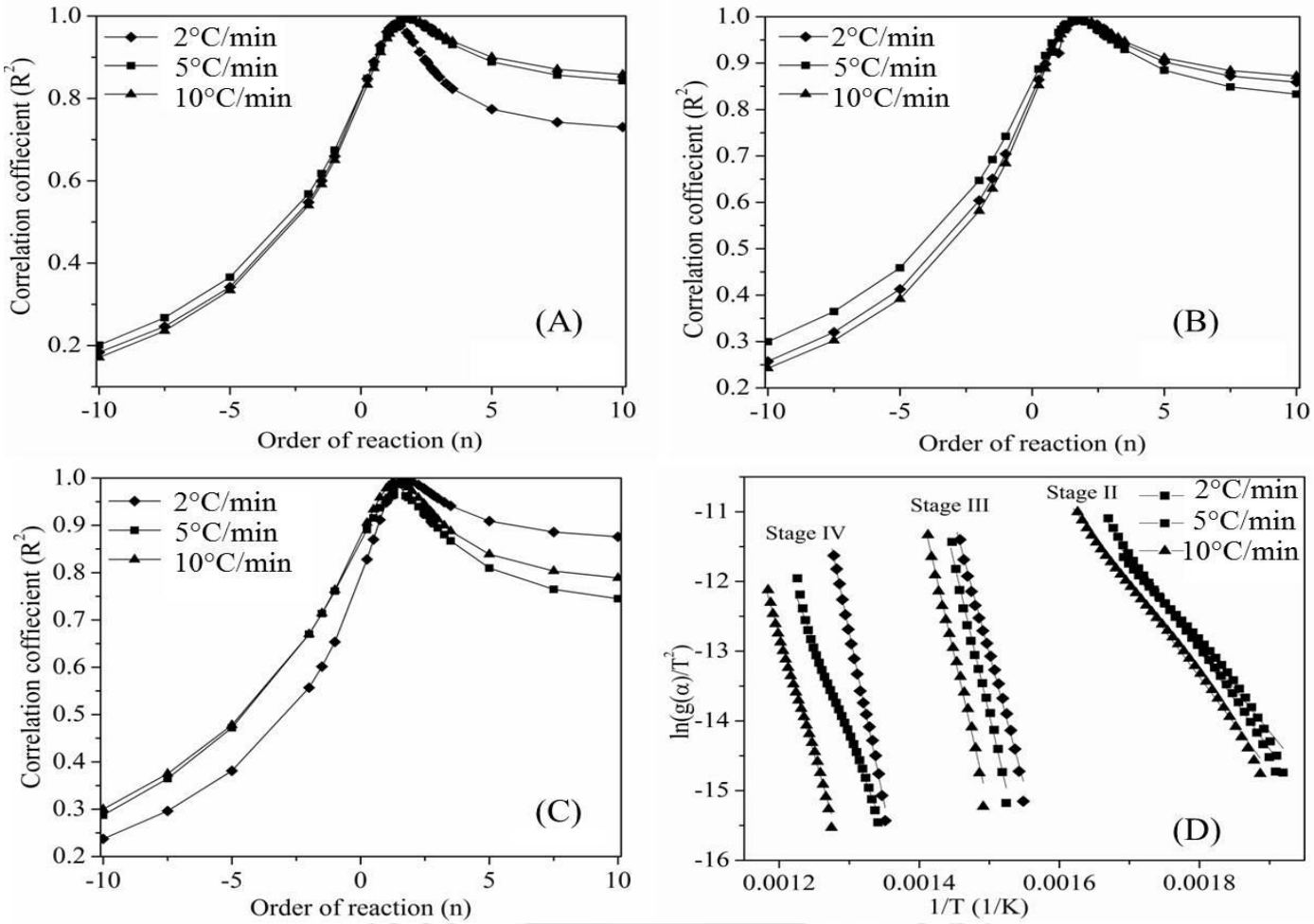

Fig. 6.10: R^2 – n plot Coats-Redfern for RSC (A): Stage II, (B): Stage III, (C): Stage IV and (D) final plot obtained at optimum R^2 value for each stage

Table 6.5: Kinetic parameters estimated using Coats-Redfern model for thermal decomposition of RSS and RSC sample

Biomass	β (°C /min)	Stage	E (kJ\ mol)	log$A$	n	R^2	E (kJ/ mol)*	log$A$*	n*
RSC	2	II	102.8 ± 0.7	8.4 ± 2.3	1.3	0.988	110.6	9.5	1.63
		III	314.1 ± 1.8	23.8± 2.8	1.85	0.995	347.8	26.4	1.82
		IV	372.2 ± 1.5	24.9 ± 2.6	1.75	0.998	293.6	18.8	1.58
	5	II	117.4 ± 0.4	10.2 ± 2.4	1.75	0.997	110.6	9.5	1.63
		III	361 ± 2.5	27.6 ± 3.4	1.75	0.993	347.8	26.4	1.82
		IV	222.8 ± 1.1	14.1 ± 2.9	1.5	0.993	293.6	18.8	1.58
	10	II	111.7 ± 0.3	9.8 ± 2.6	1.85	0.997	110.6	9.5	1.63
		III	368.3 ± 2.4	27.9 ±3.6	1.85	0.998	347.8	26.4	1.82
		IV	286 ± 0.9	17.9± 3.1	1.5	0.99	293.6	18.8	1.58
RSS	2	II	121.9 ± 0.3	10.1 ± 1.8	1.75	0.998	113.2	9.3	1.58
		III	201.7 ± 0.8	13.5 ± 2.4	1.175	0.995	204.6	13.3	1.075
	5	II	108.2 ± 0.6	8.9 ± 2.6	1.5	0.995	113.2	9.3	1.58
		III	177.4 ± 0.3	11.5 ± 2.3	1.05	0.999	204.6	13.3	1.075
	10	II	109.2 ± 1.3	8.9 ± 3.3	1.5	0.99	113.2	9.3	1.58
		III	234.7 ± 1.3	14.9 ± 3.3	1	0.998	204.6	13.3	1.075

**average values kinetic parameters (E, logA and n) for all heating rate in the same stage*

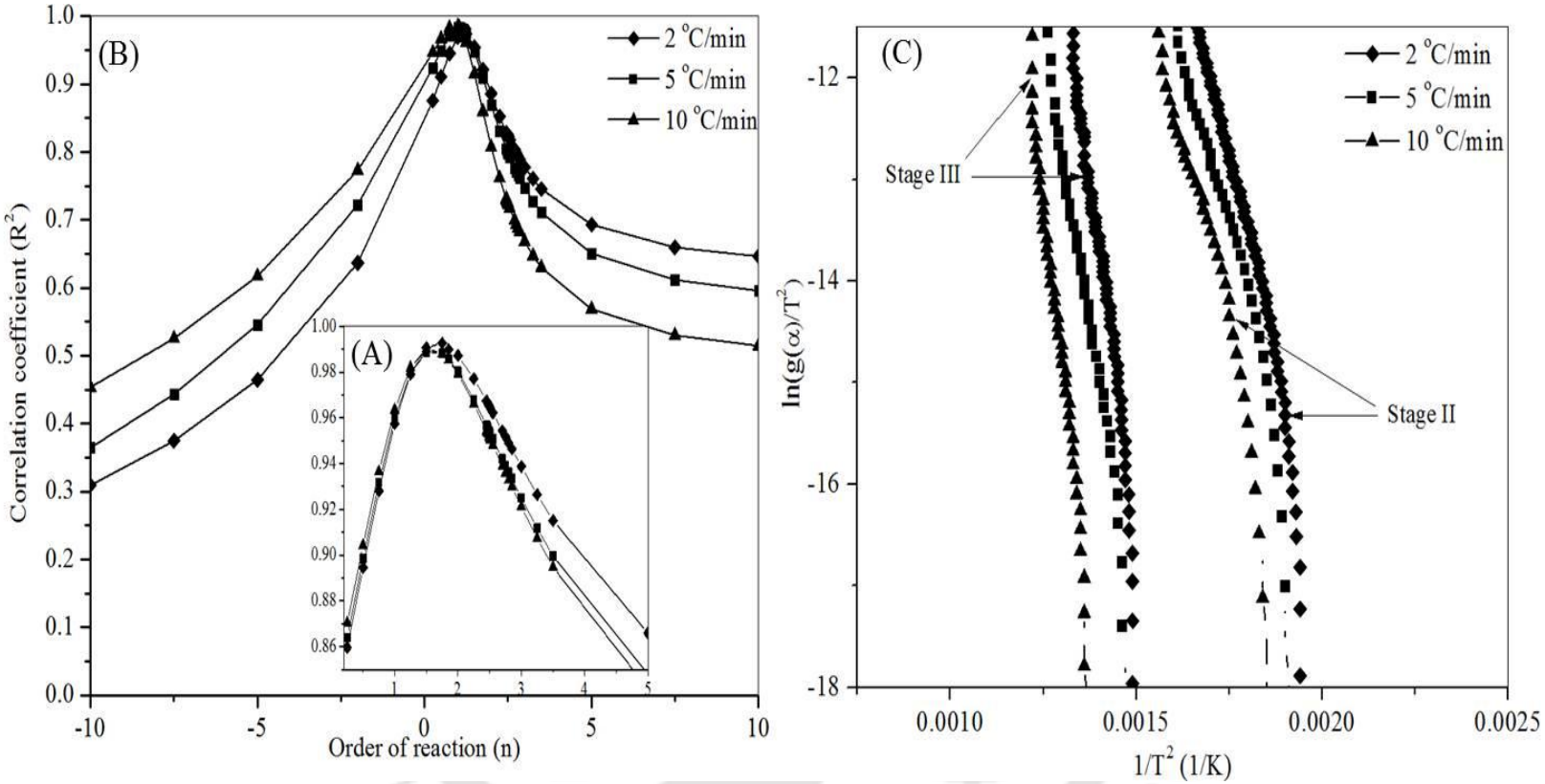

Fig. 6.11: R^2 – n plot Coats-Redfern for RSS (A): Stage II, (B): Stage III and (C): final plot obtained at optimum R^2 value for each stage

The average values of activation energy and pre-exponential factor for stage III of RSC were found to be higher compared to stage II and IV with all the methods. This is attributed to the decomposition of hemicellulose and cellulose in RSC (Table 6.1). Cellulose is thermally more stable than hemicellulose; implying that thermal decomposition for cellulose starts at higher temperature as compared to hemicellulose [13, 119, 153, 251]. Similar observation has been found in the activation energy results during thermal decomposition of RSC. In active pyrolysis stage II of RSC, increasing the heating rate from 2 to 5 ^{o}C/min resulted in an increase of activation energy (from 102.8 to 117.4 kJ/mol) and then the value decreased to 111.7 kJ/mol at 10 °C/min. Stage III of RSC shown continuous increase in *E* values with the heating rates. On the other hand, in active pyrolysis stages of RSS, a continuous increase of activation energy from 121.9–201.7 kJ/mol (heating rate 2 °C/min), 108.7–177.4 kJ/mol (heating rate of 5 ^{o}C/min) and 109.2–234.7 kJ/mol (heating rate of 10 °C/min) with conversion was observed. For stage II, III and IV of RSC, the average activation energy using Coats-Redfern method were found to be 110.6 kJ/mol, 347.8 kJ/mol and 293.6 kJ/mol, respectively. Similarly, for stage II and III of RSS, the average values of *E* were estimated as 113.2 kJ/mol and 204.6 kJ/mol, respectively. The obtained result shows a good agreement with the values reported for pistachio shell and *Musua farrea L.* cake kinetic studies [119, 153].

Invariant kinetic parameters (IKP) obtained for thermal decomposition of RSS and RSC sample are presented in Table 6.6. The values of compensation effect parameters were calculated from the slope and intercept of Fig. 6.12. The high correlation coefficient results shown in Fig. 6.13 confirmed the existence of kinetic compensation effect [152, 153, 168]. The values of compensation parameters (*a* and *b*) clearly define the decomposition of both

RSC and RSS. The obtained values of activation energy using IKP method (Table 6.6) for the corresponding active pyrolysis stages were found to be in good agreement with the average values of FRD and FWO method. Table 6.6 shows that the value of activation energy for stage III of RSC and II of RSS decomposition is higher than the next stage in each sample. The average value of activation energies obtained by CR method for final stages (stage IV of RSC and stage II of RSS) was found to be higher compared to IKP method. For this reason, the pre-exponential factor obtained by CR method was also higher compared to IKP method. The shape of $f(\alpha)$ vs. α obtained by IKP method and theoretical curve were compared for all the models listed in Table 2.4. The decomposition stages of RSC (stage II, III and IV) and RSS (stage II) followed the ideal reaction models of D1, D2, D3 and D4. These reaction behaviors have been found by assuming ideal conditions such as homogeneous particle shape, size, mixture, which may show deviation from real sample [162, 168]. In this respect, most popular form of conversion function model Sestak-Berggren (SB) (Eq. 2.23–2.25) [168] was used to evaluate the values of *m*, *n* and corrected *lnA*. As discussed before, the experimental $f(\alpha)$ and conversion (α) profiles were found in similar shapes with D1, D2, D3, and D4 reaction models. Hence, the parameters α_{max} and *m* for RSC decomposition for all active pyrolysis stages were found to be zero (0) [152, 162] (Table 6.7), while stage III of RSS at heating rates of 2 and 5°C/min did not shown clear shape to relate with theoretical conversion functions ($f(\alpha)$) listed in Table 2.4. The pre-exponential factor (intercept) and kinetic exponent, *n* (slope) were determined by direct Arrhenius method Eq. 2.25 and presented in Table 6.7. The obtained values of *n* found to be a function of heating rate, whereas the *A* values remained constant. The values of pre-exponential factor for RSC and RSS by SB model (Table 6.7) at various heating rates are in good agreement with IKP method (Table

6.6). The average kinetic exponent, *n* obtained by SB model was 4.99 (RSC, stage II), 1.37 (RSC, stage III), 0.63 (RSC, stage IV), 1.64 (RSS, stage II) and 0.38 (RSS, stage III). Finally, the average values of activation energies obtained by several kinetic methods are summarized in Table 6.8. The obtained *E* values in present study for RSS sample are higher than the values reported by Chin *et al.* [155]. This variation may be attributed to genotype of M-RSS (Malaysia origin rubber seed shell) and the kinetic method considered, overall two stages using integral approach.

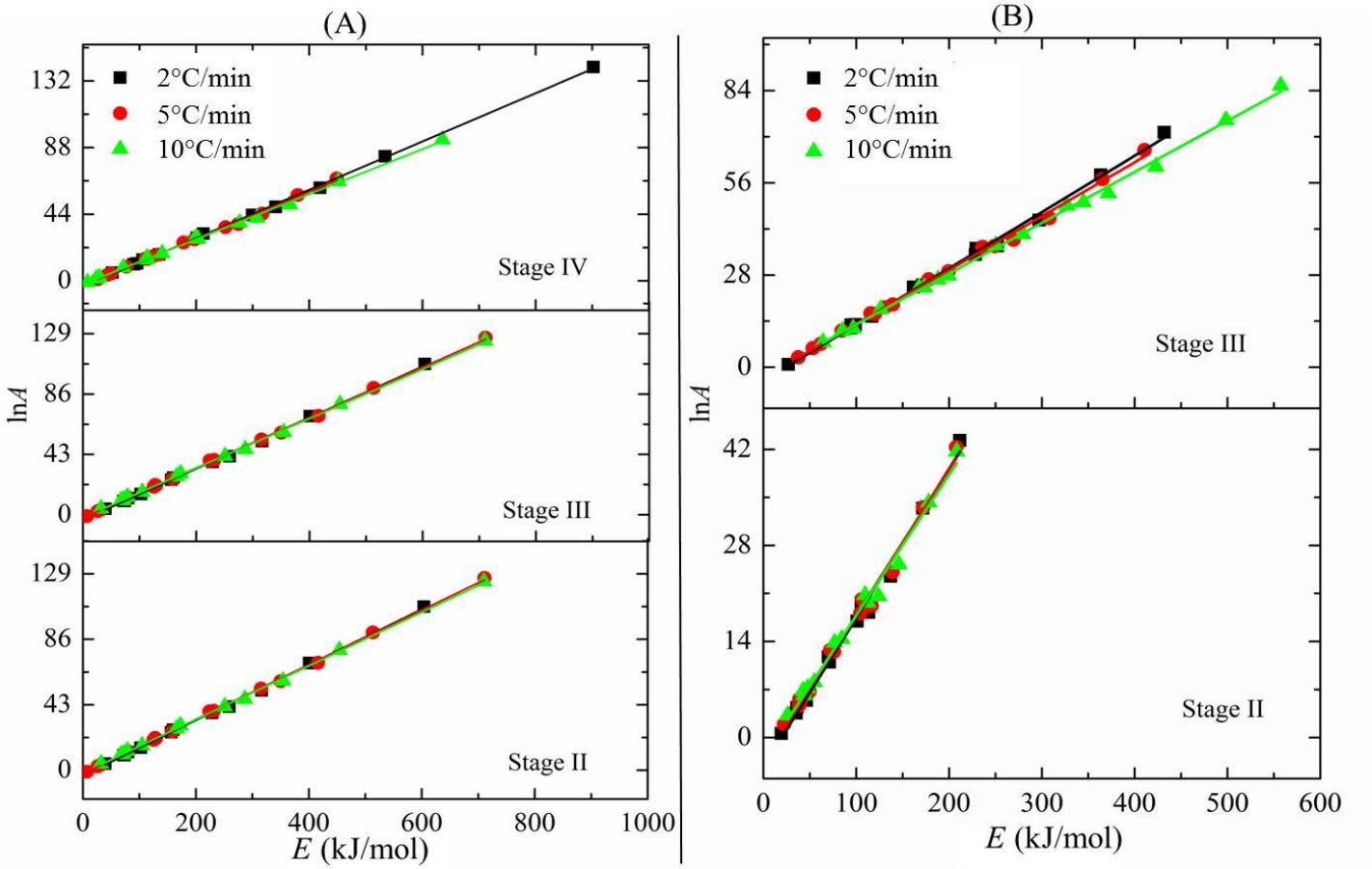

Fig. 6.12: Compensation effect observed between activation energy and pre-exponential factor for thermal decomposition process of (A) RSC and (B) RSS

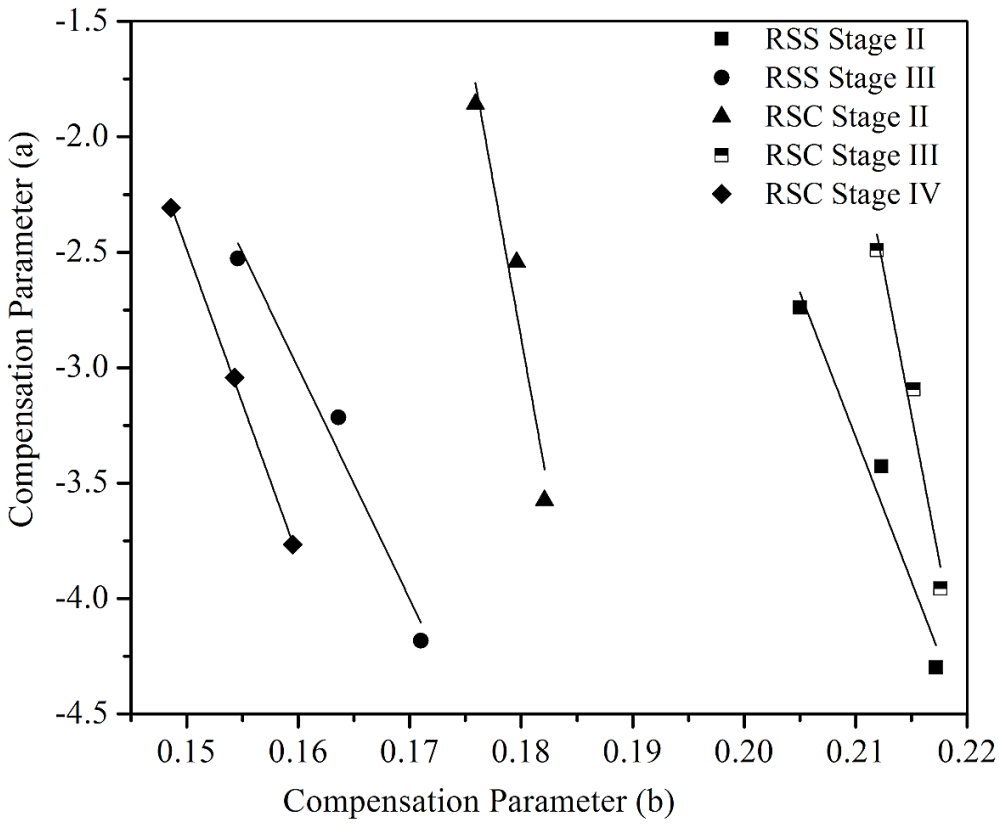

Fig. 6.13: Compensation effect parameters at three heating rates for decomposition of RSC and RSS samples using IKP method

Table 6.6: Values of compensation effect parameters and invariant kinetic parameters for active pyrolysis stage of RSC and RSS samples

Biomass	stage	β (°C/min)	a (-)	b (mol/kJ)	R^2	E_{inv} (kJ/mol)	$\ln A_{inv}$ (min^{-1})*
RSC	II	2	-3.95	0.22	0.998	252.6	51.1
		5	-3.09	0.22	0.998		
		10	-2.49	0.22	0.997		
	III	2	-3.57	0.18	0.999	269.8	45.69
		5	-2.54	0.18	0.999		
		10	-1.86	0.18	0.999		
	IV	2	-3.77	0.16	0.999	133.65	17.56
		5	-3.04	0.15	0.998		
		10	-2.31	0.15	0.999		
RSS	II	2	-4.29	0.22	0.992	125.1	22.98
		5	-3.43	0.21	0.992		
		10	-2.379	0.21	0.991		
	III	2	-4.18	0.17	0997	100.1	13.01
		5	-3.22	0.16	0.997		
		10	-2.53	0.16	0.998		

**Dimension of pre-exponential factor*

Table 6.7: Sestak-Berggren (SB) model parameters of the conversion function for RSC and RSS samples

Biomass	Stage	β (°C/min)	m	n	α_{max}	ln$A$
RSC	II	2	0	5.04	0	54.6
		5	0	4.82	0	54.77
		10	0	5.12	0	54.76
		Average	0	4.99	0	54.71
	III	2	0	1.56	0	46.75
		5	0	1.12	0	46.86
		10	0	1.42	0	46.73
		Average	0	1.37	0	46.78
	IV	2	0	0.69	0	18.37
		5	0	0.57	0	18.14
		10	0	0.62	0	18.17
		Average	0	0.63	0	18.23
RSS	II	2	0	1.709	0	23.95
		5	0	1.663	0	24.18
		10	0	1.54	0	23.90
		Average	0	1.64	0	24.00
	III	2	–	–	–	–
		5	–	–	–	13.56
		10	0.468	0.3802	0.552	13.94

Table 6.8: Comparison of kinetic parameters obtained with the value reported in the literature for different feedstocks

Name	Activation energy (kJ/mol)	Pre-exponential factor (min^{-1})	Number stages	Model type	Reference
Shell of oilseeds					
RSS	88.6–175.7	–	3	FRD	Present work
	81.6–150.7	–		FWO	
	101.57–102.9	–		KM	
	100.1–125.1	5.01×10^{5}–9.55×10^{9}		IKP	
	108.2–234.7	7.94×10^{8}–7.94×10^{17}		CR	
M-RSS	46.94–63.2	3.2×10^{6}–1.31×10^{8}	2	Integral	[151]
PS	109.4–339.8	1.66×10^{10}–1.58×10^{29}	4	Arrhenius	[149]
	156–374.2	8.91×10^{14}–1.35×10^{32}	4	Costs and Redfern	
	179.3–412.8	2.51×10^{17}–2.81×10^{35}	4	Horowitz-Metzger	
	181	–	4	FWO	
Cake of oilseeds					
RSC	102.7–321.5	–	4	FRD	Present work
	133.6–366.6	–		FWO	
	196.38–367.37	–		KM	
	133.65–269.8	4.27×10^{7}–1.58×10^{22}		IKP	
	102.8–372.2	2.5×10^{8}–7.94×10^{24}		CR	
MFDC	51.34–251.87	7.76×10^{4}–2.75×10^{22}	4	Arrhenius	[115]
	58.38–329.2	0.3×10^{3}–4.47×10^{26}	4	Costs and Redfern	
	40.40–253.87	0.2×10^{3}–4.68×10^{17}	4	MLR	
	120.5	–	4	FWO	
PC	16–178	–	2	Arrhenius	[152]
MC	37–357	–	2	Arrhenius	
JC	8–41	–	2	Arrhenius	

M-RSS:Malaysia origin rubber seed shell; PS:Pistachio shell; MFDC: Mesua ferrea L. deoiled cake, MLR: Multi-linear regression

6.3. Pyrolysis of RSS in a Semi-batch Reactor

Dehydration, depolymerization, decomposition and fragmentation reactions of three key biomass building blocks in RSS: hemicellulose, cellulose and lignin occur at elevated temperatures. TGA profiles of RSS (Fig. 6.4) samples confirmed that the active pyrolysis of RSS occurred in the temperature range of 300 °C–500 °C. Therefore, pyrolysis of RSS was conducted in a lab scale reactor (1L capacity) in the temperature range of 350 °C to 600 °C with 50 °C increment. The effect of pyrolysis temperatures (350–600 °C) and heating rates (10–40 °C/min) on product distribution (liquid, bio-char and gas) and quality (composition and energy content) were investigated.

6.3.1. *Effect of Pyrolysis Temperature on Product Distribution*

Product distribution obtained under isothermal pyrolysis, at heating rate of 30 °C/min to achieve final temperature of RSS is shown in Fig. 6.14A. The yield of bio-char decreased as the pyrolysis temperature increased from 350 °C to 600 °C. This may be due to the further decomposition, secondary and gasification reactions taking place by bio-char residue at higher temperature [127, 245, 260, 261]. Significant loss of volatile matter, dehydration of hydroxyl groups and thermal degradation of hemicellulos, cellulose and lignin also enhances the reduction of bio-char yield. A higher yield of bio-char at lower pyrolysis temperature was due to partial pyrolysis of feedstock. The liquid yield increased from 29.98 wt% to 46.14 wt% as the pyrolysis temperature increased from 350 °C to 550 °C. Further increase in pyrolysis temperature to 600 °C lead to only slight increase in the liquid yield (46.7 wt%) while bio-char yield and its calorific value decreased. Similar trends were reported by Duman *et*

al.[245]; Sansoz and Angin [125]; Singh and Shadangi [127] during the pyrolysis of cherry seed shell and castor seed. However, the gaseous product yield increased from 13.44 wt% to 25.2 wt% as the pyrolysis temperature increased from 350 °C to 600 °C. The increased in non-condensable gaseous product is due to the secondary cracking of produced vapors and decomposition of bio-char residue at higher pyrolysis temperature [262, 263]. The time required for completion of reaction decreased as the pyrolysis temperature increased, Table A6.1. Considering the factors such as completion time required, yield of liquid (46.14 wt%) and bio-char (31.92 wt%) and calorific value of bio-char (34.5 MJ/kg), the effect of heating rates on product distribution was investigated by heating the RSS sample from ambient to 550 °C.

6.3.2. Effect of Heating Rate on Product Distribution

The effect of heating rates (10– 40 °C/min) on product distribution is shown in Fig. 6.14B. The liquid yield slightly increased from 45.5 wt% to 46.14 wt% as heating rate increased from 10 °C/min to 30 °C/min and then decreased to 43.92 wt% at 40 °C/min. The gaseous product yield was found to be 20.82 wt% at 10 °C/min and 26.48 wt% at 40 °C/min, while bio-char yield at a corresponding heating rates were estimated as 33.15 wt% and 29.6 wt%, respectively. At higher heating rate, the secondary cracking and decomposition reactions of both gas (volatile matter) and bio-char residue control the product distribution; more gaseous product and less liquid and bio-char products [125, 129, 264, 265]. The calorific values of the bio-char decreased from 35.11 MJ/kg to 34.42 MJ/kg as the heating rate increased from 10 °C/min to 40 °C/min (Fig. 6.14B). Higher calorific value obtained at lower heating rate, 10 °C/min was probably due to longer residence time for volatile matter in the chamber which

enhances diffusion of volatiles in to the particle. Overall, the pyrolysis temperature dominates yield and product distribution compared to heating rate. Similar results were also reported by other researchers for pyrolysis of safflower seed press cake [125, 129]. The reaction completion time increased from 20 to 50 min as heating rate decreased from 40 to 10 °C/min as shown in Table A6.1. In addition to product distribution; completion time also depends on both heating rate and pyrolysis temperature. Calorific values of produced bio-char samples indicate that the solid products have the potential to be used as alternative solid fuel. However, based on the liquid yield, quality of bio-char and completion time; heating rate of 30 °C/min was found appropriate for pyrolysis of RSS to obtain carbon-rich solid fuel and mixture of value-added chemicals in liquid product.

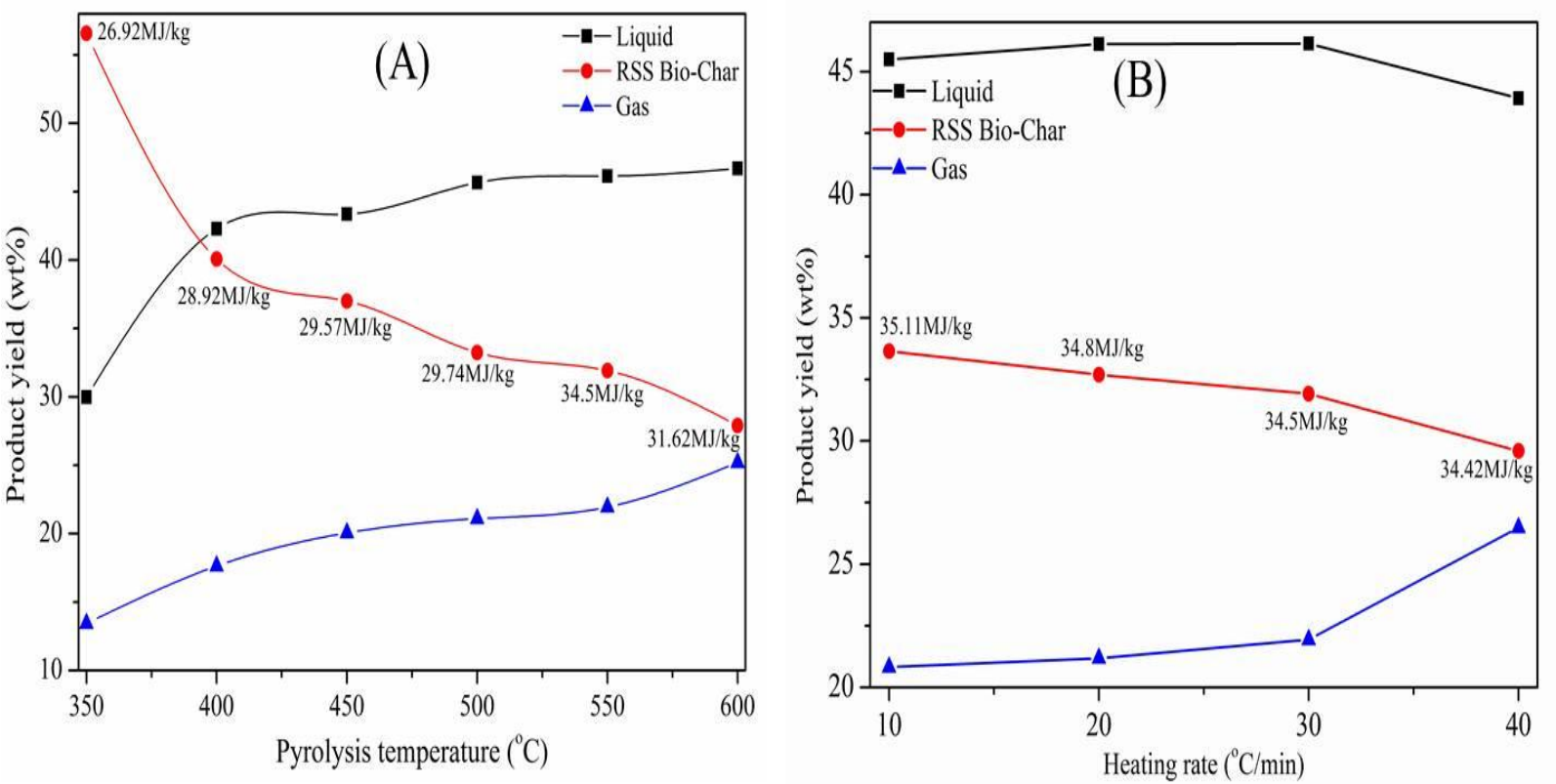

Fig. 6.14: Effect of (A) pyrolysis temperature at constant heating rate of 30 °C/min and (B) varying heating rates at pyrolysis temperature of 550 °C on product distribution

6.3.3. *Characterization of RSS Bio-Char*

The bio-char samples obtained at different pyrolysis conditions (temperatures and heating rates) were subjected for proximate, ultimate, calorific value and XRD analyses. The results of proximate and ultimate analyses are presented in Table 6.9 and Table 6.10, respectively. Pyrolysis temperature has significant effect on moisture content of bio-char [119, 130]. The moisture content of bio-char (from RSS) varied from 1.16 to 3.05 wt% as temperature increased from 350 to 600 °C, while with heating rate no significant variation was observed. The obtained values are lower than *pongamia glabra* deoiled cake bio-char [119, 130]. Non-volatile and non-combustible components of bio-char samples were measured from ash content. The ash content of bio-char varied from 1.48–1.9 wt% on dry weight basis. A portion of some gaseous and liquid-phase products left in bio-char contributes to volatile organic carbon. Volatile matter of bio-char decreased from 53.77±0.01 wt% to 16.73±0.05 wt% as pyrolysis temperature increased whereas fixed carbon content increased from 47.28±0.06 wt% to 81.36±0.06 wt% (Table 6.9A). However, the values were not significantly changed as the heating rate increased (Table 6.9B). Angin [129] and Guo and Lua [266] also reported similar observations during pyrolysis studies for safflower seed press cake and oil palm stones.

Table 6.9: Proximate analysis of bio-char samples obtained from pyrolysis of RSS at various conditions

(A)	Pyrolysis temperature (°C) at heating rate of 30 °C/min					
	350	400	450	500	550	600
VM (wt%)	53.77±0.01	29.62±0.2	25.8±0.03	22.21±0.04	18.59±0.01	16.73±0.05
Ash (wt%)	1.05±0.05	1.5±0.03	1.48±0.05	1.61±0.05	1.78±0.02	1.91±0.01
FC (wt%)	47.28±0.06	68.88±0.05	72.72±0.08	76.18±0.09	79.74±0.03	81.36±0.06
HHV (MJ/kg)	26.92±0.08	28.92±0.04	29.57±0.01	29.74±0.05	34.5±0.02	31.62±0.07
(B)	Heating rate (°C/min) for 550 °C pyrolysis temperature					
	10	20	30	40		
VM (wt%)	18.90±0.04	18.78±0.06	18.59±0.01	17.33±0.01		
Ash (wt%)	1.53±0.02	1.73±0.01	1.78±0.02	1.86±0.05		
FC (wt%)	79.57±0.06	79.49±0.07	79.74±0.03	80.81±0.06		
HHV (MJ/kg)	35.11±0.1	34.8±0.07	34.5±0.04	34.42±0.08		

FC: Fixed carbon, VM: Volatile matter

Table 6.10: Elemental composition of bio-char obtained from RSS at various pyrolysis conditions

(A)	Pyrolysis temperature (°C) at 30 °C/min heating rate					
	350	400	450	500	550	600
C (wt%)	71.59	73.02	75.95	79.64	84.12	84.89
H (wt%)	3.84	4.79	3.55	3.25	2.95	2.42
N (wt%)	1.87	1.39	1.98	1.69	1.77	1.52
S (wt%)	–	–	–	–	–	–
O* (wt%)	22.7	20.79	18.52	15.42	11.16	11.16
HC (wt%)	75.43	77.81	79.50	82.89	87.07	87.31
H/C, molar ratio	0.64	0.79	0.561	0.49	0.42	0.34
O/C, molar ratio	0.24	0.21	0.183	0.14	0.10	0.099
(B)	Heating rate (°C/min) to achieve 550 °C pyrolysis temperature					
	10	20	30	40		
C (wt%)	84.04	84.27	84.12	85.22		
H (wt%)	2.82	2.86	2.95	2.79		
N (wt%)	1.24	1.47	1.78	1.49		
S (wt%)	–	–	–	–		
O* (wt%)	11.9	11.4	11.16	10.5		
HC (wt%)	86.86	87.12	87.07	88.01		
H/C, molar ratio	0.40	0.41	0.42	0.39		
O/C, molar ratio	0.11	0.10	0.10	0.092		

**by difference*

The total organic matter (C, H and O) present in RSS and bio-char, obtained at 550 °C for heating rates of 30 °C/min (optimum condition) were found to be 96.87 wt% and 98.23 wt%, respectively. The total hydrocarbon contents (C and H) increased from 58.47 wt% (RSS) to 87.07 wt% (bio-char). It was observed that the bio-char contains less oxygen and high carbon than original RSS (Table 6.10). At higher pyrolysis temperature (≥ 550 °C), losses of hydrogen and oxygen (during pyrolysis) are due to the cleavage and cracking of weak bonds within the bio-char structure [267]. In other words, the calorific value of obtained bio-char (34.5 MJ/kg) was found to be higher than that of original feedstock, RSS (19 MJ/kg) (Table 6.1 and Table 6.9). Increasing the pyrolysis temperature produced bio-char with lower O/C ratio (Table 6.10A), probably due to decomposition of oxygen containing functionalities by decarbonylation and decarboxylation [130]. The low H/C and O/C ratios (increased aromaticity) of obtained bio-char (Table 6.10 and Fig. 6.15) indicated predominant of unsaturated carbon; carbon atoms directly bonded to other carbons [264, 268]. The energy content of produced bio-char (at 550 °C pyrolysis) was estimated to be comparable with anthracite solid fuel (32–34 MJ/kg). Higher calorific value, higher fixed carbon, lower ash and moisture content of bio-char produced from RSS pyrolysis support that the bio-char can be used as a solid fuel. Pyrolysis temperature has shown significant influence on calorific value (i.e. carbon content) of bio-char compared to heating rate (Fig. 6.14A and Fig. 6.14B). Similar observation can also be drawn from proximate (Table 6.9B), ultimate (Table 6.10B) and XRD (Fig. 6.16) analyses of bio-char samples. XRD pattern obtained for RSS and produced bio-char samples are presented in Fig. 6.16A and Fig. 6.16B. Two peaks at 2θ values around 16° and 22° for RSS sample belong to the crystalline region of cellulose [250, 269]. Since the cellulose was completely degraded during pyrolysis (≥400 °C), these peaks

disappeared in the bio-char spectra (Fig. 6.16B).

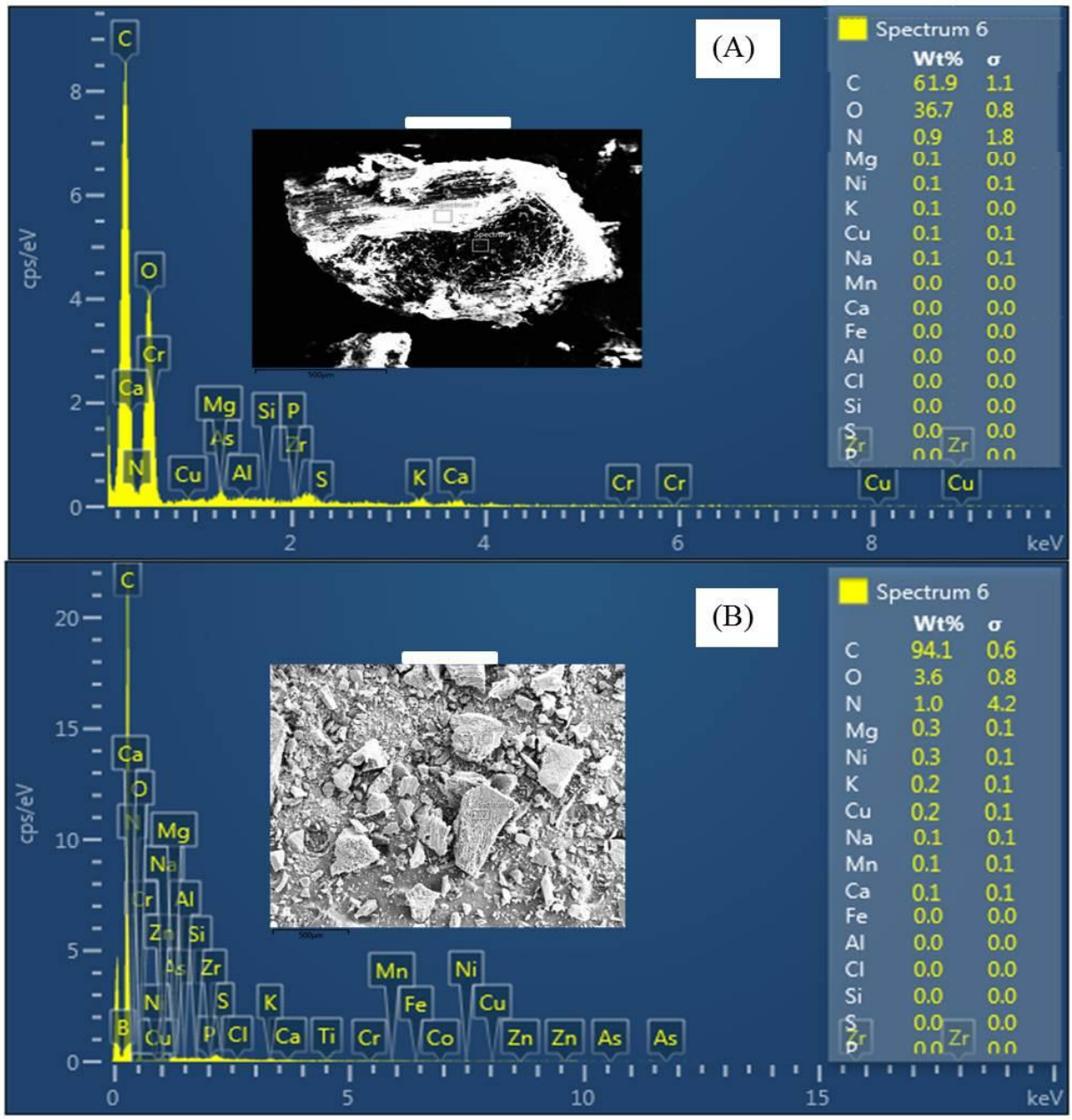

Fig. 6.15: EDX analysis of (A) raw RSS and (B) bio-char obtained from RSS at 550 °C pyrolysis temperature

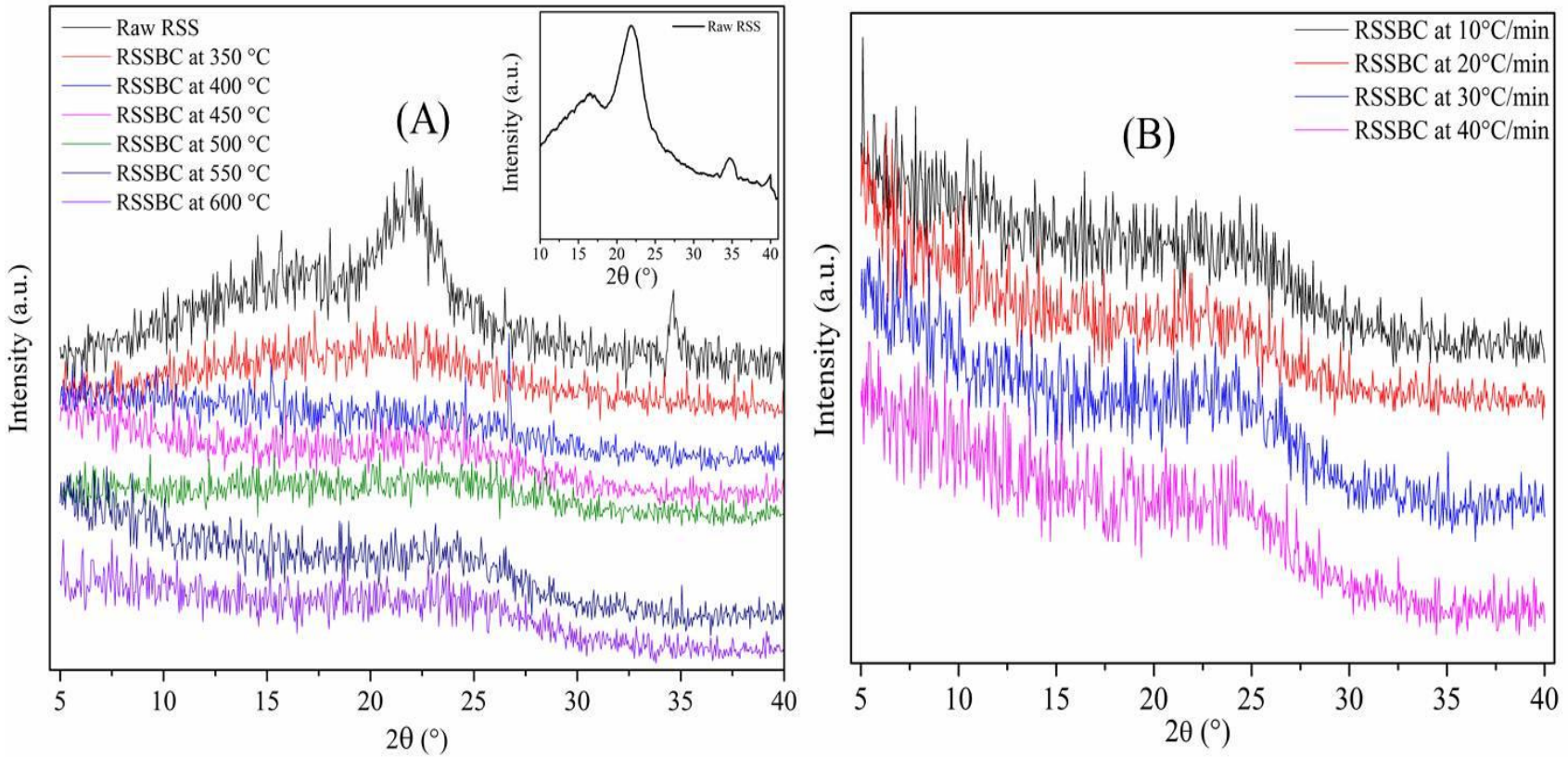

Fig. 6.16: XRD analysis of raw RSS and bio-char obtained from RSS at different (A) pyrolysis temperatures at heating rate of 30 °C/min and (B) heating rates to achieve pyrolysis temperature of 550 °C; RSSBC: rubber seed shell bio-char

The presence of mineral matter in biomass has catalytic effect on product formation rates [244, 268, 270, 271]. Generally, the mineral content of biomass depends on the soil and weather condition where the plant has grown. EDX analysis showed that the carbon content was increased from 60.5 wt% (RSS) to 94.1 wt% (bio-char) during pyrolysis (Fig. 6.15A and Fig. 6.15B). Heavy metal arsenic (As) and chromium (Cr) were found to be negligible in both RSS and bio-char sample. Hence, the obtained bio-char can be used as a feedstock for activated carbon synthesis for waste water treatment [129, 266]. The surface morphology of produced bio-char (under optimum pyrolysis condition) was studied using FESEM (Fig. 6.17). The BET surface area of bio-char was estimated to be 175.95 m^2/g with total pore volume and average pore diameter of 0.12 cm^3/g and 2.66 nm, respectively. The structured pore surface with larger area generated in bio-char during pyrolysis can be useful for liquid-solid adsorption [272]. Further, the porous nature of bio-char may help retaining soil nutrient, improving water holding capacity, and microbial activity as well as favorable for activated carbon preparation [266, 272]. The presence of inorganic elements (nutrients), observed by EDX analyses (Fig. 6.15), can also play an important role for soil fertility [130, 273].

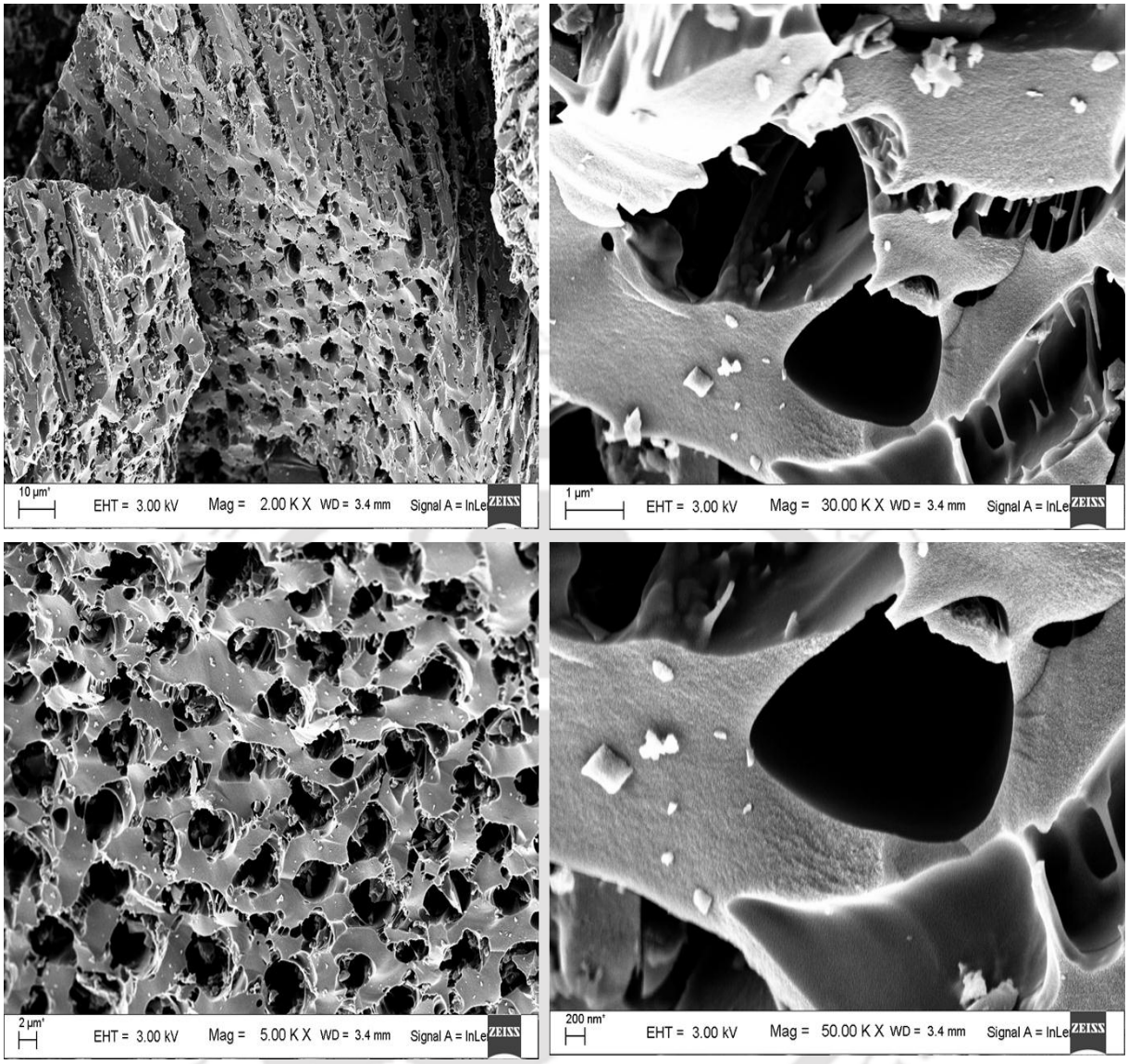

Fig. 6.17: FESEM micrographs of RSS bio-char obtained at 550 °C for 30 °C/min heating rate at different magnification (2kx, 5kx, 30kx and 50kx)

6.3.4. *Characterization of RSS Pyrolytic Liquid Product*

FT-IR spectra of produced liquid samples from the pyrolysis of RSS at various conditions are shown in Fig. 6.18A and Fig. 6.18B. Table 6.11 summarizes the presence (qualitative) of various functional groups in liquid samples. The O–H stretching vibration, due to the presence of phenolic compound and water was observed at 3400 cm^{-1} [274]. This result was attributed to decomposition of lignin and dehydration of RSS during pyrolysis [275]. Carboxylic acid in the form of acetic acid was also observed in the range of 1700–1725 cm^{-1}. Additionally, ketone and aldehydes compounds were detected as C=H stretching vibration between 1500 and 1675 cm^{-1}. Further, the presence of esters compounds at 1233 cm^{-1} and aromatic compounds (C=C ring stretching) at 1513 cm^{-1} were also identified. A semi-quantitative assessment of hydrogen atoms of oxygenated compounds and hydrocarbons (aliphatic and aromatic) was obtained from integration of appropriate region reported in literature [131, 276]. The integral values of selected regions of ^{1}H NMR are presented in Table A6.2.

Table 6.11: Functional group present in the liquid product (pyrolytic liquid) obtained from pyrolysis of RSS at different temperatures and heating rates

Characteristic peaks (cm^{-1})	Molecular vibration	Remark for functional group						
Pyrolysis Temperature (°C) for 30 °C/min			350	400	450	500	550	600
750	C–H out of plane bending	Aromatic	×	√	√	√	√	×
1046	C–O–C stretching	–	√	√	√	√	√	√
1233	C–O stretching	Esters	√	√	√	√	√	√
1367	C–H bending	Alkane	√	√	√	√	√	√
1513	C=C–C stretching	Aromatic ring	×	√	√	√	√	√
1605	C–H stretching	Alkene, carbonyl	√	√	√	√	√	√
1712	C=O stretching	ketone	√	√	√	√	√	√
2940	C–H stretching	Alkane	×	√	√	√	√	×
3400	–OH stretching	Hydroxyl, water	√	√	√	√	√	√
Heating rate (°C/min) for 550 °C			10	20	30	40		
750	C–H out of plane bending	Aromatic	√	√	√	×		
1046	C–O–C stretching	–	√	√	√	√		
1233	C–O stretching	esters	√	√	√	√		
1367	C–H bending	Alkane	√	√	√	√		
1513	C=C–C stretching	Aromatic ring	√	√	√	√		
1605	C–H stretching	Alkene, carbonyl	√	√	√	√		
1712	C=O stretching	ketone	√	√	√	√		
2940	C–H stretching	Alkane	√	√	√	×		
3400	–OH stretching	Hydroxyl, water	√	√	√	√		

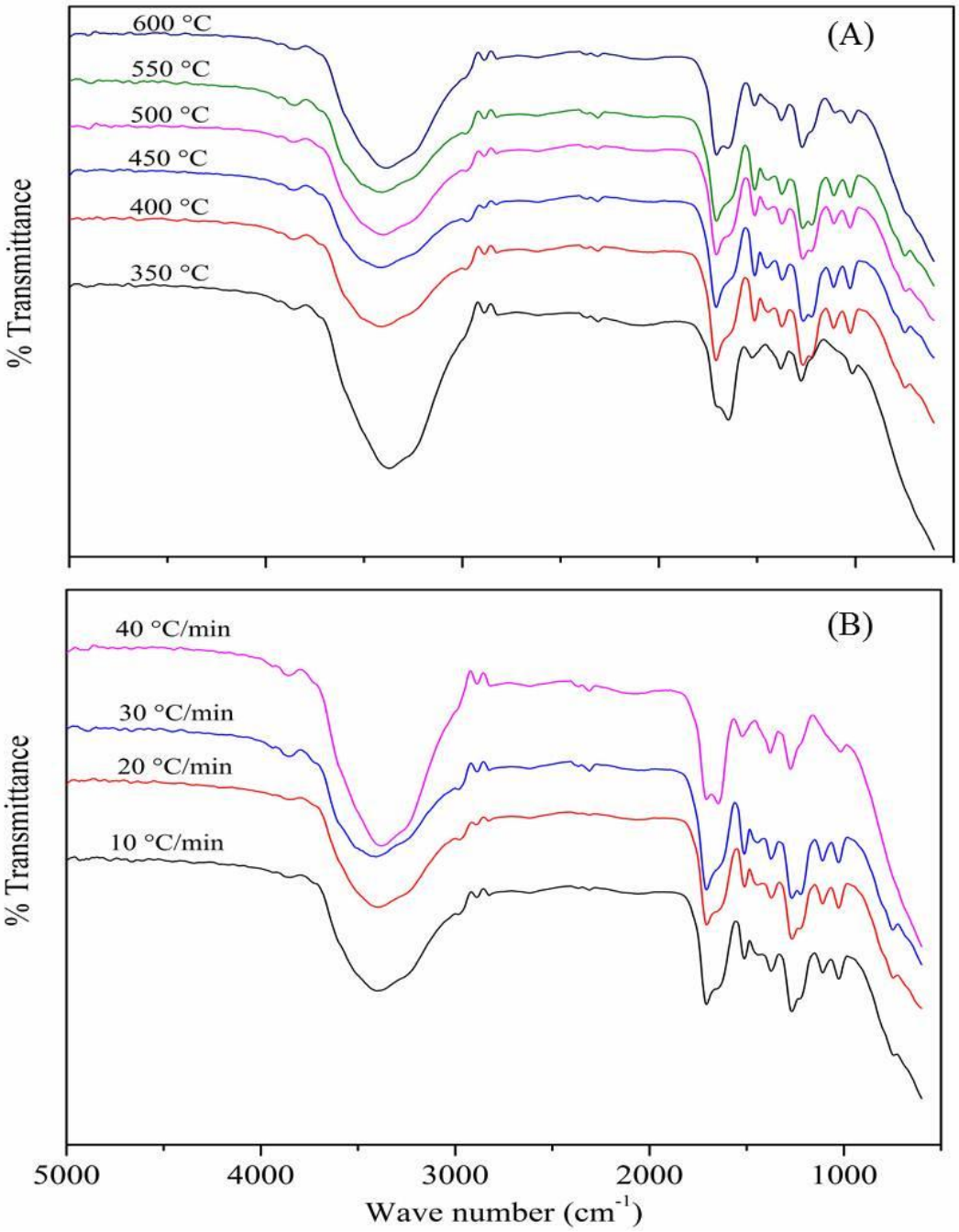

Fig. 6.18: FT-IR spectra of pyrolytic liquid from pyrolysis of RSS at various (A) pyrolysis temperatures at 30 °C/min and (B) pyrolysis heating rates at 550 °C

The chromatograms of liquid products generated from GC-MS analysis are shown in Fig. A6.1A and Fig. A6.1B. The compositions of liquid samples were determined based on the relative peak area of identified components (Table 6.12). Acetic acid, phenolic compounds, creosol, pilocarpine, benzene and 3-Hydroxy-4-methoxybenzoic acid, levoglucosan and eugenol were identified as most abundant organic products (Table 6.12). The presence of oxygenated aromatic compounds such as acid, phenols and creosol in liquid produced from the pyrolysis of shell and cake are also reported in literature [128, 276]. The highest peak area was obtained for phenolic compound and acetic acid. The acetic acid and water were produced during pyrolysis of RSS, due to the deacetylation and cleaved (depolymerised and acetyl groups) of hemicellulose [260, 275, 277]. Major phenolic compounds as phenol, 2-methoxy-, phenol, 2, 6-dimethoxy-, phenol, 4-ethyl-2-methoxy- and other trace amount of phenolic compounds were observed at higher pyrolysis temperature. These results can be attributed to decomposition of lignin [128, 278]. Further, the presence of creosol indicates the decomposition of some portion of lignin. According to GC-MS analysis, nitrogen containing organic compounds such as pilocarpine was also identified due to moderate pyrolysis temperature [261]. It is clear from Table 6.11 that the liquid product can be used as bio-chemical feedstock for production of resin, surfactant, and antioxidants, as it contains high phenolic compound [122, 279]. The liquid product can also be utilized as a hydrocarbon source for production of value added chemicals such as ethyl vinyl, resins and adhesives [280].

Table 6.12: Chemical compositions of pyrolytic liquid sample of rubber seed shell, identified by GC-MS

Pyrolysis temperature (°C) for heating rate of 30°C/min	350	400	450	500	550	600
Compound	Peak area (%)					
Acetic Acid	2.55	5.36	5.16	12.8	10.24	13.9
Acetic Acid, (acetyloxy)-	–	0.71	0.89	2.55	1.9	2.97
1-Nitro-2-propanone	–	0.2	0.25	0.6	1.17	1.71
Pilocarpine	–	0.58	0.77	2.01	1.93	3.15
Phenol	0.45	–	0.19	0.7	1.08	1.17
1,2-Cyclopentanedione, 3-methyl-	–	0.35	0.48	2.15	1.94	1.91
Benzyl alcohol	–	0.03	0.18	0.98	1.08	0.97
p-Cresol	–	–	0.24	1.13	1.73	1.51
Phenol, 2-methoxy-	–	1.68	2.61	7.59	6.88	6.95
Phenol, 3,5-dimethyl-	–	–	–	0.32	1.0	0.76
Creosol	–	1.74	2.89	11.7	15.01	11.3
1,2-Benzenediol, 3-methyl-	–	0.13	0.26	0.27	1.43	0.55
1,4-Benzenediol, 2-methoxy-	–	0.13	0.26	1.44	2.56	1.07
Phenol, 4-ethyl-2-methoxy-	–	1.08	1.38	2.63	3.95	2.5
1,2-Benzenediol, 4-methyl-	–	–	–	1.96	2.94	1.69
Phenol, 2,6-dimethoxy-	–	1.47	1.71	6.18	7.58	4.8
Benzaldehyde, 3-hydroxy-4-methoxy-	0.4	0.36	0.43	2.83	2.28	1.42
Ethanone, 1-(2,3,4-trihydroxyphenyl)-	–	1.12	1.32	4.26	5.92	3.21
Eugenol	–	0.2	0.41	1.24	4.25	1.03
Levoglucosan	–	0.56	5.0	10.7	13.17	8.75
Benzene, 1,2,3-trimethoxy-5-methyl-	–	0.63	0.64	1.65	3.1	1.30
2-Propanone, 1-(4-hydroxy-3-methoxyphenyl)-	–	0.55	0.72	2.61	3.5	2.06
Diphenyl sulfide	–	–	–	1.53	0.03	0.69
Homovanillic acid	–	–	0.62	0.68	1.35	0.65
Phenol, 2,6-dimethoxy-4-(2-propenyl)-	–	0.23	0.56	0.73	2.56	0.56
Xanthoxylin	–	–	0.23	0.72	0.86	0.55
Glycoldial, bis-O-Pentafluorobenzyloxime	–	–	0.21	0.44	0.57	0.36

Balance is peak area for solvent

6.4. Pyrolysis of RSC in Semi-batch Reactor

Similar to RSS sample, dehydration, depolymerization, decomposition and fragmentation reactions of three key biomass building blocks in RSC sample: hemicellulose, cellulose and lignin, and extractives occur at elevated temperature conditions. TGA profiles of RSC samples (Fig. 6.4) confirmed that the active pyrolysis of RSC occurred in the temperature range of 200 °C–620 °C. Therefore, lab scale reactor pyrolysis of RSC was conducted in the active pyrolysis temperature range of 350 °C to 600 °C with 50 °C increment. The effects of pyrolysis temperatures (350–600 °C) and heating rates (10–40 °C/min) on product distribution (liquid, bio-char and gas) and quality (composition and energy content) are investigated.

6.4.1. *Effect of Pyrolysis Temperature on Product Distribution*

Fig. 6.19 shows the product distribution from pyrolysis of RSC sample at a heating rate of 30 °C/min to achieve the final pyrolysis temperature of 350–600 °C. As can be seen in Fig. 6.19A, an increase in the temperature affected the yields of the products. The yield of bio-char was found to be decreased from 44.63 wt% to 23.5 wt% as temperature increased from 350 °C to 600 °C. This may be due to the decomposition of the three main components (hemicellulose, cellulose and lignin) and volatilization of volatile organic compounds (organic extractives) at higher temperature. However, bio-char was mainly produced due to primary volatilization of hemicellulose, cellulose and lignin [131, 280]. Higher yield of bio-char (unconverted) at lower pyrolysis temperature was due to partial decomposition of feedstock (RSC). Continuous decrease in the yield of bio-char is attributed to secondary cracking of solid residue. In other words, the pyrolysis conversion of RSC was increased at higher

temperature. Hence, the yield of gaseous product also increased from 21.2 wt% to 32.58 wt% as temperature increased from 350 °C to 600 °C. The yield of liquid product was increased from 34.18 wt% to 47.13 wt% as pyrolysis temperature increased from 350 °C to 500 °C. Further increase in pyrolysis temperature to 600 °C reduced the yield of liquid product to 43.93 wt% and, increased the formation of non-condensable gases due to secondary cracking of primary pyrolytic products [274]. The liquid products contain two phase such as aqueous and organic phase (bio-oil). As can be seen from Fig. 6.19A, maximum liquid yield (47.13 wt%) and 19.07 vol/wt% of bio-oil from the liquid product was obtained at 500 °C. The time required for completion of pyrolysis were found to be 50 min, 35 min and 28 min for pyrolysis temperature of 350 °C, 500 °C and 600 °C, respectively (Table A6.3). Considering the yield of liquid product (47.13 wt%), bio-char (25.27 wt%) and calorific value for bio-oil (32.72 MJ/kg) and bio-char (26.99 MJ/kg) obtained at 500 °C pyrolysis temperature was taken as optimum temperature, the effects of heating rates and co-pyrolysis RSC with waste polystyrene on product distribution and calorific value of bio-char and bio-oil were further investigated in the present study.

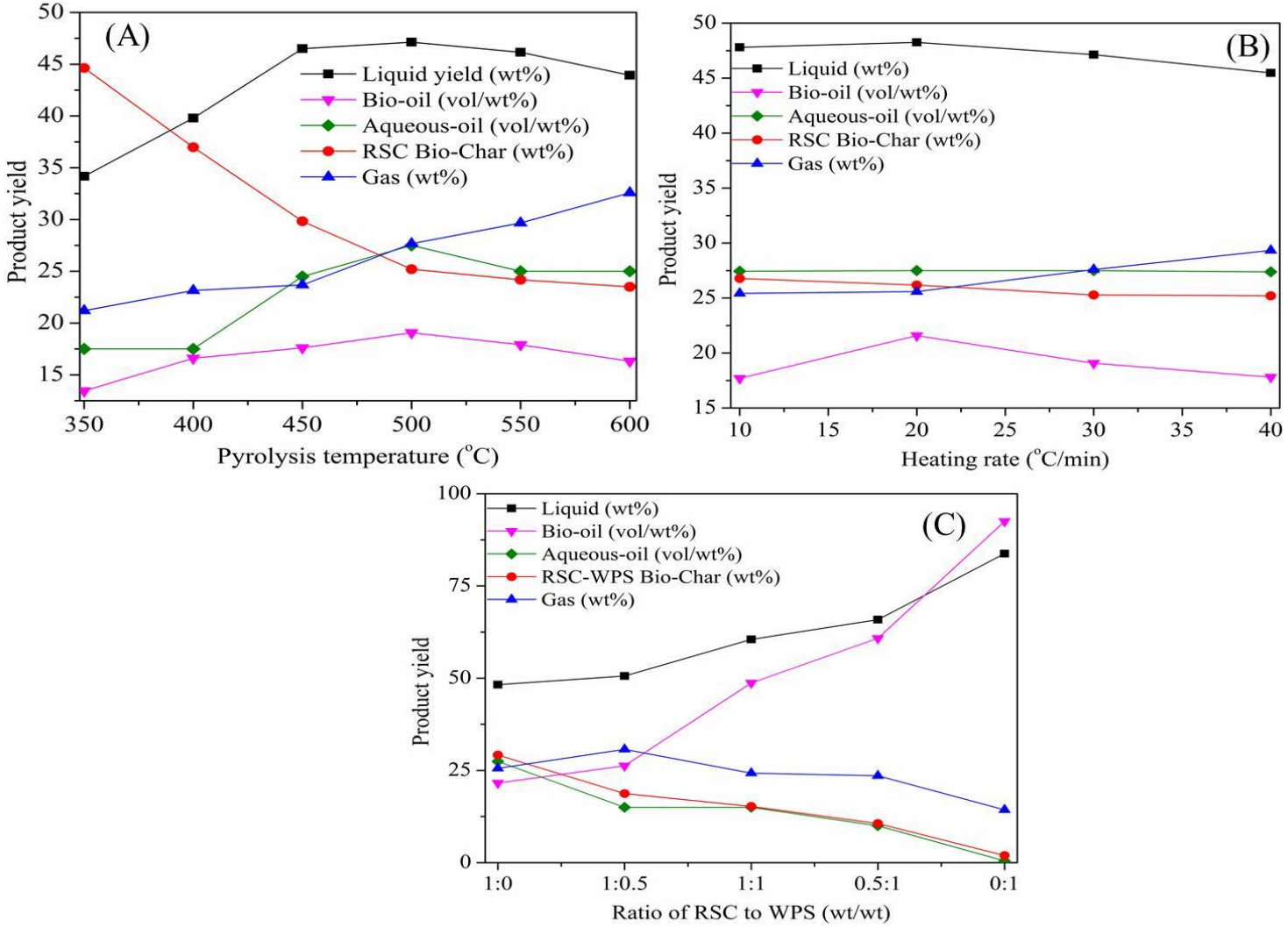

Fig. 6.19: Effect of (A) pyrolysis temperatures at heating rate of 30 °C/min and (B) heating rates for pyrolysis temperature of 500 °C and (C) co-pyrolysis for pyrolysis temperature of 500 °C on product distribution

6.4.2. *Effect of Heating Rate on Product Distribution during Pyrolysis of RSC*

Fig. 6.19B show the product distribution of RSC pyrolysis in relation to heating rates (10, 20, 30 and 40 °C/min) to reach final temperature of 500 °C. The conversion of RSC (i.e. condensable and non-condensable product) was slightly increased from 73.22 wt% to 74.8 wt% as heating rate increased from 10 °C/min to 40 °C/min. In other words, the bio-char yield decreased from 26.78 wt% to 25.2 wt% as heating rate increased from 10 °C/min to 40 °C/min. However, the yield of liquid product initially increased from 47.8 wt% to 48.25 wt% as heating rate increased from 10 °C/min to 20 °C/min and then decreased to 45.47 wt% at heating rate of 40 °C/min. The yield of bio-oil increased from 17.7 vol/wt% (10 °C/min) to 21.58 vol/wt% (20 °C/min) and then decreased to 17.8 vol/wt% (40 °C/min). In contrast, the yield of gaseous product was maximum (29.33 wt%) at heating rate of 40 °C/min and minimum at heating rate of 10 °C/min (25.42 wt%). This may be due to fast depolymerization of solid biomass to non-condensable gas formation during rapid heating rates [130]. The calorific values obtained at different heating rates (10 °C/min–40 °C/min) were found to be nearly similar in both bio-oil (32.25 MJ/kg–33.1 MJ/kg) and bio-char (26.08 MJ/kg–27.2 MJ/kg) samples. Overall, the pyrolysis heating rates to rich final temperature (500 °C) has less effect on product distribution (yield) and calorific value of bio-char and bio-oil as compared to pyrolysis temperature. The time required for completion of reaction decreased from 55 min to 28 min with an increase in the heating rate from 10 °C/min to 40 °C/min (Table A6.3). Based on the yield of bio-oil and calorific value of bio-oil and bio-char; heating rate of 20 °C/min was found to optimum for pyrolysis of RSC sample.

6.4.3. *Co-Pyrolysis RSC with Waste Polystyrene*

Now a day solid waste disposal is a great challenge for urban area around the world [246]. The volume of waste commodity plastic such as polystyrene (PS), polyethylene terephthalate (PET), low density polyethylene (LDPE), polyvinyl chloride (PVC) is increasing because of its light weight, low cost, durability, etc. Due to light weight, low cost and durability; the PS has wider application. Most of PS waste dumped landfilling sites but dumping of PS waste is not an environmental friendlily option because the plastic waste (PS) is not biodegradable [58, 281]. Co-pyrolysis of PS with biomass is a promising option to increase the calorific value of biodiesel and pyrolytic oil and, also pyrolysis (thermal cracking in an inert atmosphere) of PS to produce liquid fuel [133]. Meanwhile, use of biomass waste and PS wastes for liquid fuel generation by co-pyrolysis process is a key to overcome environmental challenges from biomass and PS waste and also improve the quality and quantity of bio-oil [155].

Influence of addition of waste polystyrene during RSC pyrolysis on product distribution and calorific value of bio-oil was investigated at optimum condition mentioned above (pyrolysis temperature of 500 °C at heating rate of 20 °C/min). The ratio of RSC to WPS (waste polystyrene) in the feed was varied as 1:0, 2:1, 1:1 and 1:2. The product distribution obtained from co-pyrolysis of RSC and WPS is presented in Fig. 6.19C. The yield of liquid product was increased from 48.25 wt% (1:0 ratio of RSC to WPS) to 65.85 wt% (1:2 ratio of RSC: WPS). In other words, the yield of bio-oil enhanced due to addition of WPS from 21.58 vol/wt% to 60.8 vol/wt%. But, the yield of gas was found to be decreased (23.55 wt%) at lower ratio of RSC to WPS (1:2 wt/wt). Similar trends were reported by Shadangi, Mohanty [135] and Abnisa *et al.* [134] during co-pyrolysis of karanja and palm shell seed with waste polystyrene, respectively. Furthermore, the calorific values of obtained co-pyrolytic bio-oil

(37.48 MJ/kg–41.1 MJ/kg) were found higher than that of thermal pyrolytic bio-oil (32.25 MJ/kg). This may be due to higher carbon to hydrogen and oxygen ratio in WPS sample [133, 134, 281]. It was also obtained that the co-pyrolysis process reduced the water content of bio-oil from 11.62 wt% to 2.38 wt%. However, the calorific values of bio-char sample obtained from co-pyrolysis were proximity similar with that of thermal pyrolytic bio-char. Furthermore, the reaction time for completion was slightly faster during co-pyrolysis of RSC with WPS sample (Table A6.3).

6.4.4. *Characterization of RSC Bio-Char*

The proximate and ultimate analyses of bio-char obtained from the pyrolysis of RSC samples at different pyrolysis conditions are shown in Table 6.13 and Table 6.14. The moisture content of produced bio-char was found to be varied from 3.96 to 4.77 wt% as the pyrolysis temperature varied from 350 °C to 600 °C. However, the variations (moisture content of bio-char) were less for different pyrolysis heating rate and co-pyrolysis bio-char. Ash, volatile matter and fixed carbon content for the produced bio-char were measured on dry basis (moisture free sample) (Table 6.13). The ash content is a measure of the non-volatile and non-combustible (inorganic minerals) component of RSC bio-char sample. The ash content of RSC bio-char increased from 12.48 wt% (350 °C) to 23.09 wt% (600 °C) at heating rate of 30 °C/min. However, the values were not changed significantly (19.99 wt% to 22.35 wt% and 20.25 wt% to 23.89 wt%) when the heating rate and ratio of RSC: WPS increased from 10 °C/min to 40 °C/min and 1:0 to 1:2, respectively. The volatile matter of RSC bio-char decreased (i.e. from 51.40 wt% to 20.94 wt%) with an increase in the pyrolysis temperature. This may be due to more bonds broken by higher energy supply to the sample. While, the

influence of heating rates on volatile matter RSC bio-char was less. The high volatile matter content of bio-char at 350 °C pyrolysis temperature suggested that the RSC sample was partially pyrolyzed. Subsequent rearrangement reactions and, release of volatile matter and gases strengthen the carbon matrix in bio-char sample which result in higher fixed carbon content and low volatile component. It was also clearly observed that, as the final pyrolysis temperature increased from 350 °C to 600 °C, the fixed carbon content of the bio-char continuously increased from 36.12 wt% to 56.97 wt%. Pyrolysis temperature had shown significant influence on characteristics properties of bio-char (i.e. carbon content (Table 6.14, product distribution Fig. 6.19A and XRD pattern Fig. 6.20 and Fig. 6.21) compared to heating rate (Fig. 6.19B). Similar observation can also be drawn from proximate (Table 6.13), ultimate (Table 6.14) and XRD (Fig. 6.16) analyses of bio-char samples. XRD pattern obtained for RSC and produced bio-char samples are presented in Fig. 6.20A–B and Fig. 6.21C. Two peaks at 2θ values around 16° and 22° for RSS sample belong to the crystalline region of cellulose [250, 269]. Since the cellulose presented in RSC was completely degraded during pyrolysis (≥400 °C), these peaks disappeared in the spectra for bio-char, Fig. 6.20A–B.

Table 6.13: Proximate analysis of bio-char obtained from pyrolysis of RSC at various pyrolysis conditions

(A)	Pyrolysis temperature (°C) at heating rate of 30 °C/min					
	350	400	450	500	550	600
MC	3.96	4.53	4.42	4.95	4.79	4.77
Volatile matter (wt%)	51.40±0.05	39.64±0.16	35.04±0.25	24.89±0.05	22.25±0.15	21.94±0.05
Ash (wt%)	12.48±0.01	15.33±0.03	18.53±0.15	20.25±0.55	21.72±0.32	23.09±0.01
Fixed carbon (wt%)*	36.12±0.06	45.03±0.29	46.43±0.4	54.86±0.6	56.03±0.47	54.97±0.06
HHV (MJ/kg)	24.6	25.41	25.45	26.99	26.99	28.43

(B)	Heating rate (°C/min) for 500 °C pyrolysis temperature			
	10	20	30	40
MC	4.32	4.46	4.95	4.46
Volatile matter (wt%)	27.01	25.86	24.89	24.68
Ash (wt%)	19.99±0.02	20.25±0.01	20.25±0.02	22.31±0.05
Fixed carbon (wt%)*	53.00	53.89	54.86	53.01
HHV (MJ/kg)	26.08	26.59	26.99	27.2

(C)	Co-pyrolysis: RSC to WPS ratio			
	0:1	2:1	1:1	1:2
MC	4.46	5.21	5.37	4.17
Volatile matter (wt%)	25.86	27.36	27.98	27.05
Ash (wt%)	20.25±0.01	21.51	21.97	23.89
Fixed carbon (wt%)*	53.89	51.13	50.05	49.06
HHV (MJ/kg)	26.99	26.91	27.02	27.12

**Calculated by difference*

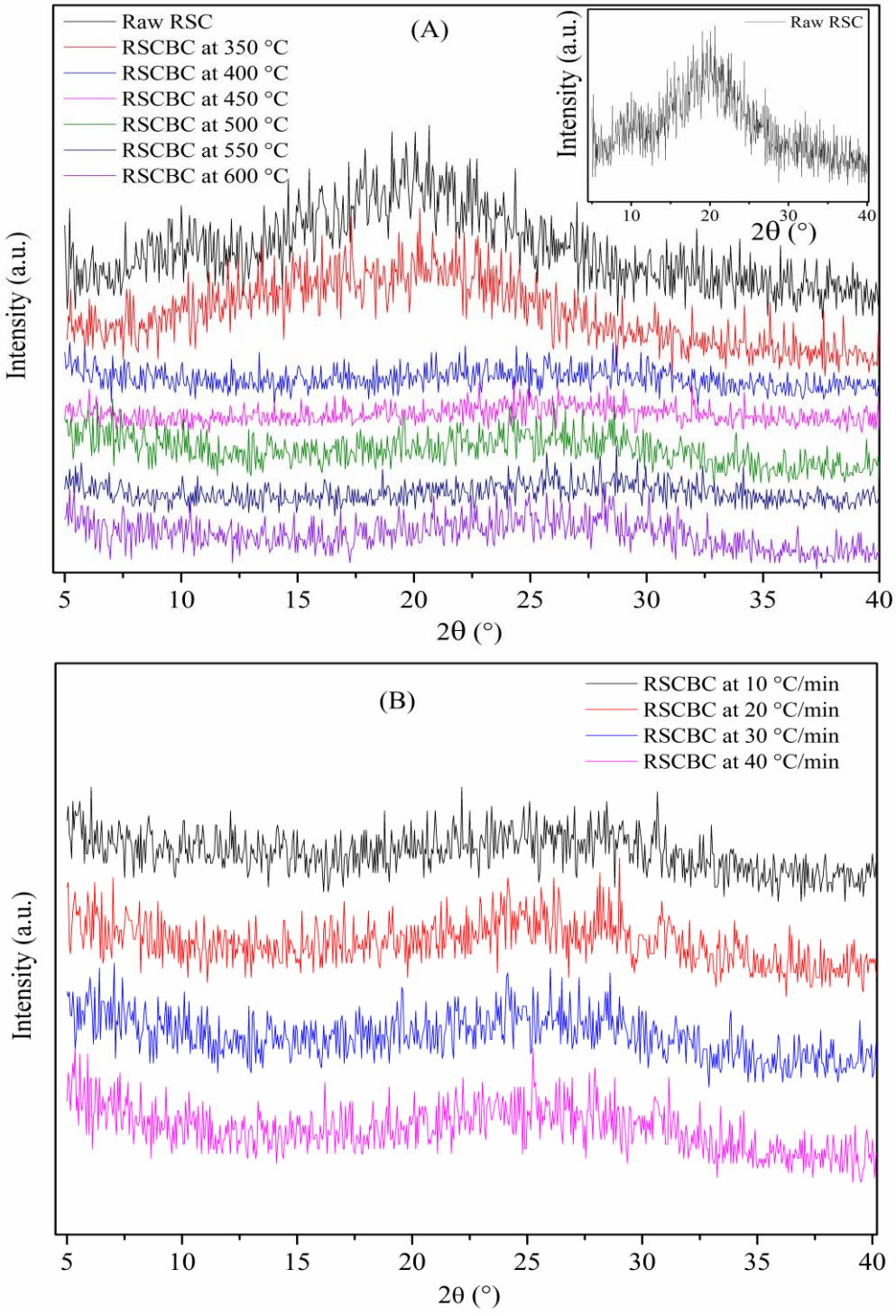

Fig. 6.20: XRD analysis of raw RSC and bio-char samples obtained from pyrolysis of RSC at different (A) temperatures at heating rate of 30 °C/min and (B) heating rates at pyrolysis temperature of 500 °C; RSCBC: rubber seed cake bio-char

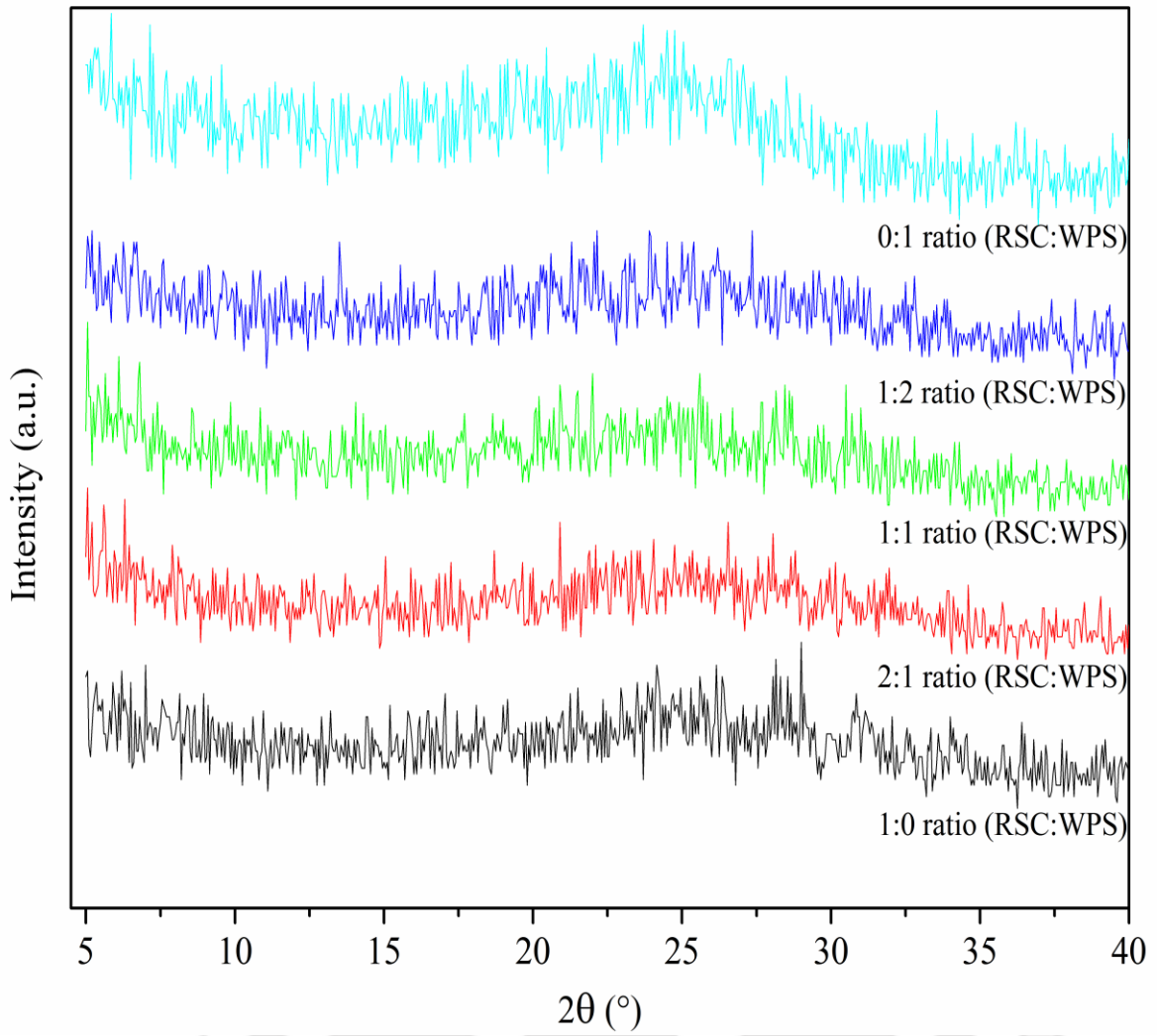

Fig. 6.21: XRD analysis of bio-char obtained from co-pyrolysis of WSP with RSC; WPS: waste polystyrene

Table 6.14: Elemental compositions of bio-char obtained from the pyrolysis of RSC at various conditions

(A)	Pyrolysis temperature (°C) at 30 °C/min heating rate					
	350	400	450	500	550	600
C (wt%)	57.75	58.97	60.28	62.34	63.29	64.38
H (wt%)	5.33	4.39	3.63	2.73	2.22	1.89
N (wt%)	8.45	8.37	7.86	7.53	6.88	6.75
S (wt%)	–	–	–	–	–	–
O* (wt%)	28.47	28.27	28.23	27.4	27.6	26.98
HC (wt%)	63.08	63.36	63.91	65.07	65.51	66.27
H/C, molar ratio	1.11	0.89	0.72	0.52	0.42	0.35
O/C, molar ratio	0.37	0.36	0.35	0.33	0.33	0.31
(B)	Heating rate (°C/min) for 550 °C pyrolysis temperature					
	10	20	30	40		
C (wt%)	61.84	62.01	62.34	63.04		
H (wt%)	2.83	2.82	2.72	2.56		
N (wt%)	7.91	7.88	7.53	7.70		
S (wt%)	–	–	–	–		
O* (wt%)	27.42	27.29	27.41	26.68		
HC (wt%)	64.67	64.83	65.06	65.6		
H/C, molar ratio	0.551	0.546	0.52	0.49		
O/C, molar ratio	0.333	0.33	0.33	0.32		
(C)	Co-pyrolysis: RSC to WPS ratio					
	1:0	2:1	1:1	1:2		
C (wt%)	62.01	62.34	63.38	64.20		
H (wt%)	2.82	2.71	2.67	2.65		
N (wt%)	7.88	7.53	7.22	7.30		
S (wt%)	–					
O* (wt%)	27.29	27.41	26.74	25.85		
HC (wt%)	64.83	65.06	66.04	66.85		
H/C, molar ratio	0.55	0.52	0.51	0.49		
O/C, molar ratio	0.33	0.33	0.32	0.30		

**by difference*

The results of elemental analysis of bio-char obtained from pyrolysis of RSC at various pyrolysis conditions are shown in Table 6.14. The total hydrocarbon content (C and H) present in produced bio-char were varied from 63.084 wt% to 66.268 wt% for pyrolysis temperature from 350 °C to 600 °C. On the other hand, the carbon content for raw RSC (54 wt%) increased to 57.751 wt% (350 °C) and 64.381 wt% (600 °C) due to volatilization of RSC. However, the hydrogen and oxygen content decreased from 5.33 wt% to 1.887 wt% and 28.467 wt% to 26.983 wt%, respectively. The values C, H and O in produced bio-char were slightly influenced by heating rate and co-pyrolysis (Table 6.14). Due to the lower content of carbon, the bio-char obtained from pyrolysis of RSC alone had slightly lower calorific value than those obtained from co-pyrolysis. The H/C and O/C molar ratios were gradually decreased as pyrolysis temperature increased, implying thatm the produced bio-chars become more aromatic and carbonaceous [129, 282]. The lower H/C and O/C ratios for bio-char also indicated that carbon atoms in the sample predominantly are unsaturated. Further, various minerals present in RSC and bio-char obtained at 500 °C pyrolysis temperature for 20 °C/min heating rate were determined by EDX (Fig. 6.22). Pyrolysis of RSC increases the concentration of inorganic minerals and carbon (Fig. 6.22).

FESEM images of RSC (Fig 6.2B), and RSC bio-char (Fig. 6.23) obtained at 500 °C pyrolysis temperature shows change on morphology of the surface due to volatilization during pyrolysis process. From RSC bio-char surface (Fig. 6.23), it was observed to have rough surface (2.00 k and 5.00 k magnification) with the different pore structure (10.00 k and 50.00 k magnification). Further the pours nature of the produced bio-char was supported by nitrogen adsorption-desorption analysis. RSC bio-char reveal that the average pore size (21.49 nm) and total pore volume (0.026 cm^3/g). The BET surface area of RSC bio-char was found to be 5

m^2/g.

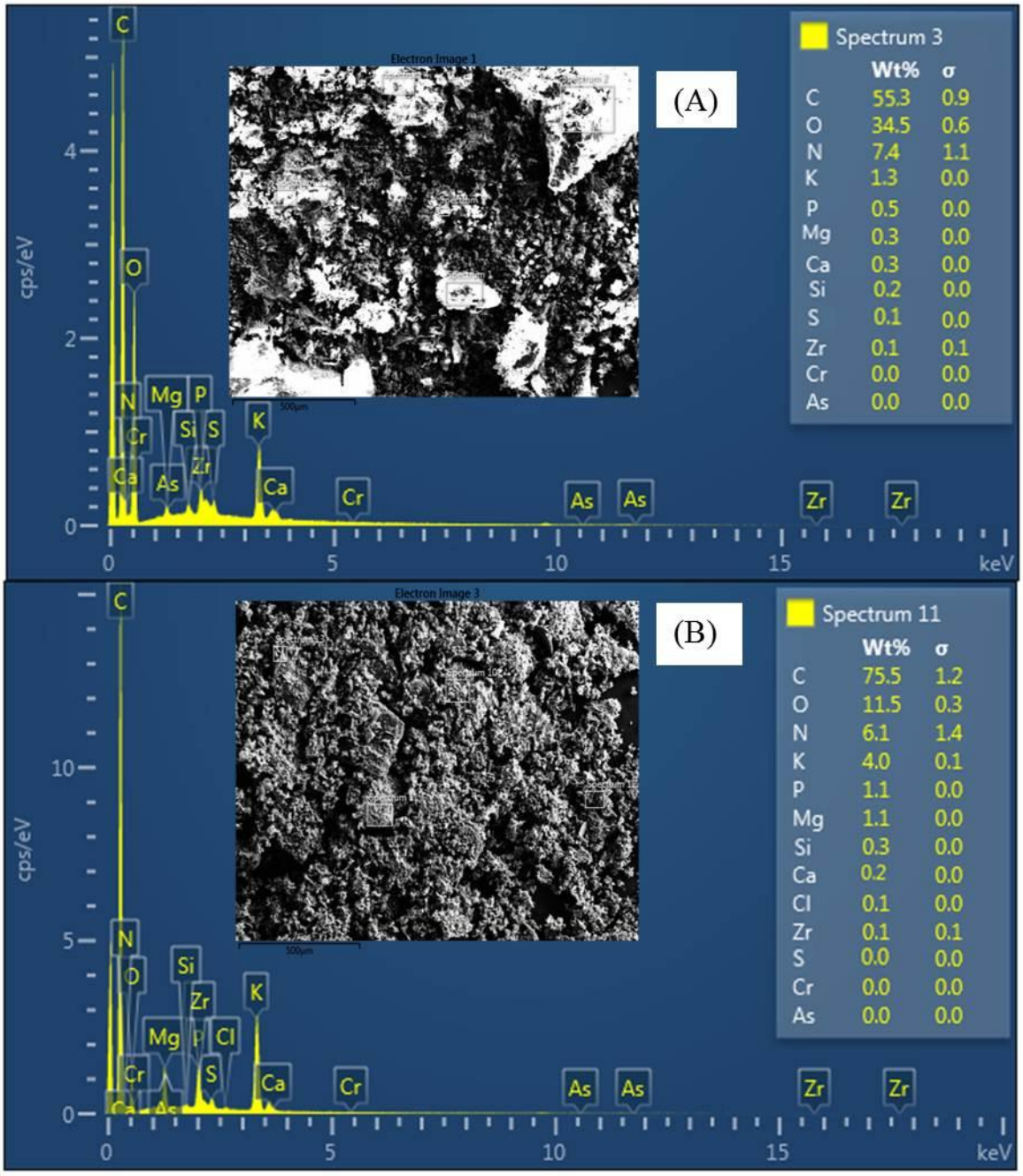

Fig. 6.22: EDX analysis of (A) raw RSC and (B) bio-char sample obtained from pyrolysis of RSC at 500 °C

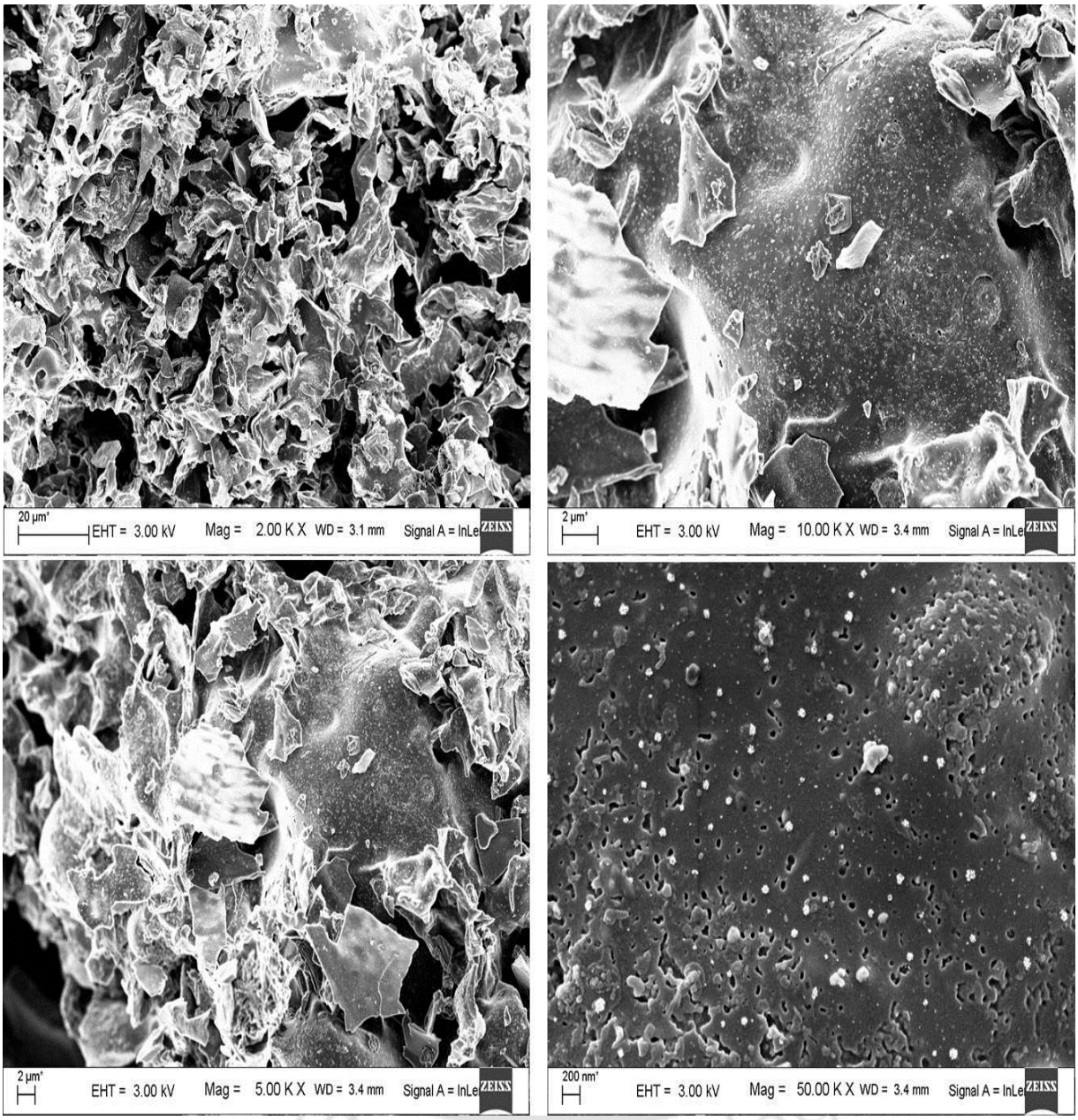

Fig. 6.23: FESEM micrographs of bio-char sample obtained from RSC at 500 °C for 30°C/min heating rate at different magnification (2kx, 5kx, 10kx and 50kx)

6.4.5. *Characterization of RSC and Co-Pyrolytic Liquid Product*

The bio-oil obtained from the pyrolysis of RSC sample was reddish brown in color. Calorific value of RSC bio-oil obtained at various pyrolysis conditions are presented in Table 6.15. The calorific value of biomass RSC 19.58 MJ/kg was increased to 22.12–41.1 MJ/kg bio-oil. Energy content analysis indicates a high calorific value of bio-oil ≥32.72 MJ/kg for higher pyrolysis temperature (>500 °C) which is close to that of transportation grade fuel. Further, addition of 50 wt% waste polystyrene to the feed RSC increased caloric value of RSC bio-oil to 37.61 MJ/kg.

Table 6.15: Calorific value of bio-oil obtained from RSC at various pyrolysis conditions

Parameter	Pyrolysis temperature (°C) at 30 °C/min					
	350	400	450	500	550	600
HHV (MJ/kg)	22.12	26.59	29.65	32.72	33.39	33.5
	Pyrolysis heating rate (°C/min) for 500 °C					
	10	20	30	40		
HHV (MJ/kg)	32.66	32.25	32.72	33.1		
	Ratio of RSC to WPS (weight basis)					
	1:0	2:1	1:1	1:2	0:1	
HHV (MJ/kg)	32.25	37.48	37.61	41.1	42.1	

The FT-IR spectra of RSC bio-oil are given in Fig. 6.24 (A–C) and summarized in Table 6.16. The signature at around 3500 cm^{-1} represents –OH stretching vibration due to phenolic and alcohol compounds in produced bio-oil. The broad signal 3500–3200 cm^{-1} slightly decreased as WPS amount increased. The aromatic structure (i.e. =C–H stretching vibration)

were observed between 3040–3000 cm^{-1}. The bending stretching as –C=C bond corresponding to aromatic skeleton was observed at signal 1680–1590 cm^{-1}. The C–O stretching vibration in the range of 1280–1250 cm^{-1} and 1050–1030 cm^{-1} were probably due to alcohol and esters presence in bio-oil. The bands at ~2970 cm^{-1}, 2950–2930 cm^{-1} and 2870–2850 cm^{-1} represent alkyl ($–CH_3$) and alkenyl ($=CH_2$) stretching vibration for aliphatic compounds. The presence of the olefinic compounds is also confirmed by the signal between 1625–1590 cm^{-1}, arising from the C=C stretching vibration. Their presence in bio-oil indicated the presence of carboxylic acids. The presence of oxygen in the bio-oil samples were represented by the signal C=O stretching between 1770–1665 cm^{-1} which indicate a carbonyl group.

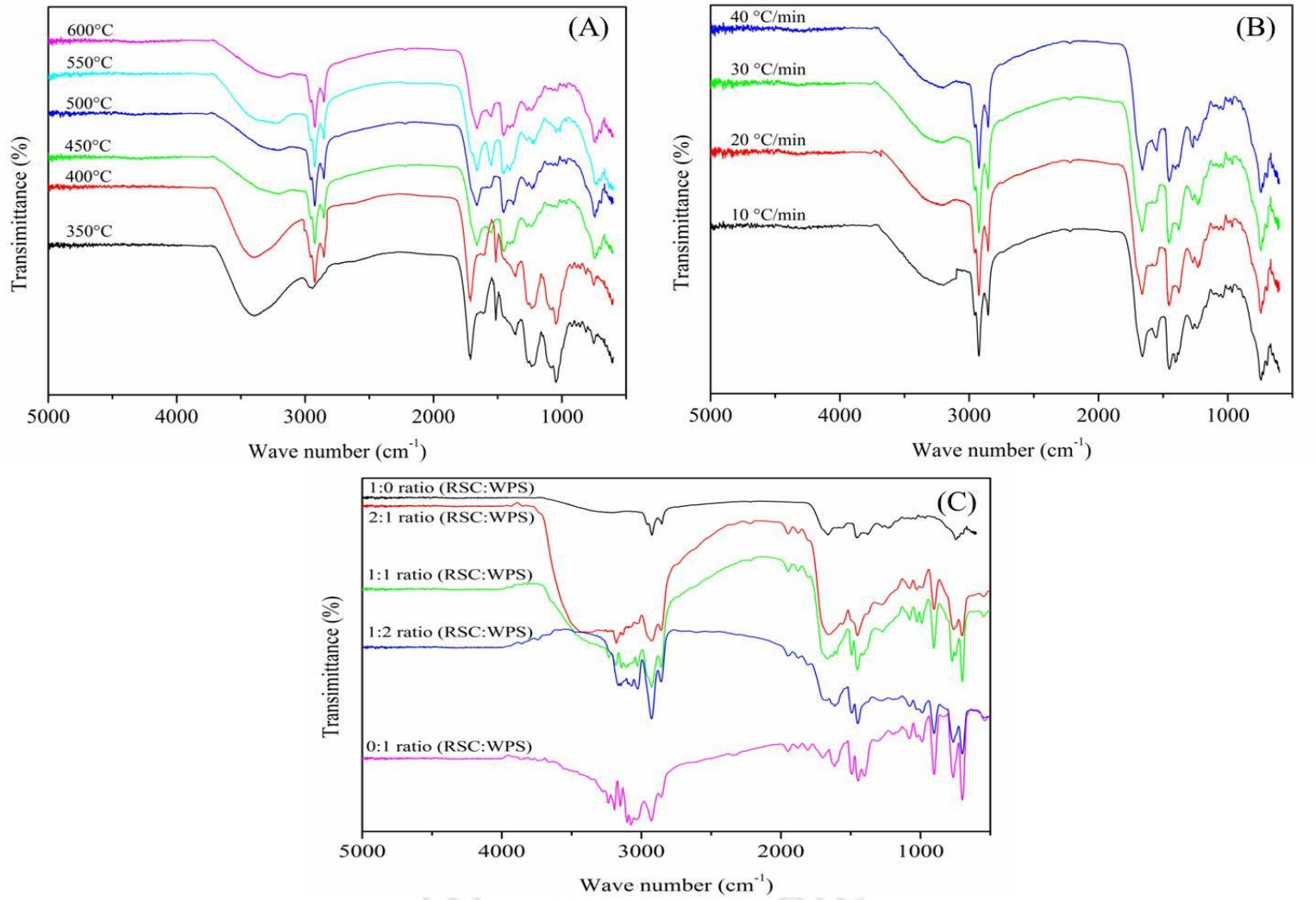

Fig. 6.24: FT-IR spectra of bio-oil obtained from RSC pyrolysis (A) at various pyrolysis temperatures at 30 °C/min, (B) at various pyrolysis heating rate at 500 °C and (C) co-pyrolysis of RSC at various compositions

Table 6.16: Functional group present in bio-oil obtained from pyrolysis of RSC samples at different pyrolysis temperatures and heating rates

Characteristic peaks (cm^{-1})	Molecular vibration	Remark for functional group						
Pyrolysis Temp (°C) for 30 °C/min			350	400	450	500	550	600
740–675	C–H out of plane bending (C–H and =C–H)	Aromatic	√	√	√	√	√	√
1275–1070	C–O–C stretching	–	√	√	√	√	√	√
1233	C–O stretching	Esters	√	√	√	√	√	√
1280–1250, 1050–1030	C–O stretching	Alcohols, phenol, ethers and esters	√	√	√	√	√	√
1367	Symmetrical C–H bending of CH_3	Aliphatic (Alkane)	√	√	√	√	√	√
1456	$–NH_2$ stretching	Nitrogenous compounds	√	√	√	√	√	√
1456 and 1377	Symmetric C–H bending vibration of aliphatic CH_3	Aliphatic	×	√	√	√	√	√
1552	C=C–C stretching	Aromatic ring	√	√	√	√	√	√
1625–1590	C=C stretching	Alkene, Carbonyl	√	√	√	√	√	√
1770–1665	C=O stretching	ketone	√	√	√	√	√	√
2870–2850	Asymmetrical C–H stretching vibration	Aliphatic CH_3 and CH_2	×	√	√	√	√	√
2980–2930	Asymmetrical C–H stretching vibration	Aliphatic CH_3 and CH_2	√	√	√	√	√	√
3040–3000	Aromatic =C–H stretching	–	×	√	√	√	√	√
3400	–OH stretching	Hydroxyl, water	√	√	√	√	√	√

Table 6.16 (Continued)

Heating rate (°C/min) for 550 °C			10	20	30	40
740–675	C–H out of plane bending (C–H and =C–H)	Aromatic	√	√	√	×
1275–1070	C–O–C stretching	–	√	√	√	√
1233	C–O stretching	Esters	√	√	√	√
1280–1250, 1050–1030	C–O stretching	Alcohols, phenol, ethers and esters	√	√	√	√
1367	Symmetrical C–H bending of CH_3	Aliphatic (Alkane)	√	√	√	√
1456	$–NH_2$ stretching	Nitrogenous compounds	√	√	√	√
1456 and 1377	Symmetric C–H bending vibration of aliphatic CH_3	Aliphatic	√	√	√	√
1552	–C=C–C stretching	Aromatic ring	√	√	√	√
1625–1590	C=C stretching	Alkene, carbonyl	√	√	√	√
1770–1665	C=O stretching	ketone				
2870–2850	Asymmetrical C–H stretching vibration	Aliphatic CH_3 and CH_2	√	√	√	√
2980–2930	Asymmetrical C–H stretching vibration	Aliphatic CH_3 and CH_2	√	√	√	√
3040–3000	Aromatic C–H stretching	–	√	√	√	√
3400	–OH stretching	Hydroxyl, water	√	√	√	√

The structural characterization by ^{1}H NMR analysis of RSC bio-oil sample was performed to obtain an overview of the bio-oil compositions. Various components of bio-oil sample were identified viz. paraffinic, olefinic, aromatics and oxygenated compounds. A semi-quantitative assessment of hydrogen atoms of oxygenated compounds and hydrocarbons (aliphatic and aromatic) was obtained from integration of appropriate region reported in literature [131, 276]. The integral values of selected regions of ^{1}H NMR are presented in Table 6.17. The chemical shift from 0.5 to 1.5 ppm representing aliphatic protons that attached to carbon atom (–CH_3, CH_2 and CH) was more populated for bio-oil obtained at higher pyrolysis temperature of 600 °C (43.5%) as compared to 350 °C pyrolysis temperature (12.6%) and co-pyrolytic bio-oil (4.25%–27.42%) (Table 6.17). The integral region from 1.5–3 ppm represents the protons on the aliphatic carbon atoms (–C=C–) which may be aromatic or olefinic [131]. Presence of lignin derived methoxy phenol was confirmed by the peaks between 4 and 6.0 ppm. The protons counts for the integral region of 5–6 ppm were found to be lower (1.92%) at 350 °C pyrolysis temperature and higher (6.18%) at 600 °C which indicate partial decomposition of RSC sample at lower temperature. The peaks between 6.0 and 9 ppm confirm the presence of oxygen and nitrogen attached with aromatic compounds. The proton percentage for integral region of 6 to 9 ppm for RSC pyrolytic bio-oils (3.31%–13.04%) was lower than that of co-pyrolytic bio-oil (26.36%–49.44%). Further support for FT-IR and ^{1}H NMR analysis was obtained from GC–MS analysis; is a very powerful hyphenated technique that is used to identify the products formed during pyrolysis of biomass. The compounds present in the pyrolytic and co-pyrolytic bio-oil were identified by comparing the mass spectra with standard compounds available from national institute of standards and technology (NIST) library. The GC-MS chromatographs of the different bio-oil samples (Fig.

A6.2A and Fig. A6.2B) and the compounds identified illustrate clearly the difference in the chemical composition of the bio-oil samples based on relative peak areas (Table 6.18–20). The major constituents of RSC pyrolytic and co-pyrolytic bio-oil comprise of aromatic, phenolic and its alkylated derivatives, heterocyclic nitrogen containing compounds (amide and nitrile), long chain fatty acids, esters, alkanes and alkenes (Table 6.18–20). The presence phenol is also evident from FT-IR and ^{1}H NMR analysis which indicates that the degradation of lignin started even at lower temperature. Acetic acid is produced through removal of acetyl groups in hemicelluloses and too a minor extend from cellulose during the pyrolysis process [131]. Among the produced compounds, hydrocarbons are valuable components of bio-oil from fuel application point of view as well as serve as important industrial chemicals and transportation fuel additives to increase octane number [274].

Table 6.17: Hydrogen based ^{1}H NMR analysis of RSC bio-oil

Hydrogen type	Chemical shift (ppm)	Temp (°C)						Heating rate (°C/min)			
		350	400	450	500	550	600	10	20	30	40
CH_3 ɤ or further from aromatic ring and parafinic CH_3	1.0–0.5	3.36	4.2	6.08	10.66	15.91	16.26	16.21	12.92	10.66	13.17
CH_3; CH_2 and CH α to aromatic ring	1.5–1.0	9.24	11.68	16.74	28.31	27.24	26.50	35.82	26.48	28.31	28.72
CH_2 and CH attached to naphthenes	2.0–1.5	3.29	4.03	5.54	9.69	9.45	12.95	12.8	8.53	9.69	9.62
CH_3; CH_2 and CH a to aromatic or aceytlenic	3.0–2.0	8.36	4.66	5.66	19.59	17.64	14.63	21.88	15.24	19.59	18.84
Total aliphatics	3.0–0.5	24.25	24.57	34.02	68.25	70.24	70.34	86.71	63.17	68.25	70.35
Hydroxyl, ring-joining, methane or methoxy	4.0–3.0	2.32	1.52	1.58	4.09	1.57	1.46	0.97	2.71	4.09	2.50
Phenols, non-conjugated olefins	6.0–4.0	68.99	70.59	59.17	16.17	16.22	16.26	11.99	22.61	16.17	14.09
Aromatics, conjugated olefins	9.0–6.0	4.43	3.31	5.23	11.19	11.97	11.94	0.32	11.59	11.19	13.04

Table 6.17 (***Continued***)	Chemical	Ratio of RSC to WPS				
Hydrogen type	shift (ppm)	1:0	2:1	1:1	1:2	0:1
CH_3 ɤ or further from aromatic ring and parafinic CH_3	1.0–0.5	12.92	8.49	8	4.32	0.89
CH_3; CH_2 and CH α to aromatic ring	1.5–1.0	26.48	18.93	21.76	12.45	3.36
CH_2 and CH attached to naphthenes	2.0–1.5	8.53	6.71	6.59	4.96	1.85
CH_3; CH_2 and CH a to aromatic or aceytlenic	3.0–2.0	15.24	21.16	17.41	17.79	11.49
Total aliphatics	3.0–0.5	63.17	55.29	53.76	39.52	17.59
Hydroxyl, ring-joining, methane or methoxy	4.0–3.0	2.71	2.56	2.04	1.03	–
Phenols, non-conjugated olefins	6.0–4.0	22.61	16.13	13.49	9.96	17.83
Aromatics, conjugated olefins	9.0–6.0	11.59	26.36	30.82	49.44	64.58

Table 6.18: Chemical compositions of RSC pyrolytic oil obtained at heating rate of 30 °C/min for various temperatures

Pyrolysis temperature (°C) for heating rate of 30 °C/min	350	400	450	500	550	600
Compound	Relative peak area (%)					
Acetic acid	0.71	6.15	2.26	2.01	2.32	2.16
1,2-Ethanediamine, N,N'-diethyl-	0.64	1.25	0.24	0.24	0.62	1.32
Pyridine	0	0.1	0.52	0.31	0.2	0.15
Ethanimidic acid, ethyl ester	0	0.19	0.73	0.3	0.81	0.92
Pyridine, 2-methyl-	0.41	1.19	0.28	0.41	0.27	0.3
Cyclobutanecarbonitrile	0.17	0.31	0.39	0.56	0.68	0.52
3-Furanmethanol	0	0.21	0.32	0.56	0.45	0.59
Benzene, 1,3-dimethyl-	1.01	1.86	1.52	0.11	2.01	2.11
Phenol	2.14	8.1	8.19	8.09	9.46	9.11
Ethylbenzene	0.15	0.33	0.11	0.27	0.52	1.09
Phenol, 2-methyl-	0	2.35	0.55	3.08	2.2	2.72
Formamide, N-methyl-N-2-pyridinyl-	0.79	9.69	7.34	9.49	9.09	8.01
Mequinol	0	0.17	0.28	1.33	0.96	1.01
4-Pyridinol	0.09	2.65	1.15	1.4	1.39	0.68
Phenol, 3,5-dimethyl-	0.31	2.29	2.79	3.36	2.73	3.51
Phenol, 2-ethyl-	0.32	3	4.06	5.56	3.33	3.69
Creosol	0.52	2.01	1.3	3.34	1.53	1.39
Phenol, 4-ethyl-2-methoxy-	0.55	2.77	1.75	4.49	2.36	1.67

Table 6.18 (Continued)

Indole	0.82	8.31	5.34	7.64	8.31	11.21
Indole, 3-methyl-	0.44	3.23	1.77	3.04	4.24	4.38
Furaltadone	3.24	3.62	3.57	1.61	4.74	6.07
Benzene, 1,2,3-trimethoxy-5-methyl-	0	0.79	0.45	2.09	0.72	0.68
N-Morpholinomethyl-isopropyl-sulfide	1.84	3.44	4.43	2.63	4.24	5.16
Bicyclo[3.1.1]heptan-3-one, 2,6,6-trimethyl-, (1.alpha.,2.beta.	0.54	0.76	1.69	0.58	2.53	2.75
7-Tetradecene	0.4	0.98	1.18	1.24	1.56	1.59
Hexadecanenitrile	1.67	1.71	2.57	1.02	4.52	3.47
Pentadecanenitrile	1.67	2.61	2.5	1.0	4.52	2.97
11,14-Octadecadienoic acid, methyl ester	21.22	12.96	21.3	19.92	5.08	4.22
Hexadecanamide	10.7	3.53	4.17	2.48	3.9	3.5
9-Octadecenamide, (Z)-	40.93	10.54	13.97	10	11.49	10.71
Tetradecanamide	8.72	2.87	3.32	1.84	3.24	2.34

Table 6.19: Chemical compositions of RSC pyrolytic oil obtained at temperature of 500 °C at various heating rates

Pyrolysis heating rate (°C/min) at temperature of 500 °C	10	20	30	40
Compound	Relative peak area (%)			
Acetic acid	2.02	2.37	2.01	1.43
1,2-Ethanediamine, N,N'-diethyl-	2.4	1.56	0.24	0.1
Pyridine	2.18	0.86	0.31	0.16
Ethanimidic acid, ethyl ester	2.18	0.85	0.3	0.16
Pyridine, 2-methyl-	0.84	0.31	0.41	0.1
Cyclobutanecarbonitrile	0.68	0.33	0.56	0.1
3-Furanmethanol	0.67	0.33	0.56	0.1
Benzene, 1,3-dimethyl-	0.27	0.1	0.11	0.13
Phenol	6.78	6.53	8.09	1.52
Ethylbenzene	0.27	0.13	0.27	0.21
Phenol, 2-methyl-	2.18	2.55	3.08	0.24
Formamide, N-methyl-N-2-pyridinyl-	8.19	7.45	9.49	1.24
Mequinol	0.52	0.3	1.33	0.04
4-Pyridinol	1.95	1.13	1.4	0.19
Phenol, 3,5-dimethyl-	2.28	1.94	3.36	0.28
Phenol, 2-ethyl-	5.45	4.2	5.56	0.43
Creosol	1.81	1.57	3.34	0.13
Phenol, 4-ethyl-2-methoxy-	2.05	1.24	4.49	0.3

Table 6.19 (Continued)

Indole	5.01	5.8	7.64	2.67
Indole, 3-methyl-	2.49	1.95	3.04	0.59
Furaltadone	3.79	1.04	1.61	1.97
Benzene, 1,2,3-trimethoxy-5-methyl-	0.74	1.29	2.09	0.48
N-Morpholinomethyl-isopropyl-sulfide	2.96	1.65	2.63	2.38
Bicyclo[3.1.1]heptan-3-one, 2,6,6-trimethyl-, (1.alpha.,2.beta.	1.3	1.45	0.58	1.15
7-Tetradecene	0.82	0.91	1.24	0.8
Hexadecanenitrile	1.41	2.11	1.02	1.8
Pentadecanenitrile	1.41	2.1	1.0	1.8
11,14-Octadecadienoic acid, methyl ester	22.56	33.23	19.92	47.08
Hexadecanamide	3.38	3.09	2.48	5.81
9-Octadecenamide, (Z)-	9.07	9.1	10	21.22
Tetradecanamide	2.34	2.56	1.84	5.41

Table 6.20: Chemical compositions of co-pyrolytic oil obtained at heating rate of 20 °C/min and 500 °C

Ratio of RSC to WPS (wt/wt)	1:0	2:1	1:1	1:2	0:1
Compound	Relative peak area (%)				
Acetic acid	2.37	0.23	0.07	0.11	0
1,2-Ethanediamine, N,N'-diethyl-	1.56	0.19	0.14	0.1	0.01
Pyridine	0.86	0.19	0.14	0.1	0.01
Ethanimidic acid, ethyl ester	0.85	0.19	0.14	0.1	0.1
Pyridine, 2-methyl-	0.31	0.01	0.01	0.004	0
Cyclobutanecarbonitrile	0.33	0.16	0.14	0.02	0
3-Furanmethanol	0.33	0.16	0.14	0.02	0
Benzene, 1,3-dimethyl-	0.1	1.19	1.39	1.09	0.11
Styrene	0	13.03	9.53	14.35	12.5
Phenol	6.53	0.58	0.45	0.08	0
.alpha.-Methylstyrene	0	1.19	1.62	1.89	0.11
Ethylbenzene	0.13	0	0	0	0
Phenol, 2-methyl-	2.55	0.14	0.12	0.03	0
Formamide, N-methyl-N-2-pyridinyl-	7.45	0.54	0.6	0.21	0
Mequinol (phenol)	0.3	0	0	0	0
4-Pyridinol	1.13	0.07	0.06	0.01	0
Phenol, 3,5-dimethyl- (phenol)	1.94	0.14	0.15	0.05	0
Phenol, 2-ethyl- (Phenol)	4.2	0.17	0.27	0.08	0

Table 6.20 (Continued)

Creosol (Phenol)	1.57	0	0	0	0
Phenol, 4-ethyl-2-methoxy- (Phenol)	1.24	0.09	0.11	0.04	0
Indole	5.8	0.66	0.62	0.23	0
Indole, 3-methyl-	1.95	0.15	0.15	0.04	0
Furaltadone	1.04	0.42	0.48	0.19	0
Benzene, 1,2,3-trimethoxy-5-methyl-	1.29	0.12	0.17	0.07	0
Benzeneacetic acid, phenylmethyl ester	0	1.47	1.19	1.71	0.53
N-Morpholinomethyl-isopropyl-sulfide	1.65	0.99	0.95	0.73	0
Bicyclo[3.1.1]heptan-3-one, 2,6,6-trimethyl-, (1.alpha.,2.beta.	1.45	0.33	0.41	0.15	0
7-Tetradecene	0.91	10.16	11.14	9.29	7.54
P-Xylene	0	3.32	4.3	3.22	0.45
1-Dodecyne	0	35.8	30.93	38.94	54.82
3-Phenyl-1-propanol, acetate	0	1.89	2.7	2.73	1.33
Hexadecanenitrile	2.11	0.4	0.52	0.2	0
Pentadecanenitrile	2.1	0.39	0.50	0.19	0
Benzene, 1,1'-(1-methyl-1,2-ethanediyl) bis-	0	1.71	1.46	2.09	1.58
Benzeneacetic acid, .alpha.-oxo-, methyl ester	0	1.3	1.44	1.72	1.1
[1,1'-Biphenyl]-4,4'-dicarbonitrile	0	2.87	3.51	4.47	5.59
11,14-Octadecadienoic acid, methyl ester	33.23	5.3	7.54	2.2	0.56
Hexadecanamide	3.09	0.68	2.03	1.76	0.73

9-Octadecenamide, (Z)-	9.1	2.02	2.18	0.26	0
Tetradecanamide	2.56	0.3	0.33	0.12	0
Not detected	0	11.27	12.33	11.38	12.91

Not detected: sum of 5 different percentage of peaks areas at different retention time

6.5. Summary

In this chapter, rubber seed shell (RSS) and rubber seed cake (RSC), the solid wastes generated during the feedstock preparation for rubber seed oil based biodiesel production were subjected to characterization. Non-isothermal TGA kinetics using various kinetic models and active pyrolysis temperature window from 350 to 600 °C were performed in semi-batch reactor. Proximate results show that the volatile matter for RSC (82.85 wt%) was higher than RSS (76.36 wt%) on dry basis. From the DTG profiles of RSS and RSC concluded that, the thermal decomposition events can broadly be divided in water evaporation and active pyrolysis zones. During active pyrolysis, decomposition of hemicellulose, cellulose, lignin and other hydrocarbon compounds occurred. More than 60% pyrolysis conversion of RSS and RSC can be obtained below 450 °C temperature. The values of R_{50} (at T_{50}) obtained from TG were found to be 5.66 wt%/min (RSS) and 1.87 wt%/min (RSC). The dependency of kinetic parameters on temperature and active pyrolysis stages was clearly observed in all kinetic methods considered. The values of activation energy obtained by IKP method are in good agreement with model-free isoconversional methods. Thus, the invariant kinetic parameters (*m, n and lnA*) obtained by IKP method are reasonably accurate and represent the decomposition profiles of RSS and RSC in multistage. The increase in activation energy for pyrolysis process has been compensated by increasing of pre-exponential factor for corresponding active pyrolysis stages.

The yields and quality of product distribution during pyrolysis of RSS and RSC were mainly influenced by pyrolysis temperature. From the studied six temperatures and four heating rates, suggested the optimum conditions as 550 °C temperature with heating rate of 30

°C/min for RSS and 500 °C temperature with heating rate of 20 °C/min for RSC. Maximum yield of RSS pyrolytic liquid (46.14 wt%) was obtained along with 31.92 wt% bio-char yield of comparable energy content with anthracite solid fuel (32–34 MJ/kg). Similarly, maximum yield of liquid (48.25 wt%) was obtained during RSC pyrolysis. The RSC pyrolytic liquid product has two clearly distinguished phases (i.e. aqueous phase and organic phase). However, the organic phase in RSS pyrolytic liquid was not clearly observed and distingushed. Hence, the RSS pyrolytic liquid was found to be not combustible to measure calorific value. On the other hands, the organic phase (bio-oil) for RSC pyrolytic liquid obtained at pyrolysis temperature 500 °C was measured to be 32.25 MJ/kg (at 20 °C/min heating rate) which is comparable with mineral fuel. Further, addition of waste polystyrene in to RSC with ratio of 1:1 enhanced the yield and energy content of bio-oil from 21.58 wt/vol% to 48.7 wt/vol% and 32.25 MJ/kg to 37.61 MJ/kg. Relatively higher concentration of phenolic, organic acid, aromatic and nitrogen containing compounds were observed in both RSS pyrolytic liquid and RSC pyrolytic bio-oil. Both RSS and RSC bio-char can be used as solid fuel for different purpose. The produced RSS bio-char was porous structure in nature with BET surface area of 175.95 m^2/g. Hence, RSS bio-char can also be used as an alternative solid fuel as well as feedstock source for activated carbon preparation for metal removal from waste water. Overall, solid by-products, RSS and RSC were found potential bio-resources for production of mixture of chemicals and solid fuels. Utilization of bio-char and bio-oil produced from RSS and RSC may help sustaining the development of biodiesel industry. Co-pyrolysis of RSC with waste polystyrene was also found to be promising to enhance the yield and energy content of bio-oil without changing pyrolysis condition.

CHAPTER VII

Overall Conclusions and Scope for Future Work

Significance of the Study and Conclusions;

Scope for Future Work

CHAPTER VII

Overall Conclusions and Scope Future Work

This chapter summarizes the conclusion drawn from the entire work presented in this dissertation. Further, this chapter focuses toward the scope for future research area which can be carried out.

9.1. Significance of the Study

This work dealt with the comprehensive utilization and characterization of rubber tree by-product (i. e. rubber seed) for biofuel production. The promising amount of oil can be extracted from rubber seed for the synthesis of methyl esters via chemical modification viz. esterification and transesterification process. The availability of rubber seed, yield of RSO, the physico-chemical characterization of the extracted RSO and prepared RSO based fatty acid methyl esters products indicates that rubber seed is a promising alternative feedstock for edible oilseed based biofuel production. Hence, the crisis between fuel and food can be partially minimized by using non-edible oilseeds for biodiesel production. Further, utilization of solid by-products, (shell and cake) obtained during extraction of oil from rubber seed, as a feedstock for bio-oil and bio-char production can offer more benefit and potency to reduce the current environmental challenge as well as sustainability of biodiesel industry. Moreover, the major conclusions obtained from each part of this study are summarized below.

Rubber seed comprises of 40–48% shell and 52–60% kernel by weight of seed. The present study showed insignificant effect on oil yield after 8 h extraction time and particle size lower than 1.22 mm. The maximum yield of RSO (49.36 wt%) was obtained at 0.08 g/ml of solute to solvent ratio, 8 h extraction time, 1.00 mm of average particle size with hexane as solvent. The value of FFA and kinematic viscosity of extracted oil (RSO) were found to be 12.12% and 30 cSt (at 24 °C). The physico-chemical characteristics of RSO revealed that it can act as a potential feedstock for biodiesel production.

Ultrasonic-assisted esterification could reduce the acid value of RSO from 24 mg KOH/g to ~2 mg KOH/g at ambient temperature (~30 °C) and the esterified oil was found to contain 17.65% transesterified product (ROME). Non-conventional techniques (ultrasonic-assisted), such as UH and UC found to enhance the rate of transesterification reaction using heterogeneous catalysts. BET results show that the total pore volume and the average pore size of the catalysts were in the following order; $Ba(OH)_2{\cdot}8H_2O$ > CL-egg shell > CaO >Na_3PO_4. The catalytic activity of tested catalyst shows that 96% conversion of ERSO to FAME using $Ba(OH)_2{\cdot}8H_2O$ could be achieved within 15 min, while for CaO, calcinated egg shell and Na_3PO_4 catalysts it took almost 3 h to achieve conversion of 97, 97.98 and 92.59%, respectively. Form the results of the study, it can be concluded that, only larger surface area of the catalyst cannot cause the great enhancement in the triglyceride conversion of oil, but both higher surface area and porous nature of the catalyst may greatly promote the diffusion of oil into the catalyst surface and/or pore and then improve the internal diffusion. Results of the transesterification process revealed that calcination reduced the catalytic activity of $Ba(OH)_2{\cdot}8H_2O$ and, decreased the conversion in the following order; non-calcinated (97%) > calcinated at 200 °C (94.83%) > calcinated at 400 °C (92.96%) > calcinated at 800 °C

(19.05%). For transesterification reaction with fresh catalyst, the optimum parameters for the highest yield (97%) using ultrasonic technique have been determined as follows: 13.20 min at 5.38 wt% catalyst loading $Ba(OH)_2 \cdot 8H_2O$ and 8.01:1 molar ratio. The obtained second-order model equation from RSM-CCD could able to predict response function based on the input parameters. The fatty acid compositions of RSO estimated by ^1H NMR technique found consists of unsaturated (80.09%) and saturated (19.91%) fatty acids. It can be concluded that, transesterification reaction does not change the fatty acid chain and degree of unsaturation of fatty acids. Thermal decomposition of RSO and its methyl esters (ROME) under an inert atmosphere showed two and one stage decomposition, respectively. The thermal stability of RSO was higher than that of its biodiesel. The average values of activation energy for RSO were estimated as 167.8, 144.85 and 144.05 kJ/mol for FRD, FWO and MCR methods, respectively. Similarly, the value for ROME were estimated as 87.7, 85.5 and 85.9 kJ/mol, respectively. TGA-FT-IR analysis of the gases evolved during decomposition detected alkanes, alkenes, aldehydes, ketones, ethers, water, carbon dioxide and carbon monoxide in their compositions. However, the absorbance of water was not detected in ROME which shows the production of high quality ester from RSO. Prepared ROME was characterized as per ASTM standard methods and found suitable for blending with diesel and/or direct uses in a diesel engine.

The rheological study of RSO and all the products (ROME, RD15, RD10 and RD5) showed nearly Newtonian fluid behaviour. The maximum BTE (i.e., 24%) which was achieved by diesel fuel at 80% load and was increased to 28.36% in RD10 at the same load with a drastic improvement of overall 13 % increase with respect to diesel fuel. An overall 5% reduction of exhaust gas temperature was achieved with RDXX blends. The notable decrease

in carbon monoxide with an overall reduction of 30% was achieved. Similarly with blends, NOx also reduced till 80% load, thereafter at maximum load it showed rise than diesel. Total hydrocarbon (THC) emission was higher during the low load (0 to 20%) and maximum load (80 to 100%) with the use of biodiesel blend, but in mid-range (40 to 80%) the emissions were in control and found lesser than diesel fuel. Overall ROME-diesel may be considered as a suitable blend which improves the engine performance as well as reduces emissions.

Solid by-product RSS and RSC generated during the RSO extraction process comprises 58.47 wt% and 52.42 wt% total hydrocarbon (C and H), respectively. Calorific values, proximate and ultimate analyses of RSC and RSS confirm that both RSC and RSS are rich in hydrocarbon content and can be suitable feedstocks for bio-oil and bio-char production. From the DTG profiles of RSC and RSS concluded that, thermal decomposition events can broadly be divided into water evaporation and active pyrolysis zones. The values of R_{50} (at T_{50}) obtained from TGA were found to be 1.87 wt%/min (RSC) and 5.66 wt%/min (RSS). The dependency of kinetic parameters on temperature and active pyrolysis stages were clearly observed in all the kinetic methods considered.

The yield and quality of product distribution from RSS and RSC pyrolysis, under six temperatures and four heating rates, suggested the optimum conditions as 550 °C temperature with a heating rate of 30 °C/min and 500 °C temperature with a heating rate of 20 °C/min for RSS and RSC, respectively. Pyrolysis of RSS at these conditions gave the maximum liquid yield of 46.14 wt% along with 31.92 wt% bio-char yield of comparable energy content with anthracite solid fuel (32–34 MJ/kg). Similarly, the maximum liquid yield of 48.25 wt% and bio-char of 26.18 wt% was obtained during RSC pyrolysis. The pyrolytic liquid obtained

during RSC pyrolysis showed two phases (i. e. aqueous phase and organic (bio-oil) phase) and can be separated by gravity. However, the organic phase for RSS pyrolytic liquid was not able to separate from aqueous phase by gravity. The calorific value of bio-oil obtained from RSC pyrolysis was 32.25 to 33.25 MJ/kg at 500 °C pyrolysis temperature. GC-MS analysis of RSS pyrolytic liquid and RSC bio-oil confirmed that the relative acid and benzene compound content was higher in the RSS pyrolytic liquid, whereas nitrogen-containing compounds were higher in the RSC bio-oil. Further, co-pyrolysis with waste polystyrene (1:1 weight basis) could enhance the liquid yield from 48.25 wt% to 60.5 wt% and increase the calorific value from 32.25 MJ/kg to 37.61 MJ/kg under identical pyrolysis conditions. In addition to the higher energy content of produced bio-char, the bio-char produced from RSS and RSC was found to be porous in nature with BET surface area of 175.95 m^2/g and 5 m^2/g and average pore size of 2.66 nm and 21.49 nm, respectively. Hence, both RSS and RSC bio-char can also be used as an alternative solid fuel as well as a feedstock source for activated carbon preparation for metal removal from waste water. Overall, RSS and RSC were found to be a potential bio-resource for the production of chemicals and solid fuel. Moreover, efficient utilization of RSS and produced bio-char may provide a sustainable solution to the development of biodiesel industry.

9.2. Scope for Future Work

Research findings in this work provided a number of insights with respect to utilization of non-edible oil seeds for biofuels and value added chemical production. There are certainly

several areas which needs further research attention. Few research areas for future work are presented as follows:

- Upgradation of pyrolytic liquid product for different applications and a bio-activated carbon synthesis from RSS/RSC bio-char for heavy metal removal from waste water are recommended scope for future study
- Reactive extraction can be studied for high FFA oilseeds (i. e. rubber seed)
- Feasibility study for the production of biodiesel from non-edible oils (i. e. rubber seed)
- Detail investigation of optimization of transesterification of ERSO using an egg shell based CaO as a catalyst can be studied
- Improvement of clod flow and thermal properties of rubber seed oil methyl esters using additives and other antioxidant
- Thermal and catalytic cracking of rubber seed oil for the production higher fraction of gasoline hydrocarbons

References

[1] Waldron K. Bioalcohol production: Biochemical conversion of lignocellulosic biomass. Cambridge: Wood head publishing Ltd; 2009.

[2] Speight JG. The biofuels handbook. Cambridge, UK: RSC Publishing; 2011.

[3] Menetrez MY. An overview of algae biofuel production and potential environmental impact. Environ Sci Technol 2012; 46:7073–85.

[4] Santori G, Nicola GD, Moglie M, Polonara F. A review analyzing the industrial biodiesel production practice starting from vegetable oil refining. Appl Energy 2012; 92:109–32.

[5] Dickerson T, Soria J. Catalytic Fast Pyrolysis: A Review. Energies 2013; 6:514–38.

[6] Ma F, Hanna MA. Biodiesel production: A review. Bioresour Technol 1999; 70:1–15.

[7] Leung DYC, Wu X, Leung MKH. A review on biodiesel production using catalyzed transesterification. Appl Energy 2010; 87:1083–95.

[8] Khan TMY, Atabani AE, Badruddin IA, Badarudin A, Khayoon MS, Triwahyono S. Recent scenario and technologies to utilize non-edible oils for biodiesel production. Renewable Sustainable Energy Rev 2014; 37:840–51.

[9] Bart JCJ, Palmeri N, Cavallaro S. Biodiesel science and technology from soil to oil. Washington, DC: Woodhead Publishing; 2010.

[10] Balat M. Potential alternatives to edible oils for biodiesel production – A review of current work. Energy Convers Manage 2011; 52:1479–92.

[11] Bankovic-Ilic IB, Stamenkovic OS, Veljkovic VB. Biodiesel production from non-edible plant oils. Renewable Sustainable Energy Rev 2012; 16:3621–47.

[12] Bokhari A, Yusup S, Ahmad MM, editors: Optimization of the parameters that affects the solvent extraction of crude rubber seed oil using response surface methodology

(RSM). In: Recent Advance in Engineering; Year of Conference; Paris:WSEAS, City: WSEAS; 2012: 28–33.

[13] Kole C, Joshi CP, Shonnard DR. Handbook of bioenergy crop plants. New York: CRC Press; 2012.

[14] Tripathi M, Sahu JN, Ganesan P. Effect of process parameters on production of biochar from biomass waste through pyrolysis: A review. Renewable Sustainable Energy Rev 2016; 55:467–81.

[15] Freedman B, Pryde EH, Mounts TL. Variables affecting the yields of fatty esters from transesterified vegetable oils. J Am Oil Chem Soc 1984; 61:1638–42.

[16] Borugadda VB, Goud VV. Biodiesel production from renewable feedstocks: Status and opportunities. Renewable Sustainable Energy Rev 2012; 16:4763–84.

[17] Atabani AE, Badruddin IA, Mahlia TMI, Masjuki HH, Mofijur M, Lee KT, et al. Fuel properties of *Croton megalocarpus*, *Calophyllum inophyllum*, and *Cocos nucifera* (coconut) methyl esters and their performance in a multicylinder diesel engine. Energy Technol 2013; 1:685–94.

[18] Behcet R. Performance and emission study of waste anchovy fish biodiesel in a diesel engine. Fuel Process Technol 2011; 92:1187–94.

[19] Zhang X, Yan S, Tyagi RD, Surampalli RY, Valero JR. Energy balance of biofuel production from biological conversion of crude glycerol. J Environ Manage 2016; 170:169–76.

[20] Ahmad R, Hamidin N, Ali UFM, Abidin CZA. Characterization of bio-oil from palm kernel shell pyrolysis. J Mech Eng Sci 2014; 7:1134–40.

[21] Mohammad TH, Lakhmiri R, Azmani A, Hassan II. Bio-oil from pyrolysis of castor shell. Int J Basic Appl Sci 2014; 14:1–5.

[22] Hassan SNAM, Ishak MAM, Ismail K, Ali SN, Yusop MF, editors: Comparison study of rubber seed shell and kernel (*hevea brasiliensis*) as raw material for bio-oil production. In: 2013 international conference on alternative energy in developing countries and emerging economies; Year of Conference City; 2014: 610–7.

[23] Abdelfatah M, Farag HA, Ossman ME. Production of biodiesel from non-edible oil and effect of blending with diesel on fuel properties. Eng Sci Technol: Int J 2012; 2:583–91.

[24] Atabani AE, Silitonga AS, Ong HC, Mahlia TMI, Masjuki HH, Badruddin IA, et al. Non-edible vegetable oils: A critical evaluation of oil extraction, fatty acid compositions, biodiesel production, characteristics, engine performance and emissions production. Renewable Sustainable Energy Rev 2013; 18:211–45.

[25] Chhetri AB, Tango MS, Budge SM, Watts KC, Islam MR. Non-edible plant oils as new sources for biodiesel production. Int J Mol Sci 2008; 9:169–80.

[26] No S. Inedible vegetable oils and their derivatives for alternative diesel fuels in CI engines: A review. Renewable Sustainable Energy Rev 2011; 15:131–49.

[27] Ahmad J, Yusup S, Bokhari A, Kamil RNM. Study of fuel properties of rubber seed oil based biodiesel. Energy Convers Manage 2014; 78:266–75.

[28] Kamalakar K, Rajak AK, Prasad RBN, Karuna MSL. Rubber seed oil-based biolubricant base stocks: A potential source for hydraulic oils. Ind Crops Prod 2013; 51:249–57.

[29] Salamatinia B, Mootabadi H, Bhatia S, Abdullah AZ. Optimization of ultrasonic-assisted heterogeneous biodiesel production from palm oil: A response surface methodology approach. Fuel Process Technol 2010; 91:441–8.

[30] Chisti Y. Biodiesel from microalgae. Biotechnololy Advances 2007; 25:294–306.

[31] Vyas AP, Verman JL, Subrahmanyam N. A review on FAME production processes. Fuel 2010; 89:1–9.

[32] Food and Agricultural Organization of the United Nations (FAO). Natural rubber, plantain areas harvested (hectare) for all countries; 2013. http://www.factfish.com/catalog/crop [accessed 14.05.15].

[33] Onoji SE, Iyuke SE, Igbafe AI, Nkazi DB. Rubber seed oil: A potential renewable source of biodiesel for sustainable development in sub-Saharan Africa. Energy Convers Manage 2016; 110:125–34.

[34] Zhu Y, Xu J, Li Q, Mortimer PE. Investigation of rubber seed yield in Xishuangbanna and estimation of rubber seed oil based biodiesel potential in Southeast Asia. Energy 2014; 69:837–42.

[35] Ramadhas AS, Jayaraj S, Muraleedharan C. Biodiesel production from high FFA rubber seed oil. Fuel 2005; 84:335–40.

[36] NEDFi databank North East rubber plantation http://databank.nedfi.com/content/rubber-production; [accesed 14.04.2015]

[37] Wang L, Weller CL. Recent advances in extraction of nutraceuticals from plants. Trends in Food Science and Technology 2006; 17:300–12.

[38] Samaram S, Mirhosseini H, Tan CP, Ghazali HM. Ultrasound-assisted extraction and solvent extraction of papaya seed oil: Crystallization and thermal behavior, saturation degree, color and oxidative stability. Ind Crops Prod 2014; 52:702–8.

[39] Wildan A, Ingrid D, Hartati I, editors: Oil extraction process from solid waste rubber seed by soxhletation and extraction solvent by stirring methods. In: International conference on chemical and material engineering; Year of Conference; Semarang, Indonesia, City; 2012: 1–4.

[40] Saxena DK, Sharma SK, Sambi SS. Comparative extraction of cottonseed oil by n-hexane and ethanol. ARPN J Eng Appl Sci 2011; 6:84–9.

[41] Ara KM, Karami M, Raofie F. Application of response surface methodology for the optimization of supercritical carbon dioxide extraction and ultrasound-assisted extraction of *Capparis spinosa* seed oil. J Supercrit Fluids 2014; 85:173–82.

[42] Lee NY, Setapar SM, Sharif NM, Ahmad A, Khatoon A, Aziz CM, et al. Extraction of rubber (*Hevea brasiliensis*) seed oil using supercritical carbon dioxide and soxhlet extraction. Res J Chem Environ 2013; 10:46–52.

[43] Eskilsson CS, Bjorkund E. Analytical-scale microwave-assisted extraction. J Chromatogr A 2000; 902:227–50.

[44] Box GEP, Draper NR. Response surfaces, mixtures, and ridge analyses. Canada: Canada: John Wiley and Sons, Inc.; 2007.

[45] Sayyar S, Abidin ZZ, Yunus R, Muhammad A. Extraction of oil from jatropha seds otimization and knetics. American Journal of Applied Science 2009; 6:1390–5.

[46] Kostic MD, Jokovic NM, Stamenkovic OS, Ralkovic KM, Milik PS, Veljkovic VB. Optimization of hempseed oil extraction by n-hexane. Ind Crops Prod 2013; 48:133–43.

[47] Adewoye TL, Ogunleye OO. Optimization of neem seed oil extraction process using response surface methodology Journal of Natural Sciences Research 2012; 2:66–75.

[48] Geo VE, Nagarajan G, Nagalingam B. Experiments on behavior of preheated rubber seed oil in a direct injection diesel engine. J Energy Inst 2008; 81:177–80.

[49] Giwa OS, Chuah LA, Adam NM. Fuel properties and rheological behavior of biodiesel from egusi (Colocynthis citrullus L.) seed kernel oil. Fuel Process Technol 2014; 122:42–8.

[50] Sharma YC, Singh B. Development of biodiesel: Current scenario. Renewable Sustainable Energy Rev 2009; 13:1646–51.

[51] Yin X, Ma H, You Q, Wang Z, Chang J. Comparison of four different enhancing methods for preparing biodiesel through transesterification of sunflower oil. Appl Energy 2012; 91:320–5.

[52] Adams C, peters JF, Rand MC, Schroer B, Ziemke MC. Investigation of soybean oil as a diesel fuel extender: Endurance tests. J Am Oil Chem Soc 1983; 60:1574–9.

[53] Prateepchaikul G, Apichato T. Palm oil as a fuel for agricultural diesel engines: Comparative testing against diesel oil. Songklanakarin Journal of Science and Technology 2003; 25.

[54] Chattaopadhyay S, Sen R. Fuel properties, engine performance and environmental benefits of biodiesel produced by a green process. Appl Energy 2013; 105:319–26.

[55] Chattha JA, Bannikov MG, Iqbal S. The performance and emissions of a direct injection diesel engine fueled with pongamia pinnata methyl esters. Energy Sources, Part A 2011; 33:890–7.

[56] Xu J, Jiang J, Zhang T, Dai W. Biofuel production from catalytic cracking of triglyceride materials followed by an esterification reaction in a scale-up reactor. Energy Fuels 2013; 27:255–61.

[57] Biswas S, Biswas P, Kumar A. Catalytic cracking of soybean oil with zirconium complex chemically bonded to alumina support without hydrogen. International Journal of Chemical Sciences and Applications 2012; 3:306–13.

[58] Ooi Y-S, Zakaria R, Mohamed AR, Bhatia S. Catalytic cracking of used palm oil and palm oil fatty acid mixture for the production of liquid fuel: Kinetic modeling. Energy Fuels 2004; 18:1555–61.

[59] Siswanto DY, Salim GW, Wibisono N, Hindarso H, Sudaryanto Y, Ismadij S. Gasoline production from palm oil via catalytic cracking using MCM-41: Determination of optimum condition. ARPN J Eng Appl Sci 2008; 3:42–6.

[60] Lima DG, Soares VCD, Ribeiro EB, Carvalho DA, Cardoso ECV, Rassi F, et al. Diesel-like fuel obtained by pyrolysis of vegetable oils. J Anal Appl Pyrolysis 2004; 71:987–96.

[61] Mubarak M, Kumar MS: An experimental study on waste cooking oil and Its emulsions as diesel engine fuel. In: *: Advances in Engineering, Science and Management (ICAESM).* Nagapattinam, Tamil Nadu (481); 2012.

[62] Melo-Espinosa EA, Piloto-Rodriguez R, Goyos-Perez L, Sierens R, Verhelst S. Emulsification of animal fats and vegetable oils for their use as a diesel engine fuel: A overview. Renewable Sustainable Energy Rev 2015; 47:623–33.

[63] Badran O, Emeish S, Abu-Zaid M, Abu-Rahma T, Al-Hasan M, Al-Ragheb M. Impact of emulsified water/diesel mixture on engine performance and environment. Int J Therm Env Eng 2011; 3:1– 7.

[64] Fayyad SM, Abu-Ein S, Al-Marahleh G, Al-Momani W, Al-Momani M, Abulghaham Z, et al. Experimental emulsified diesel and benzen investigation. Res J Appl Sci Eng Technol 2010; 2:268– 73.

[65] Graboski MS, McCormick RL. Combustion of fat and vegetable oil derived fuels in diesel engines. Prog Energy Combust Sci 1998; 24:125– 64.

[66] Taufiq-Yap YH, Lee HV, Hussein MZ, Yunus R. Calcium-based mixed oxide catalysts for methanolysis of Jatropha curcas oil to biodiesel. Biomass Bioenergy 2011; 35(2):827–34.

[67] Vieitez I, Silva C, Alcmin I, Borges GR, Corraza FC, Oliveira JV, et al. Continuous catalyst-free methanolysis and ethanolysis of soybean oil under supercritical alchol/water mixtures. Renewable Energy 2010; 35:1976–81.

[68] Manickam S, Arigela VND, Gogate PR. Intensification of synthesis of biodiesel from palm oil using multiple frequency ultrasonic flow cell. Fuel Process Technol 2014; 128:388–93.

[69] Canakci M, Gerpen JV. Biodiesel production via acid catalysis. Am Soc Agric Eng 1999; 42:1203–10.

[70] Barnwal BK, Sharma MP. Prospects of biodiesel production from vegetable oils in India. Renewable Sustainable Energy Rev 2005; 9:363–78.

[71] Canakci M. The potential of restaurant waste lipids as biodiesel feedstocks. Bioresour Technol 2007; 98:183–90.

[72] Georgogianni KG, Kontominas MG, Pomonis PJ, Avlonitis D, Gergis V. Conventional and in situ transesterification of sunflower seed oil for the production of biodiesel. Fuel Process Technol 2008; 89:503–9.

[73] Tiwari AK, Kumar A, Raheman H. Biodiesel production from jatropha oil (*Jatropha curcas*) with high free fatty acids: An optimized process. Biomass Bioenergy 2007; 31:569–75.

[74] Mostafaei B, Ghobadian B, Barzegar M, Banakar A. Optimization of ultrasonic reactor geometry for biodiesel production using response surface methodology. Journal of Agricultural Science and Technology 2013; 15:697–708.

[75] Wan Omar WNN, Amin NAS. Optimization of heterogeneous biodiesel production from waste cooking palm oil via response surface methodology. Biomass Bioenergy 2011; 35:1329–38.

[76] He B, Van Gerpen JH. Application of ultrasonication in transesterification processes for biodiesel production. Biofuels 2012; 3:479–88.

[77] Kouzu M, Kasuno T, Tajika M, Yamanaka S, Hidaka J. Active phase of calcium oxide used as solid base catalyst for transesterification of soybean oil with refluxing methanol. Appl Catal, A 2008; 334:357–65.

[78] Mootabadi H, Salamatinia B, Bhatia S, Abdullah AZ. Ultrasonic-assisted biodiesel production process from palm oil using alkaline earth metal oxides as the heterogeneous catalysts. Fuel 2010; 89:1818–25.

[79] Correia LM, Saboya RMA, Campelo NS, Cecilia JA, Rodriguez-Castellon E, Cavalcante CL, et al. Characterization of calcium oxide catalysts from natural sources and their application in the transesterification of sunflower oil. Bioresour Technol 2014; 151:207–13.

[80] Boro J, Konwar LJ, Deka D. Transesterification of non edible feedstock with lithium incorporated egg shell derived CaO for biodiesel production. Fuel Process Technol 2014; 122:72–8.

[81] Mustata F, Bicu I. The optimization of the production of methyl esters from corn oil using barium hydroxide as a heterogeneous catalyst. J Am Oil Chem Soc 2014; 91:839–47.

[82] Jain S, Sharma MP, Rajvanshi S. Acid base catalyzed transesterification kinetics of waste cooking oil. Fuel Process Technol 2011; 92:32–8.

[83] Choedkiatsakul I, Ngaosuwan K, Cravotto G, Assabumrungrat S. Biodiesel production from palm oil using combined mechanical stirred and ultrasonic reactor. Ultrason Sonochem 2014; 21:1585–91.

[84] Encinar JM, Gonzalez JF, Martinez G, Sanchez N, Pardal A. Soybean oil transesterification by the use of a microwave flow system. Fuel 2012; 95:386–93.

[85] Sajjadi B, Abdul Aziz AR, Ibrahim S. Investigation, modelling and reviewing the effective parameters in microwave-assisted transesterification. Renewable Sustainable Energy Rev 2014; 37:762–77.

[86] Pukale DD, Maddikeri GL, Gogate PR, Pandit AB, Pratap AP. Ultrasound assisted transesterification of waste cooking oil using hetrogeneous catalyst. Ultrason Sonochem 2015; 22:278–86.

[87] Nezinhe A, Danisman A. Alkali catalyzed transesterification of cottonseed oil by microwave irradiation. Fuel 2007; 86:2639–44.

[88] Gole VL, Gogate PR. A review on intensification of synthesis of biodiesel from sustainable feed stock using sonochemical reactors. Chem Eng Process 2012; 53:1–9.

[89] Chen G, Shan R, Shi J, Yan B. Ultrasonic-assisted production of biodiesel from transesterification of palm oil over ostrich eggshell-derived CaO catalyst. Bioresour Technol 2014; 171:428–32.

[90] Deng X, Fang Z, Liu Y. Ultrasonic transesterification of *Jatropha curcas L.* oil to biodiesel by a two-step process. Energy Convers Manage 2010; 51:2802–7.

[91] Sivasamy A, Cheah KY, Fornasiero P, Kemausuor F, Zinoviev S, Miertus S. Catalytic Applications in the Production of Biodiesel from Vegetable Oils. ChemSusChem 2009; 2:278–300.

[92] Helwani Z, Othman MR, Aziz N, Kim J, Fernando WJN. Solid heterogeneous catalysts for transesterification of triglycerides with methanol: A review. Appl Catal, A 2009; 363:1–10.

[93] Khan MA, Yusup S, Ahmad MM. Acid esterification of a high free fatty acid crude palm oil and crude rubber seed oil blend: Optimization and parametric analysis. Biomass Bioenergy 2010; 34:1751–6.

[94] Mathimani T, Uma L, Prabaharan D. Homogeneous acid catalysed transesterification of marine microalga *Chlorella sp.* BDUG91771 lipid- An efficient biodiesel yield and its characterization. Renewable Energy 2015; 81:523–33.

[95] Jain S, Sharma MP. Kinetics of acid base catalyzed transesterification of *Jatropha curcas* oil. Bioresour Technol 2010; 101:7701–6.

[96] Istadi I, Anggoro DD, Buchori L, Rahmawati DA, Intaningrum D. Active acid catalyst of sulphated zinc oxide for transesterification of soybean oil with methanol to biodiesel. Procedia Environmental Science 2015; 25:385–93.

[97] Lopez DE, Goodwin Jr. G, Bruce DA, Lotero E. Transesterification of triacetin with methanol on solid acid and base catalyst. Appl Catal, A 2005; 295:97–105.

[98] Shokrolahi A, Zali A, Pouretedal HR. Sulfonated porous carbon catalyzed esterification of free fatty acids. Iran J Catal 2011; 1:37–40.

[99] Keera ST, Sabagh SME, Taman AR. Transesterification of vegetable oil to biodiesel fuel using alkaline catalyst. Fuel 2011; 90:42–7.

[100] Silva C, Lima AP, Castilhas F, Filho LC, Oliveira JV. Non-catalytic production of fatty acid ethyl esters from soybean oil with supercritical ethanol in a two-step process using a microtube reactor. Biomass Bioenergy 2011; 35:526–32.

[101] Lueung DYC, Guo Y. Transesterification of neat and used frying oil: Optimization for biodiesel production. Fuel Process Technol 2006; 87:883–90.

[102] Lee JS, Saka S. Biodiesel production by heterogeneous catalysts and supercritical technologies. Bioresour Technol 2010; 101:7191–200.

[103] Putri EMM, Rachimoellah M, Santoso N, Pradana F. Biodiesel production from Kapok seed oil (*Ceiba Pentandra*) through the transesterification process by using CaO as catalyst. Global J Res Eng 2012; 12:6–12.

[104] Kawashima A, Matsubara K, Honda K. Acceleration of catalytic activity of calcium oxide for biodiesel production. Bioresour Technol 2009; 100:696–700.

[105] Oliveira DA, Benelli P, Amante ER. A literature review on adding value to solid residues: Egg shells. J Clean Prod 2013; 46:42–7.

[106] Buasri A, Chaiyut N, Loryuenyong V, Wongweang C, Khamsrisuk S. Application of eggshell waste as a heterogenous catalyst for biodiesel peroduction. Sustainable Energy 2013; 1:7–13.

[107] Viriya-empikul N, Krasae P, Puttasawat B, Yoosuk B, Chollacoop N, Faungnawakij K. Waste shells of mollusk and egg as biodiesel production catalysts. Bioresour Technol 2010; 101:3765–7.

[108] Niju S, Begum KMMS, Anantharaman N. Modification of egg shell and its application in biodiesel production. J Saudi Chem Soc 2014; 18:702–6.

[109] Khemthong P, Luadthong C, Nualpaeng W, Changsuwan P, Tongprem P, Viriya-empikul N, et al. Industrial eggshell wastes as the heterogeneous catalysts for microwave-assisted biodiesel production. Catal Today 2012; 190:112–6.

[110] Li Q, Xu J, Du W, Li Y, Liu D. Ethanol as the acyl acceptor for biodiesel production. Renewable Sustainable Energy Rev 2013; 25:742–8.

[111] Shimada Y, Watanabe Y, Sugihara A, Tominaga Y. Enzymatic alcoholysis for biodiesel fuel production and application of the reaction to oil processing. J Mol Catal B: Enzym 2002; 17:133–42.

[112] Watanabe Y, Shimada Y, Sugihara A, Tominaga Y. Stepwise ethanolysis of tuna oil using immobilized Candida antarctica lipase. J Biosci Bioeng 1999; 88:622–6.

[113] Raita M, Champreda V, Laosiripojana N. Biocatalytic ethanolysis of palm oil for biodiesel production using microcrstalline lipase in *tere*-butanol system. Process Biochem 2010; 45:829–34.

[114] Warabi Y, Kusdiana D, Saka S. Reactivity of triglycerides and fatty acids of rapeseed oil in supercritical alcohols. Bioresour Technol 2004; 91:283–7.

[115] Tan KT, Gui MM, Lee KT, Mohamad AR. An optimized study of methanol and ethanol in supercritical alcohol technology for biodiesel production. J Supercrit Fluids 2010; 53:82–7.

[116] Gimbun J, Ali S, Kanwal CCSC, Shah LA, Ghazali NHM, Cheng CK, et al, editors: Biodiesel production from rubber seed oil using activated cement clinker as catalyst. In: Malaysian Technical Universities Conference on Engineering and Technology 2012, MUCET 2012 Part 3-Civil and Chemical Engineering; Year of Conference City; 2013: 13–9.

[117] Sharma V, Das L, Pradhan RC, Nail SN, Bhatnagar N, Kureel RS. Physical properties of tung seed: An industrial oil yielding crop. Ind Crops Prod 2011; 33:440–4.

[118] Idris SS, Rahman NA, Ismail K. Combustion characteristics of Malaysian oil palm biomass, sub-bituminous coal and their respective blend via thermogravimetric analysis (TGA). Bioresour Technol 2012; 123:581–91.

[119] Chutia RS, Kataki R, Bhaskar T. Thermogravimetric and decomposition kinetic studies of *Mesua ferrea L.* deoiled cake. Bioresour Technol 2013; 139:66–72.

[120] Chaiya C, Reubroycharoen P, editors: Production of bio oil from para rubber seed using pyrolysis process. In: 10th eco-energy and matherials science and engineering (EMSES2012); Year of Conference City; 2013: 905–11.

[121] Gollakota ARK, Reddy M, Subramanyam MD, Kishore N. A review on the upgradation techniques of pyrolysis oil. Renewable Sustainable Energy Rev 2016; 58:1543–68.

[122] Volli V, Singh RK. Production of bio-oil from de-oiled cakes by thermal pyrolysis. Fuel 2012; 96:579–85.

[123] Onay O, Kockar OM. Slow, fast and flash pyrolysis of rapeseed. Renewable Energy 2003; 28:2417–33.

[124] Uzun BB, Putun AE, Putun E. Fast pyrolysis of soybean cake: Product yields and compositions. Bioresour Technol 2006; 97:569–276.

[125] Sensoz S, Angin D. Pyrolysis of safflower (*Charthamus tinctorius* L.) seed press cake: Part 1. The effect of pyrolysis parameters on the product yields. Bioresour Technol 2008; 99:5492–7.

[126] Agrawalla A, Kumar S, Singh RK. Pyrolysis of groundnut de-oiled cake and characterization of the liquid product. Bioresour Technol 2011; 102:10711–6.

[127] Singh RK, Shadangi KP. Liquid fuel from castor seeds by pyrolysis. Fuel 2011; 90:2538–44.

[128] Abnisa F, Wan Daud WMA, Sahu JN. Optimization and characterization studies on bio-oil production from palm shell by pyrolysis using response surface methedology. Biomass Bioenergy 2011; 35:3604–16.

[129] Angin D. Effect of pyrolysis temperature and heating rate on biochar obtained from pyrolysis of safflower seed press cake. Bioresour Technol 2013; 128:593–7.

[130] Chutia RS, Kataki R, Bhaskar T. Characterization of liquid and solid product from pyrolysis fo *pongamia glabra* deoiled cake. Bioresour Technol 2014; 165:336–42.

[131] Bordoloi N, Narzari R, Chutia RS, Bhaskar T, Kataki R. Pyrolysis of *Mesua ferrea* and *Pongamia glabra* seed cover: Characterization of bio-oil and its sub-fractions. Bioresour Technol 2015; 178:83–9.

[132] Thangalazhy-Gopakumar S, Al-Nadheri WMA, Jegarajan D, Sahu JN, Mubarak NM, Nizamuddin S. Utilization of palm oil sludge through pyrolysis for bio-oil and bio-char production. Bioresour Technol 2015; 178:65–9.

[133] Brebu M, Ucar S, Vasile C, Yanik J. Co-pyrolysis of pine cone with synthetic polymers. Fuel 2010; 89:1911–8.

[134] Abnisa F, Wan Doud WMA, Ramalingam S, Azemi MNB. Co-pyrolysis of palm shell and polystyrene waste mixtures to synthesis liquid fuel. Fuel 2013; 108:311–8.

[135] Shadangi KP, Mohanty K. Co-pyrolysis of Karanja and Niger seeds with waste polystyrene to produce liquid fuel. Fuel 2015; 153:492–8.

[136] Gerpen JV, Shanks B, Pruszko R, Clements D, Knothe G: Biodiesel production technology: Subcontractor report: NREL. In. Columbus: National Renewable Energy Laboratory; 2004.

[137] Berchmans HJ, Hirata S. Biodiesel production from crude *Jatropha curcas L.* seed oil with a high content of free fatty acids. Bioresour Technol 2008; 99:1716–21.

[138] Sahoo PK, Das LM, Babu MKG, Naik SN. Biodiesel development from high acid value polanga seed oil and performance evaluation in a CI engine. Fuel 2007; 86:448–54.

[139] Silitonga AS, Ong HC, Mahlia TMI, Masjuki HH, Chong WT. Characterization and production of *Ceiba pentandra* biodiesel and its blends. Fuel 2013; 108:855–8.

[140] Hingu SM, Gogate PR, Rathod VK. Synthesis of biodiesel from waste cooking oil using sonochemical reactors. Ultrason Sonochem 2010; 17:827–32.

[141] Atabani AE, Badruddin IA, Masjuki HH, Chong WT, Lee KT. Pangium edule Reinw: A promising non-edible oil feedstock for biodiesel production. Arabian J Sci Eng 2015; 40:583–94.

[142] Heywood JB (ed.): Internal combustion engine fundamentals. New York: McGraw Hill international editions; 1988.

[143] Adekiigbe A. Determination of heating value of five economic trees residue as a fuel for biomass heating system. Natural Science 2012; 10:26–9.

[144] Rao GLN, Prasad BD, Sampath S, Rajagopal K. Combustion analysis of diesel engine fueled with jatropha oil methyl ester-diesel blend. International of Journal of Green Energy 2007; 4:645–58.

[145] Knothe G. Analyzing biodiesel: Standards and other methods. J Am Oil Chem Soc 2006; 83:823–33.

[146] Yeung DKW, Lam SL, Griffith JF, Chan ABW, Chen Z, Tsang PH, et al. Analysis of bone marrow fatty acid composition using high-resolution proton NMR spectroscopy. Chem Phys Lipids 2008; 151:103–9.

[147] Pan X, Medina-Ramirez I, Mernaugh R, Liu J. Nanocharacterization and bactericidal performance of silver modified titania photocatalyst. Colloids Surf B Biointerfaces 2010; 77:82–9.

[148] Hermanek M, Zboril R, Medrik I, Pechousek J, Gregor C. Catalytic efficiency of iron(III) oxides in decomposition of hydrogen peroxide: Competition between the surface area and crystallinity of nanoparticles. J Am Oil Chem Soc 2007; 129:10929–36.

[149] Raj KAJ, Viswanathan B. Effect of surface area pore volume and particle size of P25 titania on the phase transformation of anatase to rutile. Indian J Chem 2009; 48:1378–82.

[150] Rodriguez-Navarro C, Ruiz-Agudo E, Luque A, Rodriguez-Navarro AB, Ortega-Huertas M. Thermal decomposition of calcite: Mechanisms of formation and textural evolution of CaO nanocrystals. Am Mineral 2009; 94:578–93.

[151] Pradhan S, Madankar CS, Mohanty P, Naik SN. Optimization of reactive extraction of castor seed to produce biodiesel using response surface methodology. Fuel 2012; 97:848–55.

[152] Vyazovkin S, Burnham AK, Criado JM, Pérez-Maqueda LA, Popescu C, Sbirrazzuoli N. ICTAC Kinetics committee recommendations for performing kinetic computations on thermal analysis data. Thermochim Acta 2011; 520:1–19.

[153] Acikalin K. Pyrolytic characteristics and kinetics of pistachio shell by thermogravimetric analysis. J Therm Anal Calorim 2012; 109:227–35.

[154] Chen Z, Hu M, Zhu X, Guo D, Liu S, Hu Z, et al. Characteristics and kinetic study on pyrolysis of five lignocellulosic biomass via thermogravimetric analysis. Bioresour Technol 2015; 192:441–50.

[155] Chin BLF, Yusup S, Al Shoaibi A, Kannan P, Srinivasakannan C, Sulaiman SA. Kinetic studies of co-pyrolysis of rubber seed shell with high density polyethylene. Energy Convers Manage 2014; 87:746–53.

[156] Gottipati R, Mishra S. A kinetic study on pyrolysis and combustion characteristics of oil cakes: Effect of cellulose and lignin content. J Fuel Chem Technol 2011; 39:265–70.

[157] Sbirrazzuoli N, Vincent L, Mija A, Guigo N. Integral, differential and advanced isoconversional methods complex mechanisms and isothermal predicted conversion-time curves. Chemometrics Intellig Lab Syst 2009; 96:219–26.

[158] Friedman HL. Kinetics of thermal degradation of char-forming plastics from thermogravimetry. Application to a phenolic plastic. J Polym Sci, Part C 1964; 6:183–95.

[159] Flynn JH, Wall LA. General treatment of the thermalgravimetry of polymers. J Res Natl Bur Stand, Sect A 1966; 6:487–523.

[160] Kissinger HE. Reaction kinetics in differential thermal analysis. Anal Chem 1957; 29:1702–6.

[161] Coats AW, Redfern JP. Kinetic parameters from thermogravimetric data. Nature 1964; 201:68–9.

[162] Jankovic B, Adnadevic B, Mentus S. The kinetic analysis of non-isothermal nickel oxide reduction in hydrogen atmosphere using the invariant kinetic parameters method. Thermochim Acta 2007; 456:48–55.

[163] Ebrahim-Kahrizsangi R, Abbasi MH. Evaluation of reliability of Coats-Redfern method for kinetic analysis of non-isothermal TGA. Trans Nonferrous Met Soc China 2008; 18:217–21.

[164] Niu S, Han K, Lu C, Sun R. Thermogravimetric analysis of the relationship among calcium magnesium acetate, calcium acetate and magnesium acetate. Appl Energy 2010; 87:2237–42.

[165] Niu S, Liu M, Lu C, Li H, Huo M. Thermogravimetric analysis of carbide slag A potential transesterification catalyst validation. J Therm Anal Calorim 2014; 115:73–9.

[166] Vyazovkin S, Sbirrazzuoli N. Confidence intervals for the activation energy estimated by few experiments. Anal Chim Acta 1997; 355:175–80.

[167] Craido JM. Kinetic analysis of DTG data from master curves. Thermochim Acta 1978; 24:189–.

[168] Budrugeac P, Segal E, Perez-Maqueda LA, Criado JM. The use of the IKP method for evaluating the kinetic parameters and the conversion function for the thermal dehydrochlorination of PVC from non-isothermal data. Polym Degrad Stab 2004; 84:311–20.

[169] Levchik SV, Levchik GF, Lesnikovich AI. Analysis and development of effective invariant kinetic parameters finding method based on the non-isothermal data. Thermochim Acta 1985; 92:157–60.

[170] Kim YS, Kim YS, Kim SH. Investigation of thermodynamic parameters in the thermal decomposoition of plastic waste-waste lube oil compounds. Environ Sci Technol 2010; 44:5313–7.

[171] Li H, Niu S, Lu C, Cheng S. Comparative evaluation of thermal degradation for biodiesels derived from various feedstocks through transesterification. Energy Convers Manage 2015; 98:81–8.

[172] Santos AGD, Caldeira VPS, Farias MF, Araujo AS, Souza LD, Barros AK. Characterization and kinetic study of sunflower oil and biodiesel. J Therm Anal Calorim 2011; 106:747–51.

[173] Pourmortazavi SM, Kohsari I, Teimouri MB, Hajimirsadeghi SS. Thermal behaviour kinetic study of dihydroglyoxime and dichloroglyoxime. Materials Letter 2007; 61:4670–3.

[174] Straszko J, Olszak-Humienik M, Mozejko J. Kinetics of thermal decomposition of $ZnSO_4.7H_{20}$. Thermochim Acta 1997; 292:145–50.

[175] Sunitha M, Nair RCP, Krishnan K. Kinetics of Alder-ene reaction of tris(2-allyphenoxy) triphenoxycyclotriphosphazene and bismaleimides- a DSC study. Thermochim Acta 2001; 374:159–69.

[176] Gai C, Dong Y, Zhang T. The kinetic analysis of the pyrolysis of agricultural residue under non-isothermal conditions. Bioresour Technol 2013; 127:298–305.

[177] Attah JC, Ibemesi JA. Solvent extraction of the oil of rubber, melon, pumkin and oilbean seeds. J Am Oil Chem Soc 1990; 67:25–6.

[178] Bong SC, Loh SP. A study of fatty acid composition and tocopherol content of lipid extracted from marine microalgae, nannochloropsis oculata and tetraselmis suecica,

using solvent extraction and supercritical fluid extraction. Int Food Res J 2013; 20:721–9.

[179] Mohamad M, Ali MW, Ripin A, Ahmad A. Effect of extraction process parameters on the yield of bioactive compounds from the roots of eurycoma longifolia. Jurnal Teknologi 2013; 60:51–7.

[180] Asuquo JE, Anusiem ACI, Etim EE. Extraction and characterization of rubber seed oil. Int J Mod Chem 2012; 1:109–15.

[181] Mazumdar P, Borugadda VB, Goud VV, Sahoo L. Physico-chemical characteristics of *Jatropha curcas L.* of North East India for exploration of biodiesel. Biomass Bioenergy 2012; 46:546–54.

[182] Silitonga AS, Mahlia TMI, Masjukia HH, Ong HC: *Ceiba Pentandra*: A feasible non-edible oil source for biodiesel production. In: *International Green Energy Conference and the DNL Conference on Clean Energy (IGEC-DCCE)* vol. 110; 2012: 1–9.

[183] Achinewhu SC, Akpapunam MA. Physical and chemical characteristics of refined vegetable oils from rubber seed (*Hevea brasilliensis*) and read-fruit (*Artocarpus altilis*). Qual Plant Food Human Nutrition 1985; 35:103–7.

[184] Jamieson GS, Baughman WF. Para rubber seed oil Oil and Fat Industries 1930; 7:419–21.

[185] Moser BR. Biodiesel production, properties and feedstocks. In Vitro Cell Dev Biol Plant 2009; 45:229–66.

[186] Pickles SS, Hayworth WP. Composition of para rubber-seed oil. Analyst 1911; 36:491–2.

[187] Akbar E, Yaakob Z, Kamarudin SK, Ismail M, Salimon J. Characteristic and composition of *jatropha curcas* oil seed from Malaysia and its potential as biodiesel feedstock. Eur J Sci Res 2009; 29:396–403.

[188] Juan JC, Kartika DA, Wu TY, Hin TY. Biodiesel production from *Jatropha* oil by catalytic and non-catalytic approaches: An overview. Bioresour Technol 2011; 102:452–60.

[189] Assuncao FP, Bentes MH, Serruya HA. Comparison of the stability of oils from Brazil nut, para rubber and passion fruit seeds. J Am Oil Chem Soc 1984; 61:1031–6.

[190] Borugadda VB, Goud VV. Comparative studies of thermal, oxidative and low temperature properties of waste cooking oil and castor oil. J Renewable Sustainable Energy 2013. http://dx.doi.org/10.1063/1.4830257

[191] Aigbodion AI, Bakare IO. Rubber seed oil quality assessment and authentication. J Am Oil Chem Soc 2005; 82:465–9.

[192] Dutta R, Sarkar U, Mukherjee A. Extraction of oil from crotalaria juncea seeds in a modified soxhlet apparatus: Physical and chemical characterization of a prospective bio-fuel. Fuel 2014; 116:794–802.

[193] Mirghani MES, Man YBC, Jinap S, Baharin BS, Bakar J. Application of FTIR spectroscopy in determining sesamol in sesame seed oil. J Am Oil Chem Soc 2003; 80:1–4.

[194] Chuah LF, Amin MM, Yusup S, Raman NA, Bokhari A, Klemes JJ, et al. Influence of green catalyst on transesterification process using ultrasonic-assisted. J Clean Prod 2016; 136:14–22.

[195] Sheikh RS, Choi M, IM J, Park Y. Study on the solid acid catalysts in biodiesel production from high acid value oil. Journal of Industrial and Engineering Chemistry 2013; 19:1413–9.

[196] Tang Y, Xu J, Zhang J, Lu Y. Biodiesel production from vegetable oil by using modified CaO as solid basic catalysts. J Clean Prod 2013; 42:198–203.

[197] Jacobson K, Gopinath R, Meher LC, Dalai AK. Solid acid catalyzed biodiesel production from waste cooking oil. Applied Catalysis B: Environmental 2008; 85:86–91.

[198] Zang Y, Kshirsagar G, Cannon JC. Functions of barium peroxide in sodium chlorate chemical oxygen geberators. Ind Eng Chem Res 1993; 32:966–9.

[199] Xie W, Zhao L. Production of biodiesel by transesterification of soybean oil using calcium supported tin oxides as heterogeneous catalysts. Energy Convers Manage 2013; 76:55–62.

[200] Lee HV, Yunus R, Juan JC, Taufiq-Yap YH. Process optimization design for jatropha-based biodiesel production using response surface methodology. Fuel Process Technol 2011; 92:2420–8.

[201] Leon-Reina L, Cabeza A, Rius J, Maireles-Torres P, Alba-Rubio AC, Granados LM. Structural and surface study of calcium glyceroxide, an active phase for biodiesel production under heterogeneous catalysis. Journal of Catalysis 2013; 300:30–6.

[202] Deng X, Fang Z, Liu Y, Yu CL. Production of biodiesel from Jatropha oil catalyzed by nanosized solid basic catalyst. Energy 2011; 36:777–84.

[203] Teixeira LSG, Assis JCR, Mendonca DR, Santos ITV, Guimaraes PRB, Pontes LAM, et al. Comparison between conventional and ultrasonic preparation of beef tallow biodiesel. Fuel Process Technol 2009; 90:1164–6.

[204] Sarve A, Sonawane SS, Varma MN. Ultrasound assisted biodiesel production from sesame (*Sesamum indicum L.*) oil using barium hydroxide as a heterogeneous catalyst: Comparative assessment of prediction abilities btewwen response surface methodology (RSM) and artificial neural network (ANN). Ultrasonics Sonochemistry 2015. http://dx.doi.org/10.1016/j.ultrsonch.2015.01.013

[205] Ravikumar K, Pakshirajan K, Swaminathan T, Balu K. Optimization of batch process parameters using response surface methodology for dye removal by a novel adsorbent. Chemical Engineering Journal 2005; 105:131–8.

[206] Shuit SH, Lee KT, Kamaruddin AH, Yusup S. Reactive extraction of *Jatropha curcas L.* seed for production of biodiesel: Process optimization study. Environmental Science and Technology 2010; 44:4361–7.

[207] Al-Hamamre Z, Yamin J. Parametric study of the alkali catalyzed transesterification of waste frying oil for biodiesel production. Energy Convers Manage 2014; 79:246–54.

[208] Tat ME, Van Gerpen JH. The kinematic viscosity of biodiesel. J Am Oil Chem Soc 1999; 76:1511–3.

[209] Lani NS, Ngadi N, Yahya NY, Rahman RA. Synthesis, characterization and performance of silica impregnated calcium oxide as heterogeneous catalyst in biodiesel production. J Clean Prod 2016; 146:116–24.

[210] Ko K, Rawal A, Sahajwalla V. Analysis of thermal degradation kinetics and carbon structure changes of co-pyrolysis beteen macadamia nut shell and PET using

thermogravimetric analysis and ^{13}C solid state nuclear magnetic resonance. Energy Convers Manage 2014; 86:154–64.

[211] Liu Z, Qi N, Luan Y, Sun X. Thermogravimetry-infrared spectroscopy analysis of the pyrolysis of willow leaves, stems, and branches. Adv Mater Sci Eng 2015; 2015:1–8.

[212] Li H, Niu S, Lu C, Wang Y. Comprehensive investigation of the thermal degradation characteristics of biodiesel and its feedstock oil through TGA−FTIR. Energy Fuels 2015; 29:5145–53.

[213] Ma Z, Chen D, Gu J, Bao B, Zhang Q. Determination of pyrolysis characteristics and kinetics of palm kernel shell using TGA-FTIR and model-free methods. Energy Conversion and Management 2015; 89:251–9.

[214] Volli V, Purkait MK. Physico-chemical properties and thermal degradation studies of commercial oils in nitrogen atmosphere. Fuel 2014; 117:1010–9.

[215] Oliveira LE, Giordani DS, Paiva EM, De Castro HF, Da silva MLCP. Kinetic and thermodynamic parameters of volatilization of biodiesel from babassu, palm and mineral diesel by thermogravimetric analysis (TG). J Therm Anal Calorim 2013; 111:155–60.

[216] Raodriguez RP, Sierens R, Verhelst S. Thermal and kinetic evaluation of biodiesel derived from soybean oil and higuereta oil. J Therm Anal Calorim 2009; 96:897–901.

[217] Mo Y, Zhao L, Chen C, Tan GYAT, Wang JW. Comparative pyrolysis upcycling of polystyrene waste: thermodynamics, kinetics, and product evolution profile. J Therm Anal Calorim 2013; 111:781–8.

[218] Vecchio S, Cerretani L, Bendini A, Chiavaro E. Thermal decomposition study of monovarietal extra virgin olive oil by simultaneous thermogravimetry/differential

scanning calorimetry: Relation with chemical composition. J Agric Food Chem 2009; 57:4793–800.

[219] Silitonga AS, Masjuki HH, Mahlia TMI, Ong HC, Chong WT. Experimental study on performance and exhaust emissions of a diesel engine fuelled with *Ceiba pentandra* biodiesel blends. Energy Convers Manage 2013; 76:228–36.

[220] Conceicao MM, Candeia RA, Dantas HJ, Soledade B, Fernandes VJ, Souza AG. Rheological behavior of castor oil biodiesel. Energy Fuels 2005; 19:2185–8.

[221] Borugadda VB, Goud VV. Physicochemical and rheological characterization of waste cooking oil epoxide and their blends. Waste Biomass Valorization 2016; 7:23–30.

[222] Hussain MA, Kar S, Puniyani RR. Relationship between power law coefficients and major blood constituents affecting the whole blood viscosity. J Biosci (Bangalore) 1999; 3:329–37.

[223] Tangsathitkulchai C, Sittichaitaweekul Y, Tangsathitkulchai M. Temperature effect on the viscosities of palm oil and coconut oil blended with diesel oil. J Am Oil Chem Soc 2004; 81:401–5.

[224] Maskan M. Change in colour and rheological behaviour of sunflower seed oil during frying and after adsorbent treatment of used oil. Eur Food Res Technol 2003; 218:20–5.

[225] Gloria H, Aguilera JM. Assessment of the quality of heated oils by differential scanning calorimetry. J Agric Food Chem 1998; 46.

[226] Santos JCO, Santos IMG, Souza AG. Effect of heating and cooling on rheological parameters of edible vegetable oils. J Food Eng 2005; 67:401–5.

[227] Canakcia M, Erdil A, Arcaklioglu E. Performance and exhaust emissions of a biodiesel engine. Appl Energy 2006; 83:594–605.

[228] Ramadhas AS, Muraleedharan C, Jayaraj S. Performance and emission evaluation of a diesel engine fueled with methyl esters of rubber seed oil. Renewable Energy 2005; 30:1789–800.

[229] Candeia RA, Silva MCD, Filho JRC, Brasilino MGA, Bicudo TC, Santos IMG. Influence of soybean biodiesel content on basic properties of biodiesel–diesel blends. Fuel 2009; 88:738–43.

[230] Joshi RM, Pegg M. Flow properties of biodiesel fuel blends at low temperatures. Fuel 2007; 86:143–51.

[231] Kim J, Kim DN, Lee SH, Yoo S, Lee S. Correlation of fatty acid composition of vegetable oils with rheological behaviour and oil uptake. Food Chem 2010; 118:398–402.

[232] Franco Z, Nguyen QD. Flow properties of vegetable oil–diesel fuel blends. Fuel 2011; 90:838–43.

[233] Xue J, Grift TE, Hansen AC. Effect of biodiesel fuels on diesel engine emissions. Renewable Sustainable Energy Rev 2011; 15:1098–116.

[234] Debnath BK, Sahoo N, Saha UK. Adjusting the operating characteristics to improve the performance of an emulsified palm oil methyl ester run diesel engine. Energy Convers Manage 2013; 69:191–8.

[235] Mahanta P, Mishra SC, Kushwah YS, editors: An experimental study of Pongamia pinnata L. oil as a diesel substitute In: Proceedings of the Institution of Mechanical

Engineers, Part A: Journal of Power and Energy; Year of Conference City; 2006: 803–8.

[236] Agarwal AK, Das LM. Biodiesel Development and characterization for use as a fuel in compression ignition engine. Journal of Engineering for Gas Turbines and Power 2001; 123:440–7.

[237] Agarwal AK, Rajamanoharan K. Experimental investigations of performance and emissions of karanja oil and its blends in a single cylinder agricultural diesel engine. Appl Energy 2009; 86:106–12.

[238] Silva FN, Prata AS, Teixeira JR. Technical feasibility assessment of oleic sunflower methyl ester utilisation in diesel bus engines. Energy Convers Manage 2003; 44:2857–78.

[239] Hirkude JB, Padalkar AS. Performance and emission analysis of a compression ignition engine operated on waste fried oil methyl esters. Appl Energy 2012; 90:68–72.

[240] Lapuerta M, Armas O, Rodriguez-Fernandez J. Effect of biodiesel fuels on diesel engine emissions. Progress Energy and Combustion Science 2008; 34:198–223.

[241] Huang J, Wang Y, Qin J, Roskilly AP. Comparative study of performance and emissions of a diesel engine using Chinese pistache and jatropha biodiesel. Fuel Process Technol 2010; 91:1761–7.

[242] Huang ZH, Ren Y, Jiang DM, Liu LX, Zeng K, Liu B, et al. Combustion and emission characteristics of a compression ignition engine fuelled with diesel–dimethoxy methane blends. Energy Convers Manage 2006; 47:1402–15.

[243] Aziz AA, Said MF, Awang MA, Said M: The effects of neutralized palm oil methyl esters (NPOME) on performance and emission of a direct injection diesel engine. In: *Proceedings of the 1st International Conference on Natural Resources Engineering and Technology*. Putrajaya, Malaysia; 2006: Paper No. 3383.

[244] Shadangi KP, Mohanty K. Characterization of nonconventional oil containing seeds towards the production of bio-fuel. J Renewable Sustainable Energy 2013. http://dx.doi.org/10.1063/1.4808029

[245] Duman G, Okutucu C, Ucar S, Stahl R, Yanik J. The slow and fast pyrolysis of cherry seed. Bioresour Technol 2011; 102:1869–78.

[246] Onal E, Uzun BB, Putun AE. Bio-oil production via co-pyrolysis of almond shell as biomass and high density polyethylene. Energy Convers Manage 2014; 78:704–10.

[247] Demirbas A. Effects of moisture and hydrogen content on the heating value of fuels. Energy Sources, Part A 2007; 29:649–55.

[248] Ucar S, Ozkan AR. Characterization of products from the pyrolysis of rapeseed oil cake. Bioresour Technol 2008; 99:8771–6.

[249] Garcia R, Pizarro C, Lavin AG, Bueno JL. Characterization of Spanish biomass wastes for energy use. Bioresour Technol 2012; 103:249–58.

[250] Naik SN, Goud VV, Rout PK, Jacobson K, Dalai AK. Characterization of Canadian biomass for alternative renewable biofuel. Renewable Energy 2010; 35:1624–31.

[251] Sasmal S, Goud VV, Mohanty K. Characterization of biomasses available in the region of North-East India for production of biofuels. Biomass Bioenergy 2012; 45:212–20.

[252] Zanatta ER, Reinehr TO, Awadallak JA, Kleinubing SJ, Dos Santos JBO, Bariccatti RA, et al. Kinetic studies of thermal decomposition of sugarcane bagasse and cassava bagasse. J Therm Anal Calorim 2016; 125:437–45.

[253] Abdullah SS, Yusup S, Ahmad MM, Ramli A, Ismail L. Thermogravimetry study on pyrolysis of various lignocellulosic biomass for potential hydrogen production. Int J Chem Biochem Eng 2010; 3:137–41.

[254] Ma Z, Chen D, Gu J, Bao B, Qisheng Z. Determination of pyrolysis characteristics and kinetics of palm kernel shell using TGA-FTIR and model-free integral methods. Energy Convers Manage 2015; 89:251–9.

[255] Apaydin-Varol E, Uzun BB, Onal E, Putun AE. Synthetic fuel production from cottonseed: Fast pyrolysis and a TGA/FT-IR/MS study. J Anal Appl Pyrolysis 2014; 105:83–90.

[256] Yao H, Wu Q, Lei Y, Guo W, Xu Y. Thermal decomposition kinetics of natural fibers: Activation energy with dynamic thermogravimetric analysis. Polym Degrad Stab 2008; 93:90–8.

[257] Sotoko MA, Singh R, Krishna BB, Kumar J, Bhaskar T. Non-isothermal kinetic study of de-oiled seeds cake of African star apple (*Chrosophyllum albidum*) using thermogravimetry. Helion 2016. http://dx.doi.org/10.1016/j.heliyon.2016.e00172

[258] Torquato LM, Braz CEM, Ribeiro CA, Capela JMV, Crepsi MS. Kinetic study of the co-firing of bagasse–sludge blends. J Therm Anal Calorim 2015; 121:499–507.

[259] Varma AK, Mandal P. Physicochemical characterization and kinetic study of pine needle for pyrolysis process. J Therm Anal Calorim 2016; 124:487–97.

[260] Demirbas A. The influence of temperature on the yields of compounds existing in bio-oils obtained from biomass samples via pyrolysis. Fuel Process Technol 2007; 88:591–7.

[261] Ucar S, Karagoz S. The slow pyrolysis of pomegranate seeds: The effect of temperature on the product yields and bio-oil properties. J Anal Appl Pyrolysis 2009; 84:151–6.

[262] Horen PA, Williams PT. Influence of temperature on the products from the flash pyrolysis of biomass. Fuel 1996; 75:1051–9.

[263] Sensoz S, Kaynar I. Bio-oil production from soybean (*Glycine max* L.); fuel properties of bio-oil. Ind Crops Prod 2006; 23:99–105.

[264] Williams PT, Reed AR. Pre-formed activated carbon matting derived from the pyrolysis of biomass natural fibre textile waste. J Anal Appl Pyrolysis 2003; 70:563–77.

[265] Yaman S. Pyrolysis of biomass to produce fuels and chemical feedstocks. Energy Convers Manage 2004; 45:651–71.

[266] Guo J, Lua AC. Characterization of chars pyrolyzed from oil palm stones for the preparation of activated carbon. J Anal Appl Pyrolysis 1998; 46:113–25.

[267] Kim KH, Kim J, Cho T, Choi JW. Influence of pyrolysis temperature on physicochemical properties of biochar obtained from the fast pyrolysis if pitch pin (*pinus rigida*). Bioresour Technol 2012; 118:158–62.

[268] Ghani AA, Mohd A, da Silva G, Bachmann RT, Taufiq-Yap YH, Rashid U, et al. Biochar from waste rubber-wood-sawdust and its potential use in C sequestration: Chemical and physical characterization. Ind Crops Prod 2013; 44:18–24.

[269] Nazir MS, Wahjoedi BA, Yussof A, Abdullah MA. Eco-friendly extraction and characterization of cellulose from oil palm empty fruit bunches. Bioresources 2013; 8:2161–72.

[270] Wang Z, Cao J, Wang J. Pyrolytic characteristics of pine wood in a slowly heating and gas sweeping fixed-bed reactor. J Anal Appl Pyrolysis 2009; 84:179–84.

[271] Titiloye JO, Abu Bakar MS, Odetoye TE. Thermochemical characterisation of agricultural wastes from West Africa. Ind Crops Prod 2013; 47:199–203.

[272] Shaaban A, Se S, Dimin MF, Juoi JM, Husin MHM, Mitan NMM. Influence of heating temperature and holding time on biochars derived from rubber wood sawdust via slow pyrolysis. J Anal Appl Pyrolysis 2014; 107:31–9.

[273] Kim P, Amy J, Edmunds CW, Radosevich M, Vogt F, Rials TG, et al. Surface functionality and carbon structures in lignocellulosic-derived biochars produced by fast pyrolysis. Energy Fuels 2011; 25:4693–703.

[274] Lazzari E, Schena T, Primaz CT, Maciel GPS, Machado ME, Cardoso CAL, et al. Production and chromatographic characterization of bio-oil from the pyrolysis of mango seed waste. Ind Crops Prod 2016; 83:529–36.

[275] Shadangi KP, Mohanty K. Production and characterization of pyrolytic oil by catalytic pyrolysis of niger seed. Fuel 2014; 126:109–15.

[276] Putun E, Uzun BB, Putun AE. Production of bio-fuels from cottonseed cake by catalytic pyrolysis under steam atmosphere. Biomass Bioenergy 2006; 30:592–8.

[277] Garrote G, Dominguez H, Parajo JC. Interpretation of deacetylation and hemicellulose hydrolysis during hydrothermal treatments on the basis of the severity factor. Process Biochem 2002; 37:1067–73.

[278] Feng Y, Meier D. Extraction of value-added chemicals from pyrolysis liquids with supercritical carbon dioxide. J Anal Appl Pyrolysis 2015; 113:174–85.

[279] Giannakopoulou K, Lukas M, Vasiliev A, Brunner C, Schnitzer H. Conversion of rapeseed cake into bio-fuel in a batch reactor: Effect of catalytic vapor upgrading. Microporous Mesoporous Mater 2010; 128:126–35.

[280] Andrade LA, Barrozo MAS, Vierira LGM. Thermo-chemical behavior and product formation during pyrolysis of mango seed shell. Ind Crops Prod 2016; 85:174–80.

[281] Abnisa F, Wan Doud WMA. A review on co-pyrolysis of biomass: An optional technique to obtain a high-grade pyrolysis oil. Energy Convers Manage 2014; 87:71–85.

[282] Ghani WAWA, Mohd A, da Silva G, Bachmann RT, H. T-YY, Rashid U, et al. Biochar production from waste rubber-wood-sawdust and its potential use in C sequestration: Chemical and physical characterization. Ind Crops Prod 2013; 44:18–24.

Appendix

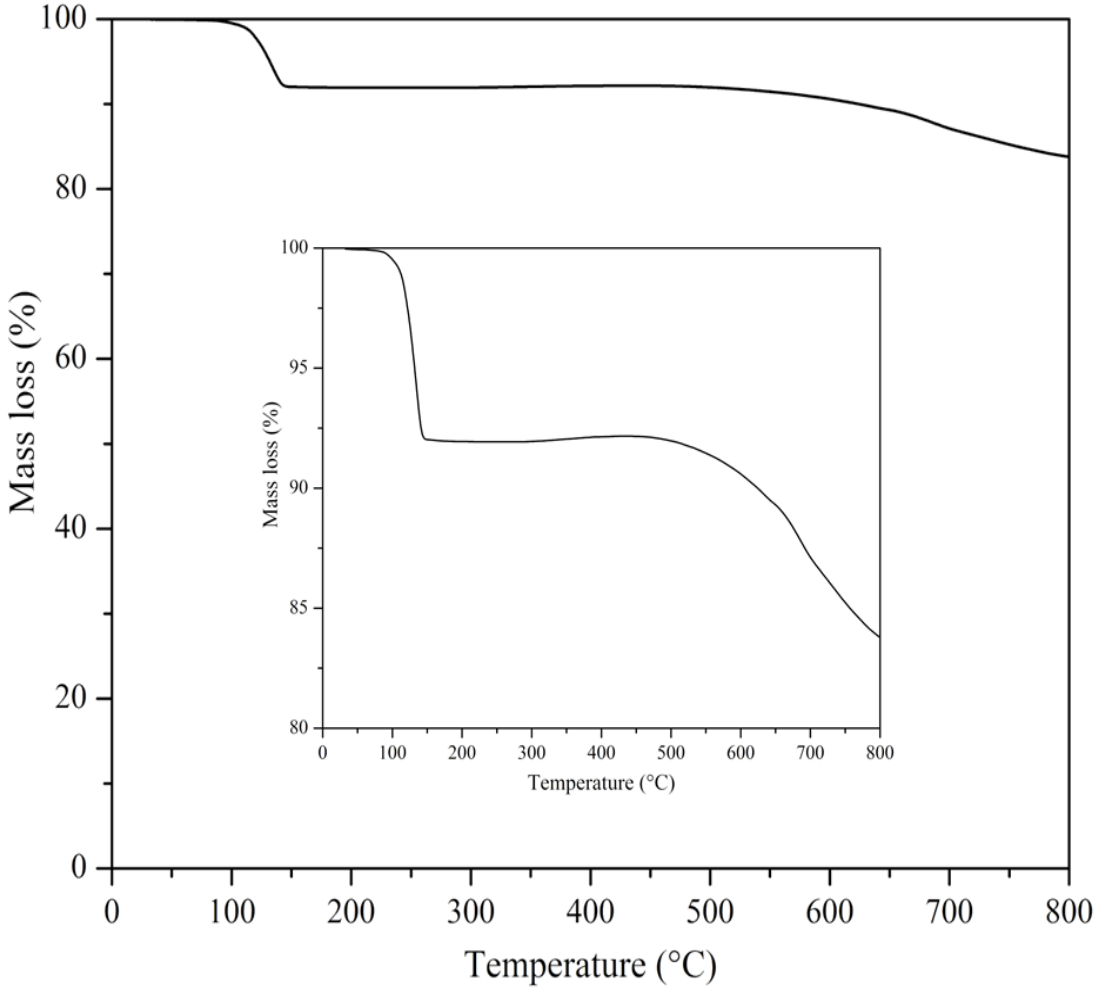

Fig. A4.1: TGA of barium hydroxide octahydrate at heating rate of 20 °C/min under nitrogen atmosphere

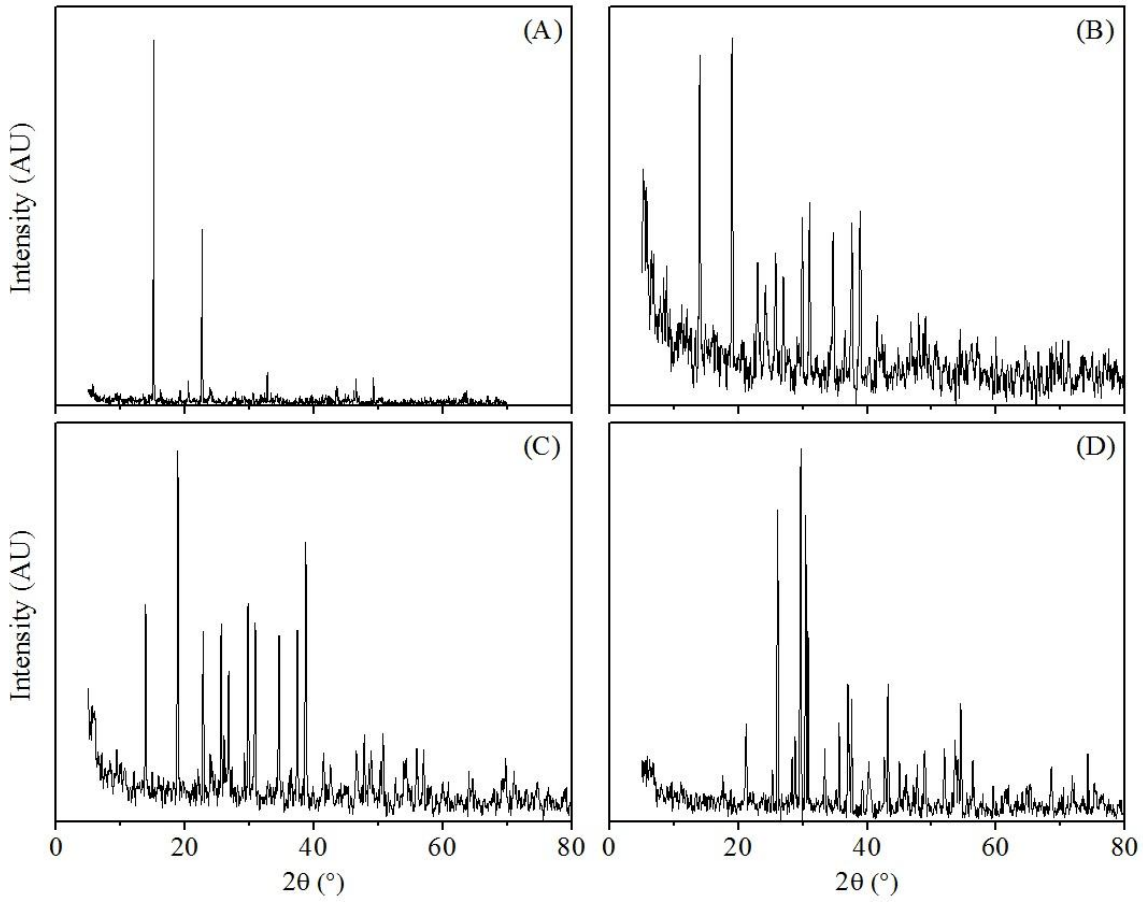

Fig. A4.2: XRD patterns of $Ba(OH)_2 \cdot 8H_2O$ catalyst (A): Non-calcinated, (B): Calcinated at 200 °C for 4.5 h, (C): Calcinated at 400 °C for 4.5 h and (D): Calcinated at 800 °C for 4 h

Increase in calcinated temperature (except for 800℃) reduces crystallite size, the catalyst becomes hardened and methanol starved inside of the catalyst and results reducing the yield of ROME. At 800℃ even though the crystallite size was measured to be higher but due to decrease in total surface area and pore volume, the ROME yield decreased.

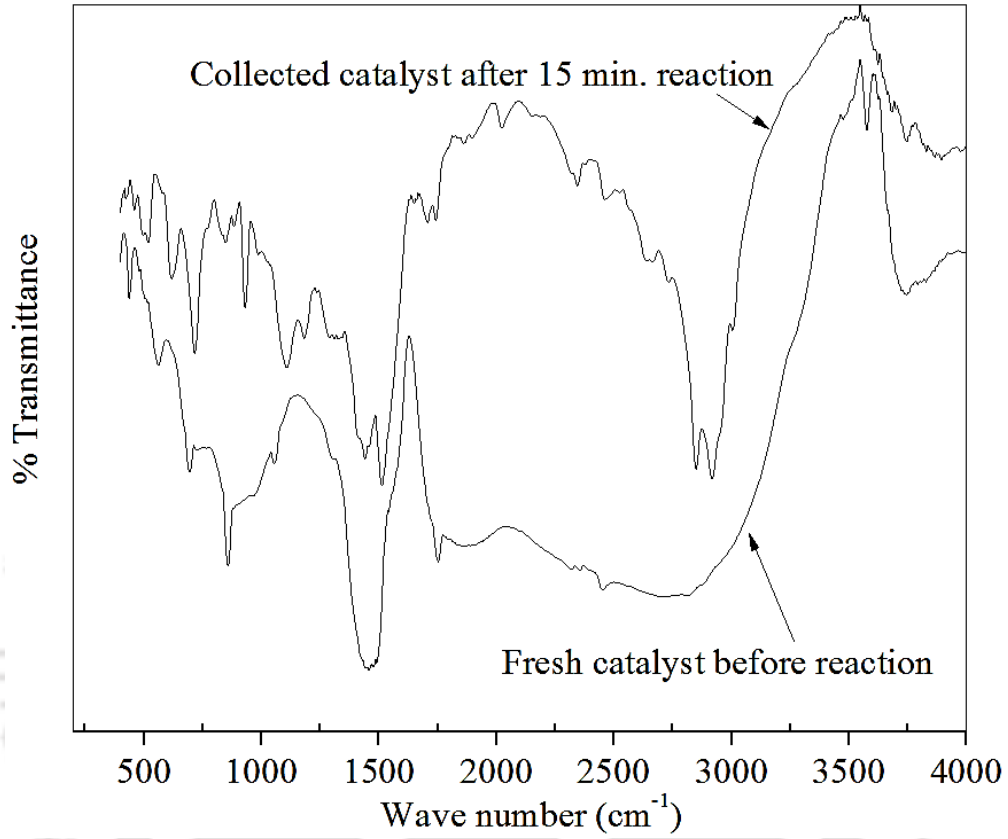

Fig. A4.3: FT-IR of $Ba(OH)_2 \cdot 8H_2O$ before and after transesterification reaction.

The signature on IR spectra of collected solid is quite different than fresh catalyst. Since the conversion of triglyceride of RSO (96%) is high at 15 min reaction time, the by-product bioglycerol reacts with the solid catalyst and forms some barium compound. As a result, the active surface of the collected catalyst is occupied by bioglycerol and catalytic activity of the $Ba(OH)_2 \cdot 8H_2O$ reduces (also observed in adsorption-desorption isotherm)

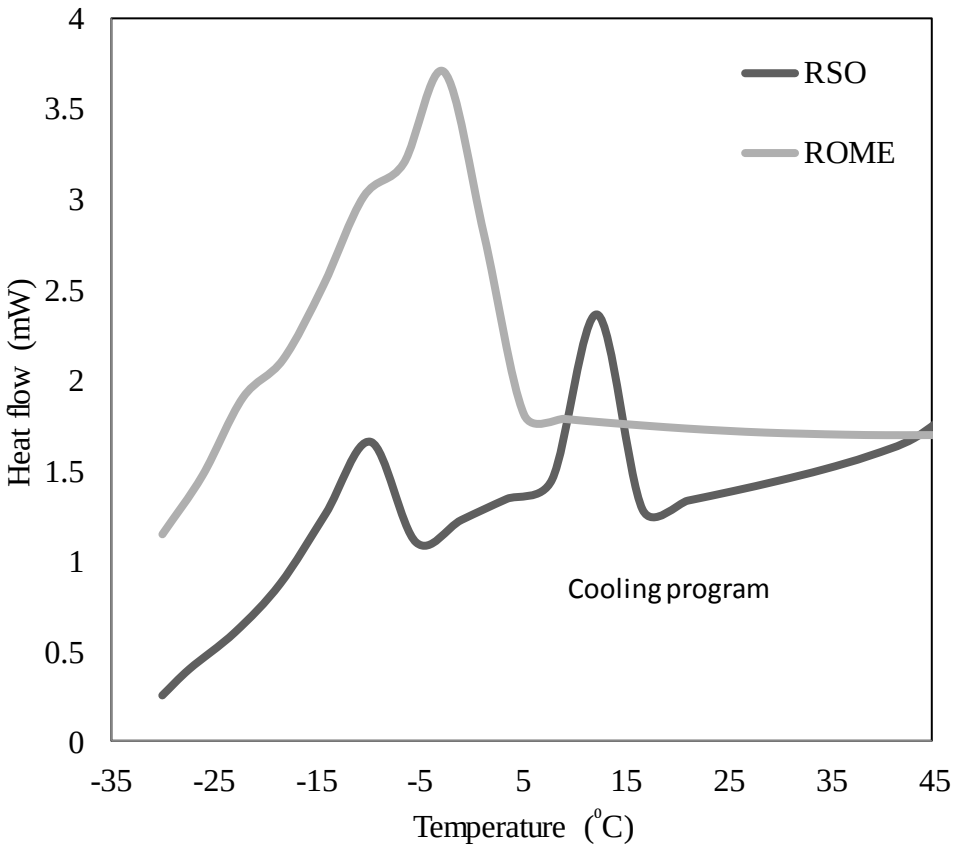

Fig. A4.4: DSC curve of RSO and ROME at cooling rate of 5 °C/min under inert atmosphere. The pour point of the produced RSO and ROME at optimum condition is obtained to be 2.13 and -3 °C.

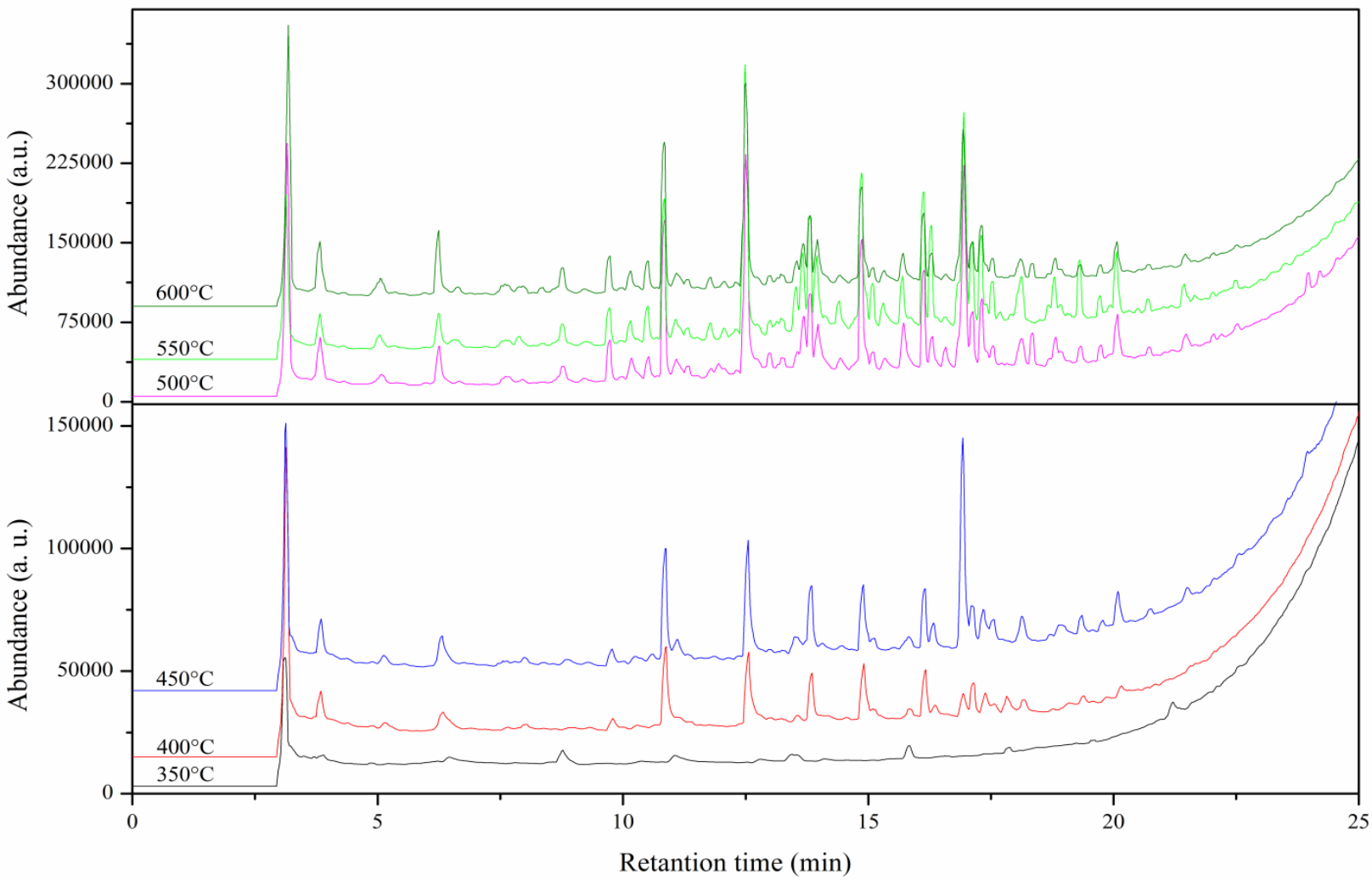

Fig. A6.1A: Signature of the components present in pyrolytic liquid obtained from pyrolysis of RSS samples at different temperatures

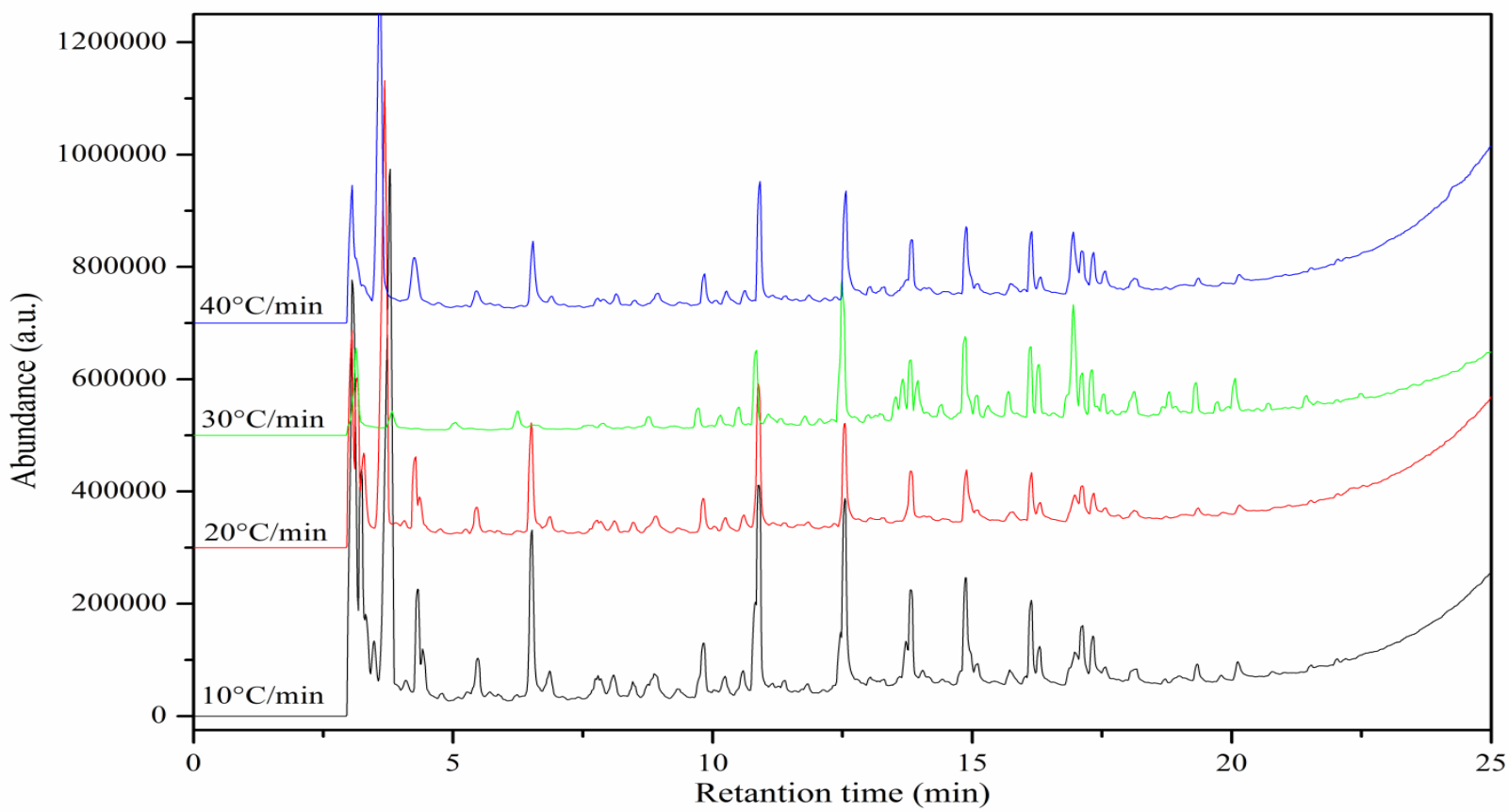

Fig. A6.1B: Signature of the components present in pyrolytic liquid obtained from pyrolysis of RSS samples at heating rates

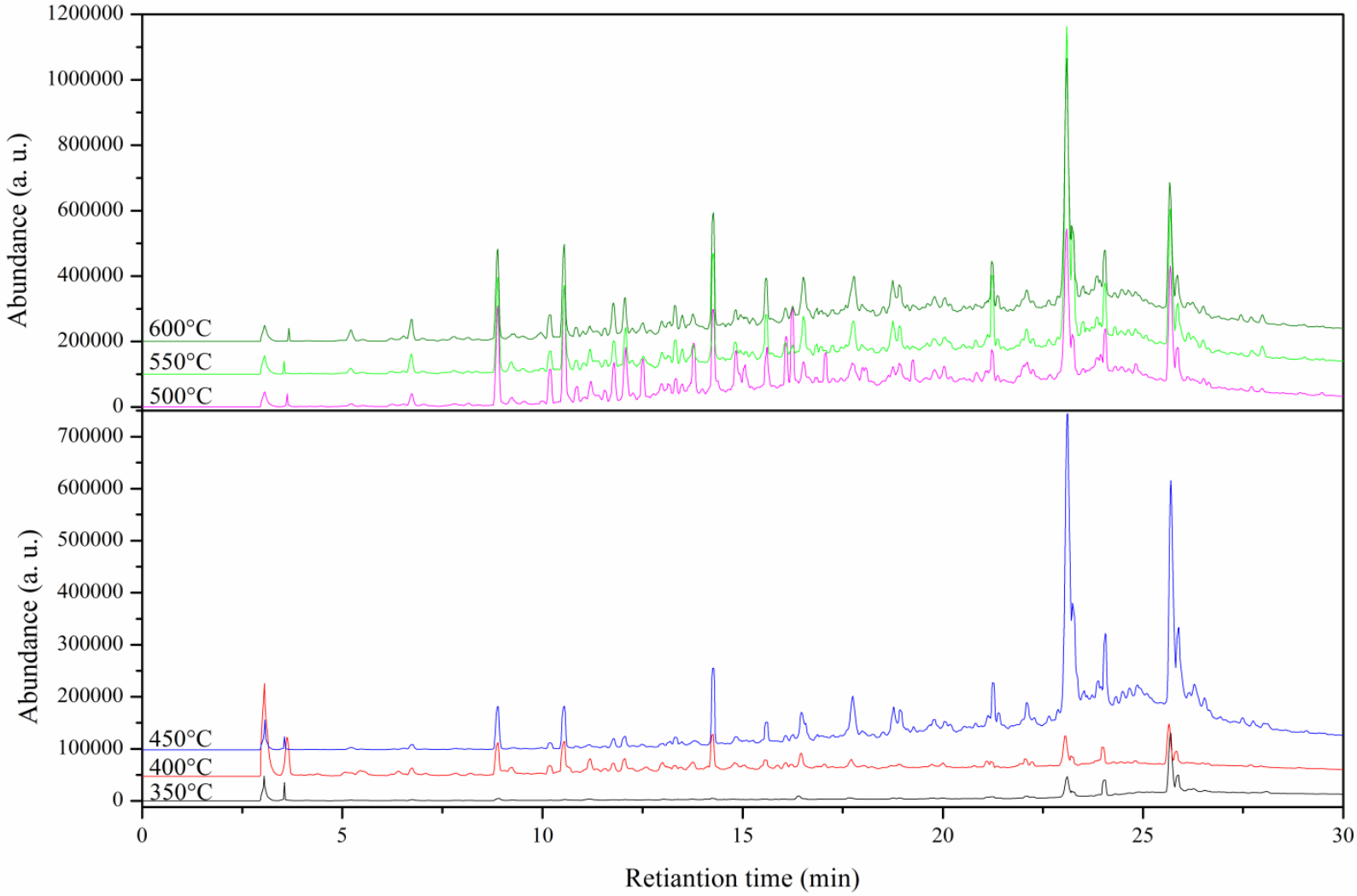

Fig. A6.2A: Signature of the components present in pyrolytic liquid obtained from pyrolysis of RSC samples at different temperature

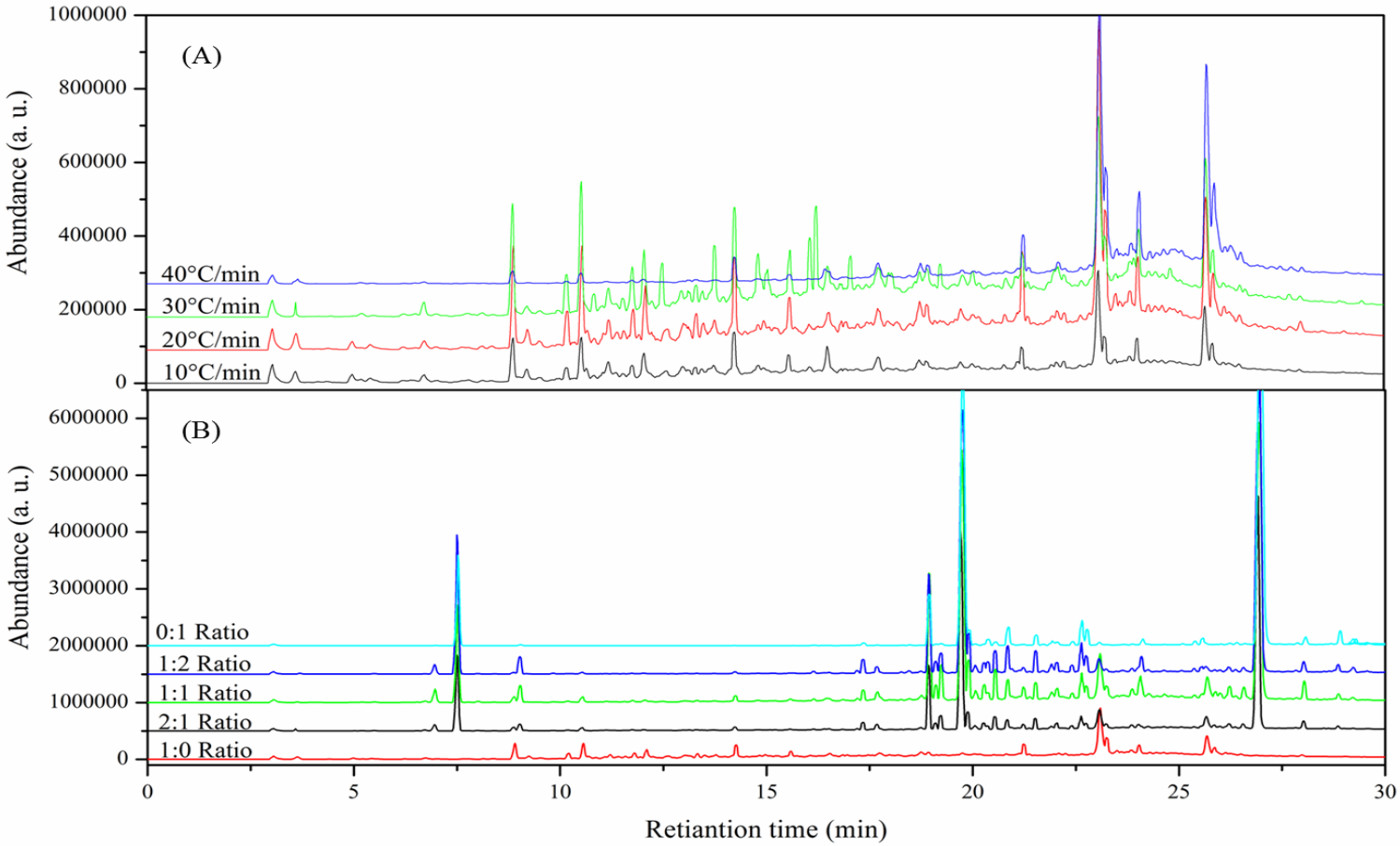

Fig. A6.2B: Signature of the components present in pyrolytic liquid obtained from pyrolysis of RSC samples (A) at different heating rates (B) different ratio of WPS

Table A6.1: Time required for completion of liquid product during RSS pyrolysis

Parameter	Pyrolysis temperature (°C) at 30 °C/min					
	350	400	450	500	550	600
Completion time for pyrolysis (min)	50	40	35	33	26	21
	Pyrolysis heating rate (°C/min) for 500 °C					
	10	20	30	40		
Completion time for pyrolysis (min)	50	30	26	20		

Table A6.2: Percentage of hydrogen based ^{1}H NMR analysis of RSS pyrolytic liquid

Hydrogen type	Chemical shift (ppm)	Pyrolysis temperature (°C)						Pyrolysis heating rate (°C/min)			
		350	400	450	500	550	600	10	20	30	40
CH3 ɤ or further from aromatic ring and parafinic CH3	1.0–0.5	0.97	1.87	2.87	3.2	4.24	3.82	4.57	4.55	4.24	4.31
CH3; CH2 and CH α to aromatic ring	1.5–1.0	1.97	3.44	4.13	4.8	7.06	5.85	6.81	6.55	7.06	5.61
CH2 and CH attached to naphthenes	2.0–1.5	1.24	3.74	4.39	5.44	6.57	7.074	7.67	7.51	6.57	8.24
CH3; CH2 and CH a to aromatic or aceytlenic	3.0–2.0	12.41	15.16	12.64	15.34	23.77	19.31	21.47	20.25	23.77	17.34
Total aliphatics	3.0–0.5	16.6	24.21	24.03	28.79	41.64	36.06	40.52	38.87	41.64	35.5
Hydroxyl, ring-joining, methane or methoxy	4.0–3.0	5.36	6.7	7.712	8.74	10.74	8.872	10.64	11.06	10.74	9.4
Phenols, non-conjugated olefins	6.0–4.0	72.72	59.43	57.25	51.52	18.33	36.63	29.37	31.91	18.33	36.67
Aromatics, conjugated olefins	9.0–6.0	5.32	9.66	11.01	10.95	29.29	18.43	19.46	18.16	29.29	18.42

Table A6.3: Time required for completion of liquid product during RSC pyrolysis

Parameter	Pyrolysis temperature (°C) at 30 °C/min					
	350	400	450	500	550	600
Completion time for pyrolysis (min)	50	48	44	35	30	28
	Pyrolysis heating rate (°C/min) for 500 °C					
	10	20	30	40		
Completion time for pyrolysis (min)	55	35	30	28		
	Ratio of RSC to WPS (weight basis)					
	1:0	2:1	1:1	1:2	0:1	
Completion time for pyrolysis (min)	35	32	30	31	31	

List of Publications

Book Chapter:

i. Ali S. Reshad, Pankaj Tiwari, and Vaibhav V. Goud, 2016, Production of Biodiesel from Renewable Resources, Chapter 9 in Biofuels: Production and Future Perspectives, Ram Sarup Singh Ashok Pandey, Edgard Gnansounou, CRC Press, Taylor & Francis Group, ISBN, 978-1498723596

Journal Publications:

i. Ali S. Reshad, Pankaj Tiwari, Vaibhav V. Goud, *Extraction of Oil from Rubber Seeds for Biodiesel Application: Process Optimization Study.* **Fuel**, 150, 636–644, 2015

ii. Ali S. Reshad, Prasenjit Barman, Ashish J. Chaudhari, Pankaj Tiwari, Vinayak Kulkarni, Vaibhav V. Goud, Niranjan Sahoo, *Rubber Seed Oil Methyl Ester Synthesis, Engine Performance, and Emission Characteristics of Blends.* **Energy & Fuels**, 29, 5136−5144, 2015

iii. Ali S. Reshad, Deoashish Panjiara, Pankaj Tiwari, Vaibhav V. Goud, *Two-step process for Production of Methyl Ester from Rubber Seed Oil Using Barium Hydroxide Octahydrate Catalyst: Process Optimization.* **Journal of Cleaner Production,** 142, 3490–99, 2017.

iv. Ali S. Reshad, Pankaj Tiwari, Vaibhav V. Goud, *Thermal Kinetic Analysis of Rubber Seed Cake and Rubber Seed Shell.* **Journal of Thermal Analysis and Calorimetry,** DOI 10.1007/s10973-017-6136-4

Manuscript communicated and to be communicated:

i. Ali S. Reshad, Pankaj Tiwari, Vaibhav V. Goud, *Thermal degradation kinetic study for rubber seed oil and its methyl esters under inert atmosphere (Under revision in Energy & Fuels)*

ii. Ali S. Reshad, Pankaj Tiwari, Vaibhav V. Goud, *Thermo-chemical conversion of waste rubber seed shell for production of mixture of value-added chemicals and fuel through pyrolysis process (Under review).*

iii. Ali S. Reshad, Pankaj Tiwari, Vaibhav V. Goud, *Co-pyrolysis of rubber seed kernel cake with waste polystyrene for fuels production (To be submitted).*

Conference Presentations (National/International):

i. Ali S. Reshad, Pankaj Tiwari, Vaibhav V. Goud, *Thermochemical treatment of rubber seed for biofuels synthesis.* 22nd International Congress of Chemical and Process Engineering CHISA 2016, 27 to 31 August 2016, Prague, Czech Republic. (Poster)

ii. Ali S. Reshad, Pankaj Tiwari, Vaibhav V. Goud, *Characterization and Utilization of Waste Rubber Seed Shell for Production of Biofuel and Mixture of Value-Added Chemicals.* International Conference on "Waste Management", Recycle-2016, 1-2 April, 2016, Indian Institute of Technology Guwahati, Guwahati, Assam, India.

iii. Ali S. Reshad, Pankaj Tiwari, Vaibhav V. Goud, *Utilization of rubber seed for biofuel synthesis*. 1st International Conference on Bioscience and Biotechnology " Molecular Life Sciences for the Development in the 21st Century", BioTech-2016, The International Institute of Knowledge Management (TIIKM), 12-13 January, 2016, Colombo, Srilanka.

iv. Ali S. Reshad, Pankaj Tiwari, Vaibhav V. Goud, *Rubber seed oil methyl ester synthesis: A comparison study of non-conventional techniques using heterogeneous catalyst*. International Conference on "Chemical Engineering: From Laboratory To Industry", CHEMCON 2015, 27-30 December, 2015, Indian Institute of Technology Guwahati, Guwahati, Assam, India.

v. Ali S. Reshad, Deoashish Panjiara, Pankaj Tiwari, Vaibhav V. Goud, *Biodiesel production using heterogeneous base catalyst: process optimization*. International Conference on "Chemical Engineering-Emerging Dimensions and Challenges Ahead", CHEMCON 2014, 27-30 December, 2014, Dr. S. S. Bhatnagar University Institute of Chemical Engineering and Technology, Panjab University, Chandigarh, India.

vi. Ali S. Reshad, Deoashish Panjiara, Pankaj Tiwari, Vaibhav V. Goud, *Methyl ester production from rubber seed oil using heterogeneous base catalyst: process optimization*. Reflux 2015, March, 27-29, Indian Institute of Technology Guwahati, Guwahati, Assam, India.

vii. Ali S. Reshad, Vaibhav V. Goud, Pankaj Tiwari, *Extraction of oil from rubber seeds for biodiesel application*. Reflux 2014, March, 29-30, Indian Institute of Technology Guwahati, Guwahati, Assam, India.